Computational Investigation of Helical Pipe Geometries From a Mixing Perspective

by

A. N. Cookson

Department of Aeronautics

Imperial College London

Prince Consort Road

London SW7 2BY

This thesis is submitted for the degree of Doctor of Philosophy of the University of London

2009

Declaration

This is to certify that the work presented in this thesis has been carried out at Imperial College London and has not been previously submitted to any other university or technical institution for a degree or award. The thesis comprises only my original work, except where due acknowledgement is made in the text.

Andrew N. Cookson

Abstract

Recent research on small amplitude helical pipes for use as bypass grafts and arterio-venous shunts suggest that in-plane mixing induced by the geometry may help prevent occlusion by thrombosis. In this thesis, a coordinate transformation of the Navier-Stokes equations is solved within a spectral/*hp* element framework to study the flow field and mixing behaviour of small-amplitude helical pipes. An apparent discrepancy between the flow field and particle trajectories is observed, whereby particle paths display a pattern characteristic of a double vortex, though the flow field reveals only a single dominant vortex. It is shown that a combination of translational and rotational reference frames changes resolves this discrepancy.

It is then proposed that joining together two helical geometries, of differing helical radii, will enhance mixing, through the phenomenon of 'streamline crossing'. An idealised prediction of the mixing is obtained by concatenating the velocity field solutions from the respective single helical geometries. The mixing is examined using Poincaré sections, residence time data and information entropy. The flow is then solved for those combined geometries showing the most improvement in mixing, with a 70% increase in mixing efficiency achieved, with only a small increase in pressure loss. It is found that although the true velocity fields vary significantly from the prediction, the overall mixing behaviour is captured, allowing the use of the idealised prediction for guiding future designs of combined geometries.

Acknowledgements

I'd like to thank first, and foremost, my supervisors Prof. Denis J. Doorly and Prof. Spencer J. Sherwin, for their excellent supervision and support. I'm also grateful to them for providing the opportunities to publish my work, both in journals and at conferences. Thanks are due the EPSRC for funding my PhD, not only making it possible, but also providing the freedom to explore the problems most interesting to me. Thanks also to Imperial College, in particular the High Performance Computing Service for their assistance in compiling and running the codes which generated many of my results.

I'd like to thank my colleagues in the Department of Aeronautics for their friendship and support, particularly my L57 officemates, past and present. Special mentions go to Donal Taylor, Peter Vincent and Adrian Lee for the stimulating high-brow discussions, and entertaining low-brow jokes.

Finally, I'd like to thank my parents and my girlfriend Sevil for their patience, support and encouragement over the past few years, without which, none of this would have been possible.

Contents

Declaration i

Abstract ii

Acknowledgements iii

Table of Contents iv

List of Figures x

List of Tables xvii

Nomenclature xviii

1 Introduction 1

1.1 Motivation 1

1.2 Bypass & access grafts 3

1.3 Flow in helical pipes 6

1.3.1 Flow in curved pipes 6

1.3.2 Steady helical pipe flow 8

1.3.2.1 Non-orthogonal coordinate system 10

1.3.2.2 Orthogonal coordinate system 13

1.3.2.3 Helically symmetric coordinate system 17

1.3.2.4 Stability of helical pipe flow 19

1.3.3 Unsteady helical pipe flow 20

1.4 Mixing 22

1.4.1 Dynamical systems approach 23

1.4.1.1 Lyapunov exponents - sensitivity to initial conditions 23

1.4.1.2 Poincaré sections 24

1.4.1.3 Baker's transform 25

1.4.2 Chaotic advection - the blinking vortex 26

1.4.3 Quantifying mixing - information entropy 31

1.5 Aims and Objectives 33

1.6 Organisation of the thesis 34

2 Numerical Methods **35**

2.1 Spectral/*hp* element methods 35

2.1.1 Method of weighted residuals 36

2.1.2 Galerkin formulation applied to the Helmholtz equation 37

2.2 Expansion basis 39

2.2.1 One dimensional expansion 39

2.2.1.1 Jacobi polynomials 40

2.2.2 Extension to two dimensions 42

2.2.3 Elemental mappings for curvilinear elements 44

2.2.4 Extension to three dimensional periodic domains 46

2.3 Solution of the Navier-Stokes equations 47

2.4 Coordinate transformation of the Navier-Stokes equations 49

2.5 Practical considerations for obtaining solutions using *Νεκταr* 52

2.5.1 Initial conditions, time step and convergence 52

2.5.2 Implementation of the pressure drop 53

2.5.3 Achieving convergence for $Re > 250$ 53

2.6 Postprocessing 54

2.6.1 Vorticity 54

2.6.2 λ_2 criterion for vortex identification 55

2.6.3 Particle tracking 56

2.6.3.1 Runge-Kutta time integration 57

2.6.3.2 Particle tracking in physical space 58

2.6.3.3 Particle tracking in parametric space 59

3 Steady Flow & Mixing in Single Helical Geometries 61

3.1 Parameters of study 61

3.2 Velocity field 64

3.2.1 Axial velocity 65

3.2.2 Pressure 67

3.2.3 Axial vorticity 67

3.3 Particle trajectory variation with helical radius 70

3.3.1 Reference frame change explanation 72

3.3.1.1 Translation velocity 73

3.3.1.2 Rotation velocity 73

3.3.2 Vector formulation for particle trajectories 75

3.3.3 Emergence of double vortex structure 78

3.3.4 Wall shear stress 80

3.4 Mixing/stirring 84

3.4.1 Entropic measure 85

3.4.2 Residence time distribution 87

3.4.3 Pressure drop in helical pipe 90

3.4.4 Extension to higher Reynolds number 92

3.4.5 Comment on validity of using straight section helical pipe . . . 95

3.5 Relevance of results to *in vivo* disease processes 96

3.6 Appropriate definition of a vortex for general pipe flows 97

3.7 Conclusions 103

4 Mixing in Multiple Helical Geometries - Idealised Model 104

4.1 Review of existing pipe-based mixing devices 104

4.1.1 Mixing devices utilising 'streamline crossing' 107

4.1.2 Linked Twist Maps 109

4.2 Multiple helical geometries 110

4.3 Mixing: idealised prediction 113

4.3.1 Particle trajectories 113

4.3.2 Residence time distributions and Poincaré sections 122

4.3.3 Entropic measure 126

4.3.4 Optimal mixing - finite time vs. infinite time 128

4.4 Conclusions 130

5 Steady Flow in Multiple Helical Geometries **132**

5.1 Introduction 132

5.1.1 Numerical implementation 132

5.2 Velocity field 135

5.2.1 Pressure loss 138

5.2.2 Wall shear stress 147

5.3 Mixing performance 148

5.3.1 Particle trajectories 148

5.3.2 Residence time distribution and Poincaré sections 155

5.3.3 Entropic measure 156

5.4 Conclusions 159

6 Conclusions and Further Work **161**

6.1 Summary of key results 161

6.2 Further work 163

6.2.1 Physiologically realistic operating conditions 163

6.2.2 Optimisation of multiple helical geometries 165

6.2.3 General pipe flows 166

Bibliography **168**

A Properties of Space Curves **179**

Publications **183**

List of Figures

1.1 Schematics of bypass grafts and arterio-venous shunt configurations . 2

1.2 Planar vs. non-planar graft geometries 4

1.3 *In vivo* results taken from Caro *et al.* (Caro, Cheshire, & Watkins 2005), which show that the helical shunt appears to prevent thrombotic occlusion, whilst the conventional graft does not. 5

1.4 Toroidal coordinate system used by Dean. 7

1.5 Different helical geometries, for increasing radius and decreasing pitch length (left-to-right). Helix (a) is typical of those proposed for use as a prosthetic graft, whilst helix (c) is approaching a toroidal geometry. Corresponding curvature and torsion values are given in Table 1.1. . . 10

1.6 Helical coordinate system used by Wang 12

1.7 Helical coordinate system used by Germano 13

1.8 Helical coordinate system used by Mestel and Zabielski 18

1.9 Physiological pressure gradient waveform (taken from (McDonald 1974)) 21

1.10 The baker's transform defined for a square. 26

1.11 The blinking vortex flow studied by Aref, operating under the blinking function defined in eqn (1.47). 28

1.12 Poincaré sections of the blinking vortex flow, for $\beta = 0.5$. As μ increases the regular regions disappear, and are replaced by chaotic trajectories. (Taken from (Aref 1984)). 29

1.13 Stirring of a square blob of particles by the blinking vortex flow for $\beta = 0.5$ and $\mu = 2.0$, at times (a) $t = 2$, (b) $t = 4$, (c) $t = 6$, (d) $t = 12$. (Taken from (Aref 1984)). 30

1.14 Concept of box-counting used in entropic measure of mixing 32

2.1 Overview of the spectral/hp element philosophy, showing spatial discretisation combined with high-order polynomial representations within each element (taken from (Sherwin & Karniadakis 2005)). 36

2.2 Modal expansion modes, $\psi(\xi)$, defined in eqn (2.23), for polynomial order $P = 5$. 42

2.3 2-D modal expansion modes, $\phi_{pq}(\xi_1, \xi_2)$, defined in eqn (2.25), for polynomial order $P = 4$. 43

2.4 Standard regions for the quadrilateral and triangular expansions, and the mapping between them. 43

2.5 2-D modal expansion modes, $\phi_{pq}(\xi_1, \xi_2)$, defined in eqn (2.29), for polynomial order $P = 4$. 44

2.6 Illustration of the use of curved mesh elements. 46

2.7 Coordinate transformation concept applied to small amplitude helical pipes 50

3.1 Examples of the helical geometries under consideration in this thesis. 63

3.2 Helical pipe geometry, $R = 0.25D$, with self-similar axial velocity profile. The origin $x = 0 = y$ is marked by a small cross. An example point on the pipe wall highlights the rotation of the velocity field along the axis 65

3.3 Axial velocity (cm/s) (upper) and axial vorticity (s^{-1}) (lower) contours at $z = 6D$. The zero level of vorticity is marked by a white line, highlighting the dominant vortical structure. 66

3.4 Radial offset of peak axial velocity, w, vs. helical radius. 66

3.5 Line-of-sight properties for increasing helical radius. The blue cross marks the location of the peak axial velocity, and the green cross the helical centreline. The black cross is the $x = 0 = y$ axis, and the dashed black circle corresponds to the line-of-sight region, which disappears when $R = 0.5D$. The outer black circle is the boundary that contains the helical pipe. 68

3.6 Pressure contour slices, taken at $z = 0$, for increasing helical radius . 69

3.7 Circulation (cm^2/s), Γ, of dominant vortex vs. helical radius 70

3.8 Particle trajectory slices at $z = 30D$ (five pitches) for varying helical radius 71

3.9 Smoke visualisation results of Yamamoto *et al* showing the double-vortex structure similar to those found in the particle tracking results presented here. $\beta_0 = \lambda/\sqrt{2\delta} = \tau/(\kappa\sqrt{(\kappa D)})$, is a measure of the relative strengths of torsion and curvature. For the purposes of comparison the geometries considered in this thesis are in the range of $\beta_0 \approx 3 - 30$. 72

3.10 In-plane velocity (cm/s) transformations to obtain particle trajectories 74

3.11 Particle trajectory slices for $R = 0.25D$, at intervals of $z = 1.5D$, from $z = 0$ to $z = 6D$, showing the rotation of the velocity field that is moving the fluid particles. 76

3.12 Vector diagram of rotation of cross-section, with a point P that lies within the plane where (r, ϕ) are the polar co-ordinates relative to the centre of the pipe cross-section. O is the axis $x = 0 = y$ and the dashed line is the projection of the helical centreline onto the plane. . 77

3.13 Comparison of in-plane velocity (cm/s) components for varying helical radius, which explains emergence of double vortex structure in particle trajectories. Left - $R = 0.1D$, Middle - $R = 0.3D$, Right - $R = 0.5D$ 79

3.14 Wall shear stress (N/cm^2) distributions for increasing helical radius. Angular position corresponds to that on the pipe boundary, with the radial value representing the magnitude of wall shear stress, $|wss|$, at that angular position. 82

3.15 Analysis of wall shear stress magnitude data. The angular location of the minimum $|wss|$ is found to be well correlated with the position of the point of separation from the wall, as shown by the particle trajectories. The correspondence between angular locations of maximum $|wss|$ and peak axial velocity, improves with helical radius, as the peak velocity moves towards the wall, thus creating larger velocity gradients there. 83

3.16 Particle trajectory slices for $R = 0.25D$ at integer multiples of the pitch length 84

3.17 Relative entropy increase, K, vs. helical radius. 86

3.18 Particle residence time distributions for varying helical radius 89

3.19 Statistics of the particle residence time distributions for varying helical radius 90

3.20 Dye visualisation results from Caro *et al.* (2005) that correspond to particle residence time statistics. The helical pipe (right) is clearly more effective at transporting the dye out of the bend than the conventional cylindrical pipe (left). 91

3.21 Pressure drop incurred for one pitch length vs. helical radius. 92

3.22 Axial velocity profiles (cm/s) and axial vorticity (s^{-1}) at $Re = 500$ for several helical geometries 94

3.23 Streamtraces of $\mathbf{V}_{in-plane}$ (cm/s) for $Re = 250$ and 500 for several helical geometries 94

3.24 λ_2 contour slices, taken at $z = 0$, for increasing helical radius. The grey region indicates the vortical structure as identified by a value of $\lambda_2 < -0.3$ 100

3.25 Q-criterion contour slices, taken at $z = 0$, for increasing helical radius. The grey region indicates the vortical structure as identified by a value of $Q > 0$. 101

3.26 Δ-criterion contour slices, taken at $z = 0$, for increasing helical radius. The grey region indicates the vortical structure as identified by a value of $\Delta > 0$. 102

4.1 Streamline crossing concept in twisted pipe configuration and combined helical geometries 106

4.2 The partitioned pipe mixer - an idealisation of the Kenics mixer. . . . 109

4.3 Particle trajectory slices, $R_A = 0.25$ and $R_B = 0.2$ 116

4.4 Particle trajectory slices, $R_A = 0.35$ and $R_B = 0.3$ 117

4.5 Particle trajectory slices, $R_A = 0.4$ and $R_B = 0.2$ 118

4.6 Particle trajectory slices, $R_A = 0.5$ and $R_B = 0.2$ 119

4.7 Particle trajectory slices, $R_A = 0.5$ and $R_B = 0.25$ 120

4.8 Particle trajectory slices, $R_A = 0.5$ and $R_B = 0.3$ 121

4.9 Initial particle distribution, coloured by total residence time of the particle over six pitch lengths. 123

4.10 Poincaré sections generated by 50 iterations of the combined mapping. 124

4.11 Relative entropy increase, K, plotted against normalised pressure drop for one pitch length of the geometry. The black line indicates the trend for the single helical geometries, and the black dot the only combined geometry that does not enhance mixing. All other combined geometries show a substantial increase in K. 127

4.12 Relative entropy increase, K, plotted against angle between the vortical dividing lines of the combined geometries. 129

5.1 Locations of the slices of the velocity field, shown on geometry $R_A = 0.2D$ and $R_B = 0.5D$ 133

5.2 Spline fit in the region of the joint, showing that the approximation to the sinusoidal functions is good, yet attaining a smooth transition at the joint 134

5.3 Comparison of the derivatives of the spline functions and the helical functions in the region of the junction. 136

5.4 Axial velocity (cm/s) contours for case $R_A = 0.2D$ and $R_B = 0.5D$, $Re = 125$. 139

5.5 Vorticity (s^{-1}) contours for case $R_A = 0.2D$ and $R_B = 0.5D$, $Re = 125$. The zero vorticity contour line is coloured white to highlight the vortical structure 140

5.6 Wall shear stress (N/cm^2) magnitude for case $R_A = 0.2D$ and $R_B = 0.5D$, $Re = 125$ 141

5.7 Axial velocity (cm/s) contours for case $R_A = 0.2D$ and $R_B = 0.5D$, $Re = 250$. 142

5.8 Axial vorticity (s^{-1}) contours for case $R_A = 0.2D$ and $R_B = 0.5D$, $Re = 250$. The zero vorticity contour line is coloured white to highlight the vortical structure 143

5.9 Wall shear stress (N/cm^2) magnitude for case $R_A = 0.2D$ and $R_B = 0.5D$, $Re = 250$ 144

5.10 Radial offset of the peak axial velocity for flow in the combined geometry of $R_A = 0.2D$ and $R_B = 0.5D$, showing the comparison with the respective single geometry results, for $Re = 125$ and $Re = 250$ . . 145

5.11 Circulation (cm^2/s) of dominant vortical structure for flow in the combined geometry of $R_A = 0.2D$ and $R_B = 0.5D$, showing the comparison with the respective single geometry results, for $Re = 125$ and $Re = 250$ 146

5.12 Streamtraces of $\mathbf{V}_{in-plane}$ (cm/s) for $R_A = 0.2D$ and $R_B = 0.5D$, $Re = 250$ 150

5.13 Streamtraces of $\mathbf{V}_{in-plane}$ (cm/s) for $R_A = 0.25D$ and $R_B = 0.5D$, $Re = 250$ 151

5.14 Particle trajectory slices, for $R_A = 0.2$ and $R_B = 0.5$ at intervals of $z = 1.5D$ 152

5.15 Particle trajectory slices, $R_A = 0.2$ and $R_B = 0.5$ 153

5.16 Particle trajectory slices, $R_A = 0.25$ and $R_B = 0.5$ 154

5.17 Residence time colour scatter plot (left) and Poincaré sections (right). 156

5.18 Relative entropy increase, K, for combined geometries, showing evolution with axial location, and comparing idealised prediction with particle tracking in actual velocity field. 158

List of Tables

1.1 Curvature and torsion data for helical curves shown in Figure 1.5 . . 9

3.1 Normalised curvature and torsion data for helical geometries under consideration (to 3 s.f.) 63

4.1 Angle (in degrees) between the vortex dividing lines in each helical geometry. The combinations selected for investigation are underlined. 112

4.2 Helical radii of the eleven combined helical geometries considered . . 113

4.3 The six combined geometries for which particle trajectory slices are shown in Figures 4.3 - 4.8 114

5.1 Pressure loss for combined helical geometries, showing the pressure loss for each component geometry, the idealised prediction (simply the mean of the components) and the actual pressure loss incurred. The values of the pressure loss have been normalised by that for Poiseuille flow at the same Reynolds number. The final row shows the correction factor to be applied to the idealised prediction of pressure loss. 147

5.2 Pressure loss, at $Re = 250$, for the two combined helical geometries considered in this Chapter, compared with the idealised prediction from Chapter 4. 159

Nomenclature

A-V	Arterio-venous
ePTFE	expanded polytetrafluoroethylene/Teflon
$\mathbf{A}$	d'Alembert body force
c	Helical pitch length parameter
D	Pipe internal diameter
R	Helical radius
R_A, R_B	Helical radii of geometries A and B in combined helical pipes
κ	Centreline curvature
τ	Centreline torsion
Dn	Dean number
Gn	Germano number
K	Relative information entropy increase
Re	Reynolds number
Tn	Torsion number
p	Pressure
x, y, z	Cartesian coordinates
u, v, w	Cartesian velocity components
$\mathbf{T}, \mathbf{N}, \mathbf{B}$	Frenet vector triad
Γ	Circulation of a vortex
$\boldsymbol{\omega}$	Vorticity vector
$\mathbf{S}$	Symmetric rate-of-strain tensor
$\boldsymbol{\Omega}$	Anti-symmetric vorticity tensor
ν	Kinematic viscosity

Chapter 1

Introduction

1.1 Motivation

There are almost 198,000 deaths each year in the UK caused by cardiovascular disease, which is just over a third of total deaths (Allender, Peto, Scarborough, Kaur, & Rayner 2008). Roughly half of these deaths are due to coronary heart disease, which is the disruption of the heart's blood supply, due to the narrowing or occlusion of the coronary arteries. The narrowing is caused by atherosclerosis, which is the accumulation of fatty deposits in the arterial wall.

Mild coronary heart disease can be treated by angioplasty, which involves widening the artery by inflating a balloon catheter inside it. More severe stenosis (narrowing) of arteries can be treated with a stent, which are fine wire mesh tubes that are inflated inside the vessel, thus acting as a scaffold to keep narrow vessels open. Many designs of stent are available, a review of which is available in (Colombo & Tobis 2000). For more severe cases, the blood flow must be redirected around the occluded region using a vascular graft, constructed either from autologous vein or synthetic materials. Vascular grafts will be the focus of this review.

Patients suffering from chronic kidney disease often require haemo-dialysis, to ar-

tificially filter out waste products from the blood. To achieve efficient dialysis a flow-rate of 350 ml/min is required, which is greater than that in the blood vessels of the limbs. It is therefore necessary to construct an access vessel that will provide this flow rate. These are often constructed from autologous vein. However, in some patients, particularly the elderly and diabetics, the vessels are too poor, and therefore synthetic grafts (Hakaim & Oldenburg 2001) must be used instead. Clinical practice also varies between countries, with the U.S. using a much greater proportion of synthetic grafts than other nations. The access vessels, often termed shunts, form a direct link between an artery and a vein, thus bypassing the resistance of the capillaries, and allowing the necessary large flow rate.

Schematics of both bypass grafts and arterio-venous (A-V) shunts are shown in Figure 1.1.

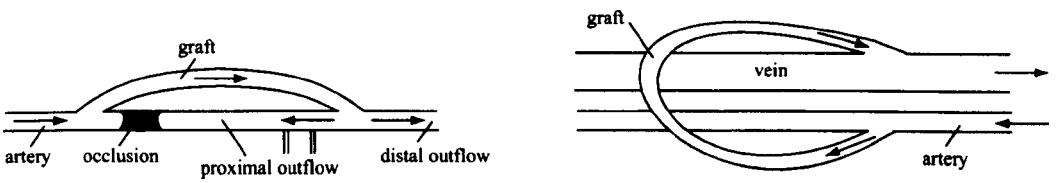


Figure 1.1: Schematics of bypass grafts and arterio-venous shunt configurations

Almost 30,000 coronary artery bypass graft (CABG) procedures are performed each year in the UK according to the British Heart Foundation (Allender, Peto, Scarborough, Kaur, & Rayner 2008), however over 50% of CABG fail within 10 years due to the development of neo-intimal hyperplasia (Bryan & Angelini 1994).

Similarly, arterio-venous shunts constructed from ePTFE (expanded polytetrafluoroethylene or Teflon) are prone to occlusion by thrombosis and intimal hyperplasia. In the United States alone there are 175,000 ePTFE grafts used for permanent vascular access. A systematic review and meta-analysis of relevant data found that one-year primary and secondary patency* rates of current ePTFE hemodialysis grafts

*Primary patency is when the graft continues to function without any intervention, whilst

are roughly 40% and 66% respectively (Huber, Carter, Carter, & Seeger 2003), with two-year primary and secondary patency rates of 27% and 51% respectively.

Briefly, intimal hyperplasia is a response to injury, resulting in the thickening of the intimal layer of the artery wall. If this thickening is substantial, it can effectively re-stenose the blood vessel, thus requiring further treatment for the patient. For artificial grafts, the intimal hyperplasia occurs at the junction between the graft and host vessel, particularly around the suture line, which may occur partially due to compliance mis-matches between the walls of the graft and artery, and partially the mechanical injury of the suture itself.

Thrombosis is simply the clotting of blood within a blood vessel, and is most familiar from deep vein thrombosis (DVT) and in the brain's arteries, often leading to strokes. Like intimal hyperplasia, thrombosis can cause occlusion, but in this case, usually forms within the graft section itself. This is because the graft surface is thrombogenic, due to the absence of endothelial cells there.

The widespread usage of bypass and access grafts mean that design changes leading to improved patency rates will have important health and economic advantages. Consequently, much research has been conducted in the past few decades to design grafts that will remain patent for far longer, ideally longer than the life-span of the patient. A brief summary of these attempts follows in Section 1.2.

1.2 Bypass & access grafts

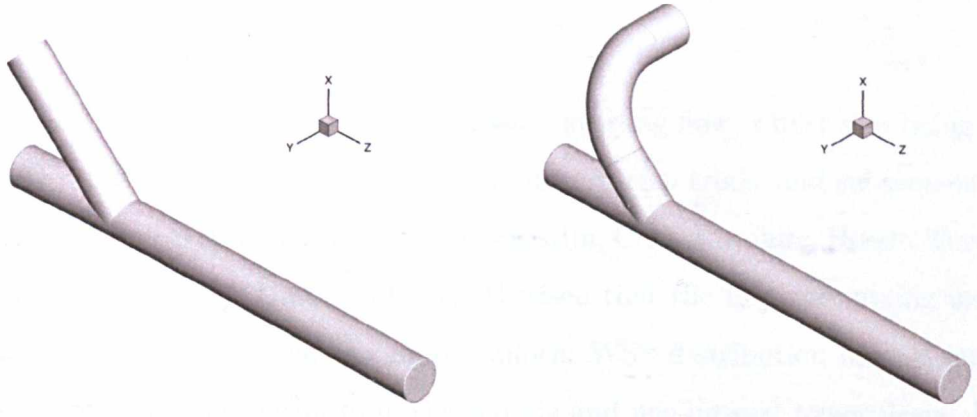
A common idealisation of bypass grafts is to assume that the graft lies in the same plane as the host artery, and simply intersects it at some angle (often taken to be 45^o), as shown in Figure 1.2(a). The flow in such a geometry usually possesses several features; planar symmetry of the secondary flow, a stagnation point on the lower wall of the host artery and extremes of wall shear stress. It is thought that all

secondary patency is when the graft requires some intervention to remain patent. Therefore, secondary patency rates reflect the additional workload that complications create.

of these factors contribute to the neo-intimal hyperplasia and thrombosis that cause grafts to become occluded.

Several design alterations have been examined in an attempt to create a more favourable flow environment, for example, changing the angle of the junction, or using a larger radius of pipe for the graft section. A tapered geometry has also been considered, but when compared with a constant diameter graft in a computational study, haemodynamic performance in terms of wall shear stress gradients showed no improvement (Tricht, Wachter, Tordoir, & Verdonck 2006), confirming results of a clinical trial (Dammers, Planken, Pouls, van Det, Burger, van der Sande, & Tordoir 2003).

A promising avenue of this research, initiated by Caro *et al.* (Caro, C. G., Doorly, D. J., Tarnawski, M., Scott, K. T., Long, Q., & Dumoulin, C. L. 1996) (Sherwin, Shah, Doorly, Peiro, Papaharilaou, Watkins, Caro, & Dumoulin 2000), is to use out-of-plane geometries, that induce fully three-dimensional, physiologically realistic swirling flows, and produce more uniform wall shear stress distributions. Figure 1.2 shows the corresponding planar and non-planar grafts studied by Sherwin *et al* (Sherwin, Shah, Doorly, Peiro, Papaharilaou, Watkins, Caro, & Dumoulin 2000). An alternative non-planar geometry that is also found to induce swirling flow, was investigated in (How, Fisher, Brennan, & Harris 2006).



(a) Planar graft (b) Non-planar graft

Figure 1.2: Planar vs. non-planar graft geometries

However, in a clinical environment, such geometries cannot be guaranteed to be preserved after wound closure. Greater control of the geometry is possible with vascular prostheses, with small amplitude helical pipes being proposed (Caro, Cheshire, & Watkins 2005) (Caro, Watkins, & Sherwin 2005). Figure 1.3, taken from an *in vivo* study by Caro *et al.* (Caro, Cheshire, & Watkins 2005), shows slices of a conventional graft, and a helical graft, which were both fitted inside a pig for eight weeks, in an A-V shunt configuration. The conventional graft is fully occluded by thrombosis, stained black for clarity, whilst the helical graft is clear throughout. This clearly demonstrates the potential improvements in patency that the helical graft appears to offer.



(a) Conventional graft (b) Helical graft

Figure 1.3: *In vivo* results taken from Caro *et al.* (Caro, Cheshire, & Watkins 2005), which show that the helical shunt appears to prevent thrombotic occlusion, whilst the conventional graft does not.

The helical geometry induces the necessary swirling flow, whilst also being mechanically robust, and has undergone preliminary *in-vivo* trials, and subsequently a preliminary clinical study (Huijbregts, Blankestijn, Caro, Cheshire, Hoedt, Tutein Nolthenius, & Moll 2007). Caro *et al.* hypothesised that the in-plane mixing induced by the helical geometry and the more uniform WSS distribution are responsible for preventing graft occlusion from thrombosis and neo-intimal hyperplasia. However, the mechanisms by which this may occur are not specified.

1.3 Flow in helical pipes

The flow in helical pipes has been investigated previously, motivated initially by basic scientific interest, but later their relevance to industrial applications such as chemical reactors and heat exchangers (Ju, Huang, Xu, Duan, & Yu 2001) (Rennie & Raghavan 2006). The realisation that physiological flows, such as that in the human aorta, involve both curvature and torsion (Caro, C. G., Doorly, D. J., Tarnawski, M., Scott, K. T., Long, Q., & Dumoulin, C. L. 1996), provided additional motivation to studying helical pipes (Zabielski & Mestel 1998), they being the simplest of such geometries. Before examining the existing literature on helical pipes flows, a basic summary of flow in curved pipes is first presented. This background provides a useful base from which to understand both the solution techniques, and the results, found in the helical pipe literature.

1.3.1 Flow in curved pipes

Secondary flow in curved pipes was first reported by Eustice (Eustice 1910), (Eustice 1911), in his experiments injecting ink into water flowing through a coiled pipe. The first theoretical treatment of the problem was given by Dean (Dean 1928), which used the toroidal coordinate system (r', α, θ) shown in Figure 1.4. The non-dimensional Navier-Stokes equations are written in this coordinate system, and then simplified. First, the velocities are rescaled to make the centrifugal-force terms the same order of magnitude as the viscous and inertial terms, as it is the centrifugal force that drives the secondary motion.

Two parameters characterise the flow in curved pipes, the Dean number, Dn and the curvature, δ. They are defined:

$$\delta = a/R \tag{1.1}$$

$$Dn = 2\delta^{1/2}Re = \left(\frac{a}{R}\right)^{1/2}\left(\frac{2a\overline{W_0}}{\nu}\right) \tag{1.2}$$

The Dean number is essentially a modified Reynolds number. The loose coiling

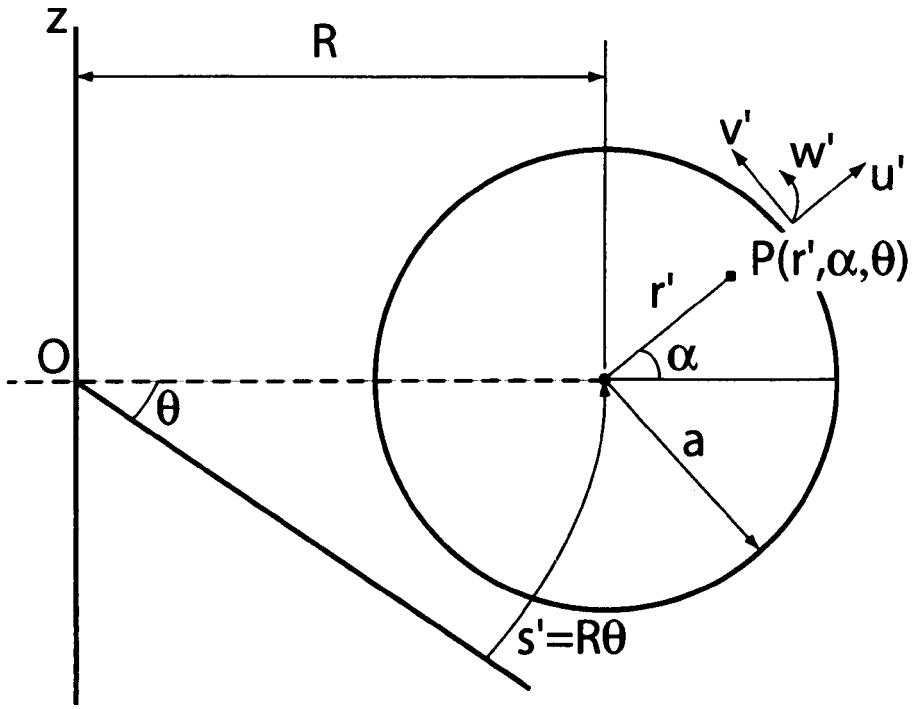


Figure 1.4: Toroidal coordinate system used by Dean.

assumption that the pipe has very small curvature, i.e. $\delta = a/R \ll 1$ is applied by setting the δ terms to zero (though not inside the Dn terms). The flow is also assumed to be fully developed, that is, independent of axial position, which gives the final formulation of the equations as:

$$\nabla_1^2 w - \frac{Dn}{2}\frac{\partial p_0}{\partial z} = \frac{Dn}{2r}(\psi_\alpha w_r - \psi_r w_\alpha) \tag{1.3}$$

$$\frac{2}{Dn}\nabla_1^4\psi + \frac{1}{r}\left(\psi_r\frac{\partial}{\partial\alpha} - \psi_\alpha\frac{\partial}{\partial r}\right)\nabla_1^2\psi = -2w\left(\sin\alpha w_r + \frac{cos\alpha}{r}w_\alpha\right) \tag{1.4}$$

with the boundary conditions

$$\psi = \psi_r = w = 0 \quad at \quad r = 1 \tag{1.5}$$

where

$$\nabla_1^2 \equiv \frac{\partial^2}{\partial r^2} + \frac{1}{r}\frac{\partial}{\partial r} + \frac{1}{r^2}\frac{\partial^2}{\partial\alpha^2} \tag{1.6}$$

For small Dean numbers the solution is a series expansion of powers of Dn.

$$w = \sum_{n=0}^{\infty} Dn^{2n} w_n(r,\alpha), \quad \psi = Dn \sum_{n=0}^{\infty} Dn^{2n} \psi_n(r,\alpha) \tag{1.7}$$

The primary flow, w_0, is Poiseuille flow, and the secondary flow, ψ_1, is a symmetric pair of counter-rotating helical vortices. A centrifugal pressure gradient is formed, which drives slower-moving fluid near the wall inward. The faster moving fluid in the core is moved, which is the second-order correction to the axial velocity, w_2. There are several consequences of the secondary flow formation; the flow rate is reduced from an equivalent Poiseuille flow, extremes of shear stress form at the inner and outer bends and the transition to turbulence is delayed.

Many further studies of flow in curved pipes have been performed since, both theoretical and numerical, summarised in the comprehensive reviews by Berger *et al.* (Berger, Talbot, & Yao 1983) and Ito (Ito 1987). It continues to be an active area of research, with recent work studying the effects of oscillatory flow, finite curvature (Siggers & Waters 2008) and elastic walls.

1.3.2 Steady helical pipe flow

A helix is a three-dimensional space curve that can be described by the parametric equations:

$$x = R\cos t, \tag{1.8}$$

$$y = R\sin t, \tag{1.9}$$

$$z = ct, \ 0 \leq t \leq 2\pi, \tag{1.10}$$

where R is the radius or amplitude of the helix and c is a constant parameter, such that the wavelength, or one pitch length, of the helix equals $2\pi c$. The curvature is denoted κ, and the torsion τ . They are defined thus:

$$\kappa = \frac{R}{R^2 + c^2}, \ \tau = \frac{c}{R^2 + c^2} \tag{1.11}$$

These expressions clearly show that the ratio of curvature to torsion is a constant, equal to R/c, indeed Lancret's theorem (Scofield 1995) states that this is a necessary and sufficient condition for a curve to be a helix.

The helical centreline equations can be written as a vector $\mathbf{R}(t)$

$$\mathbf{R}(t) = R\cos t\mathbf{i} + R\sin t\mathbf{j} + ct\mathbf{k} \tag{1.12}$$

Alternatively, this can be parameterised in terms of the arc length s, which is given by

$$s = \int_0^t \sqrt{\left(\frac{dx}{dt}\right)^2 + \left(\frac{dy}{dt}\right)^2 + \left(\frac{dz}{dt}\right)^2}\, dt \tag{1.13}$$

For a helix, the arc length simply increases linearly with the parameter t, and evaluates to

$$s = \sqrt{R^2 + c^2}\, t \tag{1.14}$$

The Frenet triad of tangent $\mathbf{T}$, normal $\mathbf{N}$ and binormal $\mathbf{B}$ unit vectors of a curve $\mathbf{R}(s)$ are defined as:

$$\mathbf{T} = \frac{d\mathbf{R}}{ds},\ \mathbf{N} = \frac{1}{\kappa}\frac{d\mathbf{T}}{ds},\ \mathbf{B} = \mathbf{T} \times \mathbf{N} \tag{1.15}$$

where κ is the curvature introduced earlier. Figure 1.5 shows several different helical geometries for varying parameter values, the properties of which are given in Table 1.1. This figure indicates that one limit of a helical geometry is a straight pipe, with the other limit a toroidal pipe.

Table 1.1: Curvature and torsion data for helical curves shown in Figure 1.5

Helix	Pitch	Radius	Curvature κ	Torsion τ
a	6	0.5	0.430	0.822
b	2	1.5	0.638	0.135
c	0.5	3	0.0796	0.00884

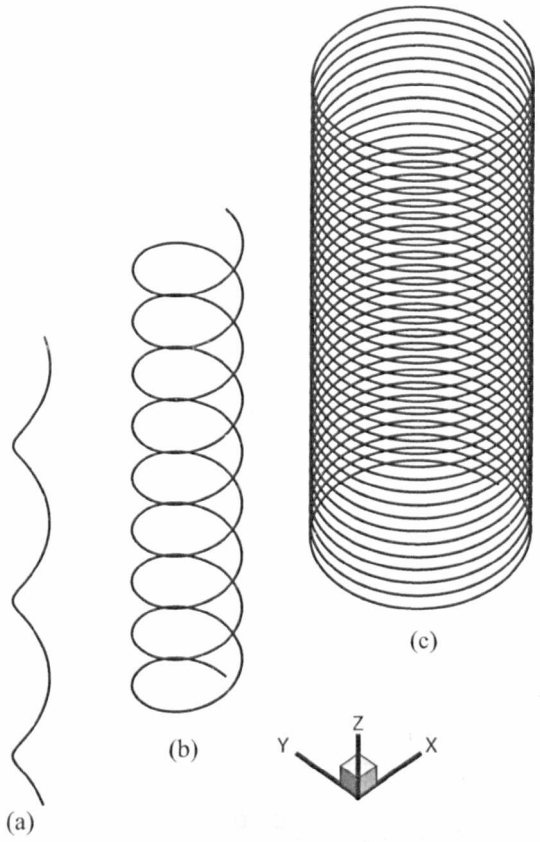


Figure 1.5: Different helical geometries, for increasing radius and decreasing pitch length (left-to-right). Helix (a) is typical of those proposed for use as a prosthetic graft, whilst helix (c) is approaching a toroidal geometry. Corresponding curvature and torsion values are given in Table 1.1.

1.3.2.1 Non-orthogonal coordinate system

The first paper to consider the problem of flow in helical pipes from a theoretical perspective was by Wang (Wang 1981), who cast the Navier-Stokes equations in a non-orthogonal helical coordinate system. This is shown in Figure 1.6, and the key details follow.

The first axis of the coordinate system is given by the vector equation of the centreline (eqns (1.8) - (1.10)):

$$\mathbf{R} = X(s)\mathbf{i} + Y(s)\mathbf{j} + Z(s)\mathbf{k} \tag{1.16}$$

where s is the arc length along the axis, and $\mathbf{i}, \mathbf{j}, \mathbf{k}$ are the standard unit vectors in a Cartesian frame. A coordinate system (r, θ, s) can then be defined, such that a Cartesian vector $\mathbf{x}$ is given by:

$$\mathbf{x} = \mathbf{R}(s) + r\cos\theta\mathbf{N}(s) + r\sin\theta\mathbf{B}(s) \tag{1.17}$$

The definition of the pipe boundary follows naturally by setting $r = D/2$, an additional parameter that is the internal radius of the pipe. That is:

$$\mathbf{x}_{WALL} = \mathbf{R}(s) + (D/2)\cos\theta\mathbf{N}(s) + (D/2)\sin\theta\mathbf{B}(s) \tag{1.18}$$

Taking the dot product of the incremental change of eqn (1.17) with itself gives:

$$d\mathbf{x}.d\mathbf{x} = (dr)^2 + r^2(d\theta)^2 + [(1 - \kappa r\cos\theta)^2 + \tau^2 r^2](ds)^2 + \underbrace{2\tau r^2 ds d\theta}_{non-orthogonality} \tag{1.19}$$

It is the last term in eqn (1.19) which highlights the non-orthogonal nature of this coordinate system. The physical consequence of this non-orthogonality is that the axial velocity w is not perpendicular to the (r, θ) plane.

Wang's analysis assumes that the pipe is long enough for end effects to be ignored, that is, the velocities are independent of s, or fully developed. In addition, both the curvature and torsion are assumed to be small, with the flow steady and laminar, for a Reynolds number of order unity.

For small curvature and torsion the axial flow w_0 is dominant, and is found to be Poiseuille flow. This allows a series expansion of the form

$$w = U\sum_{i=0}^{n}\epsilon^i w_i \tag{1.20}$$

for the axial velocity, where U is a velocity scale proportional to the axial pressure gradient, and $\epsilon = \kappa a \ll 1$, for pipe radius a. The secondary flow velocities are expanded in the following way, using u as an example:

$$u = U\sum_{i=1}^{n}\epsilon^i u_i \tag{1.21}$$

The secondary flow is therefore order-1, with stream function ψ defining the velocities as:

$$u_1 = \frac{1}{\eta}\frac{\partial\psi}{\partial\theta}, \quad v_1 = -\frac{\partial\psi}{\partial\eta} \tag{1.22}$$

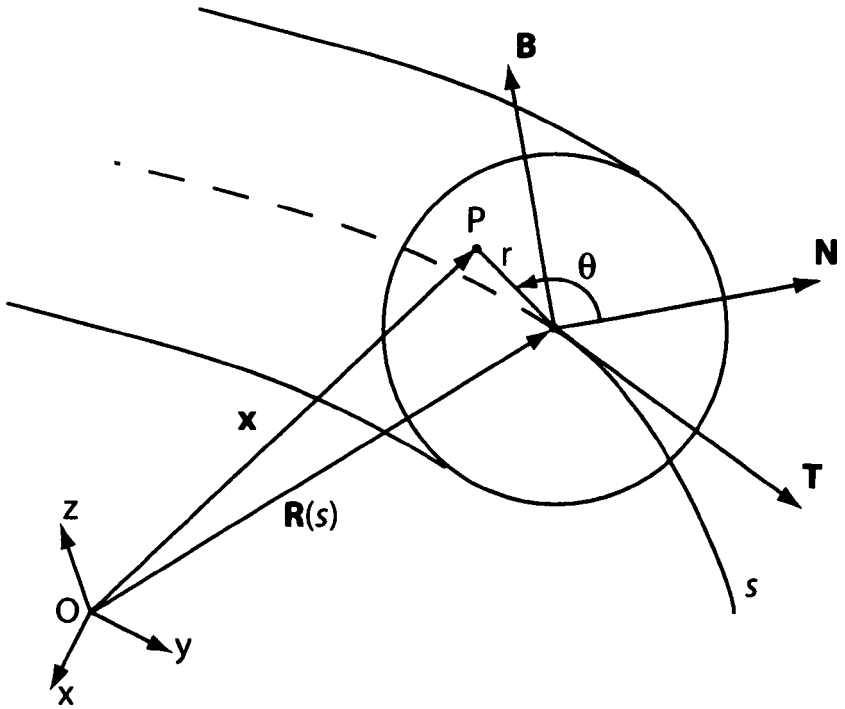


Figure 1.6: Helical coordinate system used by Wang

where η is the normalised radial position, r/a. The stream function solution is:

$$\frac{\psi}{Re} = \underbrace{\frac{sin\theta}{288}(\eta^7 - 6\eta^5 + 9\eta^3 - 4\eta)}_{Dean\ vortices} - \underbrace{\frac{1}{4}\left(\frac{\lambda}{Re}\right)(\eta^4 - 2\eta^2 + 1)}_{Torsion\ rotation} \tag{1.23}$$

The first term in eqn (1.23) is the stream function for the Dean vortices; a pure curvature effect. The second term is a pure rotation, indicated by the lack of theta dependence, which arises due to the effect of torsion on the flow, where $\lambda = \tau/\kappa$ and is a constant of order unity. Wang found that for $\lambda/Re \geq 1/24$ torsion dominates, causing a single recirculation cell in the secondary flow. It is important to note that this torsion effect is first-order, which is the same order as curvature. This is because ψ is an order-ϵ term, a first order term in this expansion,(equal to κa), and $\lambda\epsilon = \tau a$.

1.3.2.2 Orthogonal coordinate system

Germano showed that it is possible to construct an orthogonal coordinate system by replacing θ, from Wang's system, with $\theta + \phi(s) + \phi_0$, in the plane normal to the axis (Germano 1981), as shown in Figure 1.7. The Cartesian vector $\mathbf{x}$ therefore becomes:

$$\mathbf{x} = \mathbf{R}(s) + r\cos(\theta + \phi(s) + \phi_0)\mathbf{N}(s) + r\sin(\theta + \phi(s) + \phi_0)\mathbf{B}(s) \tag{1.24}$$

where

$$\phi(s) = -\int_{s_0}^{s} \tau(s')ds' \tag{1.25}$$

with ϕ_0 and s_0 taking arbitrary values. Again performing the dot product of the incremental change as before:

$$d\mathbf{x}.d\mathbf{x} = (dr)^2 + r^2(d\theta)^2 + [1 + \kappa r\sin(\theta + \phi)]^2(ds)^2 \tag{1.26}$$

which shows that the system is now orthogonal. The key result reported in this

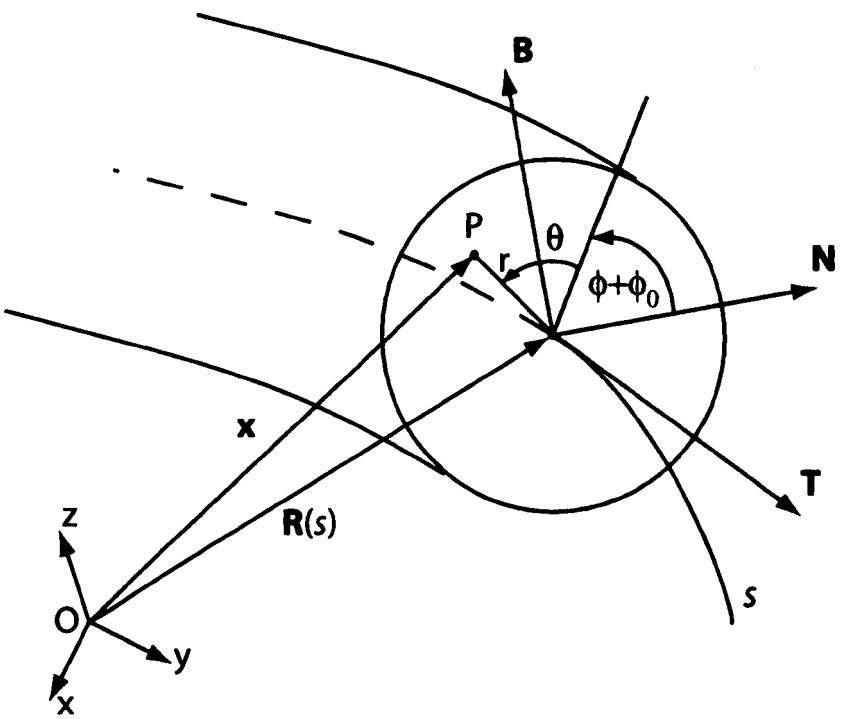


Figure 1.7: Helical coordinate system used by Germano

paper is that the torsion has only a second order effect on the flow, contrary to the findings of Wang (Wang 1981).

Germano's orthogonal formulation was subsequently used in several publications by other researchers. It has also been used to analyse flow in pipes with non-uniform curvature and torsion (Gammack & Hydon 2001). Kao (Kao 1987) used it to obtain a series expansion for small Dean number flows, but with the term $\beta^{1/2} = O(1)$, where $\beta^{1/2} = \lambda/(2\epsilon)^{1/2}$. The series expansions are of the form:

$$w = w_0 + \sum_{i=1}^{\infty} Dn^{(1+i)/2} w_i \tag{1.27}$$

for the axial velocity w, and for the streamfunction ψ

$$\psi = \psi_0 + \sum_{i=1}^{\infty} Dn^{(1+i)/2} \psi_i \tag{1.28}$$

where the leading order solution is Poiseuille flow, $w_0 = 1 - r^2$ and $\psi = 0$. It should be noted that the stream function ψ is of a modified form, shown in eqn (1.29), which is introduced to replace the continuity equation (to make the system analogous with Dean's formulation, and identical if $\beta = 0$).

$$u = \frac{1}{r}\frac{\partial \psi}{\partial \alpha} - \beta^{1/2} K^{1/2} \frac{1}{r} \int_0^r r \frac{\partial \overline{w}}{\partial \alpha} dr, \quad v = -\frac{\partial \psi}{\partial r} \tag{1.29}$$

It is clear that the second term in u, in eqn (1.29), means that the stream function is not a 'true' stream function. This means that the secondary flow can not be represented by contours of the stream function, but must be represented by velocity vector plots of (u, v). This is a direct consequence of using Germano's orthogonal coordinate system, whereas Wang's non-orthogonal system did allow a true stream function representation of the secondary flow. The results suggest that if $\beta^{1/2} = O(1)$, then torsion appears in the order-(3/2) terms in the expansion, otherwise, it is a second-order effect, as reported by Germano.

Kao then presented numerical solutions, valid for moderate Dean numbers, which show that if curvature is not small, then even for values of $\beta^{1/2}$ as low as 0.1, significant distortion of the secondary flow is found, to the extent that the second

vortex is confined to a very small region near the wall. This is qualitatively similar to the situation reported by Wang.

Germano returned to the problem of helical pipes (Germano 1989), but on this occasion, used an expansion in Dean number, rather than curvature as in the original paper (Germano 1981). The formulation is such that if there is no torsion, the original Dean equations are recovered. Investigating further the influence of torsion, Germano also examined geometries that possessed an elliptical cross-section, rather than circular. The solutions obtained show that for an elliptical boundary, the effect of torsion on the secondary flow appears in the first-order terms of the expansion. In the special case of a circular boundary, the first-order terms disappear, and the effect is reduced to second-order.

Clearly, the literature examined thus far is divided on the question of the order of the effect of torsion. The problem was finally resolved by Tuttle (Tuttle 1990). It is explained that Wang and Murata (Murata, Miyake, Inaba, & Ogawa 1981) both used non-orthogonal co-ordinate systems, requiring a covariant tensor treatment to derive the Navier-Stokes equations. However, Wang focused on the contravariant velocities (which permitted a stream function definition) whereas Murata examined the covariant components. Since Germano's co-ordinate system is orthogonal, the co- and contravariant vectors are equivalent. Tuttle shows that simple transformations relate the velocities defined in each co-ordinate system, so that Wang and Germano were both actually considering the same velocity field, but from different perspectives.

Tuttle concludes that the appropriate co-ordinate system for understanding the effect of torsion is Wang's system, whilst acknowledging that it is more convenient to work with Germano's formulation, as the co- and contravariant vectors are identical and easier to understand. Tuttle's analysis therefore supports Wang's original conclusion that the effect of torsion is first order, that is of the same order as curvature.

Liu & Masliyah (Liu 1993) analyse the Navier-Stokes equations for the flow in a loosely coiled helical pipe. Loose coiling can be achieved though a large helical

radius or large pitch, specifically they assume:

$$\kappa a \to 0, \quad , \tau a \to 0, \quad Re \to +\infty, \quad \kappa a \neq 0 \tag{1.30}$$

This reveals two dimensionless quantities that govern the flow. The first, the Dean number has already been discussed, and the second is the Germano number, Gn. Physically, Gn expresses the relative strengths of the effects of twisting, $\rho\eta U^2$, and viscosity, μU, that act on the flow, thus measuring the torsion effect. It is defined as:

$$Gn = Re\tau a \tag{1.31}$$

By considering the effect of Gn in terms of the secondary flow structure, two further dimensionless groups become significant. For large Dean numbers the dimensionless group γ must be large for Gn to have a noticeable effect on the flow, where γ is defined as:

$$\gamma = \frac{Gn}{Dn^{\frac{3}{2}}} = \frac{\tau a}{(\kappa a Dn)^{\frac{1}{2}}} \tag{1.32}$$

For small Dean numbers, $Dn < 20$, the equivalent group is γ^*

$$\gamma^* = \frac{Gn}{Dn^2} = \frac{\tau a}{(\kappa a)^{\frac{1}{2}} Dn} = \frac{\eta}{\kappa a Re} \tag{1.33}$$

Their results show that the secondary flow transitions from two vortices to one vortex at $\gamma^* > 0.039$, when $Dn < 20$, and at $\gamma > 0.2$ for $Dn \geq 20$. Unique amongst the studies discussed so far, Liu & Masliyah also examine the axial wall shear rate distribution, for varying torsion (keeping curvature ratio and Dean number fixed). It is shown that for small γ the shear rate is largest near the outer wall, but as γ increases, the maximum value moves to the inner upper wall. For large γ the distribution is approximately uniform, which in a biological context would be valuable, suggesting one possible evolutionary advantage to non-planar geometries.

A different paper, published independently and in approximately the same period as that of Liu & Masiliyah, by Chen & Jan (Chen & R. 1992), also identified the Germano parameter as significant. In this case, it is referred to as the '*torsion number*', denoted Tn, and defined equal to $2a\tau Re$, the only difference Tn and Gn is a factor of two. Chen & Jan write series solutions, expanding in both curvature

and torsion, in the following way:

$$w = w_{00} + \sum_{i=1,j=0}^{\infty} \kappa^i \tau^j w_{ij} \tag{1.34}$$

for the axial velocity, w, and for the streamfunction ψ

$$\psi = \tau\psi_{00} + \sum_{i=1,j=0}^{\infty} \kappa^i \tau^j \psi_{ij} \tag{1.35}$$

Their analysis once again confirms that the apparent difference between the results of Wang and Germano can be explained through a simple transformation of velocities.

1.3.2.3 Helically symmetric coordinate system

An alternative approach is to formulate the Navier-Stokes equations within a helically symmetric co-ordinate system (Zabielski & Mestel 1998). Figure 1.8 shows the relationship between helical coordinates and cylindrical polars. One axis is the vector $\mathbf{H}$, defined as:

$$\mathbf{H} = \frac{1}{h^2}(-\epsilon r \mathbf{e}_\theta + \mathbf{e}_z) \tag{1.36}$$

where $h^2 = 1 + \epsilon^2 r^2$, and ϵ is a pitch length parameter trivially related to c by $\epsilon = 1/c$. The two other vectors used to form an orthogonal set are $\mathbf{e}_r$ and $\mathbf{e}_\phi$, given by:

$$\mathbf{e}_\phi = h\mathbf{H} \times \mathbf{e}_r = \frac{1}{h}(\mathbf{e}_\theta + \epsilon r \mathbf{e}_z) \tag{1.37}$$

The helical symmetry means that the functions only depend on r and $\phi = \theta + \epsilon z$. This particular orthogonal co-ordinate system does allow a stream function definition, which is also helically symmetric, and hence is written $\Psi = \Psi(r, \phi)$. However despite the two-dimensional appearance of the Navier-Stokes equations, their non-linearity precludes the possibility of general analytic solutions.

Mestel & Zabielski use the helically symmetric formulation to investigate potential flow in a square-cross section, and Navier-Stokes flow in square and circular cross-section pipes. Focusing here on the circular cross-section results, geometries with curvature and torsion of order-unity were examined for increasing Dean number. For

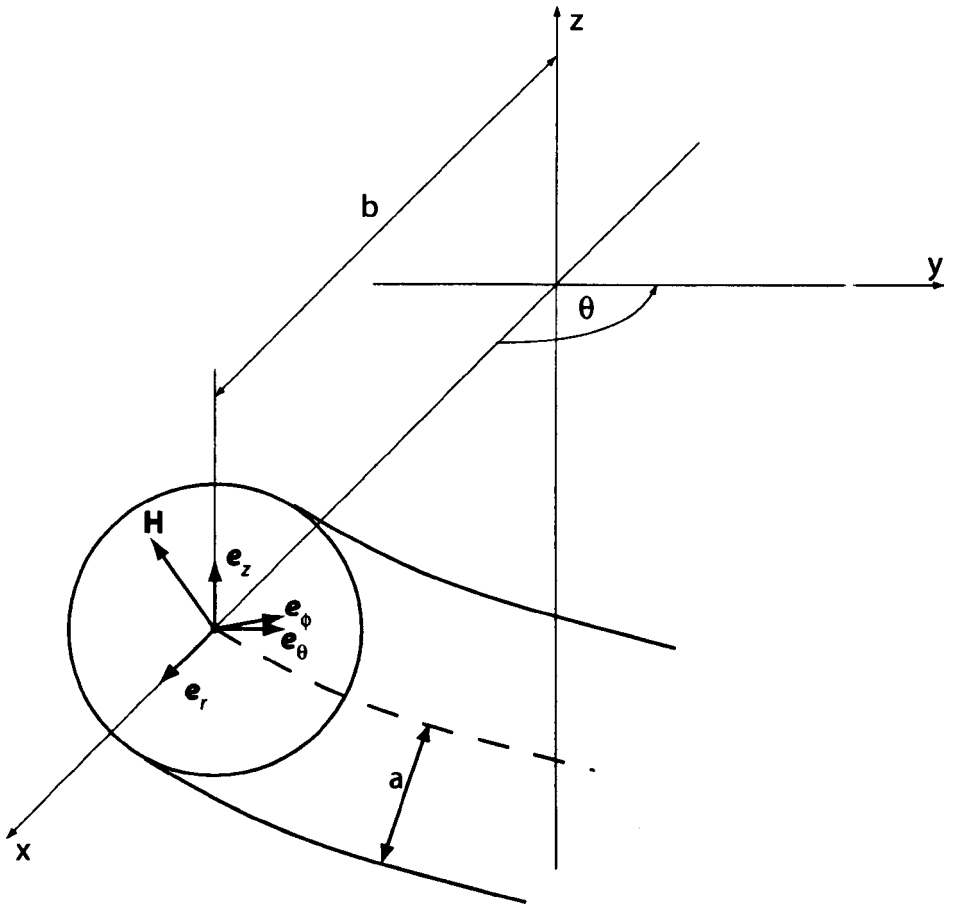


Figure 1.8: Helical coordinate system used by Mestel and Zabielski

small Dean number, the secondary flow is a single vortex, with an almost parabolic axial velocity. As Dean number is increased a second circulation region forms at the bottom of the pipe, and the peak axial velocity moves towards the outer bend. For large Dean number the secondary flow is almost symmetric, approaching the asymptotic limit.

Zabielski & Mestel end with a note on the possibility of multiple solutions for steady helical flows. Both Dennis & Ng (Dennis & Ng 1982) and Daskopolous & Lenhoff (Daskopoulos & Lenhoff 1989) report four-vortex solutions to the low-curvature Dean problem. Zabielski & Mestel found no such solutions in their study, despite not imposing any top-down symmetry, and they suspect that there are no stable,

steady four-vortex solutions in helically symmetric flows, even when it is almost axisymmetric.

1.3.2.4 Stability of helical pipe flow

The literature examined so far has only considered laminar flow, but there are some papers that have investigated the transition to turbulence in helical pipe flow. Yamamoto *et al.* performed numerical and experimental studies into the stability of helical pipe flow. It is known that the flow in curved pipes is far more stable than that in a straight pipe (Taylor 1929) (White 1929). An experimental study (Yamamoto, Akita, Ikeuchi, & Kita 1995) found that the addition of torsion had a destabilising effect on the flow. More specifically, for three different dimensionless curvatures, κa, $(0.01, 0.05, 0.1)$, increasing a torsion parameter β_0 reduces the transition Reynolds number (defined using the convention of mean axial velocity and pipe diameter), with a minimum occurring for β_0 in the range $1 - 1.3$. The lowest critical Reynolds number was found to be approximately 800 at $\beta_0 \simeq 1.3$ when $\delta = 0.1$ (note, that here, the critical Reynolds number indicates the start of transition, rather than fully developed turbulent flow). They suggest that this behaviour is directly linked with the transition from two vortices to one vortex in the secondary flow.

A numerical study (Yamamoto, Yanase, & Jiang 1998) using linear stability analysis obtained results that were in general agreement with the experiments. However, the critical Reynolds number is found to be consistently lower in the numerical study. It is thought that this is due to the time needed for the disturbances at the inlet to grow large enough for the hot-wire to detect in the experimental configuration.

In another paper by Yamamoto *et al.* (Yamamoto, Aribowo, Hayamizu, Hirose, & Kawahara 2002) experimental and numerical results are presented that visualise the flow structures in helical pipes. Once again, increasing torsion causes a transition from a two vortex structure to a single vortex. The smoke injection results confirm their previous work on turbulent transition, as when the Reynolds number reached 900 the smoke is mixed by turbulence, and no longer provides effective visualisa-

tion of the flow. Tracking particles through a numerical velocity field (obtained in (Yamamoto, Alam, Yasuhara, & Aribowo 2000)) gives good agreement with the experiments.

In summary, depending on the degree of curvature and torsion, and the Dean number, the secondary flow for steady boundary conditions is either a pair of counter-rotating vortices, with some degree of asymmetry, or a single vortex, and the axial velocity is non-axisymmetric. Whilst curvature has a stabilising influence, torsion destabilises the flow, significantly reducing the critical transition Reynolds number.

1.3.3 Unsteady helical pipe flow

Mestel & Zabielski once again used the helically symmetric coordinate system to investigate unsteady flow in helical pipes (Zabielski L. 1998). They presented an asymptotic solution for the limit of high-frequency. Numerical solutions are found for pressure gradients that are pure sinusoidal, sinusoid plus mean and a physiological pressure gradient (taken from measurements in (McDonald 1974) and shown in Figure 1.9). Qualitatively, the latter consists of a sharp peak in the first half of the cycle, termed systole, and an approximately steady component in the second half, termed diastole.

The physiological pressure gradient was applied in a geometry representative of the aortic arch, using parameters from Chandran (Chandran 1993). They found that for most of the cycle the secondary flow was a single vortex, which is particularly strong near the systolic peak. When the flow reverses in late systole, the vorticity near the wall separates into a pair of counter-rotating vortices. For the same case, but with a much smaller pitch, a double-vortex solution is found, which separates far more strongly than with non-zero torsion, as the counter-rotating vortices travel across the pipe cross-section. Zabielski & Mestel speculate that these flow conditions could be damaging to species transported in the bloodstream, e.g. platelets and red blood cells, thereby providing an evolutionary advantage to vessel geometries with

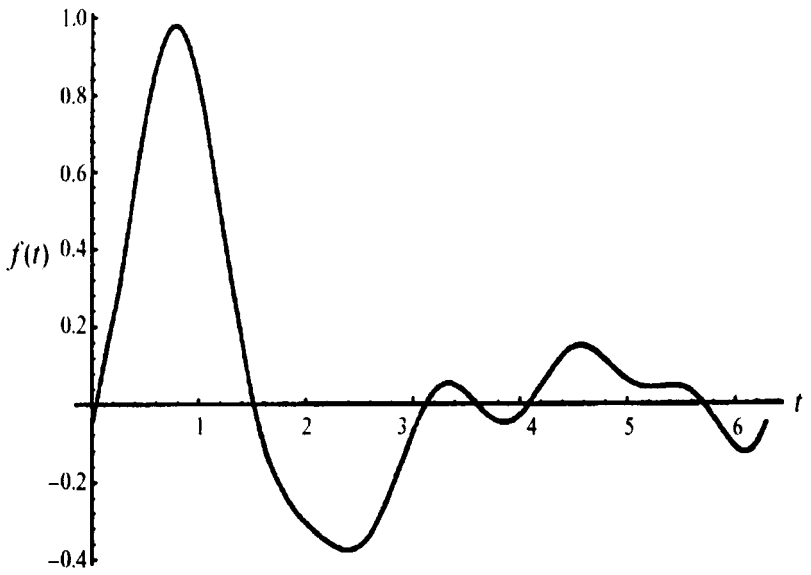


Figure 1.9: Physiological pressure gradient waveform (taken from (McDonald 1974))

non-zero torsion.

The case of low-frequency oscillatory flow, with a co-sinusoidal axial pressure gradient, was examined using a bi-parameter perturbation method by Zhang *et al.* (Zhang, Ma, Su, & Zhang 2003). It was assumed that both torsion, denoted ϵ, and Womersley number squared, denoted α^2, were small, i.e. $\ll 1$, permitting an expansion of the form, (using axial velocity w as an example):

$$w = \sum_{i=0}^{n} \epsilon^i \left(\sum_{j=0}^{n} \alpha^{2j} w_{ij} \right) \tag{1.38}$$

They found that the secondary flow changed from a double-vortex structure, to a single vortex, which then reversed its direction of rotation, over one complete cycle. The variation in stream function is found to be generally smooth, except when the pressure gradient changes sign, when there is a sharp change in the stream function.

Taken as a whole, the existing literature contains several formulations for obtaining solutions to helical pipe flow. However, being published before Caro's *in vivo* study (Caro, Cheshire, & Watkins 2005), it is understandable that none of those studies have presented an in-depth investigation of the range of geometries proposed by

Caro for use in medical applications. Furthermore, they do not present sufficiently detailed results on the phenomena thought to be biologically important in medical devices, such as wall shear stress and in-plane mixing.

1.4 Mixing

Fluid mixing of scalars is the combined processes of flow advection and molecular diffusion, which occurs across a large range of length scales and Reynolds numbers. For example, large Re and length scales are found in dispersion of pollutants in the atmosphere (Vassilicos 2002) and oceans (Wiggins 2005). At large length scales, but vanishing Re, mixing occurs in the earth's mantle (Metcalfe, Bina, & Ottino 1995), and at smaller scales, in polymer blending (Hwang & Kwon 2003) and microfluidics (Stroock, Dertinger, Ajdari, Mezic, Stone, & Whitesides 2002).

The basic equation describing fluid mixing in a continuum is the advection-diffusion equation,

$$\frac{\partial \phi}{\partial t} + \mathbf{u}.\nabla\phi = D\nabla^2\phi \tag{1.39}$$

where $\phi = \phi(\mathbf{x}, t)$ is a passive scalar, transported by a velocity field $\mathbf{u}$, and D is the molecular diffusivity coefficient, assumed constant.

The Péclet number, Pe, is the ratio of diffusional time scales, $\tau_{diffusion}$, to advective time-scales, $\tau_{advective}$.

$$Pe = \frac{\tau_{diffusion}}{\tau_{advective}} = \frac{L^2/D}{L/U} = \frac{UL}{D} \tag{1.40}$$

where U, L and D are representative velocity, length and diffusion scales respectively. A large value of Pe indicates that advection dominates diffusion, and a small value that diffusion is dominant.

If advection alone is considered, this is termed *stirring*, and can be investigated by integrating the advection equations (which will be the focus of this thesis):

$$\frac{d\mathbf{x}}{dt} = \mathbf{u}(\mathbf{x}, t) \tag{1.41}$$

Rapid mixing is achieved easily in turbulent flows, but can also be generated by laminar flows which have regular, deterministic velocity fields through a process termed chaotic advection. If the advection equations possess three or more degrees-of-freedom, e.g. 2-D unsteady flow or 3-D steady flow, their solution may display chaotic dynamics. The meaning of chaotic dynamics, and other relevant concepts for mixing are briefly explored, both from a dynamical systems perspective, Section 1.4.1, and by recourse to a classic example of mixing from the literature, Section 1.4.2.

1.4.1 Dynamical systems approach

Dynamical systems theory provides a useful framework in which to study mixing, and some of the key concepts will be discussed as a prelude to the results presented in Chapters 3, 4 & 5. Further details can be found in (Ottino 1989), and the references contained within.

Considering again the advection equation:

$$\frac{d\mathbf{x}}{dt} = \mathbf{u}(\mathbf{x}, t) \tag{1.42}$$

with $\mathbf{x} = \mathbf{X}$ at $t = 0$. The solution, $\mathbf{x} = \Phi_t(\mathbf{X})$, is termed the *flow*, and Φ_t the flow map.

As alluded to earlier, chaotic behaviour is important in mixing. One particular manifestation of chaotic dynamics is *sensitivity to initial conditions.* In the context of fluids, this means that two points initially placed close together, will rapidly diverge. A characterisation of this property is the Lyapunov exponent, a definition of which follows.

1.4.1.1 Lyapunov exponents - sensitivity to initial conditions

Consider an initial condition vector $d\mathbf{X}$ about a position $\mathbf{X}$ with length $|d\mathbf{X}|$, and orientation, $\mathbf{M} = \frac{d\mathbf{X}}{|d\mathbf{X}|}$. Let it be transported by the flow Φ_t, so that after a time

t, the vector is represented by $d\mathbf{x}$. The Lyapunov exponent, σ_i, corresponding to a particular orientation $\mathbf{M}_i$ of the initial vector $d\mathbf{X}$ is defined as:

$$\sigma_i(\mathbf{X}, \mathbf{M}_i) \equiv \lim_{t\to\infty} \left[\frac{1}{t} \ln\left(\frac{|d\mathbf{x}|}{|d\mathbf{X}|}\right)\right] \tag{1.43}$$

Put more intuitively, for a Lyapunov exponent σ_k, the length $|d\mathbf{x}|$ grows exponentially in time with σ_k, that is,

$$|d\mathbf{x}| \approx |d\mathbf{X}| e^{\sigma_k t} \tag{1.44}$$

1.4.1.2 Poincaré sections

For a spatially or temporally periodic flow, for example that in a helical pipe, it is often useful to examine the evolution of the initial conditions at intervals of a time T. The effect of the flow is then described by considering the effect of the mapping Φ_T on the initial conditions. Thus after n iterations, corresponding to n repeated applications of the flow map, the position of an initial condition $\mathbf{x}_0$ is expressed as:

$$\mathbf{x}_n = \Phi_T^n(\mathbf{x}_0) \tag{1.45}$$

Determining the flow map analytically is generally impractical, however the effect of the mapping for any initial point after intervals of time T, can be obtained by taking Poincaré sections. For a spatially periodic pipe flow the Poincaré section can be generated by determining the intersection of an advected particle with planes located at integer multiples of the pitch length. These intersections are then collapsed onto one plane, which forms the Poincaré section.

Chaotic trajectories in the flow exhibit themselves as unstructured points in the Poincaré section. If an infinite number of iterations of the mapping were calculated, a single chaotic trajectory would wander over the entire region in which it exists, tending to produce a 'blacked out' zone in a graphical representation of the location of successive intersections of the point with the Poincaré section. In most mixing systems, structured regions will also exist in the Poincaré section, visualised as a definite, continuous boundary, inside which is a void. These are known as elliptic

regions, and exist around an elliptic point. A simple example of an elliptic region are the Dean vortices, with the vortex core centreline being the elliptic point. These elliptic points are fixed points of the mapping, that is, invariant under Φ_T.

The elliptic regions are detrimental to mixing, as they form a barrier to particle transport in the cross-section. They are often referred to as islands of regular flow in the Poincaré section, as any particles which are initially placed within the island, will remain there indefinitely. Practically, this means any fluid in this region will not mix with the rest of the flow. It is therefore generally the goal when designing mixing devices to minimise the number, and size, of these islands.

1.4.1.3 Baker's transform

The baker's transform is a very simple mixing transformation, which possesses the best mixing behaviour possible (termed *measure theoretic*). The map is defined in the following way. A square, divided into two rectangles, is stretched along the y-axis to double its original height, and simultaneously squeezed along the x-axis by half, thus preserving the area. The resultant rectangle is cut in half at the x-axis, and the two parts fused side-to-side, to create a square once again. This operation is repeated, and from Figure 1.10, it is clear that this leads to finer and finer scales of the two colours. In this way, the baker's transform is mixing the initial distribution of two colours.

This concept can be applied to fluid mechanics, in the form of the horseshoe map, which stretches and folds (rather than cutting) in a similar manner to the baker's transform. This stretching and folding mechanism is an advective process, which can produce large concentration gradients, across which species will rapidly diffuse.

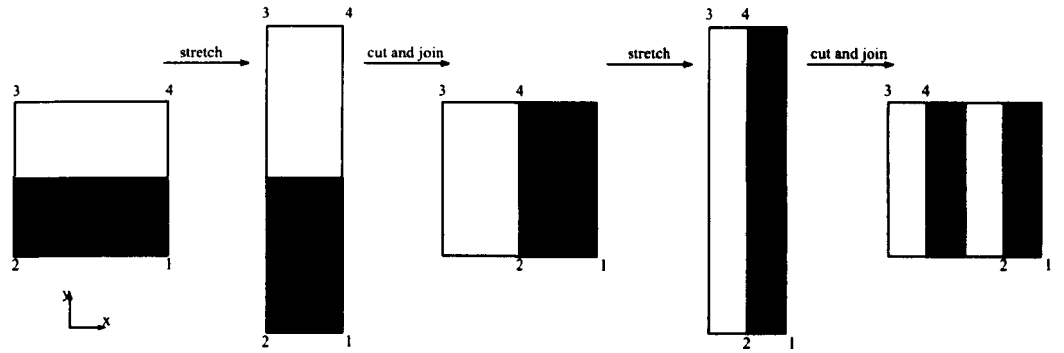


Figure 1.10: The baker's transform defined for a square.

1.4.2 Chaotic advection - the blinking vortex

The first usage of the term *chaotic advection* was by Aref in his 1984 paper "Stirring by Chaotic Advection" (Aref 1984). The system Aref examined is a very simple, prototypical, mixing flow. Within a circular boundary of radius a, a point vortex, of circulation Γ, is placed at a location z_v, as shown in Figure 1.11, within the complex plane. The corresponding image vortex, v_i, with circulation $-\Gamma$, is therefore placed at a^2/z^*, which is outside the domain (the $*$ notation indicating complex conjugation). The velocity of a particle, at a location p, is then given by:

$$\dot{p}^* = \frac{\Gamma}{2\pi i}\{(p - z_v)^{-1} - (p - \frac{a^2}{z_v^*})^{-1}\} \tag{1.46}$$

If the position of the vortex, z_v, remains constant, or merely precesses along a circular path at a constant speed, the system remains integrable. However, if some degree of discontinuity is introduced into the system, the condition of integrability can be broken, and chaotic trajectories generated. A stirring function that introduces discontinuity is the blinking protocol given by:

$$z_v(t) = \begin{cases} +b, & (nT \leq t < (n + \frac{1}{2})T), \\ -b, & ((n + \frac{1}{2})T \leq t < (n + 1)T), \end{cases} \tag{1.47}$$

where $n = 0, \pm 1, \pm 2, ...$, and b and T are constants. The system is completely parametrised by two dimensionless quantities, β and μ, which are defined thus:

$$\beta = \frac{b}{a} \tag{1.48}$$

$$\mu = \frac{\Gamma T}{2\pi a^2} \tag{1.49}$$

Conceptually, β is a dimensionless amplitude of the blinking oscillation. and μ is a dimensionless period of the particle motion. Before giving a brief summary of the effects of varying these parameter values, it is useful for the purposes of comparison, to consider the case of a single point vortex, as discussed by Vassilicos (Vassilicos 2002). Indeed, these idealised two-dimensional systems are a useful analogue for the three-dimensional flows considered in this thesis.

For a steady flow, the streamlines around a point vortex are fixed concentric circles. The velocity field, defined in polar coordinates, is given by:

$$\dot{r} = 0, \quad \dot{\theta} = \frac{\Gamma}{2\pi r} \tag{1.50}$$

Physically this constitutes a local shear environment that stretches material elements, and a folding mechanism due to the angular rotation, both of which combine to create a spiral structure in the material elements. Crucially, the stretching of the material length is linear in time. In the context of Lyapunov exponents, this corresponds to a value of $\sigma_k = 0$. The study by Aref shows that by introducing the unsteady, blinking protocol, much faster stretching of material lines can be achieved, a point discussed in detail by Vassilicos (Vassilicos 2002), a summary of which will be given shortly.

The blinking vortex system was analysed by Aref using both Poincaré sections, and the advection of an initial blob of particles. Figure 1.12 shows Poincaré sections taken from (Aref 1984). For a fixed value of β, increasing μ was found to increase the area of extent of the regions of chaotic advection. As the blinking period tended to infinity, the flow was found to become chaotic everywhere, although this is hardly a practical result. Conversely, decreasing the period, so that each vortex is only active

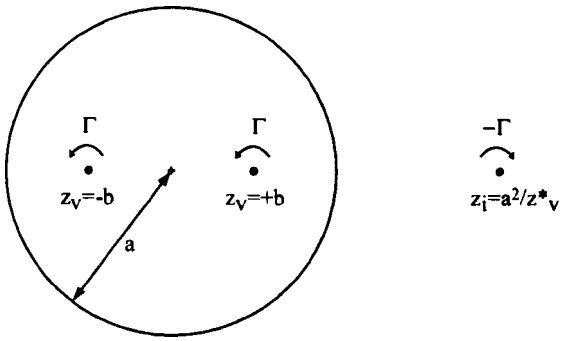


Figure 1.11: The blinking vortex flow studied by Aref, operating under the blinking function defined in eqn (1.47).

for a very short time, causes the particles to lie on level sets of the flow, forming islands of confinement. In this case, the particles are effectively experiencing the velocity field that would result if both vortices were simultaneously active.

For a fixed value of μ, increasing β, was also found to increase the size of the regions of chaotic advection. If β is small, then the velocity field only changes a small amount with each blinking period, obviously counter-productive to the intentions of the device. Increasing β up to 0.7, further increases the discontinuity in the consecutive velocity fields, therefore more efficiently generating chaotic particle trajectories. Beyond a value of 0.7, the point vortex is closer to its image than it is to the other point vortex, changing the structure of the Poincaré sections, specifically, the chaotic regions are more diffuse, and it is difficult to quantify their extent in the same way as for $\beta < 0.7$.

Figure 1.13 shows the time history of a square blob of particles, initially placed on the y-axis, which has been advected by the blinking vortex. At $t = 2$ and $t = 4$, the stretching and folding mechanism of the alternating vortices is clear. As t increases, the particles are increasingly dispersed, and due to their finite number, the filament structures become poorly resolved. It is, however, now obvious, how chaotic advection can result in effective mixing in fluid mechanical systems.

Figure 1.12 shows that many of the Poincaré sections contain both regular and chaotic regions. Vassilicos explains that for region of global chaos, after asymptot-

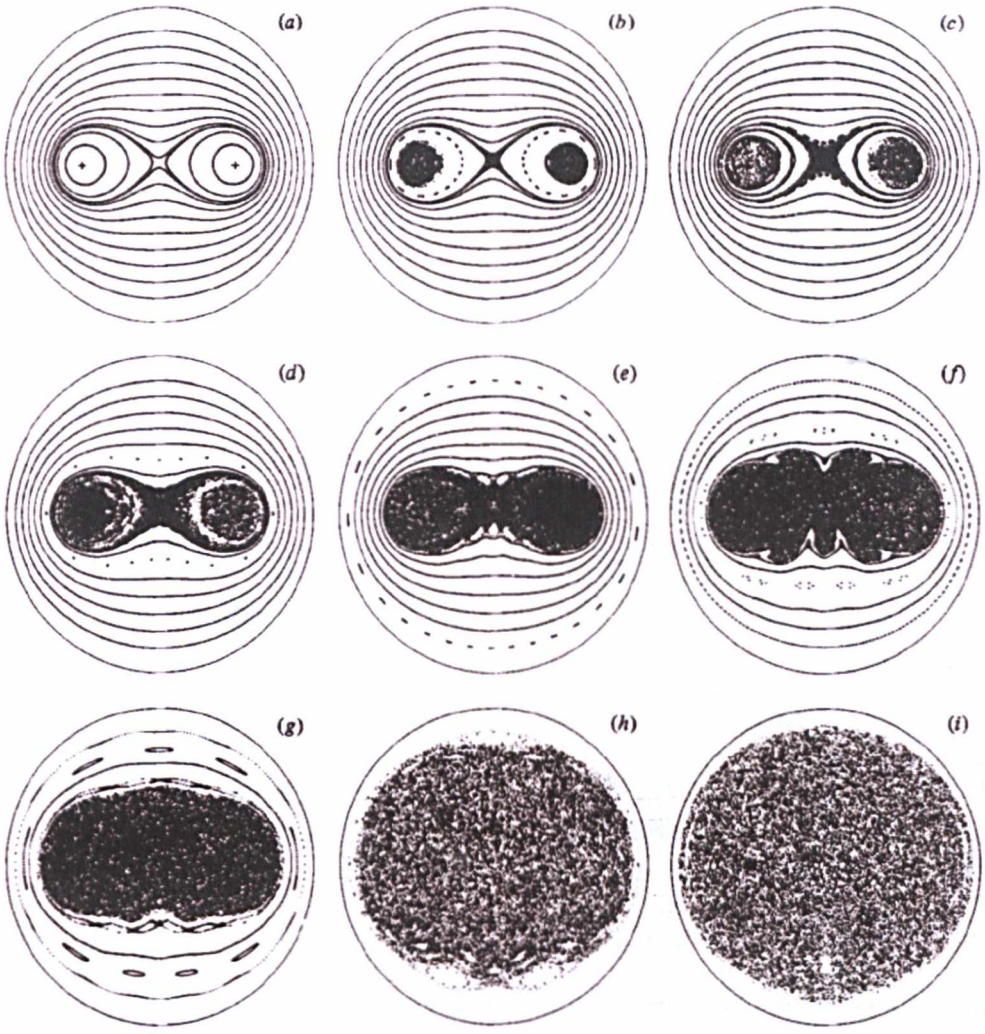


Figure 1.12: Poincaré sections of the blinking vortex flow, for $\beta = 0.5$. As μ increases the regular regions disappear, and are replaced by chaotic trajectories. (Taken from (Aref 1984)).

ically large times, the growth of material elements becomes truely exponential. A Lyapunov exponent is then well-defined and identical for every initial position in that region. However, in practice, the time taken for convergence to the Lyapunov exponent can be very large, such that the material lines may be stretched linearly in parts of the flow, or only weakly exponentially. For flows with coexisting regular and chaotic regions, after large time, exponents of zero will be found in the regular regions, and in the chaotic regions, different positive Lyapunov exponents specific to each region.

Initially, there was some scepticism regarding the prevalence of chaotic advection

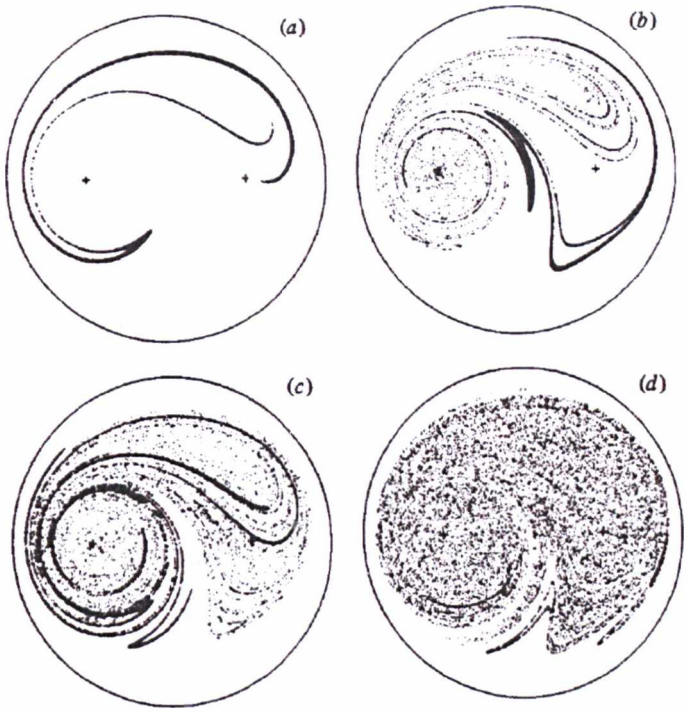


Figure 1.13: Stirring of a square blob of particles by the blinking vortex flow for $\beta = 0.5$ and $\mu = 2.0$, at times (a) $t = 2$, (b) $t = 4$, (c) $t = 6$, (d) $t = 12$. (Taken from (Aref 1984)).

in real fluid flows, (Aref & Balachandar 1986), but the large volume of published research on the topic, has provided evidence to dispel such doubts, with chaotic advection observed in all manner of flows. References to a few examples follow, but the list is by no means exhaustive.

For examples of chaotic advection in cavity flows, see (Ling 1993) & (Krasnopolskaya, Meleshko, Peters, & Meijer 1999). In a similar way, chaotic advection is found to exist in the pulmonary alveoli (Butler & Tsuda 1997) and idealisations of them (Laine-Pearson & Hydon 2006). Chaotic advection has also been observed in the thermal convection problem of Rayleigh-Bénard flow (Camassa & Wiggins 1991).

Mixing devices that use stirring rods, generate chaotic trajectories efficiently, even in Stokes flow, (M.D. Finn 2004) and advection enhanced mixing can also be generated in serpentine microchannels (Liu, Stremler, Sharp, Olsen, Santiago, Adrian, Aref, & Beebe 2000), and other pipe based devices (Khakhar 1986) (Khakhar, Franjione,

& Ottino 1987). Recent research on the original blinking vortex system, provides insights into the operating protocols that maximise the production of chaotic trajectories (Kin & Sakajo 2005). Further developments on the theoretical underpinnings of mixing can be found in (Ottino 1989), (Sturman, Ottino, & Wiggins 2006) & (Wiggins & Ottino 2004).

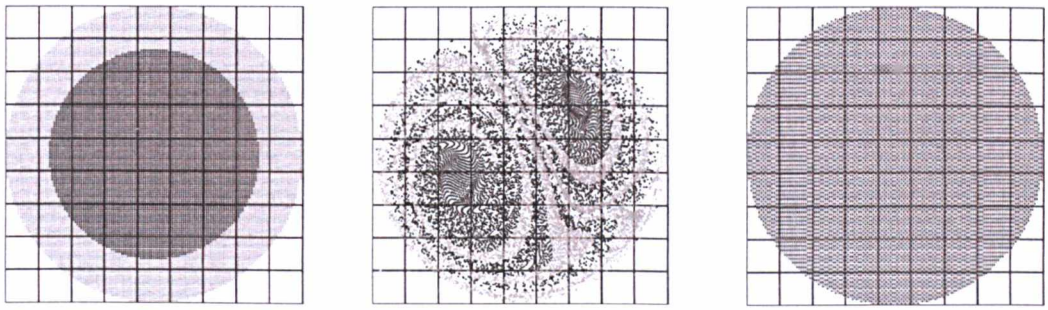
1.4.3 Quantifying mixing - information entropy

Conceptually, mixing can be thought of as the reduction of non-uniformity (as illustrated by the baker's transform), or equivalently, the increase of disorder. Information entropy was first defined by Shannon (Shannon 1948), and can be interpreted as a measure of disorder, naturally leading to its use in such diverse fields as mixing in polymer processing (Wang, Manas-Zloczower, & Kaufman 2003), (Wang, Manas-Zloczower, & Kaufman 2005b), (Wang, Manas-Zloczower, & Kaufman 2005a), chaotic micromixers (Kang & Kwon 2004) and aerosol mixing in the lung (Butler & Tsuda 1997). Here the formulation used is that introduced by (Kang & Kwon 2004). They tracked passive, coloured particles, which are either black or white, through a chaotic micromixer, taking sections of the trajectories at axial locations of interest, and having superimposed a grid onto the section, applied eqn (1.51).

$$S = -\sum_{i=1}^{N_c} \left[w_i \sum_{k=1}^{N_s} (n_{i,k} \log n_{i,k}) \right] \tag{1.51}$$

In eqn (1.51), i is the cell index, k is the species index, w_i is the weighting factor for each cell, N_c the number of cells, N_s the number of species (i.e. different colours of particles) and $n_{i,k}$ is the particle number fraction of the k^{th} species in the i^{th} cell. The weighting factor w_i is defined so that it is zero if a cell contains no particles, or only particles of a single species/colour; within such a cell the particle distribution is uniform, and therefore should contribute zero to the entropy summation, i.e. disorder can only occur if particles of different colours are present. If the cell contains

particles of more than one colour, $w_i = 1$. The box counting concept is illustrated in Figure 1.14, using a reduced number of boxes, along with the corresponding terms used in eqn (1.52). In Figure 1.14 particles of only two colours are considered and this is used throughout this work.



(a) S_0: Initial distribution (b) S: $R = 0.25D$ at $z = 30D$ (c) S_{max}: Perfect mixing

Figure 1.14: Particle distributions overlaid with an illustrative grid, to demonstrate the concept of box-counting used in the entropic measure of mixing

It is clear from Figure 1.14(a) that the initial distribution is very poorly mixed, with only a few of the boxes containing particles of both colour. Figure 1.14(b) is a sample result from Chapter 3, and it shows that after a mixing process has been applied to the initial particle distribution, particles of both colours are found in many more cells, which eqn (1.51) clearly shows leads to a larger value of entropy. Figure 1.14(c) shows the particle distribution that yields the maximum value of entropy, when every cell contains an equal number of each colour of particle.

As a value considered in isolation, the entropy calculated in eqn (1.51) has little meaning. Again following Kang and Kwon we define a relative entropy measure K, which quantifies the increase in entropy of the particle distribution at a particular cross-section from that of the inlet distribution of particles. This is then normalised by the maximum possible entropy increase from the inlet particle distribution, and is defined in eqn (1.52).

$$K = \frac{S - S_0}{S_{max} - S_0} \tag{1.52}$$

From the above it can be appreciated that when K is equal to zero, no mixing has occurred, and when K equals one, the mixing is maximised.

1.5 Aims and Objectives

Whilst the benefits of helical geometry in vascular conduits have yet to be firmly established, they appear promising. There are several potential applications of helical geometry in a clincal context; bypass grafts, A-V shunts and arterial stents (Coppola & Caro 2008a). Furthermore, helical geometries have been proposed as a good model of the larger arteries. Given that the fundamental fluid mechanics governing the mixing of such configurations has not been systematically explored, it is of particular interest to examine this topic. The primary aim of the thesis is to examine the fluid dynamical properties of helical pipe geometries, and following this, the secondary goal is to examine the effect of flow structure on mixing. The emphasis is thus to understand the basic physical mechanisms involved, which can then be used to guide future designs of medical devices based on helical geometries.

To achieve these aims the following specific objectives have been identified.

1. Investigate how a range of parameter values within the geometric configurations of physiological interest affect the flow structure
2. Investigate stirring behaviour of flow in periodic helical pipe geometries
3. Identify geometries that produce optimal stirring, whilst minimising pressure loss
4. Propose novel refinements of helical geometries that will generate enhanced stirring

Note, that henceforth, the term mixing will be used to denote stirring, since it is assumed that the stirring behaviour will accurately model the mixing.

1.6 Organisation of the thesis

Chapter 2 contains the details of the numerical methods used, respectively, to solve the Navier-Stokes equations in helical geometries, and for post-processing the results to analyse Eulerian and Lagrangian properties of the flow. Chapter 3 examines the flow in a single helical geometry for physiologically relevant Reynolds number, assuming a periodic boundary condition in the axial direction. Based on the results in Chapter 3 a means of enhancing mixing is proposed, which involves combining different helical pipe geometries in series. An idealised prediction of the resultant mixing in such geometries is presented in Chapter 4. Chapter 5 contains a detailed examination of the velocity field and mixing behaviour in these combined helical geometries, again assuming steady flow and periodic boundary conditions. Finally, Chapter 6 summarises the findings of the thesis, and suggests future avenues of research. Appendix A contains a brief summary of relevant properties of space curves and splines.

Much of the work described in Chapter 3 has been published in *Annals of Biomedical Engineering* as 'Mixing Through Stirring by Steady Flow in Small Amplitude Helical Tubes'. The velocity field results of Chapter 5, in addition to some details of the numerical method from Chapter 2, have been published in *The Journal of Computational and Applied Mathematics* as 'Using Coordinate Transformation of Navier-Stokes Equations to Solve Flow in Multiple Helical Geometries'. The full details of the publications, including oral presentations, resulting from this thesis are given in a separate section at the end.

Chapter 2

Numerical Methods

This chapter details the various numerical methods used to solve for, and analyse, the flow in helical geometries. Section 2.1 describes the principles behind the spectral/*hp* element used to approximate a velocity field, and Section 2.3 details the splitting scheme used to solve the Navier-Stokes equations. Section 2.4 contains the derivation of a coordinate transformation of the Navier-Stokes equations which is used to define the helical geometry. Finally, Section 2.6 details the various post-processing tools used to analyse the flow, including particle tracking algorithms and Eulerian diagnostics.

2.1 Spectral/*hp* element methods

The spectral/*hp* element method can be used to solve the equations of fluid motion. At its core, is the representation of the solution by piecewise functions. If the solution is represented on a single element, this is a pure spectral method, and is common in direct numerical simulation studies of turbulence. In order to resolve fine geometric features that may exist, h refinement is used, i.e. dividing the domain into many sub-domains that each contain their own representation of the solution within that sub-domain. By increasing the order of the function, often a polynomial,

so-called p refinement, fine scales in the flow can be efficiently captured. When both h and p are refined in concert, exponential convergence to the solution is achieved. Figure 2.1 illustrates this philosophy for a two-dimensional complex geometry. This method is therefore numerically efficient, more so than a commercial finite-volume package, particularly for obtaining time-dependent flow solutions.

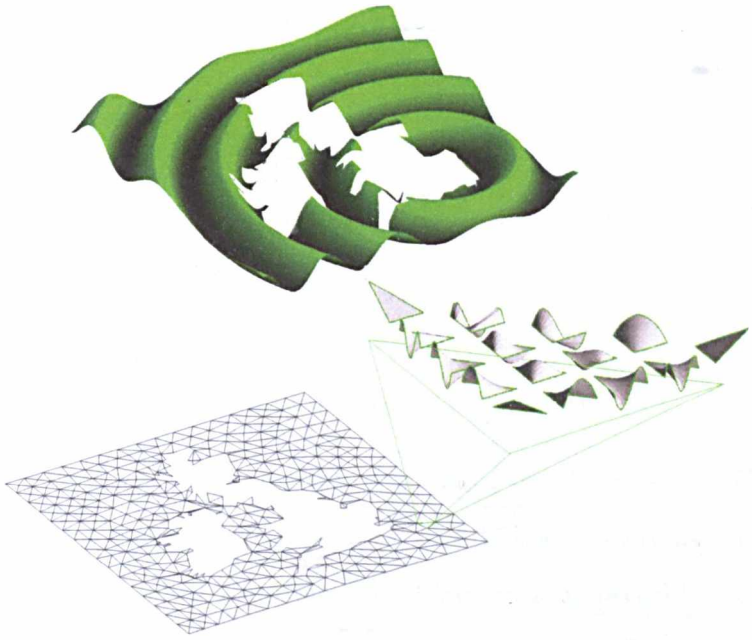


Figure 2.1: Overview of the spectral/hp element philosophy, showing spatial discretisation combined with high-order polynomial representations within each element (taken from (Sherwin & Karniadakis 2005)).

2.1.1 Method of weighted residuals

Consider a linear differential equation, in a domain Ω, subject to appropriate initial and boundary conditions.

$$L(u) = 0 \tag{2.1}$$

An accurate, but approximate, representation of the solution $u(\mathbf{x}, t)$ can be written in the form

$$u^{\delta}(\mathbf{x}, t) = u_0(\mathbf{x}, t) + \sum_{i=1}^{N_{dof}} \hat{u}_i(t)\Phi_i(\mathbf{x}) \tag{2.2}$$

where $\Phi_i(\mathbf{x})$ are analytic functions termed trial or expansion functions, $\hat{u}_i(t)$ are the associated unknown coefficients, and $u_0(\mathbf{x}, t)$ satisfies the boundary conditions. Substituting $u^{\delta}(\mathbf{x}, t)$ into eqn (2.1) means there will be a non-zero error or residual, denoted R

$$L(u^{\delta}) = R(u^{\delta}) \tag{2.3}$$

In order to determine the coefficients $\hat{u}_i(t)$, a constraint must be applied. In this case, it is that the Legendre inner product of the residual with respect to a weight, or test, function is equal to zero.

$$\int_{\Omega} v_j(\mathbf{x})R(\mathbf{x})d\mathbf{x} = 0 \quad j = 1, ..., N_{dof} \tag{2.4}$$

This procedure gives rises to the method's name of weighted residuals. As $N_{dof} \rightarrow \infty$, and convergence is reached, the residual R clearly goes to zero as the approximate solution approaches the exact solution. There are various possible choices for both the expansion function and the test function, for details see (Sherwin & Karniadakis 2005). In this thesis the Bubnov-Galerkin method is used, which is when the test function is selected to be equal to the trial function, that is, $v_j = \Phi_j$.

2.1.2 Galerkin formulation applied to the Helmholtz equation

The Galerkin formulation is now applied to a linear partial differential equation, the one-dimensional Helmholtz equation

$$\frac{\partial^2 u}{\partial x^2} - \lambda u + f = 0 \tag{2.5}$$

where λ is a real positive constant. Boundary conditions apply, for example, Dirichlet or Neumann conditions, respectively:

$$u(x_A) = g_D \quad ; \quad \frac{\partial u}{\partial x}(x_B) = g_N \tag{2.6}$$

for a domain Ω, composed of the region $x_A < x < x_B$.

Applying the method of weighted residuals, eqn (2.5) is multiplied by a test function $v(x)$, and the resulting equation integrated over the domain Ω.

$$\int_{x_A}^{x_B} v\frac{\partial^2 u}{\partial x^2}dx - \int_{x_A}^{x_B} \lambda v u dx + \int_{x_A}^{x_B} v f dx = 0 \tag{2.7}$$

Integrating the first term by parts gives

$$\int_{x_A}^{x_B} \frac{\partial v}{\partial x}\frac{\partial u}{\partial x}dx + \int_{x_A}^{x_B} \lambda v u dx = \int_{x_A}^{x_B} v f dx + \left[v\frac{\partial u}{\partial x}\right]_{x_A}^{x_B} \tag{2.8}$$

The final term in eqn (2.8) evaluates to $v(x_b)g_N$, since the test functions are defined to be zero on Dirichlet boundary conditions, which in this case is at x_A, with a Neumann condition at x_B.

$$\int_{x_A}^{x_B} \frac{\partial v}{\partial x}\frac{\partial u}{\partial x}dx + \int_{x_A}^{x_B} \lambda v u dx = \int_{x_A}^{x_B} v f dx + v(x_b)g_N \tag{2.9}$$

The substitution of the approximate solution into eqn (2.9) is now made, with $u(x)$ approximated by $u^\delta(x)$ and the test function $v(x)$ by $v^\delta(x)$. The approximate solution can be decomposed into a known function u^D, which satisfies the Dirichlet boundary conditions, and an unknown homogeneous function u^H, which is set to zero on the Dirichlet boundaries, that is:

$$u^\delta = u^H + u^D \tag{2.10}$$

where $u^H(x_A) = 0$ and $u^D(x_A) = g_D$. Substituting into eqn (2.9) yields

$$\begin{aligned}\int_{x_A}^{x_B} \frac{\partial v^\delta}{\partial x}\frac{\partial u^H}{\partial x}dx + \int_{x_A}^{x_B} \lambda v^\delta u^H dx &= \int_{x_A}^{x_B} v^\delta f dx + v^\delta(x_b)g_N - \int_{x_A}^{x_B} \frac{\partial v^\delta}{\partial x}\frac{\partial u^D}{\partial x}dx \\ &\quad - \int_{x_A}^{x_B} \lambda v^\delta u^D dx\end{aligned} \tag{2.11}$$

All the terms on the right hand side of eqn (2.11) are known, which allows this finite linear algebraic system to be solved. Writing the expansion representation of $u(x)$ in matrix form

$$u^\delta = \sum_{i=1}^{N} \hat{u}_i(t)\phi_i(x) = \mathbf{\Phi}^T\hat{\mathbf{u}} \tag{2.12}$$

where $\mathbf{\Phi}^T$ and $\hat{\mathbf{u}}$ are vectors, which when multiplied, form the summation to obtain u^δ. Substituting eqn (2.12) into eqn (2.11) converts it into the following matrix problem

$$\mathbf{A}\hat{\mathbf{u}} = \mathbf{f} \tag{2.13}$$

where $\mathbf{A}$ is a constant matrix consisting of summations of the inner products of the homogeneous expansion functions and their derivatives, that is,

$$\mathbf{A} = \int_{x_A}^{x_B} \frac{\partial \mathbf{\Phi}}{\partial x}\frac{\partial \mathbf{\Phi}^T}{\partial x}dx + \lambda \int_{x_A}^{x_B} \mathbf{\Phi}\mathbf{\Phi}^T dx \tag{2.14}$$

The system is forced by the vector $\mathbf{f}$ which comprises the original forcing function f and the applied boundary conditions

$$\mathbf{f} = \int_{x_A}^{x_B} \mathbf{\Phi} f dx + \mathbf{\Phi}(x_B)g_N - \int_{x_A}^{x_B} \frac{\partial \mathbf{\Phi}}{\partial x}\frac{\partial \mathbf{\Phi}^T}{\partial x}dx\hat{\mathbf{u}}^D - \lambda \int_{x_A}^{x_B} \mathbf{\Phi}\mathbf{\Phi}^T dx\hat{\mathbf{u}}^D \tag{2.15}$$

Thus far the formulation has only considered an expansion in a single element. For domains discretised by more than one element, the matrix $\mathbf{A}$ is formed from N_{el} submatrices, $\mathbf{A}_e$, one from each individual element. These matrices contain a local expansion that represents the solution within that element. By sharing degrees of freedom at the element boundares, the global matrix $\mathbf{A}$, when assembled from the local expansions, will typically have fewer degrees of freedom than would be expected from $N_{el} \times N_{dof}$.

2.2 Expansion basis

In this section the functions used to represent the solution within an element, and the method by which a domain is decomposed into many elements, in one and higher dimensions, are discussed.

2.2.1 One dimensional expansion

The solution domain is partitioned into several non-overlapping elements, each containing a local polynomial expansion. It is convenient to define a standard element,

which has a specific mapping to it from each element in the domain. The polynomial basis is defined within the standard element, and operations such as differentiation and integration, are then performed in the standard element, through the use of the chain rule. For an element with boundaries defined as,

$$\Omega_e \{x | x_{e-1} \leq x \leq x_e\} \tag{2.16}$$

and a one-dimensional standard element defined,

$$\Omega_{st} \{\xi | -1 \leq \xi \leq 1\} \tag{2.17}$$

the local coordinate ξ is given by

$$\xi = 2\frac{x - x_{e-1}}{x_e - x_{e-1}} - 1 \quad x \in \Omega^e \tag{2.18}$$

The global modes can be expressed in terms of the local modes $\phi_p(\xi)$ and therefore the approximate solution u^δ can be written as

$$u^\delta(x) = \sum_{i=0}^{N_{dof}-1} \hat{u}_i \mathbf{\Phi}_i(x) = \sum_{e=1}^{N_{el}} \sum_{p=0}^{P} \hat{u}_p^e \phi_p^e(\xi) \tag{2.19}$$

with appropriate conditions to fix the relationship between the global and local modes at the element boundaries, since there are more total local modes than global.

It is desirable, for reasons of numerical efficiency and matrix conditioning, that the expansion basis has orthogonal, or near-orthogonal, properties. An additional requirement is that C^0 continuity exists between the approximate solutions in each element. This is accomplished by constructing the local modes such that only a few of them have magnitude at the elemental boundaries. The rest of the modes are zero at the ends of the interval. This technique is known as the *boundary* and *interior* decomposition.

2.2.1.1 Jacobi polynomials

The particular class of expansion basis that is used, is a *modal* or *hierarchical* basis. This means that a lower-order set of expansions, is fully contained within the higher-order set. This is convenient, since extra polynomial modes can be added without

altering the existing basis functions. One property of modal bases, is that evaluating a function at a specific point requires all of the modal functions to be evaluated at that point.

An orthogonal set of polynomials commonly used to construct modal p-type elemental expansions, are Jacobi polynomials, written $P_p^{\alpha,\beta}(x)$. They are the family of solutions to a singular Sturm-Liouville problem* in the range $-1 < x < 1$, which is written

$$\frac{d}{dx}\left[(1-x)^{1+\alpha}(1+x)^{1+\beta}\frac{d}{dx}P_p^{\alpha,\beta}(x)\right] = \lambda_p(1-x)^{\alpha}(1+x)^{\beta}P_p^{\alpha,\beta}(x) \tag{2.20}$$

where

$$\lambda_p = -p(\alpha+\beta+p+1) \tag{2.21}$$

Crucially, the polynomials satisfy the following orthogonal relationship:

$$\int_{-1}^{1}(1-x)^{\alpha}(1+x)^{\beta}P_p^{\alpha,\beta}(x)P_q^{\alpha,\beta}(x)dx = C\delta_{pq} \tag{2.22}$$

where C is a constant depending on α, β and p. The solution to eqn (2.20) can be calculated using a three-term recursion relationship, given in (Sherwin & Karniadakis 2005).

In the standard element, $\Omega_{st}\ \{\xi | -1 \leq \xi \leq 1\}$, a modal p-type basis, with a boundary-interior decomposition, can be constructed using the particular Jacobi polynomials, $P_{p-1}^{1,1}(\xi)$.

$$\psi_p(\xi) = \begin{cases} (\frac{1-\xi}{2}), & p = 0, \\ (\frac{1-\xi}{2})(\frac{1+\xi}{2})P_{p-1}^{1,1}(\xi), & 0 < p < P, \\ (\frac{1+\xi}{2}), & p = P, \end{cases} \tag{2.23}$$

For the case $P = 5$, these expansion modes are plotted in Figure 2.2. The Jacobi polynomials are defined such that only modes 0 and P have a value of one at the boundary. All the other modes, the so called *interior* modes, are zero there. The boundary modes are linear functions, with the interior modes polynomials of increasing order.

*Originally formulated for describing thermal conduction problems.

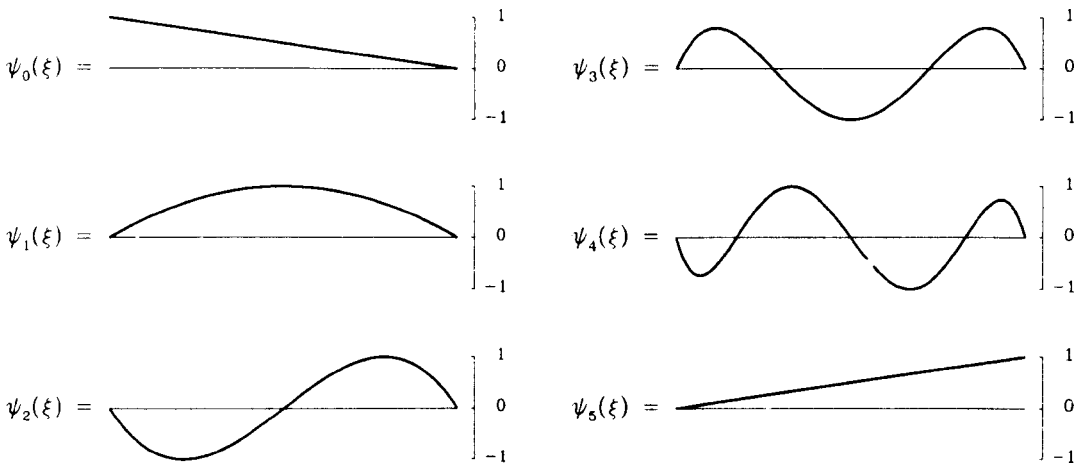


Figure 2.2: Modal expansion modes, $\psi(\xi)$, defined in eqn (2.23), for polynomial order $P = 5$.

2.2.2 Extension to two dimensions

As in one-dimension, use is made of a standard two-dimensional element, within which the numerical operations are performed. This standard region, Q^2, is the bi-unit square, defined

$$\Omega_{st} = Q^2 = \{-1 \leq \xi_1, \xi_2 \leq 1\} \tag{2.24}$$

The simplest means of creating a 2-D basis within this standard element, is to simply take the tensor product of the one-dimensional expansion basis in each of the Cartesian directions (ξ_1, ξ_2), that is,

$$\phi_{pq}(\xi_1, \xi_2) = \psi_p^a(\xi_1)\psi_q^a(\xi_2) \ , \quad 0 \leq p, q, \ p \leq P_1, \ q \leq P_2 \tag{2.25}$$

where P_1 and P_2 may differ in each direction. Figure 2.3 shows the modes corresponding to eqn (2.25) for $P = 4$. A boundary and interior decomposition is still supported by these new expansion modes.

In order to permit a tensor type basis within triangular elements, a "collapsed" coordinate system is defined, which is a mapping from the quadrilateral coordinate

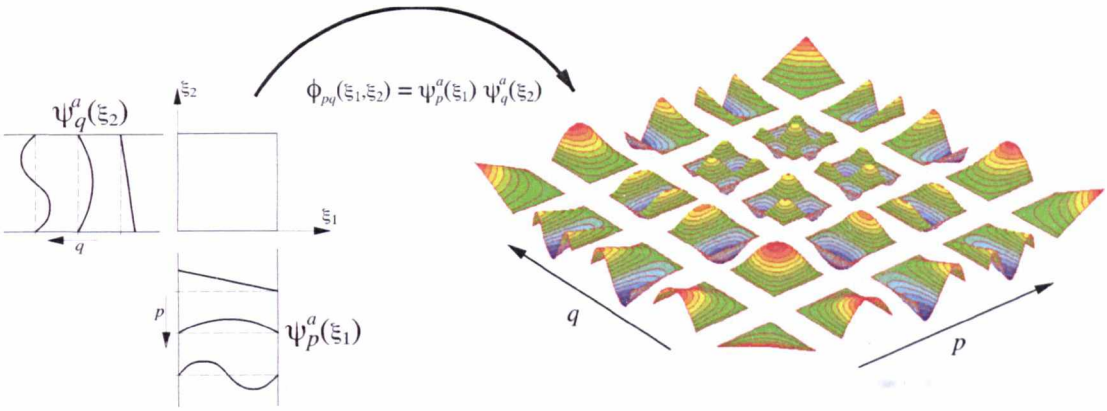


Figure 2.3: 2-D modal expansion modes, $\phi_{pq}(\xi_1, \xi_2)$, defined in eqn (2.25), for polynomial order $P = 4$.

system to the triangular coordinate system. The following transformation is applied

$$\eta_1 = 2\frac{1+\xi_1}{1-\xi_2} - 1 \tag{2.26}$$

$$\eta_2 = \xi_2 \tag{2.27}$$

so that the triangular standard element is defined

$$T^2 = \{-1 \leq \eta_1, \eta_2 \leq 1\} \tag{2.28}$$

The quadrilateral and triangular standard elements, and the correspondence between them are shown in Figure 2.4.

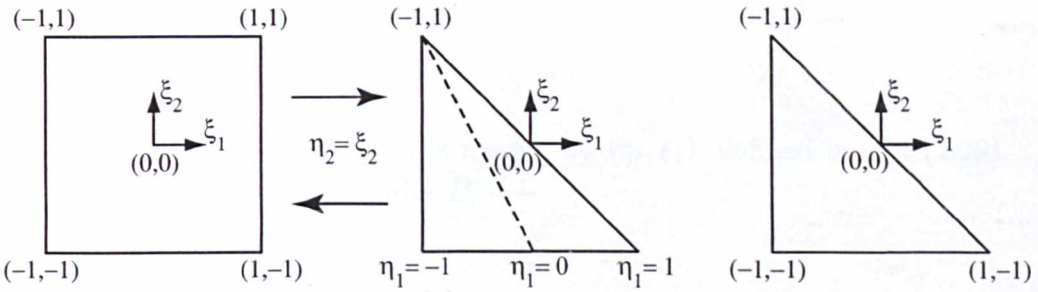


Figure 2.4: Standard regions for the quadrilateral and triangular expansions, and the mapping between them.

The expansion basis in the triangular element is actually the product of a one-dimensional tensor, and a two-dimensional tensor in the second coordinate η_2, that

is,

$$\phi_{pq}(\xi_1, \xi_2) = \psi^a_p(\eta_1)\psi^b_{pq}(\eta_2) \tag{2.29}$$

where ψ^b_{pq}, $(0 \leq p \leq P,\ 0 \leq q \leq Q)$, is defined as

$$\psi^b_{pq}(z) = \begin{cases} \psi^a_q(z), & p = 0,\ 0 \leq q \leq Q, \\ (\frac{1-z}{2})^{p+1}, & 1 \leq p < P,\ q = 0, \\ (\frac{1-z}{2})^{p+1}(\frac{1+z}{2})P^{2p+1,1}_{q-1}(z), & 1 \leq p < P,\ 1 \leq q < Q, \\ \psi^a_q(z), & p = P,\ 0 \leq q \leq Q, \end{cases} \tag{2.30}$$

This basis again allows for boundary and interior decomposition, and the repetition of edge modes on each side of the element, shown in Figure 2.5 facilitates tessellation of the elements into a global expansion, preserving C^0 continuity.

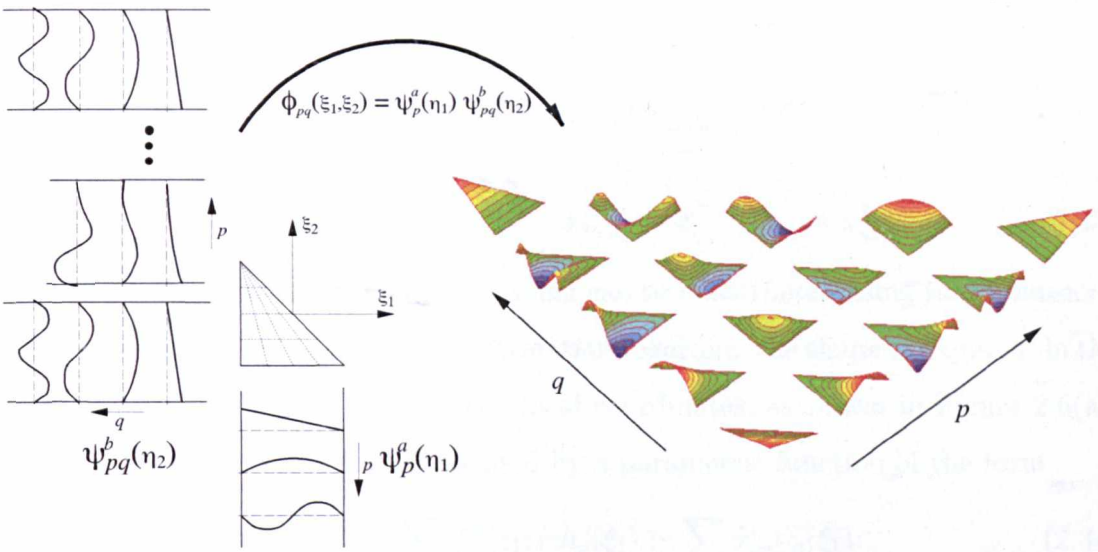


Figure 2.5: 2-D modal expansion modes, $\phi_{pq}(\xi_1, \xi_2)$, defined in eqn (2.29), for polynomial order $P = 4$.

2.2.3 Elemental mappings for curvilinear elements

The concept of mapping elements to a standard element can be extended to general curvilinear elements. This allows large elements, with p-refinement, to be used to mesh complex, curved geometries, without requiring a very fine h discretisation.

For the geometries considered in this thesis, it is used to mesh a circular boundary with only a small number of elements, which would otherwise require a very fine azimuthal discretisation.

To understand how curvilinear elements can be implemented, first consider the mapping for a straight-sided quadrilateral element, which is,

$$x_i = \chi_1(\xi_1,\xi_2) = x_i^A \frac{1-\xi_1}{2}\frac{1-\xi_2}{2} + x_i^B \frac{1+\xi_1}{2}\frac{1-\xi_2}{2} + x_i^D \frac{1-\xi_1}{2}\frac{1+\xi_2}{2} + x_i^C \frac{1+\xi_1}{2}\frac{1+\xi_2}{2}, \quad i = 1,2 \tag{2.31}$$

where x_i^A etc., are the vertex coordinates. It is noted that the polynomials correspond to the $p = 0$ and $p = P$ modes of the modal expansion basis given in eqn (2.23). Writing more generally:

$$x_i = \chi_i(\xi_1,\xi_2) = \sum_{p=0}^{p=P_1}\sum_{q=0}^{q=P_2} \hat{x}_{pq}^i \phi_{pq}(\xi_1,\xi_2) \tag{2.32}$$

where $\phi_{pq} = \psi_p^a(\xi_1)\psi_q^a(\xi_2)$ and $\hat{x}_{pq}^i = 0$, except at the vertex modes which have a values of

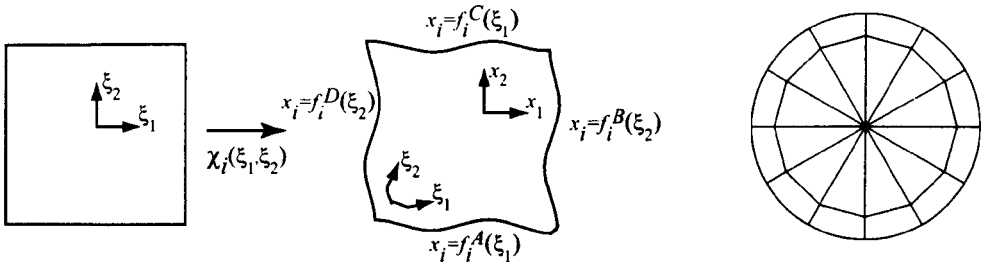
$$\hat{x}_{00}^i = x_i^A \quad \hat{x}_{P_1 0}^i = x_i^B \quad \hat{x}_{P_1 P_2}^i = x_i^C \quad \hat{x}_{0P_2}^i = x_i^D \tag{2.33}$$

This illustrates that the elemental mapping can be constructed using the expansions modes. For a curved edge, further information regarding the shape is required, in the form of mappings of the shape in the local coordinates, as shown in Figure 2.6(a). These mappings are usually represented by a parametric function of the form

$$f^A(\xi_1) \simeq \sum_{p=0} f^A(\xi_1, i) h_p(\xi_1) \simeq \sum_{p=0} \hat{x}_{p0}^i \psi_p(\xi_1) \tag{2.34}$$

using the modal expansion basis. For a circular boundary this function is simply the parametric polar representation $x = \rho\cos\theta$ and $y = \rho\sin\theta$, but for other geometries could be a spline representation.

The meshes used in this thesis were created using the software package *GiD*. Figure 2.6(b) shows the mesh used in this thesis, containing triangular elements in the core of the flow, and quadrilateral elements near the wall, showing the curved edges that capture the circular boundary. This particular mesh was used with a 9^{th} order polynomial expansion to obtain spatially converged solutions.



(a) Relating a general curved element to the standard region (ξ_1, ξ_2)

(b) 2-D mesh used to discretise cross-section, including use of curved elements at the wall

Figure 2.6: Illustration of the use of curved mesh elements.

2.2.4 Extension to three dimensional periodic domains

The expansion basis can be extended to 3D elements such as prisms and tetrahedra. However, since these elements are not used to generate the results presented in this thesis, no details will be given about this. However, a special form of a 3D expansion can be used if a homogeneous coordinate exists in the domain.

A three-dimensional basis $\phi_{pqr}(\xi_1, \xi_2, \xi_3)$ can be constructed by multiplying a 2-D basis $\phi^{2D}_{pq}(\xi_1, \xi_2)$ with a complete expansion in ξ_3 in the following way

$$\phi_{pqr}(\xi_1, \xi_2, \xi_3) = \phi^{2D}_{pq}(\xi_1, \xi_2)\varphi_r(\xi_3) \tag{2.35}$$

The choice of $\varphi_r(\xi_3)$ is dependent on the boundary conditions applied at the ends of the domain, for Dirichlet or Neumann conditions a polynomial basis may be used. For a cylindrical domain, with periodic boundary conditions, a Fourier basis expansion is the obvious, and common, choice. That is

$$\varphi_r(\xi_3) = e^{ir\beta\xi_3}, \ \beta = \frac{2\pi}{L_{\xi_3}} \tag{2.36}$$

For example, the velocities are stored in the following form:

$$\mathbf{v}(x, y, z, t) = \sum_{m=0}^{M-1} \mathbf{v}_m(x, y, t)e^{i\beta mz} \tag{2.37}$$

2.3 Solution of the Navier-Stokes equations

The low Reynolds number, incompressible Navier-Stokes equations, discretised using the spectral/*hp* method, are solved using the high-order splitting scheme introduced in (Karniadakis, Israeli, & Orszag 1991), which has been implemented in the flow solver *Νεκταr*.

Consider the Navier-Stokes equations

$$\frac{\partial \mathbf{v}}{\partial t} = -\nabla p + \nu \mathbf{L}(\mathbf{v}) + \mathbf{N}(\mathbf{v}) \tag{2.38}$$

$$Q \equiv \nabla . \mathbf{v} = 0 \tag{2.39}$$

where $\mathbf{v}$ is the velocity vector, p is the static pressure, ν the kinematic viscosity, and $\mathbf{L}$ and $\mathbf{N}$ are linear and non-linear operators respectively.

Integrating eqn (2.38) in time, for a time step Δt yields

$$\mathbf{v}^{n+1} - \mathbf{v}^n = -\int_{t_n}^{t_{n+1}} \nabla p \, dt + \nu \int_{t_n}^{t_{n+1}} \mathbf{L}(\mathbf{v}) \, dt + \int_{t_n}^{t_{n+1}} \mathbf{N}(\mathbf{v}) \, dt \tag{2.40}$$

where t_n is the time after n steps, i.e. $n\Delta t$, for which the solution is known. This time integration is then decomposed into several substeps in the following way. The non-linear term is approximated via an explicit scheme, in this case, a J_e^{th} order Adams-Bashforth method

$$\frac{\hat{\mathbf{v}} - \mathbf{v}^n}{\Delta t} = \sum_{q=0}^{J_e-1} \beta_q \mathbf{N}(\mathbf{v}^{n-q}) \tag{2.41}$$

where β_q are appropriate weights, see (Sherwin & Karniadakis 2005). The pressure substep is

$$\frac{\hat{\hat{\mathbf{v}}} - \hat{\mathbf{v}}}{\Delta t} = -\nabla \bar{p}^{n+1} \tag{2.42}$$

where $\bar{p}^{n+1}$ is the scalar field that ensures that the final velocity field is incompressible. For reasons of stability, the linear term is approximated via an implicit scheme, in this case, a J_i^{th} order Adams-Moulton scheme.

$$\frac{\mathbf{v}^{n+1} - \hat{\hat{\mathbf{v}}}}{\Delta t} = \nu \sum_{q=0}^{J_i-1} \gamma_q \mathbf{L}(\mathbf{v}^{n+1-q}) \tag{2.43}$$

where γ_q are appropriate weights, again see (Sherwin & Karniadakis 2005). Dirichlet boundary conditions $\overrightarrow{v}_0$

$$\mathbf{v}^{n+1} = \overrightarrow{v}_0 \tag{2.44}$$

are applied. It is assumed that the intermediate velocity field $\hat{\mathbf{v}}$ satisfies the incompressibility constraint

$$\nabla.\hat{\mathbf{v}} = 0 \quad in \ \Omega \tag{2.45}$$

When substituted into eqn (2.42), it leads to a Poisson equation for the pressure

$$\nabla^2 \bar{p}^{n+1} = \nabla.\left(\frac{\hat{\mathbf{v}}}{\Delta t}\right) \quad in \ \Omega \tag{2.46}$$

This is solved subject to the following boundary condition

$$\frac{\partial \bar{p}^{n+1}}{\partial n} = -\frac{\overrightarrow{v}_0.\mathbf{n} - \hat{\mathbf{v}}.\mathbf{n}}{\Delta t} \quad on \quad \partial\Omega \tag{2.47}$$

Splitting errors can be minimised by using a mixed implicit/explicit boundary condition for the pressure (Karniadakis, Israeli, & Orszag 1991) which is solved subject to the following boundary condition

$$\frac{\partial \bar{p}^{n+1}}{\partial \mathbf{n}} = \mathbf{n}.\left[\sum_{q=0}^{J_c-1} \beta_q \mathbf{N}(\mathbf{v}^{n-q}) + \nu \sum_{q=0}^{J_i-1} \gamma_q \mathbf{L}(\mathbf{v}^{n+1-q})\right] \quad on \quad \partial\Omega \tag{2.48}$$

The final velocity field at the next time step, $\mathbf{v}^{n+1}$, is obtained by solving the Helmholtz equation (previously discussed in Section 2.1.2) which is forced by the velocity field $\hat{\mathbf{v}}$. As an example, for clarity, consider a first-order Adams-Moulton scheme, which reduces eqn (2.43) to:

$$\Delta t \gamma_0 \mathbf{L}(\mathbf{v}^{n+1}) - \mathbf{v}^{n+1} + \hat{\mathbf{v}} = 0 \tag{2.49}$$

which is clearly the multi-dimensional formulation of the one-dimensional Helmholtz equation in eqn (2.5).

To solve the Navier-Stokes equations in a three dimensional periodic domain, using the Fourier basis described in Section 2.2.4, the Fourier transform of the Navier-Stokes equations is taken. This essentially reduces the problem to m two dimensional Navier-Stokes equations, assuming an explicit treatment of the non-linear terms:

$$\frac{\partial \mathbf{v}_m}{\partial t} = -\tilde{\nabla}_m p_m + \nu \tilde{\nabla}_m^2 \mathbf{v}_m + \widehat{[\mathbf{v} \cdot \nabla \mathbf{v}]} \quad in \ \Omega_m, \ m = 0, \ldots, M-1 \tag{2.50}$$

where the 'hat' signifies the Fourier transform, and the equations are solved on the M two-dimensional slices Ω_m. The linear differential operators are also modified, and are:

$$\tilde{\nabla}_m = \left(\frac{\partial}{\partial x}, \frac{\partial}{\partial y}, im\beta\right), \quad \left(\tilde{\nabla}_m^2 = \frac{\partial^2}{\partial x^2} + \frac{\partial^2}{\partial y^2} - \beta^2 m^2\right) \tag{2.51}$$

Within the 2-D planar mesh, high-order C_0-continuous polynomial basis functions are used, with both triangular elements and quadrilateral elements with curved boundaries. This approach has several advantages; no remeshing is required for each geometry, computational time is smaller than for a full 3-D mesh, and the overhead on parallelisation is small since for most of the time step each Fourier mode is solved independently.

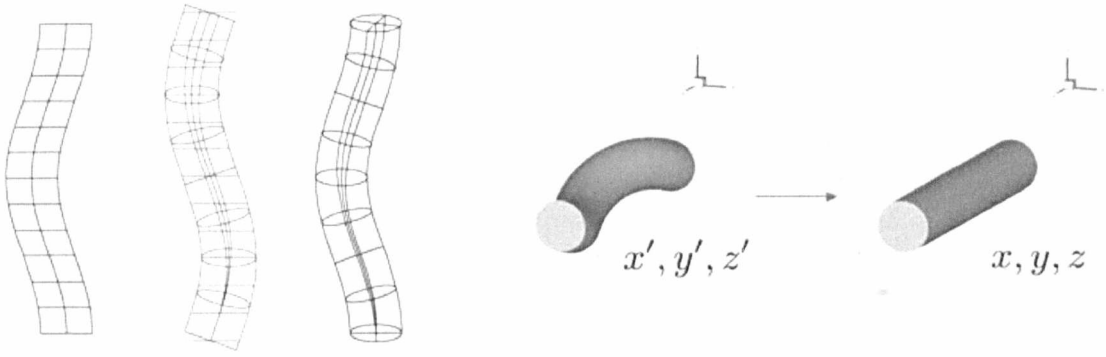
2.4 Coordinate transformation of the Navier-Stokes equations

For the range of values of R and c under consideration, the resultant helical pipe geometry can be well approximated by a circular cross-section simply translated by a helical centreline. The validity of this approximation is illustrated in Figure 2.7(a). This approximation can be conceptually reversed by performing a coordinate mapping from a helical geometry to a cylindrical geometry. The mapping is then applied to the Navier-Stokes equations, which are then solved in the cylindrical domain, but with an additional d'Alembert body-force term which represents that applied to the flow by the original geometry. A coordinate transformation has been used previously to investigate the bluff body flows in (Newman 1996) and channel flow in (Koberg 2008). The mathematical details follow.

In a coordinate system (x', y', z'), the non-dimensional Navier-Stokes equations are:

$$\frac{\partial \mathbf{u}'}{\partial t'} + (\mathbf{u}' \cdot \nabla')\mathbf{u}' = -\nabla' p' + \frac{1}{Re}\nabla'^2 \mathbf{u}', \tag{2.52}$$

$$\nabla' \cdot \mathbf{u}' = 0, \tag{2.53}$$



(a) Comparison of helical pipe (right) with approximation (left)

(b) Transformation of solution domain coordinate system

Figure 2.7: Coordinate transformation concept applied to small amplitude helical pipes

A coordinate transformation is defined, as illustrated in Figure 2.7(b):

$$x = x' - \xi_x(z'), \tag{2.54}$$

$$y = y' - \xi_y(z'), \tag{2.55}$$

$$z = z', \tag{2.56}$$

$$t = t', \tag{2.57}$$

For a helix, the mapping terms $\xi_x(z')$ and $\xi_y(z')$ are simply those that define a helical centreline:

$$\xi_x(z') = R\cos(z'/c), \tag{2.58}$$

$$\xi_y(z') = R\sin(z'/c), \tag{2.59}$$

Using the chain rule, the partial derivative operators transform to the following:

$$\frac{\partial}{\partial x'} = \frac{\partial}{\partial x}, \tag{2.60}$$

$$\frac{\partial}{\partial y'} = \frac{\partial}{\partial y}, \tag{2.61}$$

$$\frac{\partial}{\partial z'} = \frac{\partial}{\partial z} - \frac{\partial \xi_x}{\partial z}\frac{\partial}{\partial x} - \frac{\partial \xi_y}{\partial z}\frac{\partial}{\partial y}, \tag{2.62}$$

$$\frac{\partial}{\partial t'} = \frac{\partial}{\partial t}, \tag{2.63}$$

Taking the time derivatives of eqns (2.54)-(2.56), produces the transformations for velocity and pressure:

$$u = u' - w'\frac{\partial \xi_x}{\partial z}, \tag{2.64}$$

$$v = v' - w'\frac{\partial \xi_y}{\partial z}, \tag{2.65}$$

$$w = w', \tag{2.66}$$

$$p = p', \tag{2.67}$$

Substituting all the modified terms into eqn (2.52) produces the Navier-Stokes equations in a coordinate system (x, y, z):

$$\frac{\partial \mathbf{u}}{\partial t} + (\mathbf{u}\cdot\nabla)\mathbf{u} = -\nabla p + \frac{1}{Re}\nabla^2\mathbf{u} + \mathbf{A}(\mathbf{u}, p, \xi_x, \xi_y), \tag{2.68}$$

$$\nabla\cdot\mathbf{u} = 0, \tag{2.69}$$

Note that the mapping is divergence free, that is, it satisfies:

$$\frac{\partial \xi_x}{\partial x} + \frac{\partial \xi_y}{\partial y} = 0 \tag{2.70}$$

Consequently the continuity equation is unaltered, so that:

$$\frac{\partial u'}{\partial x'} + \frac{\partial v'}{\partial y'} + \frac{\partial w'}{\partial z'} = \frac{\partial u}{\partial x} + \frac{\partial v}{\partial y} + \frac{\partial w}{\partial z} \tag{2.71}$$

The d'Alembert body force term, $\mathbf{A}(\mathbf{u}, p, \xi_x, \xi_y)$, has components A_x, A_y and A_z. A_x and A_y both contain the convective derivative of the z-component of the transformed Navier-Stokes equations. Substituting this into A_x, removes the time derivative of w, producing:

$$\begin{aligned} A_x = & \left[-\frac{d\xi_x}{dz}\frac{d\xi_y}{dz}\frac{\partial p}{\partial y} - w^2\frac{d^2\xi_x}{dz^2} + \frac{d\xi_x}{dz}\frac{\partial p}{\partial z} - \left(\frac{d\xi_x}{dz}\right)^2\frac{\partial p}{\partial x}\right] \\ & + \frac{1}{Re}\left[-2\frac{d\xi_y}{dz}\frac{\partial w}{\partial y}\frac{d^2\xi_x}{dz^2} - 2\frac{d\xi_y}{dz}\frac{\partial^2 u}{\partial y \partial z} - \frac{d^2\xi_x}{dz^2}\frac{\partial u}{\partial x} + 2\frac{d\xi_x}{dz}\frac{d\xi_y}{dz}\frac{\partial^2 u}{\partial x \partial y}\right. \\ & - 2\frac{d^2\xi_x}{dz^2}\frac{\partial w}{\partial x}\frac{d\xi_x}{dz} + \left(\frac{d\xi_y}{dz}\right)^2\frac{\partial^2 u}{\partial y^2} + 2\frac{\partial w}{\partial z}\frac{d^2\xi_x}{dz^2} - \frac{d^2\xi_y}{dz^2}\frac{\partial u}{\partial y} \\ & \left. + w\frac{d^3\xi_x}{dz^3} - 2\frac{d\xi_x}{dz}\frac{\partial^2 u}{\partial x \partial z} + \left(\frac{d\xi_x}{dz}\right)^2\frac{\partial^2 u}{\partial x^2}\right] \end{aligned} \tag{2.72}$$

A_x and A_y have the same form, and therefore only A_x is shown. The z-component A_z is:

$$\begin{aligned} A_z &= \left[\frac{d\xi_x}{dz}\frac{\partial p}{\partial x} + \frac{d\xi_y}{dz}\frac{\partial p}{\partial y}\right] \\ &+ \frac{1}{Re}\left[\left(\frac{d\xi_x}{dz}\right)^2\frac{\partial^2 w}{\partial x^2} + \left(\frac{d\xi_y}{dz}\right)^2\frac{\partial^2 w}{\partial y^2} + 2\frac{d\xi_x}{dz}\frac{d\xi_y}{dz}\frac{\partial^2 w}{\partial x \partial y}\right. \\ &- \left.\frac{\partial w}{\partial x}\frac{d^2\xi_x}{dz^2} - \frac{\partial w}{\partial y}\frac{d^2\xi_y}{dz^2} - 2\frac{d\xi_x}{dz}\frac{\partial^2 w}{\partial x \partial z} - 2\frac{d\xi_y}{dz}\frac{\partial^2 w}{\partial y \partial z}\right] \end{aligned} \tag{2.73}$$

The d'Alembert terms are treated explicitly in the solver by simply adding them to the non-linear term $\mathbf{N}(\mathbf{v})$, eqn (2.38), at each time step, which is implemented within the source file *convective.c*. To both verify and validate the implementation of the d'Alembert terms, the following test was performed.

Consider a large domain with a uniform flow solution of $\mathbf{u} = (0, 0, 1)$, from which a helical pipe geometry is extracted. Within this helical pipe the flow solution will also be $\mathbf{u} = (0, 0, 1)$. If this domain is then mapped to the cylinder, the solution will become $\mathbf{u} = ((R/c)sin(z/c), -(R/c)cos(z/c), 1)$. Performing a computation using this solution as a velocity boundary condition on the cylinder walls, will yield this same solution throughout the domain, assuming that the d'Alembert terms have been correctly implemented. When this computation was performed, the desired solution was obtained immediately to machine precision throughout the entire domain, demonstrating that the code was correct.

2.5 Practical considerations for obtaining solutions using *Nεκταr*

2.5.1 Initial conditions, time step and convergence

To perform the first simulations, the velocity field was initialised to a Poiseuille flow solution, corresponding to the applied pressure gradient. Subsequent computations

were restarted from the solutions at a lower Reynolds number (typically in intervals of 50) or a smaller helical radius. As the Reynolds number increased, it was necessary to reduce the time step in order to maintain stability.

In order to test for convergence of the solution, the polynomial order was increased until the velocity and pressure at sample points in the flow changed less than 0.5%, and integrated measures of volume flow rate and total force on the wall varied by only a few thousandths of a percent. The solution was time-stepped until it converged in time to machine precision. The final solutions used a 9th order polynomial in the cross-section, with 8 Fourier modes in the axial direction for a single helix and 32 Fourier modes for the multiple helical geometries.

2.5.2 Implementation of the pressure drop

The flow is driven by a constant pressure gradient in the axial direction. This is implemented as a forcing term in the code, and is introduced into the explicit time integration of the Helmholtz equation sub-step. Due to the unknown functional relationship between pressure gradient and flow rate, a degree of trial and improvement was required to achieve the desired Reynolds number. However, in practice, it became possible to interpolate or extrapolate, as appropriate, to obtain the likely required pressure gradient for a new Reynolds number or particular geometric parameter.

2.5.3 Achieving convergence for $Re > 250$

It was found that obtaining converged solutions at Reynolds numbers higher than 500 was problematic. For a geometry with $R = 0.1D$, a value of $Re = 700$ could be achieved, but for $R = 0.5D$, it was found that $Re = 500$ was the empirical limit. This suggests that the magnitude of the body force terms grew too large to be dealt with successfully by the current implementation. Due to time constraints, no new code development was possible. However, the following measures were taken

to attempt to reach convergence:

1. Changing the polynomial order and number of Fourier modes
2. Reducing the time step significantly (by a factor larger than the increase in Re)
3. Reducing the size of the increase in pressure gradient from one computation to the next

For future studies, which require convergence at higher Reynolds number, a more subtle treatment of the d'Alembert terms may be required. For example, the explicit integration of these terms could be performed in a separate sub-step, rather than being lumped with the convective terms. This would allow a more appropriate integration scheme, and order, to be used for the d'Alembert terms. Further, it is possible that some of terms could be linearised and treated implicitly, whilst some of the pressure gradient terms could be included in the Poisson equation sub-step, leaving the remaining non-linear terms to be integrated explicitly.

2.6 Postprocessing

2.6.1 Vorticity

Vorticity is a vector quantity, strictly a *pseudo-vector*, defined as the curl of the velocity field:

$$\boldsymbol{\omega} = \nabla \times \mathbf{u} \tag{2.74}$$

The velocity field file created by *Nεκταr* is in the mapped, cylindrical domain. Therefore to calculate the vorticity in the helical domain requires that the partial derivatives are modified according to eqns (2.60)-(2.63), which, for example modifies the axial vorticity in the following manner:

$$\omega_z = \underbrace{\frac{\partial v}{\partial x} - \frac{\partial u}{\partial y}}_{vorticity} + \underbrace{\frac{\partial w}{\partial x}\frac{\partial \xi_y}{\partial z} - \frac{\partial w}{\partial y}\frac{\partial \xi_x}{\partial z}}_{mapping\ terms} \tag{2.75}$$

The x-component of vorticity is modified thus (with the y-component altered similarly):

$$\omega_x = \underbrace{\frac{\partial w}{\partial y} - \frac{\partial v}{\partial z}}_{vorticity} + \underbrace{\frac{\partial \xi_x}{\partial z}\frac{\partial v}{\partial x} + \frac{\partial \xi_y}{\partial z}\frac{\partial v}{\partial y} - \frac{\partial \xi_y}{\partial z}\frac{\partial w}{\partial z} - w\frac{\partial^2 \xi_y}{\partial z^2} + \left(\frac{\partial \xi_y}{\partial z}\right)^2 \frac{\partial w}{\partial y} + \frac{\partial \xi_x}{\partial z}\frac{\partial \xi_y}{\partial z}\frac{\partial w}{\partial x}}_{mapping\ terms} \tag{2.76}$$

2.6.2 λ_2 criterion for vortex identification

A common vortex identification scheme used in biomedical flows (Doorly, Sherwin, Franke, & Peiro 2002) (Pitt 2005) is the λ_2 criterion proposed by Jeong & Hussain (Jeong & Hussain 1995). They define a vortical core as an area of pressure minimum, whilst neglecting the effects of unsteady straining and viscosity. This information on the local minima (or otherwise) of pressure is contained in the Hessian of the pressure, $p_{,ij}$, which is obtained through the following analysis.

First, consider that the velocity gradient tensor $\nabla \mathbf{u}$ can be decomposed into symmetric and anti-symmetric parts. The symmetric part $\mathbf{S}$ is the rate-of-strain tensor:

$$\mathbf{S} = \frac{1}{2}\left[\nabla \mathbf{u} + \nabla \mathbf{u}^T\right] \tag{2.77}$$

The anti-symmetric part $\mathbf{\Omega}$ is the vorticity tensor:

$$\mathbf{\Omega} = \frac{1}{2}\left[\nabla \mathbf{u} - \nabla \mathbf{u}^T\right] \tag{2.78}$$

Taking the gradient of the Navier-Stokes equation and substituting in (2.77) and (2.78) gives:

$$-\frac{1}{\rho}p_{,ij} = \frac{d\mathbf{S}}{dt} + (\mathbf{SS} + \mathbf{\Omega\Omega}) + \frac{d\mathbf{\Omega}}{dt} + (\mathbf{S\Omega} + \mathbf{\Omega S}) - \nu\nabla^2(\mathbf{S} + \mathbf{\Omega}) \tag{2.79}$$

Where $\frac{d}{dt}$ is the material derivative $\frac{\partial}{\partial t} + \mathbf{u} \cdot \nabla$. Note also that $\mathbf{SS} = S_{ij}S_{jk}$. However, Jeong and Hussain show that the transport of $\mathbf{\Omega}$ is given by:

$$\frac{d\mathbf{\Omega}}{dt} = -(\mathbf{S\Omega} + \mathbf{\Omega S}) + \nu\nabla^2(\mathbf{S} + \mathbf{\Omega}) \tag{2.80}$$

By removing these terms and the unsteady strain term, $\frac{d\mathbf{S}}{dt}$, leaves an expression for the pressure Hessian:

$$-\frac{1}{\rho}p_{,ij} = (\mathbf{SS} + \mathbf{\Omega\Omega}) \tag{2.81}$$

When $p_{,ij}$ has two positive eigenvalues, this indicates that a local pressure minimum exists at that point in the plane of the two eigenvectors associated with these eigenvalues. Since the tensor $(\mathbf{SS} + \mathbf{\Omega\Omega})$ is symmetric, it can have only real eigenvalues, which can be ordered thus:

$$\lambda_1 \geq \lambda_2 \geq \lambda_3 \tag{2.82}$$

Therefore for two eigenvalues of $(\mathbf{SS} + \mathbf{\Omega\Omega})$ to be negative, we simply need to test for the condition $\lambda_2 < 0$. These regions are revealed by plotting isosurfaces of λ_2 for a value slightly smaller than 0, which produces smoother, more coherent figures.

Doorly *et al.* (Doorly, Sherwin, Franke, & Peiro 2002) present an alternative derivation of the λ_2 criterion, by considering the relative acceleration of a particle about a point. Expanding the velocity as a series to first order, the acceleration can be found. A vortex is then defined as existing if the radial component of acceleration is negative for any orientation of the vector between the two points in the plane. This leads to the same eigenvalue criterion of $(\mathbf{S}^2 + \mathbf{\Omega}^2)$.

As for the vorticity calculation, the λ_2 criterion is calculated using the appropriate mappings of velocity and partial differential operators.

2.6.3 Particle tracking

As a physical process, mixing is a combination of advection and diffusion. Advection, by stretching and folding the flow, creates large concentration gradients across which species can rapidly diffuse. However, previous research has found that for bypass

graft flows it is sufficient to consider advection alone, since even the smallest elements in blood, such as platelets, possess very low effective diffusivity. Adding a diffusion model makes little difference to the results, except perhaps in areas of the velocity field where there is recirculating flow (Doorly, Sherwin, Franke, & Peiro 2002). Therefore, rather than solving the advection-diffusion equation, we need only to integrate the advection equations (2.83), with respect to time. Strictly, mixing where only advection is considered should be termed "stirring".

$$\frac{d\mathbf{x}}{dt} = \mathbf{u}(\mathbf{x}, t) \tag{2.83}$$

The numerical integration of eqn (2.83), i.e.

$$\mathbf{x}^{n+1} = \mathbf{x}^n + \int_{t^n}^{t^{n+1}} \mathbf{u} dt \tag{2.84}$$

is equivalent to tracking mass-less, passive computational particles through the velocity field. Particle tracking facilities are available in many scientific visualization packages, such as Visual3 (R. Haimes 1991) and PLOT3D (Walatka, Buning, Pierce, & Elson 1990). The algorithms used in these packages generally assume that the velocity field is represented in a linear piecewise format, and therefore do not achieve the requisite accuracy when used with the high-order representation of *Νεκταr*. Coppola *et al.* (Coppola, Sherwin, & Peiro 2001) developed a particle tracker which interpolates directly from the high-order polynomial representation of the velocity field, and is thus more accurate than a scheme using a linear interpolation mesh. The existing code was only able to process 2-D and 3-D velocity field data, and therefore was modified to interpolate velocity fields stored using the combined 2-D & Fourier representation used in this thesis.

2.6.3.1 Runge-Kutta time integration

An explicit Runge-Kutta scheme is used for the time integration:

$$\mathbf{x}^{n+1} = \mathbf{x}^n + \Delta t \sum_{i=1}^{s} b_i \mathbf{u}_i \tag{2.85}$$

where

$$\mathbf{u}_i = \mathbf{u}\left(\mathbf{x}^n + \Delta t \sum_{j=1}^{i-1} a_{ij}\mathbf{u}_j, t^n + c_i\Delta t\right) \tag{2.86}$$

s is the number of stages of the Runge-Kutta scheme, and Δt is the time step. The values b_i, c_i and a_{ij} are the coefficients from the *Butcher array*, which takes the following form:

$$\begin{array}{c|ccc} c_1 & a_{11} & \cdots & a_{1s} \\ \vdots & \vdots & & \vdots \\ c_s & a_{s1} & \cdots & a_{ss} \\ \hline & b_1 & \cdots & b_s \end{array}$$

For a four-stage scheme the coefficients take the following specific values:

$$\begin{array}{c|cccc} 0 & & & & \\ \frac{1}{2} & \frac{1}{2} & & & \\ \frac{1}{2} & 0 & \frac{1}{2} & & \\ 1 & 0 & 0 & 1 & \\ \hline & \frac{1}{6} & \frac{1}{3} & \frac{1}{3} & \frac{1}{6} \end{array}$$

The velocity field generated by Nektar is in the transformed coordinate system. It is both simpler and faster to track the particles in the transformed coordinates and then map their final position back to the original coordinate system at the end of the calculations.

In order to perform the time integration it obviously necessary to determine the velocity of a particle at a position $\mathbf{x}^n$. With the spectral/*hp* elements used here, there are two ways of accomplishing this. The first to be discussed, is tracking in physical space, and is the method used in this thesis. The other method is to track the particles in parametric space, which will be briefly described for the purposes of comparison.

2.6.3.2 Particle tracking in physical space

To track particles in physical space, that is, the space of the solution $\mathbf{x} \in \Omega$, it is necessary to determine the element containing the particle, and its local position

within that element, $\boldsymbol{\xi}_i$. Once determined, the velocity can be interpolated using the high order expansion basis within the element.

A mapping exists from physical space to the standard elements, discussed in Section 2.2.1, which is denoted:

$$\mathbf{x}_i = \chi(\boldsymbol{\xi}_i) \tag{2.87}$$

It is the inverse problem which must be now solved, that is,

$$\boldsymbol{\xi}_i = \chi^{-1}(\mathbf{x}) \tag{2.88}$$

For curvilinear elements and bilinear mappings of straight-sided quadrilateral elements, it is non-trivial to determine the inverse mapping χ^{-1}. To do so, the Newton-Raphson method is applied to the finding the zero of the following problem

$$\mathbf{F}(\xi_i) = \chi(\boldsymbol{\xi}_i) - \mathbf{x}_i \tag{2.89}$$

The Newton-Raphson iteration of eqn (2.89) is

$$\mathbf{J}_e \cdot \left[\xi_i^{k+1} - \xi_i^k\right] = -\mathbf{F}(\boldsymbol{\xi}_i^k), \quad \mathbf{J}_e = \frac{\partial \mathbf{F}}{\partial \boldsymbol{\xi}} = \frac{\partial \chi}{\partial \boldsymbol{\xi}} \tag{2.90}$$

where k is an iteration counter, i is the discrete point and $\mathbf{J}_e$ is the Jacobian of the mapping. In three-dimesions the Newton-Raphson procedure requires three interpolation operations to determine $\chi(\boldsymbol{\xi}_i)$, and nine operations to determine $\mathbf{J}_e^{-1}$, per iteration. For the curved quadrilateral elements used in this thesis, typically four, and occasionally six, iterations of the Newton-Raphson procedure were required to determine the local particle position within the element.

2.6.3.3 Particle tracking in parametric space

To track particles in parametric space, the physical space velocity is transformed into the standard element, and the particle's position tracked within the standard element. That is, the equation to be integrated is:

$$\frac{d\boldsymbol{\xi}^e}{dt} = \mathbf{u}_\xi^e(\boldsymbol{\xi}, t) \tag{2.91}$$

where the transformed velocity in the standard element, $\mathbf{u}_\xi^e(\boldsymbol{\xi}, t)$, is obtained via the chain rule

$$u_{\xi_i} = \frac{d\xi_i}{dt} = \frac{d\xi_i}{dx_1}\frac{dx_1}{dt} + \frac{d\xi_i}{dx_2}\frac{dx_2}{dt} + \frac{d\xi_i}{dx_3}\frac{dx_3}{dt}, \quad i = 1, 2, 3 \tag{2.92}$$

However, since the geometric derivatives, i.e $d\xi_i/dx_1$, are only piecewise continuous, it is necessary to determine the location of the intersection of the particle with the element boundary, so that it can be tracked into the next element. This requires an iterative approach, which is unfortunately ill-conditioned when it is used in curvilinear spectral/*hp* elements.

The physical and parametric space tracking methods can be combined to form several other strategies, the details of which can be found in (Coppola, Sherwin, & Peiro 2001) and (Sherwin & Karniadakis 2005).

The use of the combined two-dimensional mesh and Fourier expansion, in addition to the benefits already described, also enables better performance for the particle tracking. The Fourier expansion can be considered as transforming the two-dimensional mesh into a three-dimensional mesh, which utilises only a single element in the z direction. Therefore, it is trivial to determine the local elemental position of the particle in that direction. Therefore, the computational cost associated with determining the inverse mapping is reduced from that which would be incurred, were a truly three-dimensional mesh used.

Chapter 3

Steady Flow & Mixing in Single Helical Geometries

This Chapter discusses both the velocity field and mixing properties of flow in small amplitude helical pipes, which have periodic velocity boundary conditions in the axial direction. It begins with a description of the geometric and flow parameters to be investigated, in Section 3.1. The velocity field is examined in Section 3.2, in particular the axial velocity and secondary flow structures, with the resultant mixing behaviour explained and quantified in Sections 3.3 & 3.4 respectively. The relevance of the results to the *in vivo* disease process of thrombosis is outlined in Section 3.5. Possible implications of the results for flows in general pipe geometries possessing arbitrary curvature, torsion and twist are discussed in Section 3.6, before conclusions are presented in Section 3.7.

3.1 Parameters of study

For the approximate helical pipe geometry used throughout this work, which was introduced in Section 2.4, the pipe boundary is defined as:

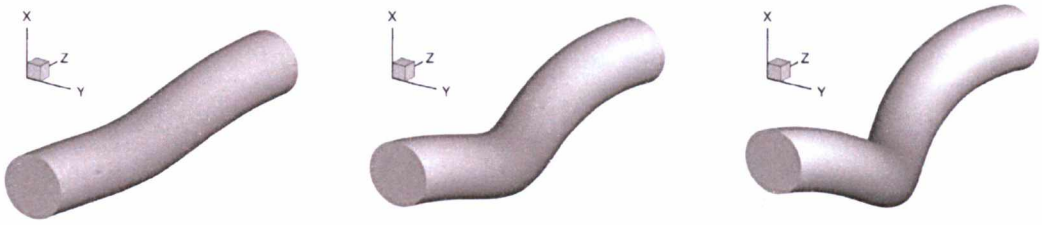
$$\mathbf{x} = \mathbf{R}(t) + (D/2)\cos\theta\mathbf{i} + (D/2)\sin\theta\mathbf{j} \tag{3.1}$$

where $\mathbf{R}(t)$ is the helical centreline equation. Comparison with eqn (1.18), reveals that the effect of the approximation is to replace $\mathbf{N}(t)$ & $\mathbf{B}(t)$ with $\mathbf{i}$ & $\mathbf{j}$ respectively, and θ is now measured relative to the x-axis, or $\mathbf{i}$, and not the $\mathbf{N}$ vector (see Figure 1.6). One consequence of the geometry approximation is that the pipe cross-section viewed normal to the centreline is now slightly elliptical rather than circular as it would be for a true helical geometry, and rotates with the Frenet triad. The non-circularity of the cross-section is small however, particularly for the values of $R < 0.25D$. The impact of this on the velocity field is discussed in Section 3.2.

A Reynolds number of 250, defined as $\frac{\overline{w}D}{\nu}$, ($\overline{w}$ is the mean axial velocity, and ν the kinematic viscosity), is used for the majority of the flow computations to match representative physiological conditions in a bypass graft, as used in other studies (Sherwin, Shah, Doorly, Peiro, Papaharilaou, Watkins, Caro, & Dumoulin 2000) (Moore, Steinman, Prakash, Johnston, & Ethier 1999). Caro *et al.* coin the term, small amplitude helical technology (SMAHT), to describe the geometries used for clinical applications, which have small helical radius, but large pitch length. The upper limit of the helical pitch length that can be used for SMAHT is set by the physical space constraints of the clinical application, with the lower limit determined by the necessity to preserve the general morphology of the SMAHT. Within these limits it is expected that the flow field will undergo only small changes with respect to varying pitch, relative to those induced by varying the radius. Therefore in this study, and taking the geometries used by Caro *et al.* as a guide, all the helical geometries will have a pitch of six pipe diameters, $6D$, with the helical radius varying from $0.1D$ to $0.5D$ in increments of $0.05D$. Three such geometries are shown in Figure 3.1.

Before examining the results for the velocity field, it should be noted that, contrary to the case of a curved pipe, for all the geometries considered here their curvature increases with helical radius. The curvature of a helix was defined in Chapter 1, but is given again here for convenience:

$$\kappa = \frac{R}{R^2 + c^2} \tag{3.2}$$



(a) R = 0.1D, Pitch = 6D (b) R = 0.3D, Pitch = 6D (c) R = 0.5D, Pitch = 6D

Figure 3.1: Examples of the helical geometries under consideration in this thesis.

This function is such that for all cases where $R < c$, the curvature will increase with radius. For the geometries investigated here $c = 3D/\pi \approx D$, with R varying from $0.1D$ to $0.5D$, clearly within this range. The maximum curvature then occurs for $R = c$, beyond which curvature decreases with radius. Torsion has essentially the same functional form as curvature, with R and c simply interchanged. Therefore for fixed R and varying c it behaves in the same way as curvature. However, c is fixed in this study, which simply means that torsion decreases with increasing R for all the geometries considered. To aid interpretation of the results, particular values of dimensionless curvature and torsion have been calculated, and are located in Table 3.1.

Table 3.1: Normalised curvature and torsion data for helical geometries under consideration (to 3 s.f.)

Pitch	Radius	Curvature κ	Torsion τ
6	0.1	0.0542	0.518
6	0.2	0.105	0.502
6	0.3	0.150	0.477
6	0.4	0.187	0.445
6	0.5	0.215	0.411

In what follows we assume blood to be a Newtonian fluid, which is a reasonable approximation for flow in the larger blood vessels (Friedman 1993), and used in the

majority of studies in this field. Only steady flow is examined at present, which for modelling A-V shunt flow is acceptable, as relatively low pulsatility has been found in renal dialysis access shunt flow (Caro, Cheshire, & Watkins 2005). For flow in artery bypass grafts it is a poorer approximation, but a significant portion of the pulsatile flow cycle is quasi-steady, so that the vortical flow structures may be similar, though as recognised in (Doorly 1999), unsteadiness can play a large role in vascular mixing. Furthermore, it is sensible to develop a satisfactory understanding of the physics involved in the the steady flow case, before attempting the more complicated case of time-dependent flow.

3.2 Velocity field

The velocity field in the helical pipe is self-similar throughout the pipe, but is translated by the helical centreline, and rotates through 2π (with the Frenet triad) over one pitch length, as illustrated in Figure 3.2. It is therefore only necessary to show a single slice of the velocity field for each geometry, which are taken at $z = 0$. The geometry approximation and coordinate system used to obtain these results conveniently avoid the problems of representing the velocity field that are associated with the formulations described in Section 1.3. However, as noted in Section 3.1 the cross-section normal to the centreline is now slightly elliptical. This non-circularity will enhance the effect of torsion on the flow as suggested by Tuttle, leading to greater than expected asymmetry of the secondary flow structures. A study on flow in helical pipes of elliptical cross-section (Hadi & Sharma 2002) suggests that at the Reynolds number considered in this thesis, the secondary flow is very similar in form to the that for a circular cross-section. Only at very low Reynolds number do the in-plane streamlines change in form, from an elliptical to a hyperbolic structure.

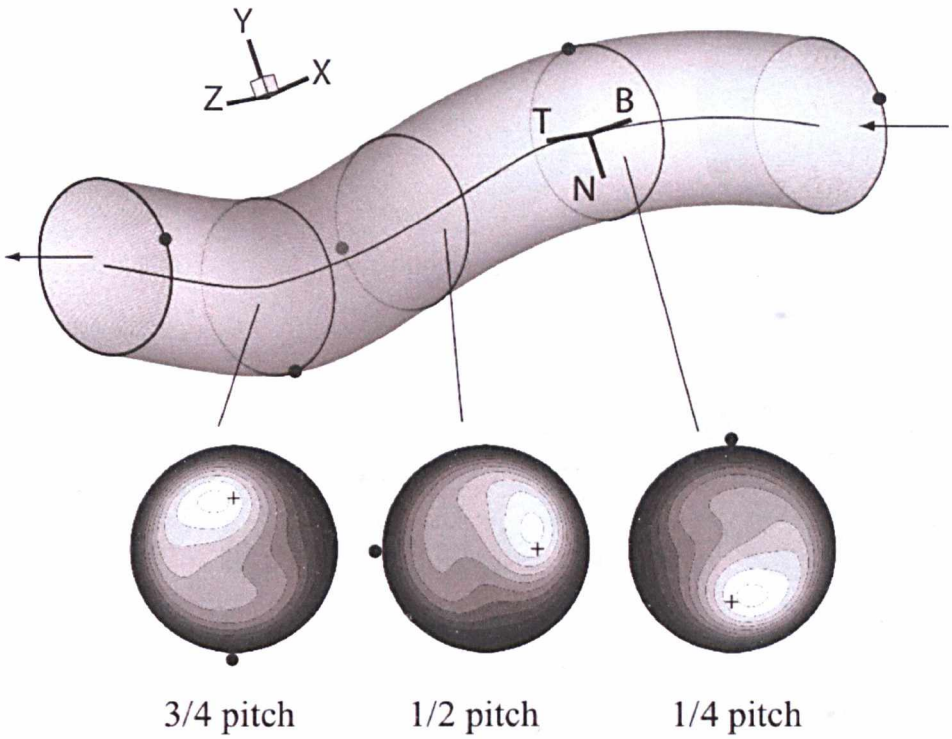


Figure 3.2: Helical pipe geometry, $R = 0.25D$, with self-similar axial velocity profile. The origin $x = 0 = y$ is marked by a small cross. An example point on the pipe wall highlights the rotation of the velocity field along the axis

3.2.1 Axial velocity

Figures 3.3(a) - 3.3(c) show contour plots of the axial velocity, where the axial direction is the z-axis in the Cartesian frame. For $R = 0.1D$ the axial velocity profile is close to that of Poiseuille flow, with only a small displacement of the peak velocity. As R increases, the profile becomes more asymmetric, with the peak axial velocity moving towards the wall.

Figure 3.4 is a plot of the radial offset of the peak axial velocity versus helical radius. The offset increases rapidly with helical radius up to $R = 0.25D$, but beyond this the rate of change of the offset is much smaller. Indeed, the data suggests that the value is reaching an asymptotic limit by $R = 0.5D$, which is due to the presence of the

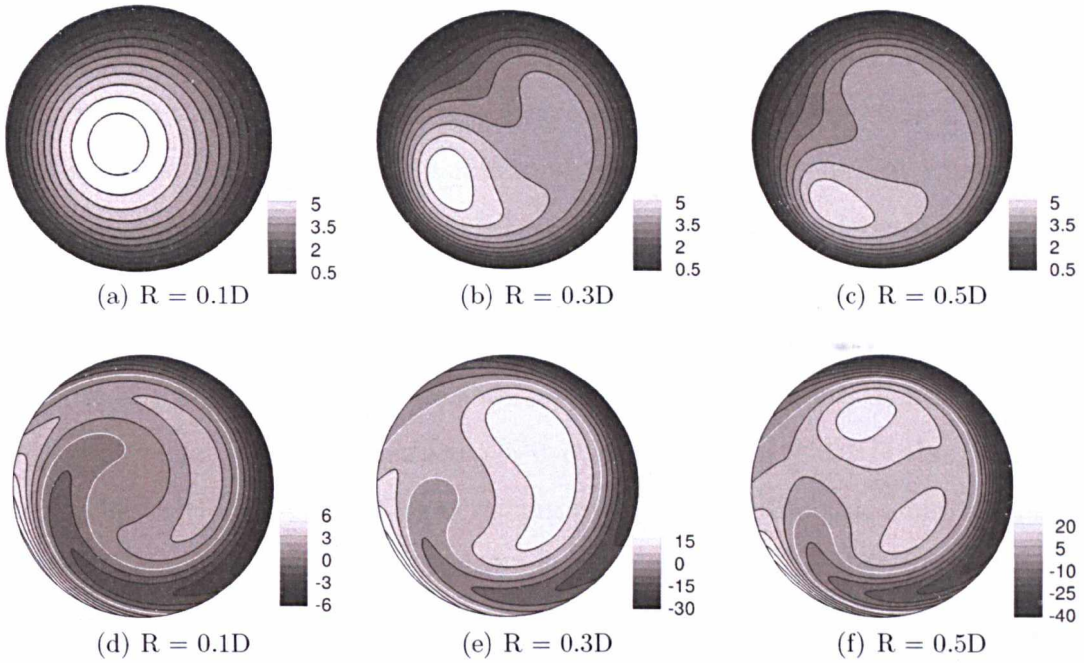


Figure 3.3: Axial velocity (cm/s) (upper) and axial vorticity (s^{-1}) (lower) contours at $z = 6D$. The zero level of vorticity is marked by a white line, highlighting the dominant vortical structure.

wall, and the no-slip boundary condition existing there. For a bend flow the peak

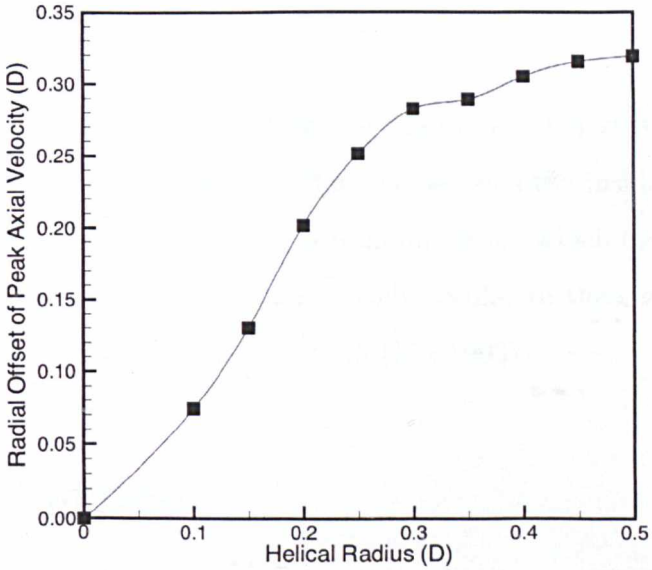


Figure 3.4: Radial offset of peak axial velocity, w, vs. helical radius.

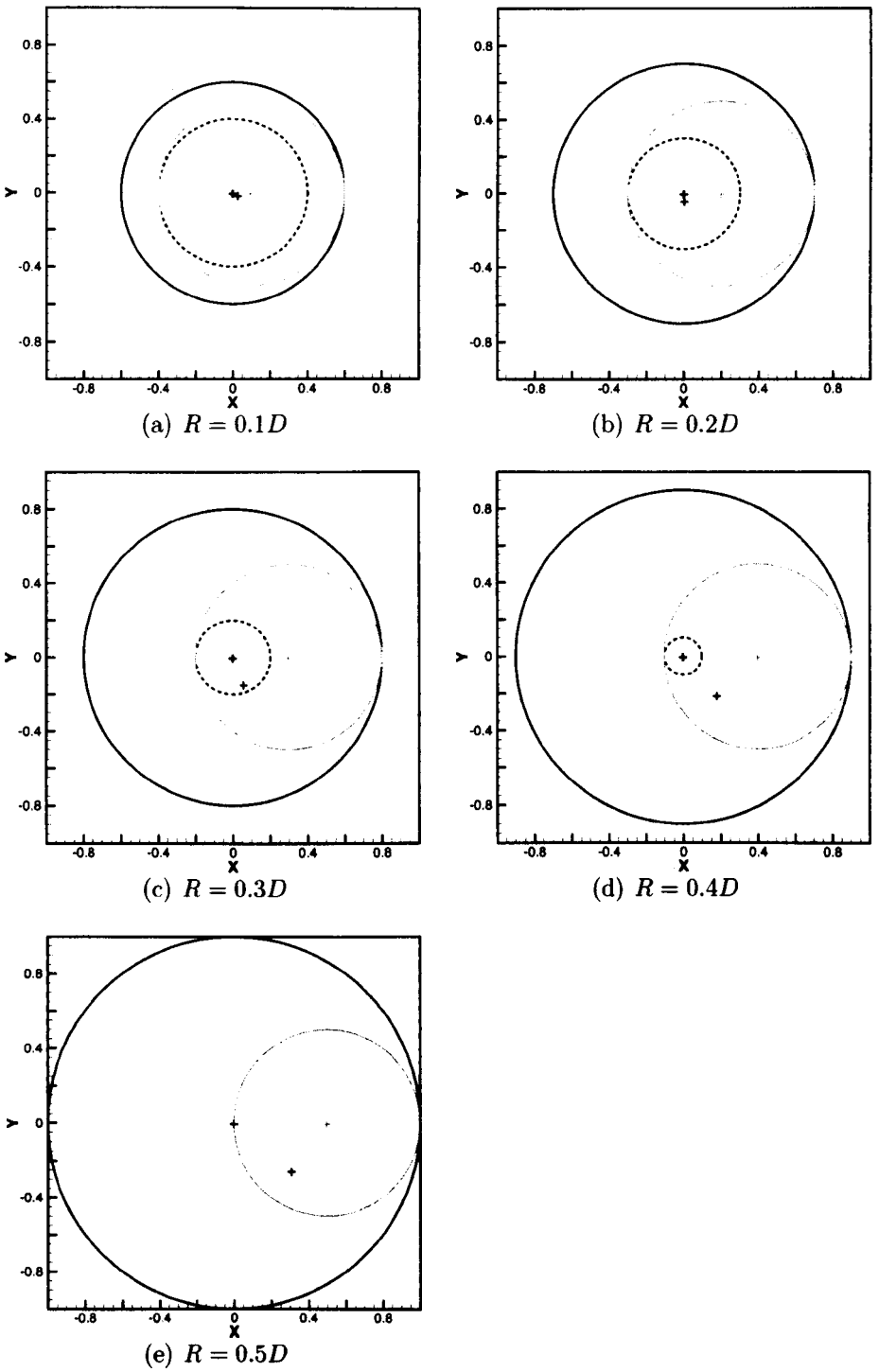
axial velocity is shifted to the outer curve, due to the centrifugal effects. However, in this case, the opposite is true. For all the geometries examined here, $R \leq D/2$, which means that a line-of-sight exists for all geometries except when $R = D/2$, i.e. apart from the latter, it is possible to see at least part of the exit when looking down the pipe axis $x = 0 = y$. Therefore the path of least resistance for the flow is through the region possessing line-of-sight, and this region is, by definition, near the inner bend. The lower resistance obviously means that the highest velocities will exist in this region. Figure 3.5 shows this line-of-sight region with the axis and peak axial velocity location marked. It is clear that for $R \leq 0.3D$ the peak axial velocity lies within the line-of-sight region, and at a radial location approximately equal to the axis (relative to the centre of the cross-section), which is confirmed by the nearly linear section on Figure 3.4, in the range $R = 0.1D - 0.3D$. There is however an angular offset from the axis, due to the effect of torsion. For $R > 0.3$ the region possessing line-of-sight becomes very small, and located very close to the wall, too close for the peak velocity to exist there due to the no-slip condition. This explains the distinct change in behaviour of the offset of peak axial velocity that occurs at $R = 0.3D$ on Figure 3.4.

3.2.2 Pressure

The contour plots of pressure are shown in Figure 3.6. For small helical radius the contours merely reflect the pressure difference between the inside and outside of the bend. For $R > 0.2$ a distinct pressure minimum forms, which indicates the presence of a strong vortical core. Results qualitatively similar to these are reported in (Liu 1993) (see Figures 6 and 10 respectively in (Liu 1993)).

3.2.3 Axial vorticity

Figures 3.3(d) - 3.3(f) show the corresponding contour plots of the axial vorticity, ω_z. A white contour line at $\omega_z = 0$, highlights the regions of positive and negative

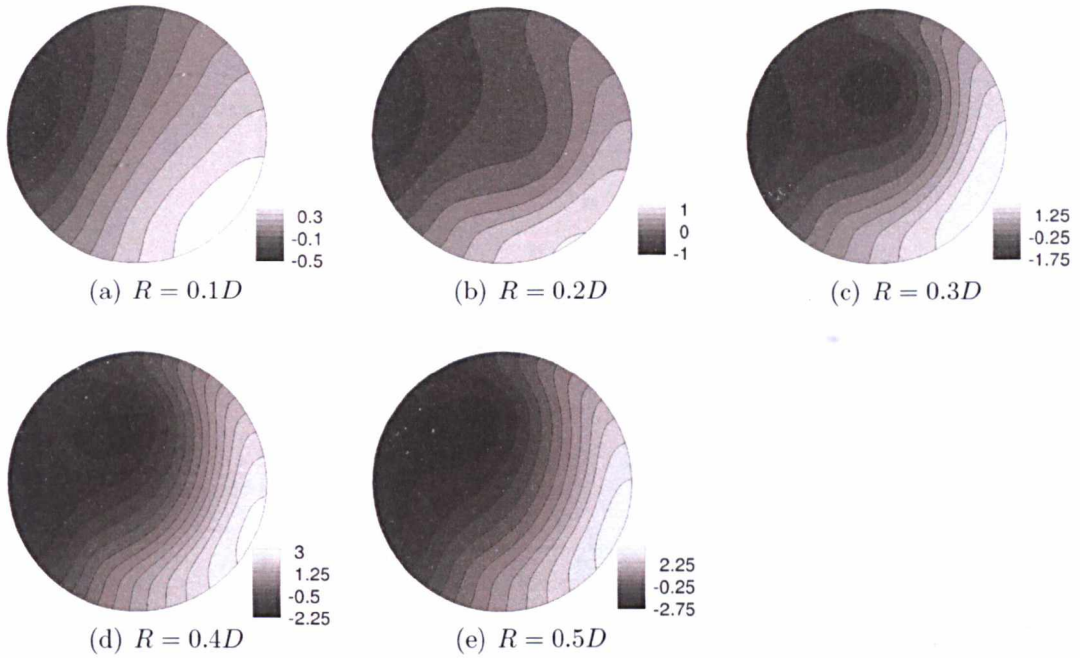


(a) $R = 0.1D$ (b) $R = 0.2D$

(c) $R = 0.3D$ (d) $R = 0.4D$

(e) $R = 0.5D$

Figure 3.5: Line-of-sight properties for increasing helical radius. The blue cross marks the location of the peak axial velocity, and the green cross the helical centreline. The black cross is the $x = 0 = y$ axis, and the dashed black circle corresponds to the line-of-sight region, which disappears when $R = 0.5D$. The outer black circle is the boundary that contains the helical pipe.



(a) $R = 0.1D$ (b) $R = 0.2D$ (c) $R = 0.3D$

(d) $R = 0.4D$ (e) $R = 0.5D$

Figure 3.6: Pressure contour slices, taken at $z = 0$, for increasing helical radius

vorticity, showing more clearly the vortical structure. For all cases there is a large region of positive vorticity, indicating that a single vortex dominates the flow, with a slight counter rotation near the wall. The existence of solutions of this nature has been reported previously by other researchers (Zabielski & Mestel 1998) (Yamamoto, Aribowo, Hayamizu, Hirose, & Kawahara 2002). The contiguous region of positive vorticity is then integrated over the area bounded by the zero contour of vorticity, which lies within the region where polar position $r \leq 0.45D$, to obtain the circulation Γ. This process therefore excludes the extremes of vorticity existing at the wall. The variation of Γ with helical radius, shown in Figure 3.7, is similar in manner to that of the radial offset of peak axial velocity, up to a helical radius of $0.25D$. At greater values of helical radius the rate of increase in Γ is merely reduced, whereas the peak axial velocity offset appears to asymptote. As mentioned earlier, the location of the peak axial velocity is limited by the wall and the no-slip boundary there. The circulation of the vortex, by contrast, is expected to increase with radius, since the curvature also increases, and correspondingly the centrifugal force acting on the fluid.

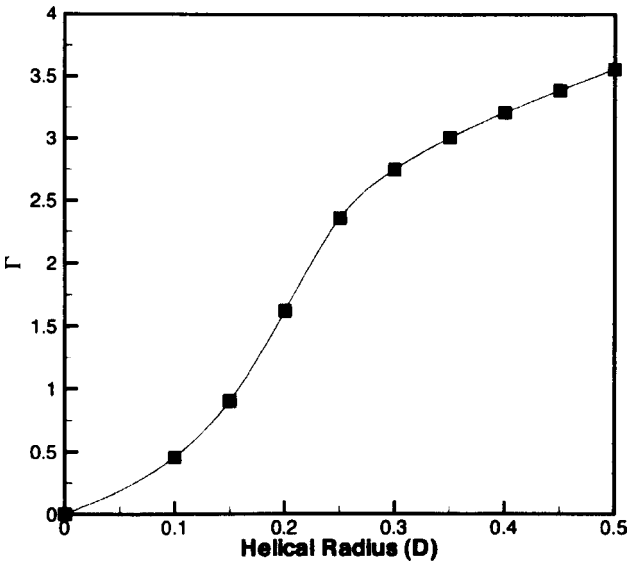
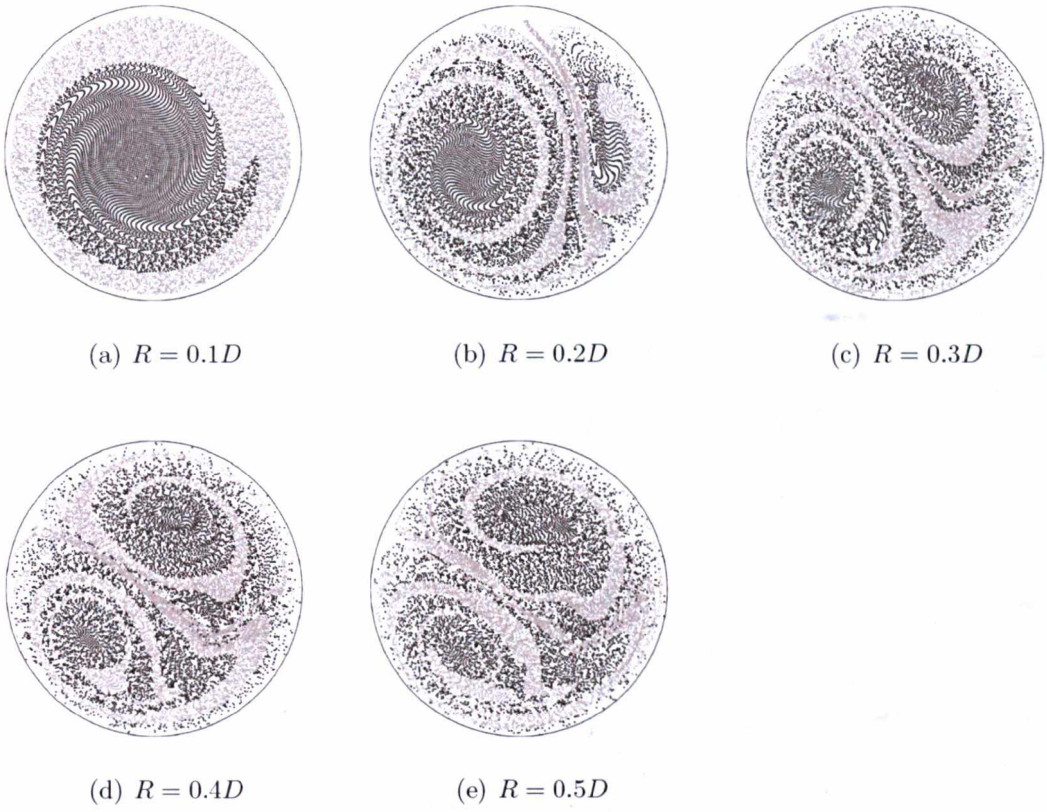


Figure 3.7: Circulation (cm^2/s), Γ, of dominant vortex vs. helical radius

3.3 Particle trajectory variation with helical radius

In examining the mixing characteristics of the flow in these helical geometries we will first look at the qualitative behaviour of fluid particles, before quantifying the mixing using the entropy measure introduced in Section 1.4.3. An initial distribution of 15371 particles are seeded at the nodes of a uniform grid, truncated by the circular cross-sectional boundary (a particle density of approximately $19600/D^2$). The particles are tracked through the helical geometries for a total of five pitch lengths, a distance of $30D$, a reasonable limit in terms of probable length constraints of clinical applications of a bypass graft. The inlet particle distribution is coloured by radius such that there are an equal number of grey and black particles. Besides their use in the entropy calculation, particle colouring indicates the degree of exchange of near wall particles with the core fluid. This is thought to be relevant to biological applications, where wall-transfer processes are implicated in disease initiation and progression (Nielsen 1996).



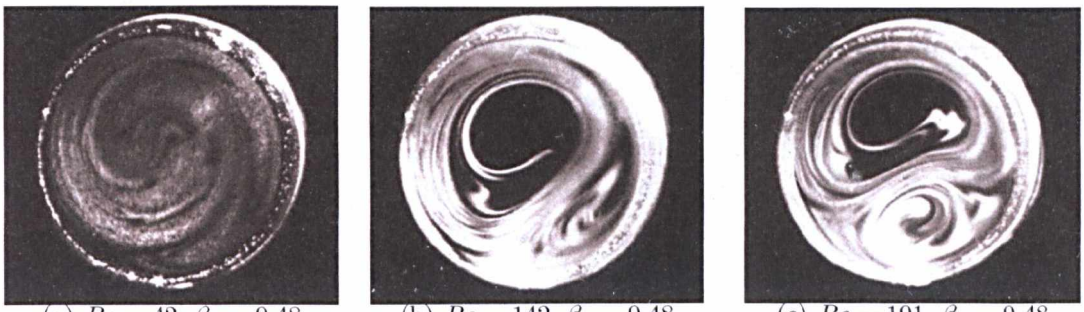
(a) $R = 0.1D$ (b) $R = 0.2D$ (c) $R = 0.3D$

(d) $R = 0.4D$ (e) $R = 0.5D$

Figure 3.8: Particle trajectory slices at $z = 30D$ (five pitches) for varying helical radius

Figure 3.8 shows slices of the particle trajectories taken at $z = 30D$ for increasing helical radius. Viewing the individual plots of Figure 3.8 in sequence reveals the gradual transition of the particle trajectories from a single vortex to a double vortex structure, despite Figures 3.3(f)-3.3(f) indicating that there is only a single dominant vortical structure for all the radii investigated. This counter-intuitive phenomenon has also been reported by (Yamamoto, Aribowo, Hayamizu, Hirose, & Kawahara 2002) in both their computational particle tracking and smoke visualisation results. In their numerical velocity fields, a single dominant vortex is obtained, but the corresponding particle tracking results showed a double vortex structure. The smoke visualisation results they obtained correspond well to the particle trajectories. It is clear from Figure 3.9 that the structures observed in the smoke visualisation of Yamamoto *et al*, are similar to those in the particle tracking results presented in

this thesis. Yamamoto *et al* suggest that this feature occurs due to a combination of the secondary and axial velocities. This is essentially correct, but a more complete and detailed explanation is offered in the following.



(a) $Re = 42$, $\beta_0 = 0.48$ (b) $Re = 142$, $\beta_0 = 0.48$ (c) $Re = 191$, $\beta_0 = 0.48$

Figure 3.9: Smoke visualisation results of Yamamoto *et al* showing the double-vortex structure similar to those found in the particle tracking results presented here. $\beta_0 = \lambda/\sqrt{2\delta} = \tau/(\kappa\sqrt{(\kappa D)})$, is a measure of the relative strengths of torsion and curvature. For the purposes of comparison the geometries considered in this thesis are in the range of $\beta_0 \approx 3 - 30$.

3.3.1 Reference frame change explanation

Attempting to relate the in-plane stirring to the velocity field is complicated by the fact that the planar cross-section is both translating and rotating. Therefore to interpret the motion of particles we must remove the effects of the plane's translation and rotation. The helical symmetry essentially means that the axial position of each particle can be decoupled from its motion in the cross-sectional plane for a suitable co-ordinate transformation, and transformation of the velocity field, thus simplying the task of particle tracking. Note that the following arguments are only kinematic in nature, and are not concerned with the dynamics.

It is thus proposed that the velocity in the planar cross-section is written according to the following vector equation:

$$\mathbf{V}_{in-plane} = \mathbf{V}_{Cartesian} - \mathbf{V}_{translation} - \mathbf{V}_{rotation} \tag{3.3}$$

3.3.1.1 Translation velocity

The translation velocities are found by differentiating the helical centreline equations, eqns (1.8)-(1.10), with respect to time. Using the chain rule and writing $w = dz/dt$ for the axial velocity, the corresponding rate of change of position of the helix centreline is given by:

$$\dot{x}_{translation} = -(wR/c)\sin(z/c) \tag{3.4}$$

$$\dot{y}_{translation} = (wR/c)\cos(z/c) \tag{3.5}$$

with $\mathbf{V}_{translation} = \dot{x}_{translation}\mathbf{i} + \dot{y}_{translation}\mathbf{j}$. This means that the streamtraces of $\mathbf{V}_{translation}$ are simply straight parallel lines. For example, at $z = 6$ (for $c = 3/\pi$), $\dot{x}_{translation} = 0$, and $\dot{y}_{translation} = wR/c$, which indicates simple straight vertical lines.

3.3.1.2 Rotation velocity

As we have already observed, the flow profile in a helical pipe also rotates in a self similar manner, along the length of the helix. Given a pitch length of $2\pi c$, the apparent rate of rotation of a point at a distance r from the pipe centre, travelling at an axial velocity w is given by:

$$\dot{\theta}_{rotation} = w/c \tag{3.6}$$

and therefore the tangential velocity is:

$$\mathbf{V}_{rotation} = (wr/c)\ \mathbf{e}_\theta \tag{3.7}$$

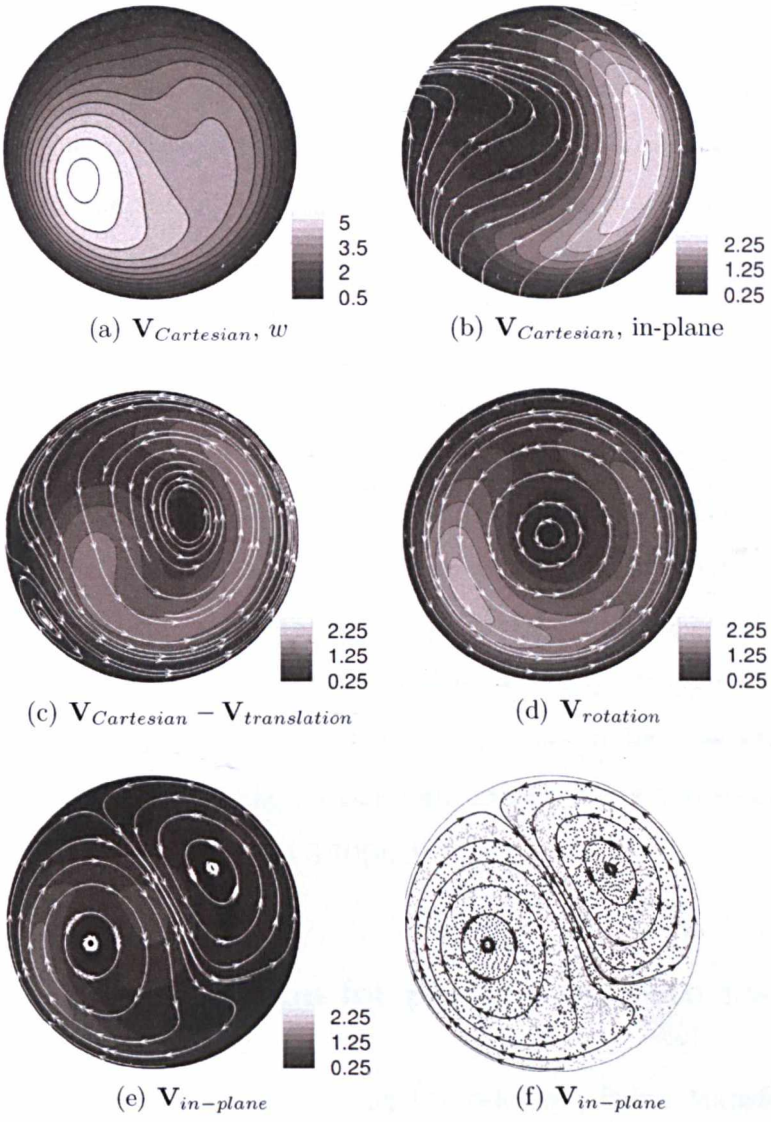
Resolving this into x and y components, such that $\mathbf{V}_{rotation} = \dot{x}_{rotation}\mathbf{i} + \dot{y}_{rotation}\mathbf{j}$ gives:

$$\dot{x}_{rotation} = -(wr/c)\sin(z/c) \tag{3.8}$$

$$\dot{y}_{rotation} = (wr/c)\cos(z/c) \tag{3.9}$$

The sign of rotation of this velocity is the same as that of the Cartesian vortex in the flow. Therefore when the rotating reference frame velocity is subtracted from

the Cartesian in-plane flow, the resulting in-plane flow field depends on the relative strengths of these two contributions, and their distribution of velocity magnitude within the plane.



(a) $\mathbf{V}_{Cartesian}$, w (b) $\mathbf{V}_{Cartesian}$, in-plane

(c) $\mathbf{V}_{Cartesian} - \mathbf{V}_{translation}$ (d) $\mathbf{V}_{rotation}$

(e) $\mathbf{V}_{in-plane}$ (f) $\mathbf{V}_{in-plane}$

Figure 3.10: In-plane velocity (cm/s) transformations to obtain particle trajectories

Removing the translation velocity produces the velocity field, $\mathbf{V}_{Cartesian} - \mathbf{V}_{translation}$, streamtraces of which are shown in Figure 3.10(c). This in-plane flow is now confined to the cross-section, forming one large vortex, and a small counter rotating vortex near the wall. This flow corresponds approximately, but not exactly, to the single

vortex identified by the axial vorticity contour plots of Figures 3.3(d) - 3.3(f). This axial vorticity was calculated from the velocity components in the un-mapped co-ordinate system (x, y, z). Consider the position $z = 0$, where the translation velocity is simply $\dot{x}_{translation} = 0$, and $\dot{y}_{translation} = wR/c$. If the translation velocity used the mean axial velocity $\bar{w}$, (therefore constant for every point in the plane), rather than w, (which varies with position), then the vorticity calculated in the translated frame would be the same as that in the original Cartesian system, since the constant does not contribute to the velocity gradients. However, even though w is used, much of the cross-section has an axial velocity that is fairly uniform, except near the wall and at the peak velocity. This means that the effect on the axial vorticity, is similar to using $\bar{w}$.

To emphasise the rotation of the velocity field that is advecting the fluid particles, Figure 3.11 show slices of the particle trajectories for $R = 0.25D$, within the first pitch length of the geometry at intervals of $z = 1.5D$. It is clear from comparing Figure 3.16(b) with Figure 3.10(e) that the particle tracking could be performed equivalently in a plane, using the velocity field $\mathbf{V}_{in-plane}$ obtained earlier, and the translational and rotational displacements simply accounted for afterwards. It is clear from these figures that the particles are indeed being transported by the velocity $\mathbf{V}_{in-plane}$, shown in Figures 3.10(e) & 3.10(f).

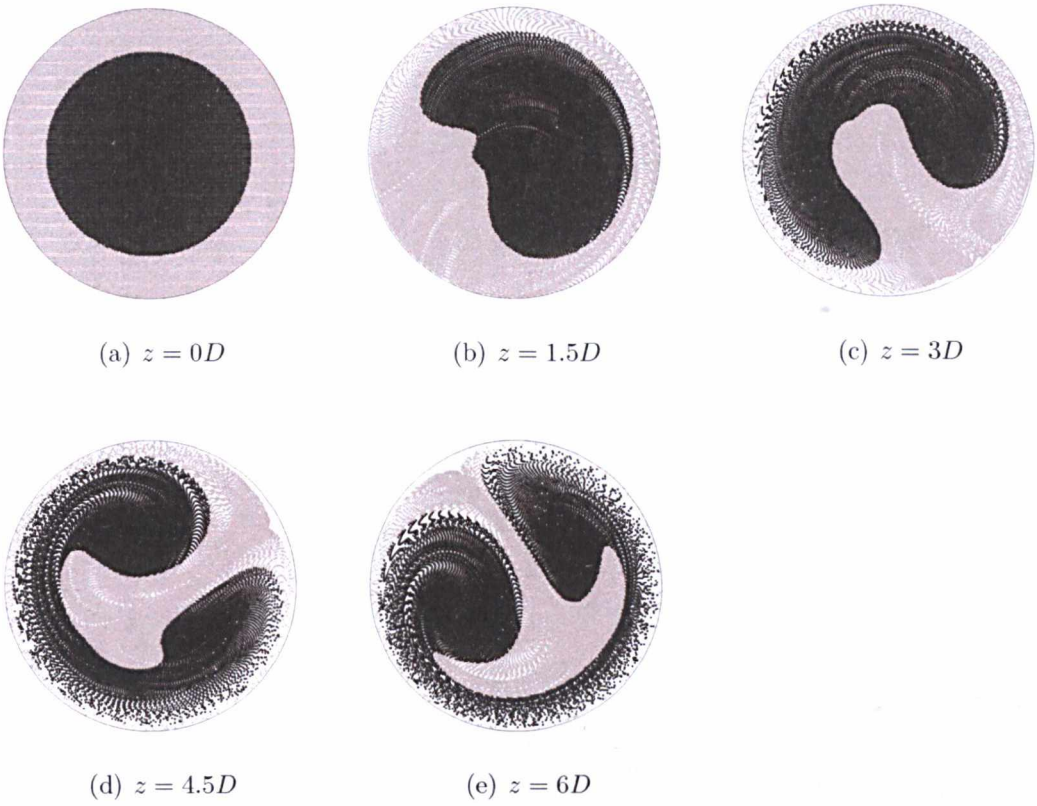
3.3.2 Vector formulation for particle trajectories

An alternative means of conceptualising the reference frame transformation is to consider the vector location of a point P in the cross-section, as shown in Figure 3.12. where θ, eqn (3.10), is simply the parameter t introduced in eqn (1.8).

$$\theta = \frac{z}{c} \tag{3.10}$$

Writing the position vector of P as:

$$\mathbf{r}_P = \mathbf{x}_P + \mathbf{y}_P \tag{3.11}$$



(a) $z = 0D$ (b) $z = 1.5D$ (c) $z = 3D$

(d) $z = 4.5D$ (e) $z = 6D$

Figure 3.11: Particle trajectory slices for $R = 0.25D$, at intervals of $z = 1.5D$, from $z = 0$ to $z = 6D$, showing the rotation of the velocity field that is moving the fluid particles.

where $\mathbf{x}_P$ and $\mathbf{y}_P$ are given by

$$\mathbf{x}_P = R\cos(z/c)\mathbf{i} + r\cos(z/c+\phi)\mathbf{i} \tag{3.12}$$

$$\mathbf{y}_P = \underbrace{R\sin(z/c)}_{translation}\mathbf{j} + \underbrace{r\sin(z/c+\phi)}_{rotation}\mathbf{j} \tag{3.13}$$

Differentiating with respect to time yields.

$$\dot{\mathbf{x}}_P = -(wR/c)\sin(z/c)\mathbf{i} - (wr/c)\sin(z/c+\phi)\mathbf{i} \tag{3.14}$$

$$\dot{\mathbf{y}}_P = \underbrace{(wR/c)\cos(z/c)}_{translation}\mathbf{j} + \underbrace{(wr/c)\cos(z/c+\phi)}_{rotation}\mathbf{j} \tag{3.15}$$

The second terms in eqns (3.14) & (3.15) correspond to the rotational velocity of eqn (3.7), but resolved into x and y components. Comparison with the first terms of these equations shows that the translation velocity is another rotational velocity,

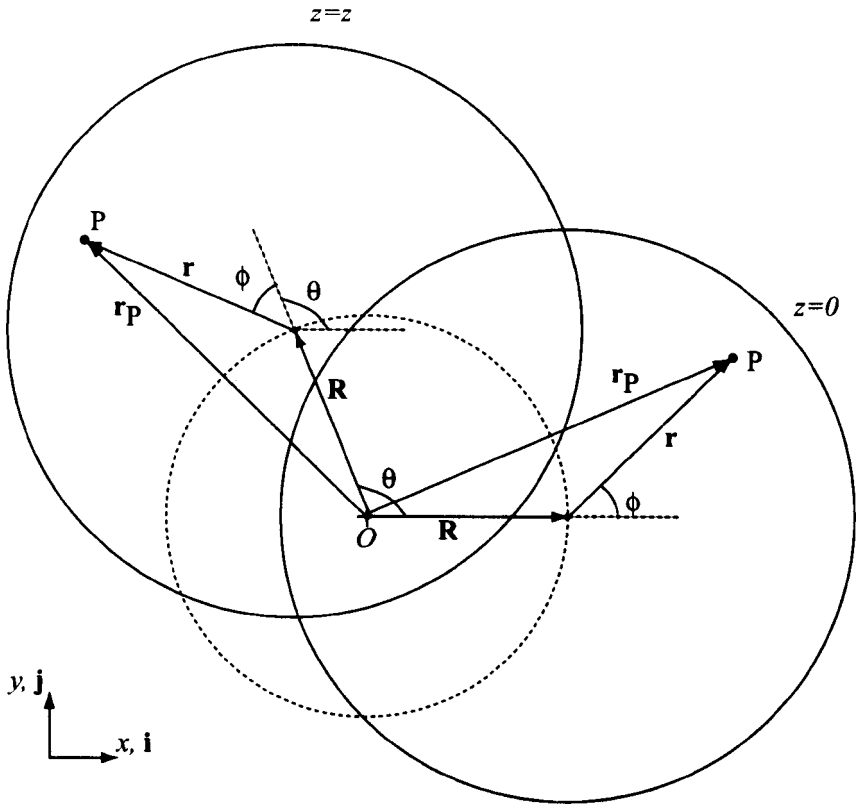


Figure 3.12: Vector diagram of rotation of cross-section, with a point P that lies within the plane where (r, ϕ) are the polar co-ordinates relative to the centre of the pipe cross-section. O is the axis $x = 0 = y$ and the dashed line is the projection of the helical centreline onto the plane.

but this time the radius of rotation is the helical radius R, rather than the local polar co-ordinate r of the particle P.

The velocity transformations obtained are actually of the same form as those that appear in the co-ordinate mapping used in the numerical scheme. This implies that the velocity transformations can be viewed as either those associated with a different reference frame for each particle that translates and rotates with a uniform velocity, or a co-ordinate transformation. Of course, the particle tracking could be performed in a co-ordinate system derived from arbitrary transformations of the Cartesian system. The point is that the transformations used here reveal information about the underlying motion of the particles.

The co-ordinate transformation view of $\mathbf{V}_{in-plane}$ also indicates that the rotational mapping could be applied, after the translational mapping, to the Navier-Stokes equations. This would allow for more general problems to be solved within the Fourier representation, as the rotational mapping allows for the provision of non-axisymmetric wall boundaries, such as ridges, quadrilaterals or ellipses. Furthermore, it also allows for the inclusion of twist (a property of the wall), in addition to torsion (a centreline property). The periodic length of the twist could also be different to that of the centreline.

3.3.3 Emergence of double vortex structure

Knowing that the particle velocity, $\mathbf{V}_{in-plane}$, is given by eqn (3.3), the emergence of the double-vortex structure in the particle trajectories can be explained by examining the change in $\mathbf{V}_{Cartesian}$, $\mathbf{V}_{translation}$ and $\mathbf{V}_{rotation}$ with helical radius. Figure 3.13 shows each of these components for the geometries $R = 0.1D$, $R = 0.3D$ and $R = 0.5D$.

Beginning with the Cartesian velocity field, it is sufficient to consider the behaviour of $\mathbf{V}_{Cartesian} - \mathbf{V}_{translation}$, as this is approximately the same as considering the vortical structure. It is clear from Figures 3.13(d) - 3.13(f) that the structure of $\mathbf{V}_{Cartesian} - \mathbf{V}_{translation}$ only changes slightly with helical radius. The velocity magnitudes increase with R, in a trend similar to that shown for Γ, as expected.

Considering now $\mathbf{V}_{rotation}$, whilst the structure is the same for all geometries, the magnitude, and the distribution of the velocity magnitude, changes. Specifically, the location of the peak magnitudes shifts towards the wall, in correspondence with the change in axial velocity profile. The multiplication factor of r in $\mathbf{V}_{rotation}$ means that the peak velocities are of much greater amplitude for larger values of R. It is this increase, and its position within the plane, which causes the formation of a double-vortex structure in $\mathbf{V}_{in-plane}$.

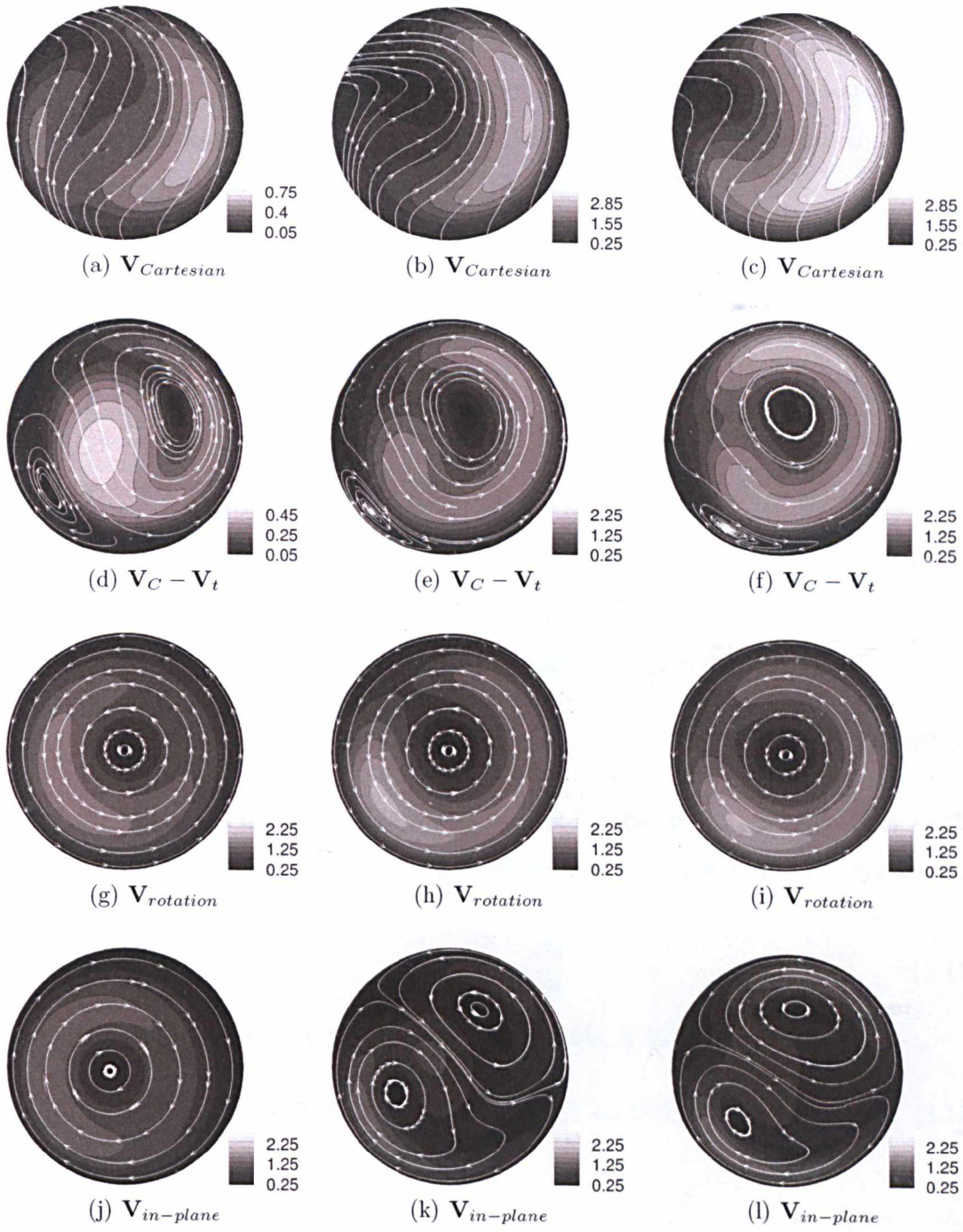


Figure 3.13: Comparison of in-plane velocity (cm/s) components for varying helical radius, which explains emergence of double vortex structure in particle trajectories. Left - $R = 0.1D$, Middle - $R = 0.3D$, Right - $R = 0.5D$

3.3.4 Wall shear stress

Wall shear stress, and its spatial and temporal gradients, has been a much studied quantity in cardiovascular fluid mechanics since Caro *et al.* showed that it was linked to the progression of atherosclerosis (Caro, Fitz-Gerald, & Schroter 1971). The postulated mechanism in this case relates to the response of the endothelial cells, which line the arterial walls, to the wall shear stress imposed by the fluid motion. For grafts constructed from ePTFE this mechanism is not present, however, it has been suggested by Mestel & Zabielski (Zabielski & Mestel 1998) that helical flow is a good model for the flow in many of the larger blood vessels, and therefore it is instructive to consider the WSS distribution in the small amplitude helical geometries. Additionally, the interaction of wall transport phenomena and WSS, may play a role in preventing the development of thrombosis in the grafts.

For an incompressible, Newtonian fluid, wall shear stress is defined as:

$$\boldsymbol{\tau}_w = \mu\boldsymbol{\omega} \times \mathbf{n} \tag{3.16}$$

where $\boldsymbol{\omega}$ is the vorticity vector, defined in eqn (2.74) and $\mathbf{n}$ the normal vector to the surface. For a surface defined parametrically in the form $\mathbf{x}(\theta, t)$ the surface normal vector $\mathbf{n}$ is defined as:

$$\mathbf{n} = \frac{\partial \mathbf{x}}{\partial \theta} \times \frac{\partial \mathbf{x}}{\partial t} \tag{3.17}$$

For the approximate helical pipe used in this thesis, $\mathbf{x}$ is defined as:

$$\mathbf{x} = (R\cos t + (D/2)\cos\theta)\mathbf{i} + (R\sin t + (D/2)\sin\theta)\mathbf{j} + ct\mathbf{k} \tag{3.18}$$

Therefore $\mathbf{n}$ is:

$$\mathbf{n} = ((D/2)c\cos\theta)\mathbf{i} + ((D/2)c\sin\theta)\mathbf{j} + R(D/2)(\sin t\cos\theta - \cos t\sin\theta)\mathbf{k} \tag{3.19}$$

The WSS magnitude, $|wss|$, distributions, at $z = 0$, are shown in Figure 3.14, for the geometries $R = 0.1D - 0.5D$, in increments of $0.1D$. Figure 3.15 shows the variation of the angular location of the minimum and maximum values of $|wss|$ with helical radius. Also in Figure 3.15 are the angular locations of the peak axial velocity, and

the separation point of particles from the pipe wall. As expected from the other quantities associated with the velocity field, the $|wss|$ plots change greatly up to $R = 0.3D$, but only marginally above this. In particular, the shear distribution becomes increasingly elongated, and a notch forms in the upper-left quadrant at the minimum value of $|wss|$. The values given in Figure 3.14 are in N/cm^2. To convert to a typical physiological value the following scaling factor can be applied:

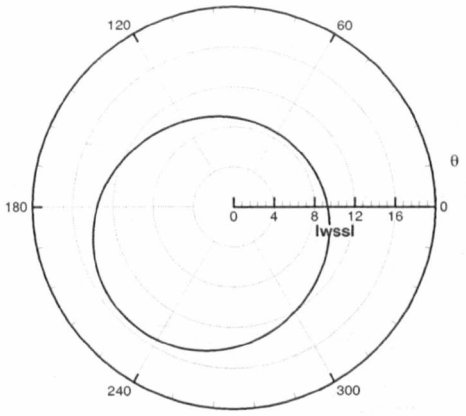
$$2\frac{|wss|_{helix}}{|wss|_{Poiseuille}}\frac{D}{4}\frac{\Delta p}{\Delta z} = 0.0483.|wss|_{helix}\ Pa \tag{3.20}$$

using the pressure gradient given in Section 3.4.3, and assuming $D = 0.005\ m$.

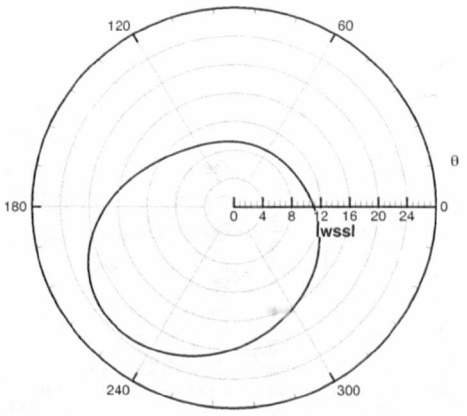
The correspondence between the angular position of the peak axial velocity and maximum $|wss|$ improves as the helical radius increases. This is due to the movement of the peak axial velocity towards the lower-left wall, which causes larger velocity gradients to exist in this region, and therefore a larger contribution to the wall shear stress. The wall shear stress, linked as it is with axial velocity, is therefore also similarly affected by the line-of-sight concept discussed in Section 3.2.1. Obviously the correspondence is not exact, due to the other components of shear that contribute to the overall shear stress magnitude.

A strong correspondence also exists between the location of the minimum value of $|wss|$ and the point at which the particle trajectories separate from the pipe wall. For $R = 0.1D$ and $R = 0.15D$, only a single vortex exists in the particle trajectory, and hence these points have been marked as zero on Figure 3.15. At $R = 0.2D$ a second vortex has formed, however, it is small, and its influence on $|wss|$ is weak. For $R \geq 0.25D$ the second vortex is firmly established, leading to the strong correlation between the location of minimum $|wss|$ and the separation point of the particles. For these geometries the minimum is easily identified as a distinct notch in the polar plots of Figure 3.14. Approximately diametrically opposed to the separation point, is the location of particle reattachment. Although a maximum in $|wss|$ is not achieved here, a discernible increase in magnitude does occur as this point on the plot is approached.

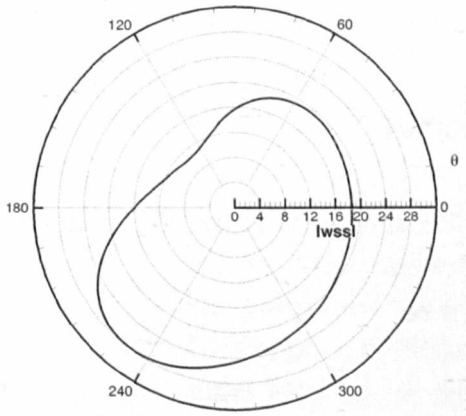
This wall shear stress behaviour differs from that in a planar curved pipe. For the



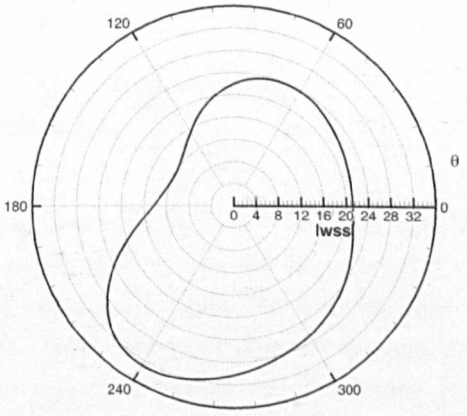
(a) $R = 0.1D$



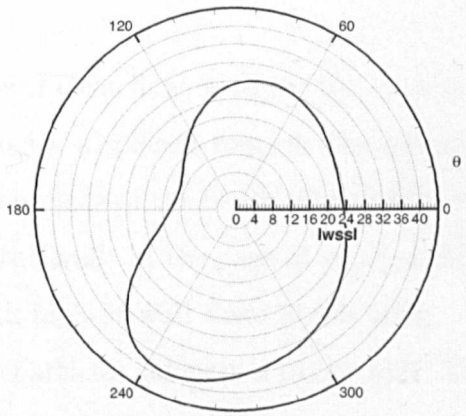
(b) $R = 0.2D$



(c) $R = 0.3D$



(d) $R = 0.4D$



(e) $R = 0.5D$

Figure 3.14: Wall shear stress (N/cm^2) distributions for increasing helical radius. Angular position corresponds to that on the pipe boundary, with the radial value representing the magnitude of wall shear stress, $|wss|$, at that angular position.

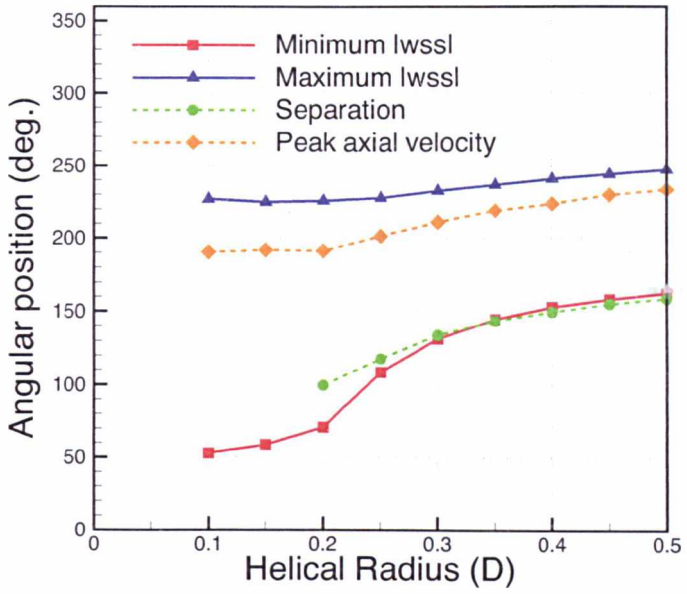
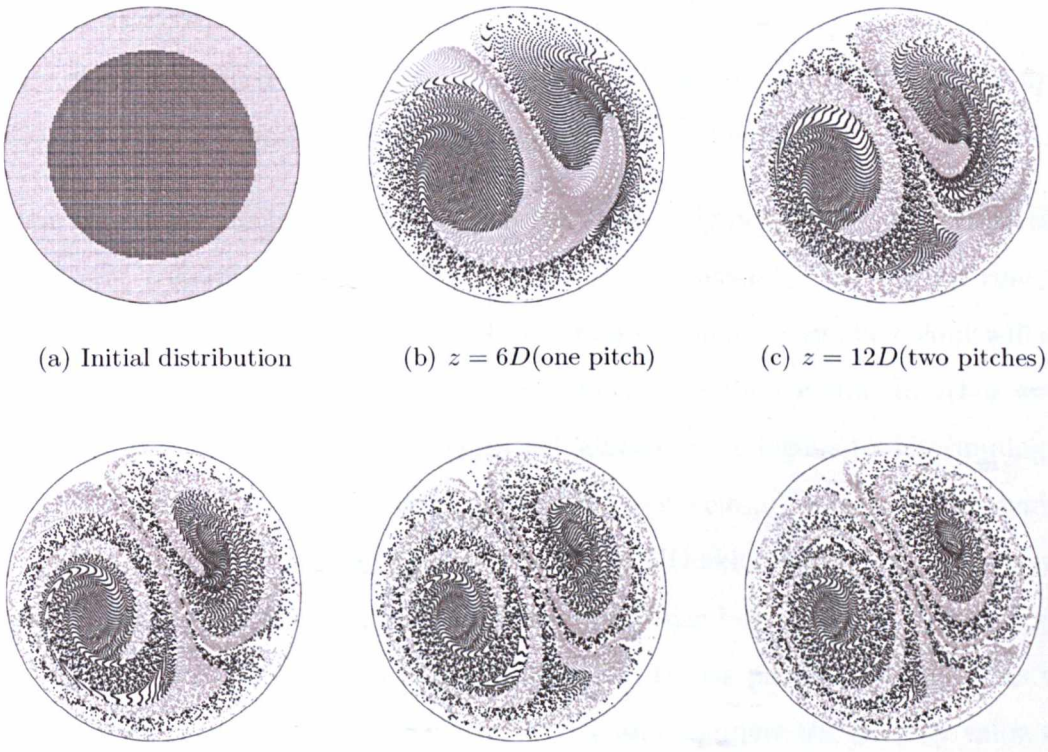


Figure 3.15: Analysis of wall shear stress magnitude data. The angular location of the minimum $|wss|$ is found to be well correlated with the position of the point of separation from the wall, as shown by the particle trajectories. The correspondence between angular locations of maximum $|wss|$ and peak axial velocity, improves with helical radius, as the peak velocity moves towards the wall, thus creating larger velocity gradients there.

case of Dean flow, with the two symmetric counter-rotating vortices, and a peak axial velocity displaced towards the outer bend, the maximum value of $|wss|$ occurs at the outside of the bend. This coincides with the region where particles are advected to the wall. In the case of small amplitude helical pipes, this link has been broken, with highest wall shear stress values occuring approximately 90 degrees away from the particles' advection to the wall. This may have implications for the behaviour of red blood cells, platelets and the endothelial cell layer in arteries, and consequently any disease progression. This is discussed further in Section 3.5.

3.4 Mixing/stirring

Figure 3.16 shows the particle trajectory slices for the geometry $R = 0.25D$, starting with the initial distribution and then each subsequent integer pitch length. Comparing the particle distributions at successive downstream locations, the initial concentric colour distribution is seen to become increasingly mixed. Closer examination of the individual plots reveal common features of the particle distribution, such as the location of the dividing line between the two vortex-like regions. Although visible in all the plots, the finer structures within each of the two regions become better illuminated with each additional pitch length, since the particle colours are more uniformly distributed within the domain.



(a) Initial distribution (b) $z = 6D$(one pitch) (c) $z = 12D$(two pitches)

(d) $z = 18D$(three pitches) (e) $z = 24D$(four pitches) (f) $z = 30D$(five pitches)

Figure 3.16: Particle trajectory slices for $R = 0.25D$ at integer multiples of the pitch length

3.4.1 Entropic measure

To quantify the mixing behaviour, we now employ the concept of information entropy. This method of characterising mixing relies on two levels of statistical sampling. The first is the seeding of the flow with particles, which will determine the quality of the resolution of the flow features. The second is the box-counting used to calculate the information entropy. Care must therefore be taken both with the number of particles, and the number of boxes, specifically, $N_{particles}/N_{species} \gg N_{boxes} \gg 1$.

Even if this condition is satisfied, it should be noted that the entropy of a given particle distribution will decrease as the number of boxes increases. In fact as $N_{boxes} \to \infty$, the entropy S will disappear to zero; that is, entropy only exists by virtue of the coarse-graining process of box-counting. This property means that it is not straightforward to compare the entropy values calculated for different applications unless the number of particles and boxes are identical.

In eqn (1.51), the definition of entropy is such that only boxes that contain particles of different colours contribute to the entropy summation. This implies that if a sufficient number of boxes are used, a box containing more than one colour will only do so along the boundary of the interface that divides the colours. In other words, with appropriate resolution, the entropy calculation is analogous to determining the length of the interface that separates the particle species. This point was made in relation to the intensity of segregation measure by (Khakhar 1986), but holds equally well for information entropy, as both measures utilise box-counting. This suggests that one way to validate the entropic measure is to use particle distributions with known, or easily determined, interface lengths, and compare the entropy value with the interface length. Unfortunately, as (Krasnopolskaya, Meleshko, Peters, & Meijer 1999) notes, the measure cannot, in general, be validated this way for an arbitrary number of boxes. However, it is certainly possible to validate the measure for a limited range of particle distributions, which is the approach taken here.

Tests were performed with progressively increasing numbers of concentric rings of particles of different colours. The total interface length of the rings increases linearly with the number of rings. The test cases showed that for roughly 60,000 particles, 10,000 boxes are needed for the entropy calculation, so that the variation in entropy is also linear. Calculations were performed for several cases using 61,527 particles, to validate the data generated using 15,371 particles. For the bulk of the particle tracking, performed with roughly 15,000 particles, the entropy calculation was performed with 2,500 boxes, commensurate with the findings from the test cases.

Figure 3.17 shows the normalised entropy increase, K, plotted against helical radius. It is clear that entropy increases, and therefore mixing, for all cases, apart from $R = 0.1D$. Furthermore, Figure 3.17 shows that there is a sharp increase in mixing up to and including $R = 0.25D$, beyond which there is only a small increase in K with increasing helical radius at five pitch lengths. The mixing performance of

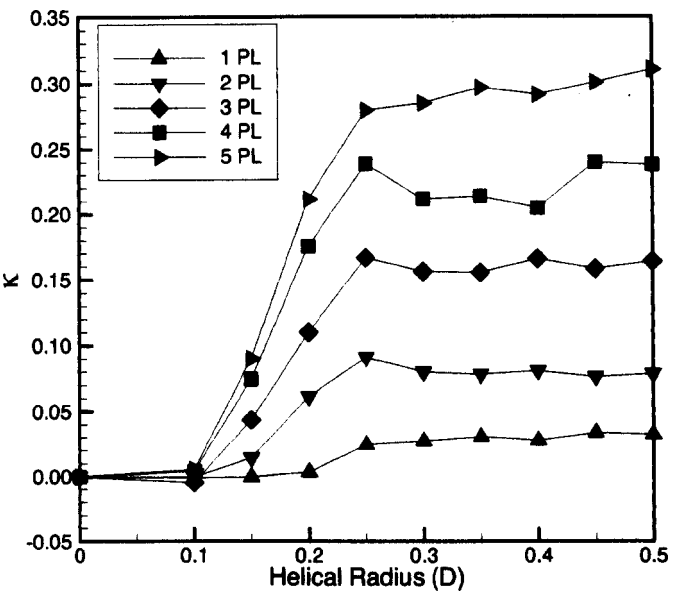


Figure 3.17: Relative entropy increase, K, vs. helical radius.

helical pipes is actually rather poor when compared with that of typical industrial mixers, though this may not matter for biological applications. The poor mixing

is due to the single or double elliptic regions that exist in the helical pipe, which industrial mixers are generally designed to avoid. A means of eliminating these elliptic regions in helical pipe flows is proposed in Chapters 4 & 5.

3.4.2 Residence time distribution

Thus far we have examined only the in-plane mixing, however dispersion of the particles in the axial direction is also of relevance. For the particles tracked in Section 3.3 the time taken to travel through one pitch length was recorded. The mean and standard deviation of the residence times are shown in Figure 3.19. It is clear that both quantities vary in a similar fashion, and since a lower mean residence time is desirable, the trend is the same as for K in Figure 3.17. The lower average residence time with increasing radius is due to the greater in-plane mixing, which means that more of the particles are brought into the core of the flow, and thus experience the high axial velocities there. The smaller standard deviation, by definition, means that the residence times are closer to the mean value, and hence the residence time distribution is more uniform for the larger radii.

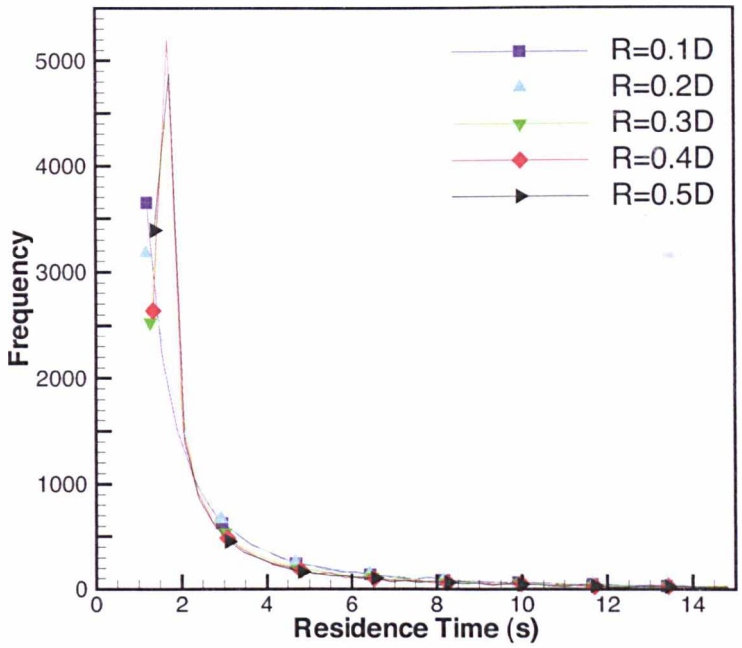
For $R = 0.1D$ the single vortex in the particle trajectories, and the almost parabolic axial velocity profile, means that the particles will move along paths of roughly constant axial velocity, which does not reduce the non-uniformity of the particle residence time. For $R = 0.15D$ the particle motion is still a single vortex, however the axial velocity is now slightly more asymmetric. Therefore circular paths around this will yield a slightly averaged residence time for some particles, but the effect is small overall, and hence there is no appreciable reduction in mean residence time, and only a slight reduction in standard deviation. Furthermore, their distributions, Figure 3.18(a) have the same general shape as that for Poiseuille flow (which does not exhibit mixing behaviour). The effect can be seen more clearly by examining Figure 3.18(b), which shows a plot of the *log* of frequency versus the *log* of time.

The residence time distribution for Poiseuille flow has a t^{-2} dependence, which

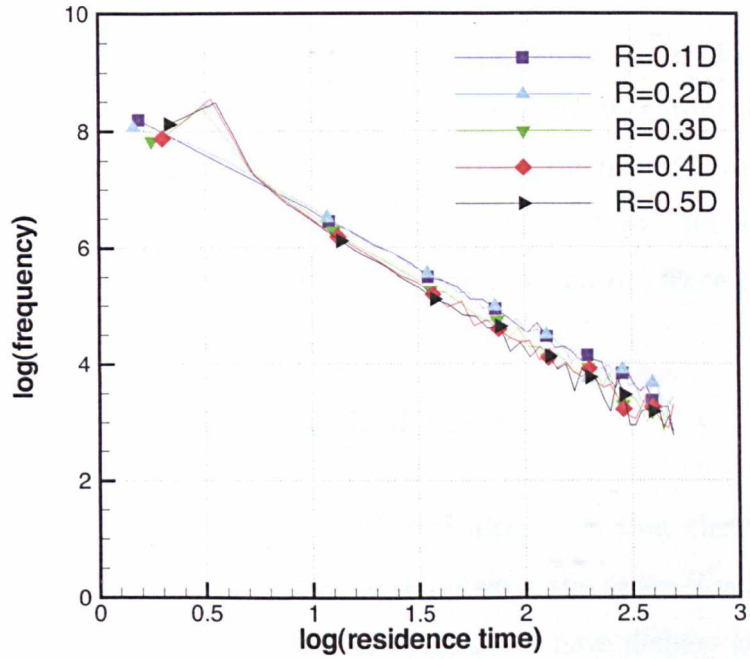
corresponds to a straight line on a *log* - *log* plot, with a gradient of -2. Figure 3.18(b) shows that for the geometries with $R = 0.1D$ and $R = 0.2D$, the relationship is also a straight line, the gradient of which is very close indeed to -2. The effect of mixing is now very clear, as the other three geometries deviate significantly from a straight line in the range of $\log(t) = 0.3 - 0.7$. This peak corresponds to the peak shown in Figure 3.18(b), and visually the effect of mixing on the frequency distribution is now much clearer. This peak means that the lines for these cases are lower than $R = 0.1D$ & $R = 0.2D$, indicating clearly that fewer particles are now present for long residence times. Interestingly, the gradients of these lines are also very close to -2, suggesting that the appearance of the peak in the distribution is not affecting the general nature of the frequency distribution for long residence times.

The formation of the double-vortex causes the change in residence time properties. Even at $R = 0.2D$, when the second vortex is very small, the reduction in mean and standard deviation is significant. These reductions occurs for two reasons, although they are both part of the same phenomenon. Firstly, particles are now transported from near the wall, where residence times are large, to the core of the flow, where they are small, thus reducing the mean residence time. Secondly, the particles within the core of the flow, now move across the plane, rather than the almost circular paths associated with the single vortex. They therefore experience a wider range of axial velocities, which is augmented by the increased asymmetry of the axial velocity profile, thereby contributing to the reduction in the mean residence time. As the second vortex becomes substantially larger at $R = 0.25D$, a correspondingly large reduction is observed in the mean residence time. However, for $R = 0.3D$ and greater, the size of the second vortex, and the asymmetry of the axial velocity profile changes only slightly, yielding correspondingly small changes in residence time distributions.

These results are a quantitative representation of the dye visualisation data presented in (Caro, Cheshire, & Watkins 2005), the key figures from which are reproduced here in Figure 3.20. The U-bend constructed from conventional tube shows



(a) Frequency vs. time



(b) log(frequency) vs. log(time)

Figure 3.18: Particle residence time distributions for varying helical radius

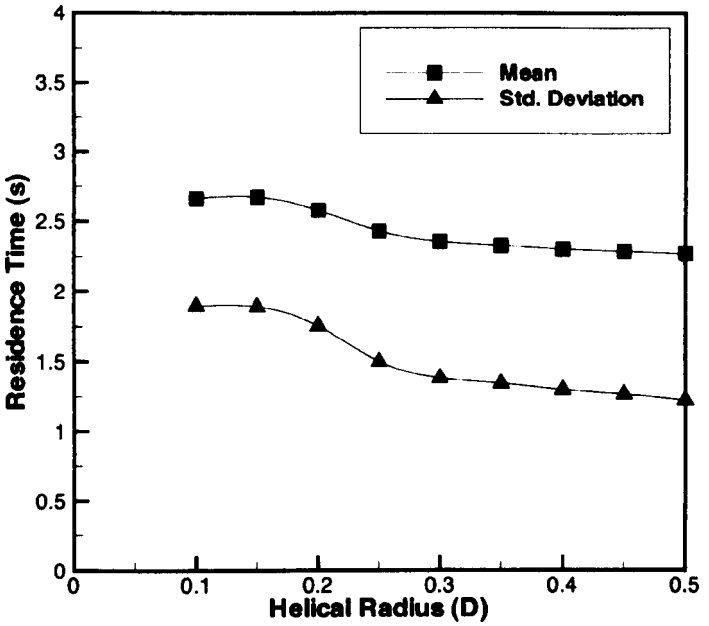


Figure 3.19: Statistics of the particle residence time distributions for varying helical radius

significant dye resident close to the walls, as expected of Poiseuille flow, where the $1/(1-(r/R)^2)$ nature of the residence time function (distinct from the distribution) means it becomes very large as $r \to R$. By contrast, the helical tubing has removed most of the dye near the wall, a direct consequence of the double-vortex in the particle motion, and indicated by the reduction in mean residence time.

3.4.3 Pressure drop in helical pipe

A key result from quantifying the degree of mixing, is that there is a relatively small difference in the mixing performance between the cases $R = 0.25D$ and $R = 0.5D$. Therefore if enhanced in-plane mixing, as we have defined and measured it, is responsible for the apparent improved performance of the SMAHT A-V shunts used by (Caro, Cheshire, & Watkins 2005), it would appear that a helical geometry with $R = 0.25D$ should be just as effective at preventing thrombogenic occlusion,

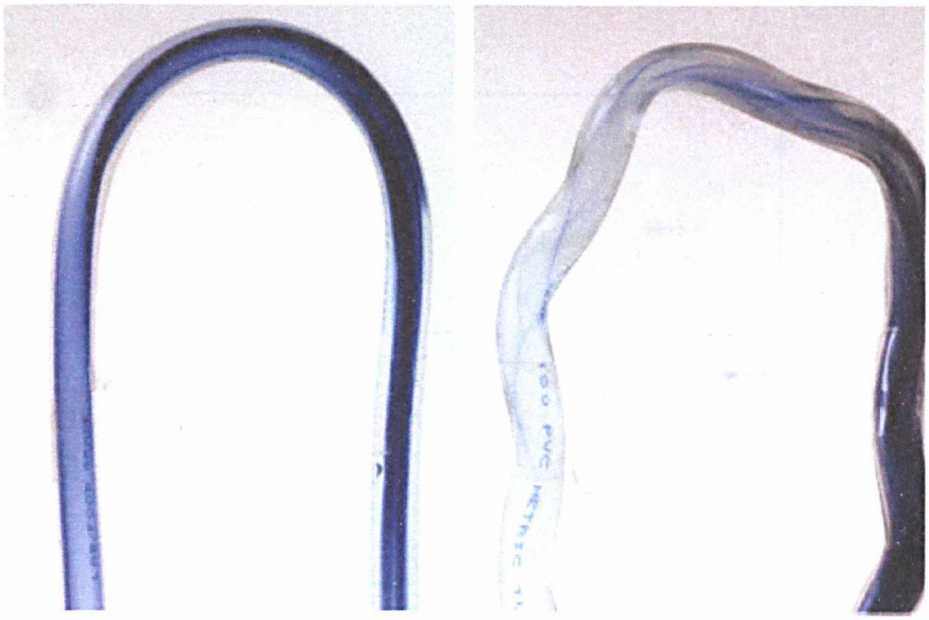


Figure 3.20: Dye visualisation results from Caro *et al.* (2005) that correspond to particle residence time statistics. The helical pipe (right) is clearly more effective at transporting the dye out of the bend than the conventional cylindrical pipe (left).

as the $R = 0.5D$ geometry. A further consideration when selecting a geometry for possible medical applications is the magnitude of the pressure drop across one pitch length of the helix. As the helical radius increases, pressure losses will arise from both the greater arc length of the helix, and the energy required to drive the vortical structure. Figure 3.21 shows the variation of this pressure drop with helical radius, indicating that the pressure loss for $R = 0.5D$ is approximately 1.6 times larger than for $R = 0.25$, but without a corresponding increase in the degree of mixing.

To provide an indication of the physiological pressure drop that would occur in a straight pipe, the following formula can be used, with appropriate parameter values:

$$\Delta p = \frac{4\mu^2 LRe}{\rho(D/2)^3} \tag{3.21}$$

Assuming $\mu = 0.0027\ Ns/m^2$, $D = 0.005\ m$, $\rho = 1060\ kg/m$ and $Re = 250$, the pressure drop over a distance $L = 6D = 0.03\ m$ is approximately 13 Pa.

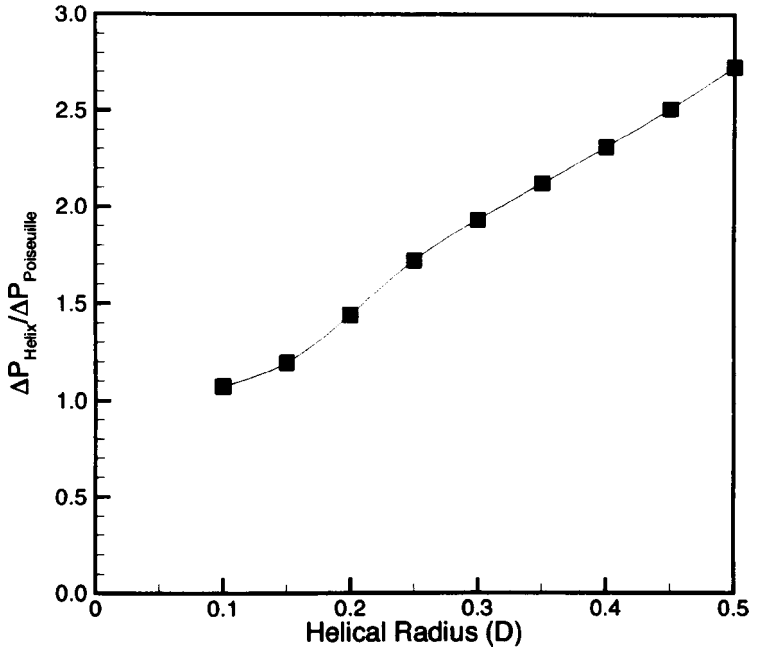


Figure 3.21: Pressure drop incurred for one pitch length vs. helical radius.

3.4.4 Extension to higher Reynolds number

The results presented are relevant to application of a bypass graft or arterial stent, that is a Reynolds number of 250. However, for a A-V shunt the Reynolds number will be in the range of $900 - 1800$. In order to provide some indication of the mixing expected for operating conditions appropriate for an A-V shunt, flow solutions have been obtained for a selection of geometries at higher Reynolds numbers.

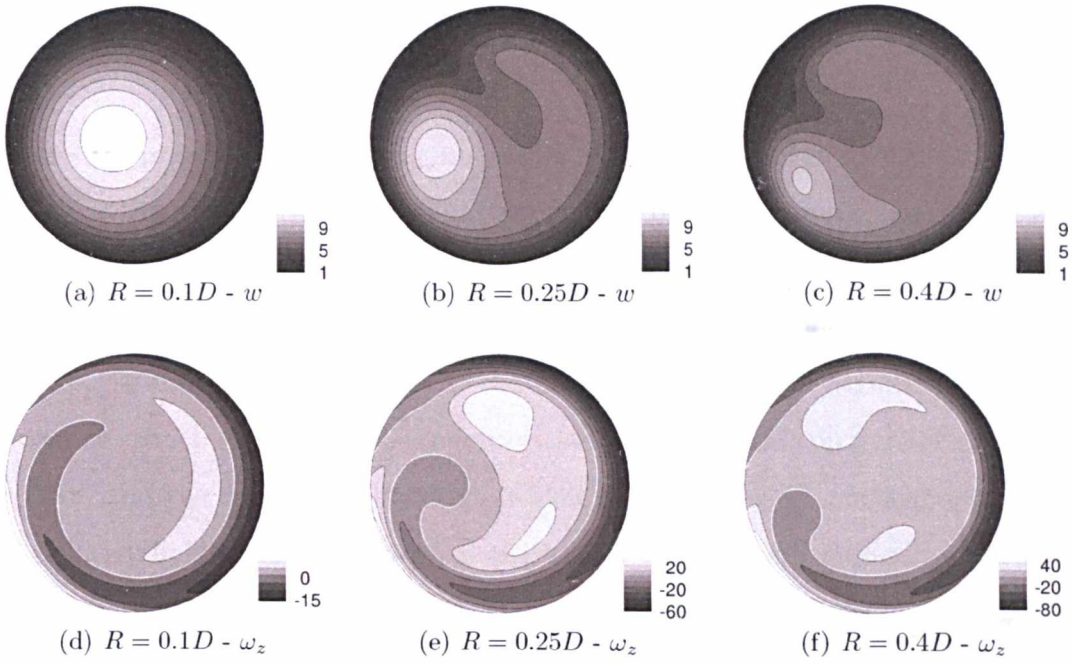
Figure 3.22 shows axial velocity and vorticity contour plots for three geometries at a Reynolds number of 500. It is clear that no significant changes in the velocity field have occurred, and this is is reflected in the particle trajectories. Figure 3.23 shows streamtraces of $\mathbf{V}_{in-plane}$ for the cases $R = 0.1D$, $0.25D$ & $0.4D$, at Reynolds numbers of approximately 250 and 500. It is clear that there is only a slight difference in structure between the two Reynolds numbers, although the magnitudes are obviously different. The second (upper) vortex which forms with increasing R, occupies slightly more of the cross-section at $Re = 500$, the difference being smaller

for $R = 0.4D$. Extrapolating these results to $Re \approx 900 - 1000$, it is predicted that the helical radius at which "sufficient" mixing is generated will be slightly smaller than for $Re = 250$.

These results come with the caveat that the precise Reynolds number at which flow transitions to turbulence within helical geometries is not properly characterised as a function of geometric parameters. One study that attempted to understand this phenomenon (Yamamoto, Yanase, & Jiang 1998) investigated geometries similar to those considered in this study, with comparative pitch lengths, though not for values of R as small as here (none of the geometries possessed line-of-sight). Their results suggest that transition occurs at values of Re smaller than for a straight pipe O(2000), possibly as low as $Re = 800$, depending on the geometry. An interesting property of the flow is that torsion is initially destabilising, but beyond a certain point, increasing torsion will increase the critical transition Reynolds number. If the flow does transition to turbulence then we concede that the results presented here will no longer apply. It is clear that a careful analysis of the stability of such flows is needed, but this is beyond the scope of the present investigation.

To lend further weight to the conclusions, for $R = 0.1D$ at $Re \approx 700$ the particle trajectory structure is still a single vortex. If a second vortex had been present, this would have suggested that the optimal geometry were to be found at a significantly smaller helical radius.

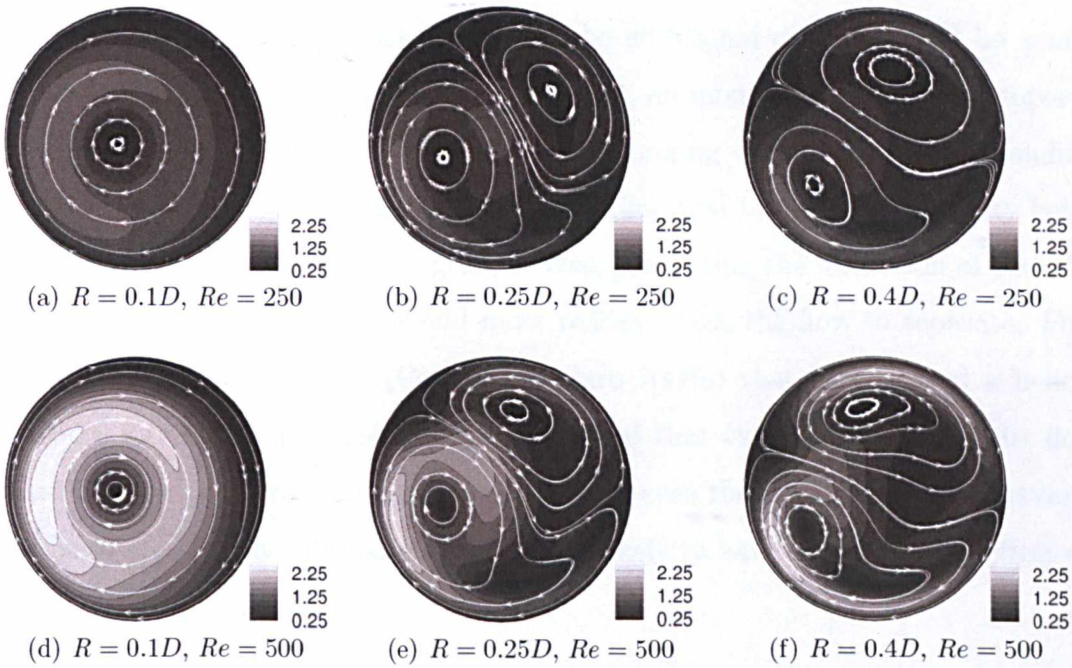
Obtaining converged solutions for Reynolds numbers higher than 500 was found to be problematic for geometries with $R \geq 0.25D$. This is thought to be a numerical instability associated with the mapping technique, and its explicit treatment of these terms, since the terms are proportional to both velocity and helical radius. Although the mapping technique has been used elsewhere at higher Reynolds numbers, the pertubation to the flow from the geometry was much smaller, e.g. only a small Gaussian bump on the wall in a channel flow (Koberg 2008). Contrast that to the helical pipe case, where the whole domain is substantially affected by the mapping.



(a) $R = 0.1D$ - w (b) $R = 0.25D$ - w (c) $R = 0.4D$ - w

(d) $R = 0.1D$ - ω_z (e) $R = 0.25D$ - ω_z (f) $R = 0.4D$ - ω_z

Figure 3.22: Axial velocity profiles (cm/s) and axial vorticity (s^{-1}) at $Re = 500$ for several helical geometries



(a) $R = 0.1D$, $Re = 250$ (b) $R = 0.25D$, $Re = 250$ (c) $R = 0.4D$, $Re = 250$

(d) $R = 0.1D$, $Re = 500$ (e) $R = 0.25D$, $Re = 500$ (f) $R = 0.4D$, $Re = 500$

Figure 3.23: Streamtraces of $\mathbf{V}_{in-plane}$ (cm/s) for $Re = 250$ and 500 for several helical geometries

3.4.5 Comment on validity of using straight section helical pipe

The results presented in this Chapter are for a helical pipe formed around a straight axis. In a bypass graft configuration there will be curvature along most of the pipe, which means that the mixing induced by the helical geometry would supplement that caused by the Dean-like secondary flow in a simple curved pipe. To a first approximation, assuming linear behaviour, the flow in a helical tube formed on a curved centreline, can be taken as the superposition of symmetric counter-rotating Dean vortices, and the corresponding single-vortex swirling flow of a helical tube. Since the velocity field in the helical pipe varies only slightly with increasing radius for $R > 0.25$, the helical contribution to the resultant flow in a curved helical tube will not vary significantly in this parameter range. Therefore, despite the precise mixing behaviour differing from the straight helical case, the ranking of geometries from a mixing perspective should not be altered by the presence of additional curvature.

Whilst the additional curvature is relevant to the A-V shunt application, for the cases of a bypass graft and arterial stent, the additional curvature will be small, and negligible in its effect. Related to this point, an interesting structural property of helical tubes is their improved resistance to kinking when subjected to bending moments, compared to conventional straight cylindrical tubes. This property helps to guarantee the geometry of the graft *in vivo*, preventing the formation of extreme curvatures due to kinks, that would more readily cause the flow to separate. Furthermore, a recent study by (Coppola & Caro 2008b) that investigated a helical geometry formed on a curved centreline showed that even at $Re = 600$ the flow remained attached throughout the bend, so that even though the mixing behaviour may be altered, the additional curvature is unlikely to have a pathological effect on the flow.

3.5 Relevance of results to *in vivo* disease processes

Unfortunately only a single helical geometry was tested *in vivo* by Caro *et al.* (Caro, Cheshire, & Watkins 2005). To test the hypothesis that in-plane mixing is the mechanism responsible for preventing thrombotic occlusion, it is necessary to perform *in vivo* tests with at least one other geometry, but ideally several others. In the absence of this experimental data, we use some existing data in the literature, to attempt a more complete explanation of how the flow in helical pipes prevents the formation of thrombosis.

Consider the thrombosis activation parameter defined by Ramstack *et al.* to be

$$\dot{\gamma} \times t \tag{3.22}$$

where $\dot{\gamma}$ is the shear rate

$$\dot{\gamma} = \frac{\partial v_z}{\partial r} + \frac{\partial v_r}{\partial z} \tag{3.23}$$

since their flow is axisymmetric, and t is the exposure time of the particle to $\dot{\gamma}$. If this product is greater than 1000, procoagulant platelet factor 3 (FP3) is released (Ramstack, Zuckerman, & Mockros 1979). For Poiseuille flow, the axial distance needed for this factor to reach 1000 reduces with proximity to the wall. It is also independent of flow rate, since the faster the flow, the greater the shear rate value will be, but with a reduced exposure time, both effects cancelling out each other.

For a helical pipe flow, large shear rates are still to be found near the wall, but by moving particles away from the wall, they are removed from both the regions of high shear, and the slow flow. Therefore, the reduction in mean particle residence time within the pipe reduces the number of particles experiencing the largest shear rates, and their exposure to high shear for long residence times. One way to quantitatively assess the total shear exposure of a particle is that used by Sherwin *et al.* (Sherwin, Doorly, Franke, & Peiro 2002), in their study of model arterial bypass grafts.

First, an equivalent stress is defined, using the Huber-Henky-von-Mises criterion, as

described in (Bludzuweit 1994):

$$\sigma_e = \frac{1}{\sqrt{2}}\left[(\sigma_{11}-\sigma_{22})^2+(\sigma_{22}-\sigma_{33})^2+(\sigma_{11}-\sigma_{33})^2+6(\sigma_{12}^2+\sigma_{23}^2+\sigma_{13}^2)\right]^{\frac{1}{2}} \quad (3.24)$$

where

$$\sigma_{ij} = \mu\left(\frac{\partial u_i}{\partial x_j}+\frac{\partial u_j}{\partial x_i}\right) \quad (3.25)$$

The shear exposure $E(\mathbf{x}, t_0, T)$, over a time interval T, is the integral of this stress taken along a particle trajectory:

$$E(\mathbf{x}, t_0, T) = \frac{1}{T\bar{\tau}_w}\int_{t_0-T}^{t_0}\sigma_e(\mathbf{x}(t))dt \quad (3.26)$$

where $\bar{\tau}_w$ is the temporally averaged wall shear stress in a corresponding straight pipe. A proper analysis of this warrants a full study, and will therefore be left for future work.

The *in vivo* results published in (Caro, Cheshire, & Watkins 2005) show that not only does the helical graft appear to prevent thrombosis within the graft itself, it also prevents the formation of intimal hyperplasia in the junction downstream of the graft. Previous studies (Papaharilaou, Doorly, & Sherwin 2002) (Sherwin, Shah, Doorly, Peiro, Papaharilaou, Watkins, Caro, & Dumoulin 2000) have shown that swirling flow, that is, a single vortical structure in the secondary flow, may be beneficial due to more equal wall shear stress distributions and elimination of stagnation regions. The swirling flow discovered in the results presented here, and the *in vivo* results of Caro *et al.*, seem to confirm this.

3.6 Appropriate definition of a vortex for general pipe flows

In Section 3.3 the apparent discrepancy between a single vortical structure of the secondary flow, and the double-vortex structure of the particle trajectories, was resolved through a coordinate, and corresponding velocity, transformation. This allows the velocity field experienced by the particles to be obtained, which clearly

contain two distinct vortex-like structures. Naturally, this leads to the question, of whether axial vorticity is a useful determinant of vortical structures in helical pipe flows, or whether some other measure is more appropriate. The following discussion considers this question, and is in fact relevant for any pipe flow that possesses both curvature and torsion.

It is deceptively difficult to provide a general method of identifying vortical structures within an arbitrary velocity field. Whilst qualitatively a vortex may be described in terms of 'circulatory motion of matter' or 'whirling or swirling motion', translating this into a precise mathematical definition is not straightforward. Intuitive indicators such as examining vorticity distributions or pressure minima are unreliable and may provide both false positive and false negative results. For example, vorticity may be large in parallel shear flows, which clearly do not contain any vortices. Many different criteria have been proposed that improve on these simple indicators, including the λ_2 criterion introduced in Section 2.6.2. A brief description follows of three vortex criteria, which are then applied to the helical pipe velocity fields.

An important property of the following criteria, is that they are all Gallilean-invariant. That is, they are unaffected by coordinate changes of the form:

$$\tilde{\mathbf{x}} = \mathbf{Q}\mathbf{x} + \mathbf{u}t \tag{3.27}$$

where $\mathbf{Q}$ is a constant proper orthogonal tensor, and $\mathbf{u}$ is a constant velocity vector. These measures all begin with the velocity gradient tensor decomposition:

$$\nabla\mathbf{v} = \mathbf{S} + \mathbf{\Omega} \tag{3.28}$$

These terms were described in more detail in Section 2.6.2, but briefly $\mathbf{S}$ represents the rate of strain and $\mathbf{\Omega}$ the rotation or vorticity.

The first measure to consider is the Q-criterion of Hunt, Wray & Moin (Hunt, Wray, & Moin 1998) that defines the regions of the flow where

$$Q = \frac{1}{2}[|\mathbf{\Omega}|^2 - |\mathbf{S}|^2] > 0 \tag{3.29}$$

as a vortex, due to the domination of vorticity over strain. Note for a tensor $\mathbf{A}$, $|\mathbf{A}|$ is the tensor norm defined by $(trace[\mathbf{A}\mathbf{A}^T])^{1/2}$. By considering the behaviour of the velocity field around a point, in a reference frame moving with that point, Chong, Perry & Cantwell devised the Δ-criterion (Chong, Perry, & Cantwell 1990). This actually incorporates the quantity Q, and identifies vortices as regions where, the vorticity is sufficently strong so as to cause the rate-of-strain tensor $\mathbf{S}$ to be dominated by the rotation tensor $\mathbf{\Omega}$. They show that this corresponds to the velocity gradient tensor possessing complex eigenvalues, which for incompressible flow, can be tested with the following condition:

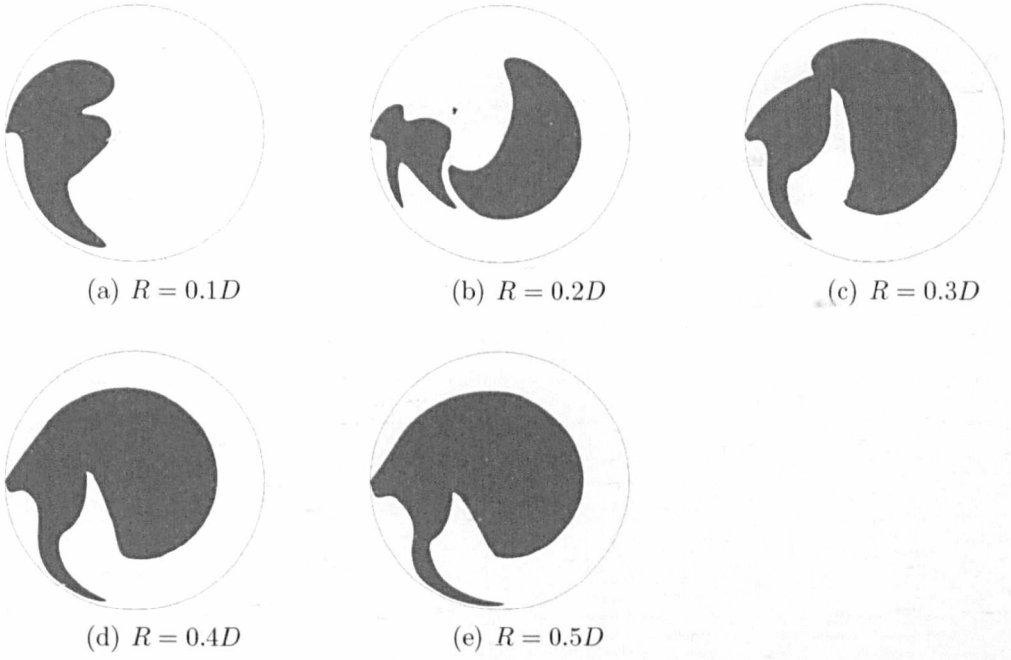
$$\Delta = \left(\frac{Q}{3}\right)^3 + \left(\frac{det\nabla\mathbf{v}}{2}\right)^2 > 0 \tag{3.30}$$

The third measure is the λ_2 criterion of Jeong & Hussain (Jeong & Hussain 1995), described fully in Section 2.6.2. To summarise, it identifies vortices as regions where the second eigenvalue of $\mathbf{S}^2 + \mathbf{\Omega}^2$ is negative.

These measures are applied to the velocity fields for five helical geometries, and the vortex identified by them, shown in Figures 3.24 - 3.26.

For all measures the structure identified is clearly a single vortex that dominates the cross-section. This is in agreement with the axial vorticity results presented in Figures 3.3(d) - 3.3(f). Note that for $R = 0.1D$ the λ_2 criterion does not appear to identify the vortical structure as expected. It is thought this is due to the weakness of the structure and the corresponding lack of a pressure minimum, as shown in Figure 3.6(a).

Whilst these measures are formulated to be Galilean invariant, Haller shows, using λ_2 as an example, that they are not invariant under general transformations that include both translation and rotation (Haller 2005). For unsteady flows, there is no single correct frame of reference, and arguing that the definition of a vortex should not vary with the particular choice of frame, Haller introduces an *objective* definition of a vortex, which is unaffected by general changes of reference frame. The mathematical details of this definition are lengthy, and will not be reproduced here, but in qualitative terms the criterion identifies vortices as regions of objective



(a) $R = 0.1D$ (b) $R = 0.2D$ (c) $R = 0.3D$

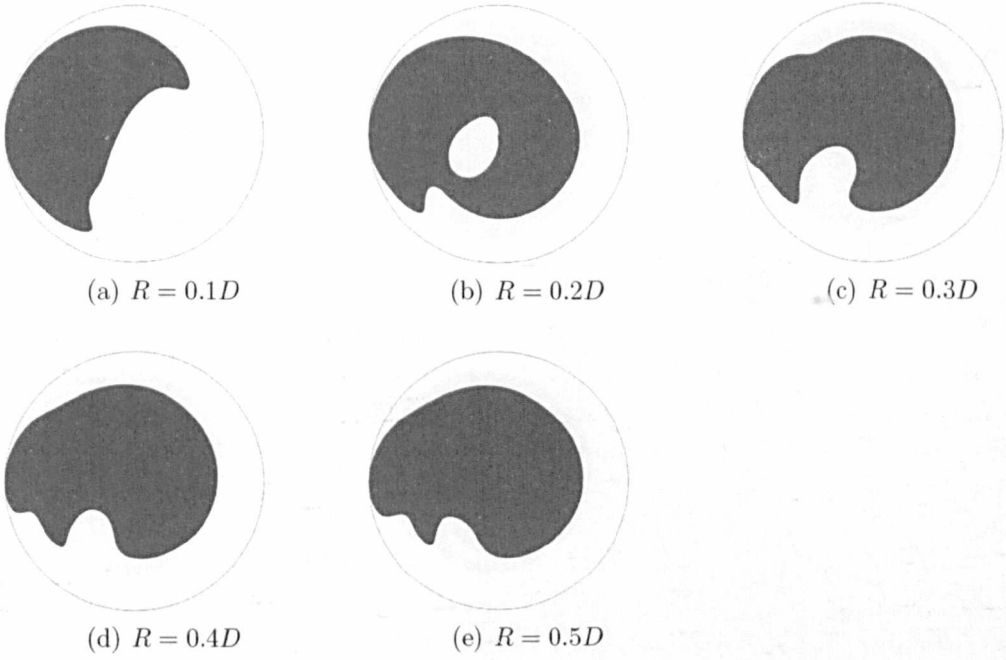
(d) $R = 0.4D$ (e) $R = 0.5D$

Figure 3.24: λ_2 contour slices, taken at $z = 0$, for increasing helical radius. The grey region indicates the vortical structure as identified by a value of $\lambda_2 < -0.3$

Lagrangian stirring. For most flows, there is an excellent correspondence between Haller's objective vortex definition, and local maxima of the largest finite-time Lyapunov exponent field. This can be determined directly from the particle trajectories, by differentiating the position of the particles with respect to their initial location, thereby determining the linearised flow map. These exponents are sometimes referred to as Direct Lyapunov Exponents.

Haller notes that the Galilean-invariant criteria presented in Figures 3.24 - 3.26 are identifying regions of instantaneous Eulerian stirring, using non-objective quantities. Cucitore *et al.* (Cucitore, Quadrio, & Baron 1999) describe vortices as material tubes of low particle dispersion, with which Haller's definition is in agreement. It seems clear that the particle trajectory results for helical pipe flows meet the definition of vortices as given by both Cucitore and Haller, with the distinction between Eulerian and Lagrangian stirring referred to by Haller, clearly important for helical pipes.

As shown in Section 3.3 the particle trajectories can be explained by removing both



(a) $R = 0.1D$ (b) $R = 0.2D$ (c) $R = 0.3D$

(d) $R = 0.4D$ (e) $R = 0.5D$

Figure 3.25: Q-criterion contour slices, taken at $z = 0$, for increasing helical radius. The grey region indicates the vortical structure as identified by a value of $Q > 0$.

translating and rotating motions. However, the velocity of this motion is different for each particle, and thus is different from the traditional concept of a reference frame, which has a single velocity for the entire domain. In effect, each fluid particle is deemed to have its own reference frame, a concept used in the formulation of the Δ-criterion, however, in this case the local reference frame was not permitted to rotate. This reference frame usage is not the same as that referred to by Haller, however a simple transformation of the velocity field shows their equivalence.

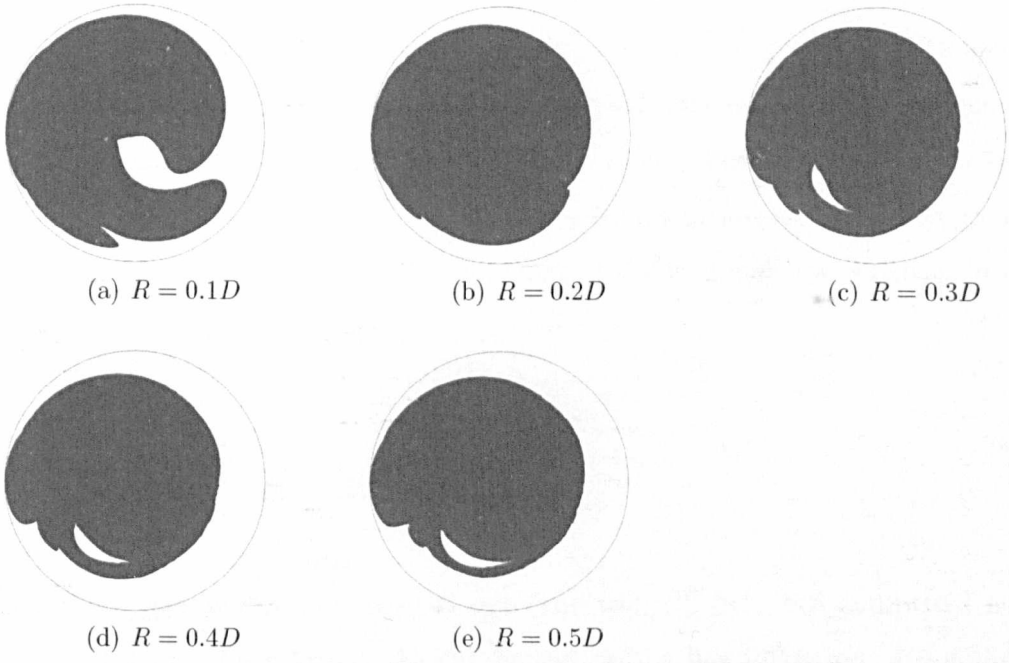
Consider the definitions of u and w:

$$u = \frac{dx}{dt} \tag{3.31}$$

$$w = \frac{dz}{dt} \tag{3.32}$$

The rotational velocity from Section 3.3.1.2 is

$$\dot{\theta}_{rotation} = \frac{d\theta}{dt} = \frac{w}{c} \tag{3.33}$$



(a) $R = 0.1D$ (b) $R = 0.2D$ (c) $R = 0.3D$

(d) $R = 0.4D$ (e) $R = 0.5D$

Figure 3.26: Δ-criterion contour slices, taken at $z = 0$, for increasing helical radius. The grey region indicates the vortical structure as identified by a value of $\Delta > 0$.

Dividing u by w produces a normalised u velocity u^*. The equivalent transformation is also applied to v.

$$u^* = \frac{u}{w} = \frac{dx}{dz} \tag{3.34}$$

This mapping was used in (Hwang & Kwon 2003) and (Kang & Kwon 2004), which is valid as along as the axial velocity does not change sign, i.e. $w > 0$ throughout the domain, a condition which is satisfied here. The rotation of the velocity field is now

$$\frac{d\theta}{dz} = 1/c \tag{3.35}$$

which is constant across the domain. These transformations show that the velocity field is equivalent to 2-dimensional time varying flow in which the time variable has been replaced by z. In this formulation the rotating reference frame now has a constant rotation of $1/c$ throughout, which is now commensurate with Haller's example.

For the flow considered here, the helical symmetry of the velocity field permits vari-

ous transformations of the coordinate system that allow the prediction of the particle trajectories and the related vortical structures. For a pipe geometry with arbitrarily varying curvature, torsion and twist, such transformations will not, in general, be possible, rendering the definition of an appropriate reference frame difficult. The objective definition of a vortex overcomes such difficulties, and therefore may be an appropriate tool for analysing the unsteady, 3-dimensional flow existing in arterial blood flow.

3.7 Conclusions

For all the geometries investigated here the velocity field has comprised a single, dominant vortical structure. As the helical radius has increased, a double-vortex structure emerged in the particle trajectories. This apparent discrepancy can be resolved by applying a sequence of translating and rotating reference frame changes to the velocity field. Furthermore, this result has implications for the appropriate representation of vortical structures in pipe flows, with objective measures such as Direct Lypapunov Exponents perhaps being most suitable.

The particle mixing is directly determined by the formation of the double-vortex structure, with quantitative measures of mixing asymptoting as the helical radius tends to $0.5D$. This implies that the optimal geometry for medical applications, in terms of mixing vs. pressure loss, is $R = 0.25D$, for a Reynolds number of 250. As a general design rule, for any given Reynolds number, the optimal geometry is likely to be one with the smallest helical radius, that still produces a double-vortex structure in the particle motion.

Chapter 4

Mixing in Multiple Helical Geometries - Idealised Model

This Chapter examines an idealised model for the mixing behaviour of geometries composed of different helical pipes. It begins with a summary of previous research on various designs of mixing devices in Section 4.1, before describing the geometric and flow parameters to be investigated in this thesis in Section 4.2. The mixing results of the combined helical geometries are presented in Section 4.3, and conclusions are presented in Section 4.4.

4.1 Review of existing pipe-based mixing devices

The results of Chapter 3 show that the degree of mixing possible in a helical pipe, for a fixed Reynolds number, is limited by the formation of the double-vortex structure in the particle trajectories. These structures are two separate elliptic regions, or islands, separated by a barrier to mixing, across which no particles can cross (except by diffusion). This limits the degree of mixing that can be generated, meaning that the helical pipe is a rather poor mixing device, compared with those used in industrial applications. These pipe based mixers can destroy islands of regular

flow by using internal baffles, forced wall motion and electro-osmotic forcing. In the context of bypass grafts these options are either impractical or physiologically undesirable. Therefore a means of enhancing mixing within the graft is sought that does not require these technologies.

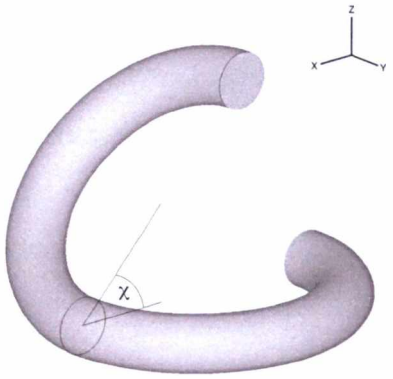
In their seminal paper (Jones, Thomas, & Aref 1989), Jones, Thomas & Aref, show that chaotic advection (Aref 1984) can be generated by concatenating 180^o curved sections of pipe, with some twist angle χ at each junction, which ranges from 0^o to 180^o. Their configuration is shown in Figure 4.1(a). They use the first-order Dean solution which has a Poiseuille profile for the axial velocity. As the flow is steady, by dividing the u and v components by w, a mapping between cross-sectional planes of constant θ can be defined

$$\frac{dx}{d\theta} = \frac{\gamma}{1152}(4 - 5x^2 - 23y^2 + x^4 + 8x^2y^2 + 7y^4) \tag{4.1}$$

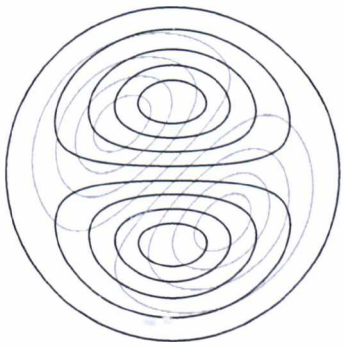
$$\frac{dy}{d\theta} = \frac{\gamma}{192}xy(3 - x^2 - y^2) \tag{4.2}$$

where γ determines the strength of the Dean vortices, and is the product of Re and the pressure gradient driving the flow. It was assumed that fully-developed Dean flow solutions existed in each section of pipe, and that the transition between each section was instantaneous. Although they acknowledge that this is physically unrealistic, it is explained that a flow scenario similar to this can be generated experimentally by inserting straight pipe segments between each curve. The straight pipe allows the Dean vortices to decay between each curved segment. In this way, the general topological structures are captured in the approximation, even though it won't predict the exact behaviour of the fluid particles. This approximation is, they acknowledge, more realistic for small values of χ. As χ approaches 180^o this would require that the vortices in the first bend would have to be completely destroyed, and new vortices of the opposite sign created, rather than merely a slight change in orientation of the vortices for the case of small χ.

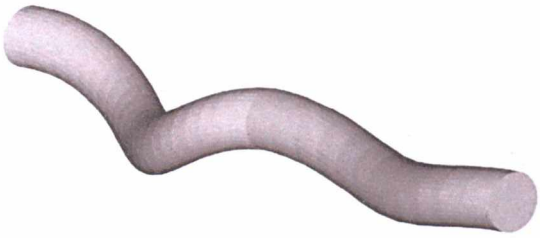
The results of Chapter 3 showed that the in-plane velocity field in a helical pipe



(a) Twisted pipe configuration used by Jones *et al.* for $\chi = 45^o$



(b) Dean flow streamlines crossing at 45^o



(c) A combined helical pipe geometry for $R = 0.5$ and $R = 0.25$



(d) Streamline crossing for helical pipe flows, $R = 0.5$ and $R = 0.25$

Figure 4.1: Demonstration of the concept of streamline crossing, which Jones *et al.* found to produce excellent mixing through chaotic advection

can be a double vortex structure with varying sizes/strengths of vortex and varying angle of vortical dividing line. It is proposed that a similar regime of 'streamline crossing', to that of Jones *et al.* (Jones, Thomas, & Aref 1989), can be achieved by concatenating two different helical geometries. One such example is shown in Figure 4.1(c) for the geometries $R = 0.25D$ and $R = 0.5D$. The corresponding in-plane streamlines are shown in Figure 4.1(d), and clearly illustrates the concept of 'streamline crossing', whereby the streamlines of consecutive flows intersect at some angle.

The first remark to make on the twisted pipe results, is that due to the symmetry of

the Dean flow mapping, denoted **M**, the Poincaré section of the combined geometry possesses a line of symmetry at an angle $\frac{1}{2}\chi$. This is clearly visible for the islands of mixing that exist in the Poincaré sections. Results are presented for various values of both χ and γ, and their effect on the particle motion summarised. χ is the *twist* angle introduced earlier, and γ determines the magnitude of the Dean flow velocities, as can be seen from eqns (4.1 & 4.2).

For a fixed value of γ, increasing the twist angle χ produces chaotic trajectories in a greater portion of the cross-section, with the maximum value occurring at an angle of approximately 90^o. As χ increases beyond this, an increasing number of islands of regular flow form in the cross-section, consequently reducing the area where chaotic trajectories exist. Further, a small deviation in χ from 0^o, produces more chaotic trajectories, than an equivalent deviation from 180^o. For small values of χ the chaotic trajectories exist only near the boundary, and in a narrow band across the diameter, with the large overlap of the Dean vortices causing the formation of large island regions.

For a fixed value of χ, increasing the vortex strength, γ, increases the fraction of chaotic trajectories. This is in agreement with the blinking vortex results presented in Chapter 1, and is to be expected, since within a fixed axial distance, in this case, a 180^o section of curved pipe, will cause particles to travel a longer distance, enhancing the particle separation, and hence mixing. This result means that examining the topology of the overlap of the component Poincaré sections is not sufficient for determining the resultant mixing behaviour.

4.1.1 Mixing devices utilising 'streamline crossing'

The results of Jones *et al.* demonstrate that 'streamline crossing' can efficiently generate chaotic advection, and can be achieved from very simple geometric configurations. A brief summary of some other flows that utilise streamline crossing follows.

A much studied example is the Partitioned Pipe Mixer (PPM), which is an idealisation of the Kenics® static industrial mixer. The Kenics mixer is an attempt to generate the baker's transform in its cross-sectional mixing. Further details of the Kenics® mixer can be found at (Chemineer 2009).

The PPM is a cylindrical pipe, which contains two plates, set at some angle to each other, which partition the pipe into two semi-circular ducts, as illustrated in Figure 4.2. The plates remain fixed, with the axial flow driven by a pressure gradient, and the cylinder wall rotated to generate the secondary flow. The streamlines of this secondary flow are somewhat similar to that in Dean flow, however, in this case, both vortices rotate in the same direction. For a Stokes flow solution, a dimensionless parameter β, termed *mixing strength*, determines the flow:

$$\beta = \frac{4v_R L}{3\nu\bar{v}_z R} \tag{4.3}$$

where v_R is the rotational velocity of the wall, L the length of the plates and $\bar{v}_z$ the mean axial velocity.

It is found that increasing β, which can be thought of as roughly equivalent to γ from eqn (4.1), is correlated with reducing the number and size of islands in the Poincaré sections. It is also found that the axial velocity profile has a significant effect on the structure of the Poincaré section, as does making the adjacent sections of pipe counter-rotating, rather than co-rotating. The latter change seeming to produce more efficient mixing.

'Streamline crossing' has been utilised to generate efficient mixing in microchannels (Stroock, Dertinger, Ajdari, Mezic, Stone, & Whitesides 2002) at low Reynolds number, such as might be used for analysis of DNA and proteins. For a rectangular duct, Stroock *et al.* show that a pattern of grooves created on the flow of the duct generates a secondary flow consisting of one large recirculating region, and one small one. By periodically altering the groove pattern, the line dividing the two elliptic regions is moved from one side to the other, clearly a regime of streamline crossing. The results display excellent mixing characteristics, and after fifteen iterations, an initial condition is found to be perfectly mixed.

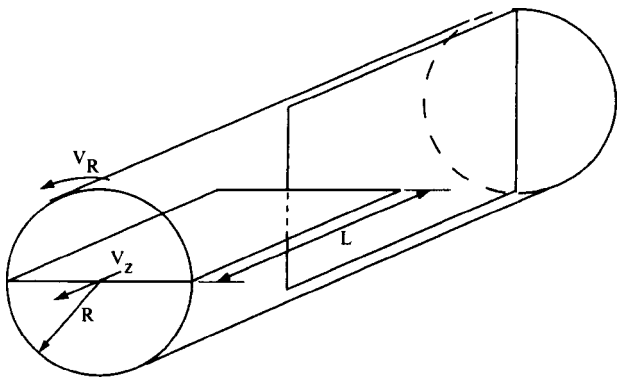


Figure 4.2: The partitioned pipe mixer - an idealisation of the Kenics mixer.

A different mechanism is proposed by Qian & Bau, which generates similar secondary flow structures to that in (Stroock, Dertinger, Ajdari, Mezic, Stone, & Whitesides 2002). They use an electroosmotic flow, driven by a uniform electrical field, but with varying potential distributions at the wall, obtained for example by varying the wall coating materials.

4.1.2 Linked Twist Maps

A recent development in the study of mixing systems, is the application of a mathematical formalism associated with Linked Twist Maps (LTMs) (Sturman, Ottino, & Wiggins 2006). Originally developed to study astrophysical dynamics, Sturman *et al* have shown that several results relating to LTMs can be used to prove the existence of regions of perfect, or Bernoulli, mixing in a linked twist map. They show that the blinking vortex of Aref, described in Chapter 1 can be trivially shown as equivalent to a LTM. Jones *et al* remark that the twisted pipe flow can be considered as a series of blinking vortex systems, an intuitive comparison that can be made mathematically precise through the formalism of LTMs.

Franjione & Ottino define a duct flow as a steady three-dimensional isochoric flow that is composed of a re-circulating two-dimensional cross-sectional flow, and a

unidirectional axial flow that is independent of the axial coordinate (Franjione & Ottino 1991). Stated mathematically this is:

$$\frac{\partial \mathbf{u}}{\partial t} = 0 \tag{4.4}$$

$$\nabla.\mathbf{u} = 0 \tag{4.5}$$

$$\frac{dx}{dt} = \frac{\partial \psi(x,y)}{\partial y} \tag{4.6}$$

$$\frac{dy}{dt} = -\frac{\partial \psi(x,y)}{\partial x} \tag{4.7}$$

$$\frac{dz}{dt} = k(x,y) \tag{4.8}$$

The results of Chapter 3 show that the particle trajectories clearly meet this definition of a duct flow. Franjione & Ottino show that the stretch of a line element in such a flow, increases linearly in time, imposing a fundamental bound on the mixing efficiency that can be achieved, as is also the case for a single point vortex. Sturman *et al.* show that duct flows can be constructed as an Linked Twist Map, using a sequence of coordinate transformations (Sturman, Ottino, & Wiggins 2006), (Wiggins & Ottino 2004), and thus is fundamentally equivalent to the blinking vortex system.

Unfortunately, the mathematical results that guarantee regions of perfect, i.e. Bernouilli, mixing, only apply to a small range of LTM systems, and are not yet sufficiently general to encompass cases where the cross-section contains more than one LTM. However, the existing results do lend weight to the concept of 'streamline crossing' as an efficient means of generating mixing, and this formalism may become useful in the future.

4.2 Multiple helical geometries

By concatenating helical pipe geometries of differing helical radii, as in Figure 4.1(c), a streamline crossing flow environment similar to that of Jones *et al* can be generated (Jones, Thomas, & Aref 1989). There are, however, a few differences between

them, which may complicate the application of the conclusions presented in (Jones, Thomas, & Aref 1989). In the twisted pipe configuration the secondary flow was composed of symmetric, counter-rotating Dean vortices, and therefore the only parameter that was varied was the *twist* angle χ. For the helical pipe flows, the secondary flow is no longer symmetric, with the size of the second vortex increasing with R. In addition, the strength, or velocity magnitudes, of the in-plane flow also change with R. Therefore, in addition to providing valuable information for design optimisation, these results may also provide insights for all flows utilising streamline crossing.

If an alternating sequence of right and left-handed helical pipes were placed end-to-end, then the possibility for even greater enhancement of mixing is likely to occur (although not guaranteed). However, the validity of the idealisation made here is much reduced for these geometries, since it requires that a vortex is first destroyed, and then a new flow initiated of the opposite sense, in the same way as values of $\chi \rightarrow 180^o$ did in (Jones, Thomas, & Aref 1989). This would increase the transition distance between the two flows, and indeed the generation of the vortical structure in the second pipe may interact with the existing vortex, as occurs in double bend flows for $Re \geq 250$ (Pitt 2005). This might prove beneficial for mixing, but can not be reliably predicted by simply concatenating velocity fields. Furthermore, from an engineering standpoint, the width form factor of such a design would be much larger than a single helical geometry, with the joint between the two pipes a possible mechanical weakness, both of which make it unsuitable for use as a medical device. Therefore, only helical pipes of the same 'handedness' or chirality will be used.

In Chapter 3 a total of nine geometries were investigated. These nine base geometries provide 81 combined geometries. However, the order of the geometries is essentially unimportant, and nine of the 81 are simply repeated helical geometries, i.e. just the standard single helical geometry. This leaves a total of 36 combined geometries in the parameter space, a strategic selection of which will be examined.

A straight line can be drawn between the two effective in-plane vortical structures

that approximately divides the cross-section into two regions. Table 4.1 shows the angles between these lines, for a combined helical geometry. This angle is essentially the same as the twist angle used by Jones *et al.*, and is a key component of generating the desired mixing enhancements. Note that for $R = 0.1D$ and $0.15D$, the particle trajectories are a single vortical structure, and therefore are not considered for use in the combined geometries. A selection of 11 geometries is made that provides a useful cross-section of the possible angles, which are summarised in Table 4.2. Strictly, it is not only the angle that will vary with these combinations, however, the change in particle trajectories in the range $R = 0.35D - 0.5D$ is small, so that the change in crossing angle can be considered to be the most significant parameter. Furthermore, the pressure loss for these combinations will be larger than for other combinations of similar crossing angle, and therefore are unlikely to be optimal from a mixing versus pressure loss perspective.

Table 4.1: Angle (in degrees) between the vortex dividing lines in each helical geometry. The combinations selected for investigation are underlined.

R	**0.2**	**0.25**	**0.3**	**0.35**	**0.4**	**0.45**	**0.5**
0.2	**0**	-17	-28	-34	-37	-40	41
0.25	<u>17</u>	**0**	-11	-17	-20	-23	-24
0.3	<u>28</u>	<u>11</u>	**0**	-6	-9	-12	-13
0.35	<u>34</u>	<u>17</u>	<u>6</u>	**0**	-3	-6	-7
0.4	<u>37</u>	20	<u>9</u>	3	**0**	-3	-4
0.45	40	23	12	6	3	**0**	-1
0.5	<u>41</u>	<u>24</u>	<u>13</u>	7	4	1	**0**

Henceforth, the helical radius of first geometry will be denoted R_A, and that of the second, R_B.

Table 4.2: Helical radii of the eleven combined helical geometries considered

Helix A	0.25	0.3	0.3	0.35	0.35	0.35	0.4	0.4	0.5	0.5	0.5
Helix B	0.2	0.2	0.25	0.2	0.25	0.3	0.2	0.3	0.2	0.25	0.3

4.3 Mixing: idealised prediction

Whilst acknowledging that the precise mixing behaviour may not be captured, an idealised prediction of the degree of mixing can be made by concatenating the velocity fields from two single helix geometries (previously obtained in Chapter 3). This is computationally less expensive, and allows a larger parameter space to be examined, leaving the most promising geometries to be investigated more fully later (see Chapter 5). Furthermore, it is hoped that the results will provide general insights into all mixing flows utilising the principle of streamline crossing. In particular, it may help to understand the roles that asymmetry and strength of the vortical structures play in the mixing of the system, as it is suspected that the asymmetry of the vortical systems will provide enhanced mixing when compared with symmetric vortices. A paper by Ottino *et al.* (Franjione & Ottino 1992) shows that by identifying and then systematically destroying symmetries in sequences of Poincaré maps, efficient chaotic mixing can be designed into a mixing system. With no symmetries present in the systems under investigation, this process has effectively already been accomplished.

4.3.1 Particle trajectories

Figures 4.3 - 4.8 show slices of the particle trajectories taken at multiples of $z = 6D$, for a selection of the geometries, up to and including $z = 36D$. These geometries have been selected on the basis of their results being of particular interest, and are given in Table 4.3.

Starting with Figure 4.4, it is not clear whether there has been any mixing enhance-

Table 4.3: The six combined geometries for which particle trajectory slices are shown in Figures 4.3 - 4.8

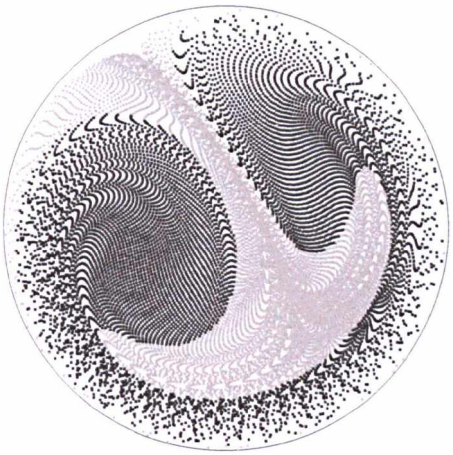
Helix A	0.25	0.35	0.4	0.5	0.5	0.5
Helix B	0.2	0.3	0.2	0.2	0.25	0.3
Figure No.	4.3	4.4	4.5	4.6	4.7	4.8

ment. The small difference in the component flows, means that a double-vortex structure remains coherent in all the particle slices. Also, from a biological viewpoint, particles initially near the wall, remain there for much of the geometry, which is likely to be unfavourable. Considering Figure 4.3 shows an improvement in mixing from Figure 4.4. The greater change in flow between geometries, is clearly beneficial, and although the structure of the underlying flow is clear in the first four slices (Figures 4.3(a) - 4.3(d)), the increasingly fine filaments, particularly of the grey particles, begin to obscure this in the final two slices (Figures 4.3(e) & 4.3(f)). However, a persistent region of black particles exists in the left side of the domain, trapped in an island of regular flow, caused by the close overlay of the streamlines in that area.

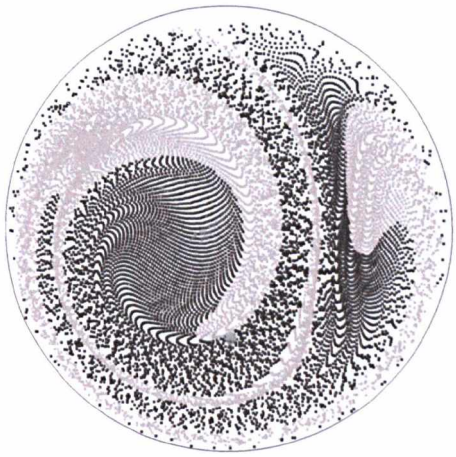
Comparing Figures 4.5 & 4.6 reveals very similar patterns of mixing. As in Figure 4.3 the underlying structure of the streamlines is visible in the first few slices, but is even more successfully destroyed in the later slices. The similar structure is due to the similar streamlines of the component geometries, as there is only a small change when R increases from $0.4D$ to $0.5D$. Nevertheless, this change appears to lead to an enhancement in the mixing, with the grey particles more finely distributed in the final slice for $R_A = 0.5$, Figure 4.6(f) than they are for $R_A = 0.4$, Figure 4.5(f). These particle trajectory slices clearly demonstrate that although the geometry $R = 0.2D$ is poor at mixing by itself (due to the small second vortex), when placed in combination with other helical geometries, it does generate excellent theoretical mixing.

The final sets of particle trajectories to be examined are Figures 4.7 & 4.8. As for

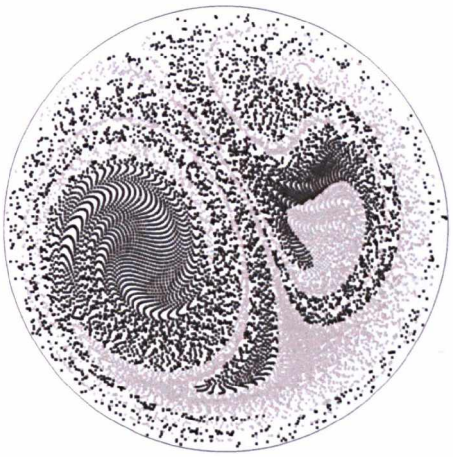
the previous two cases, the change in the streamlines of one component geometry is small. However, once again, this change is sufficient to lead to a visible improvement in the quality of mixing. Although a double-vortex structure is visually coherent for most of the slices, Figure 4.7, corresponding to $R_A = 0.5D$ & $R_A = 0.25D$ consistently causes thinner structures to evolve in the grey particles, indicative of better mixing.



(a) 1 Pitch Length



(b) 2 Pitch Lengths



(c) 3 Pitch Lengths



(d) 4 Pitch Lengths

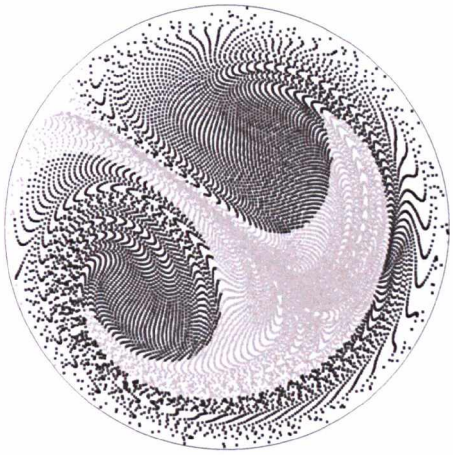


(e) 5 Pitch Lengths

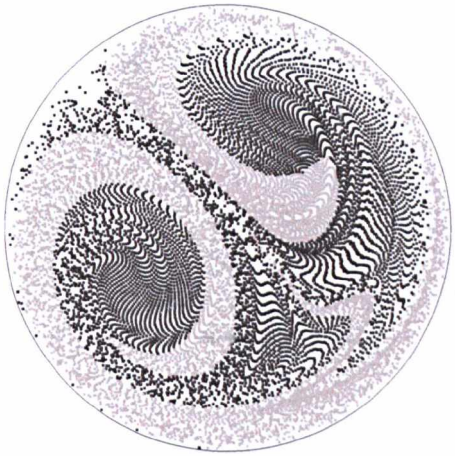


(f) 6 Pitch Lengths

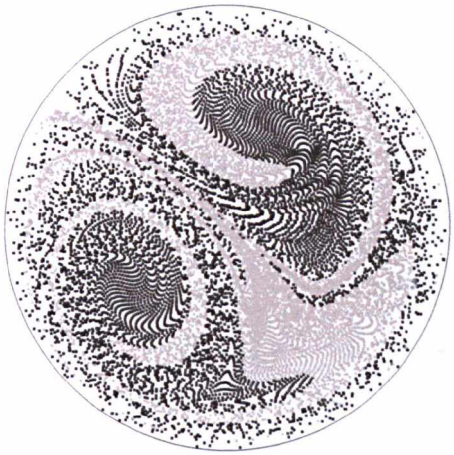
Figure 4.3: Particle trajectory slices, $R_A = 0.25$ and $R_B = 0.2$



(a) 1 Pitch Length



(b) 2 Pitch Lengths



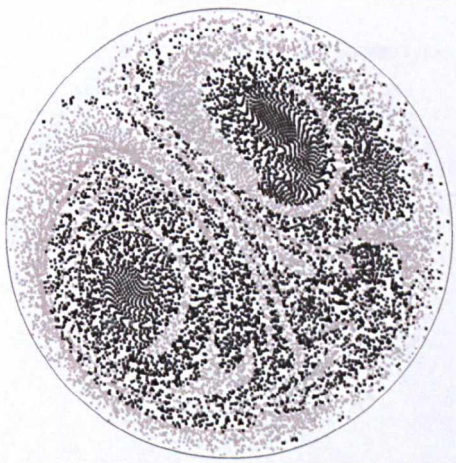
(c) 3 Pitch Lengths



(d) 4 Pitch Lengths

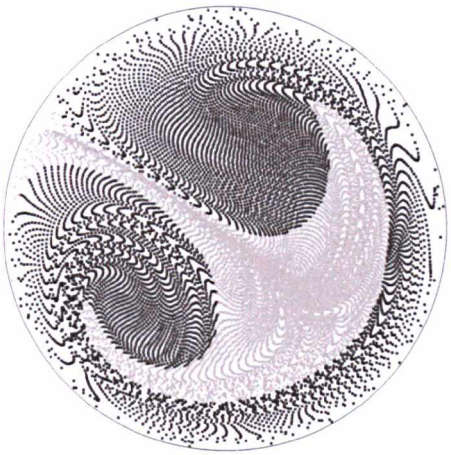


(e) 5 Pitch Lengths

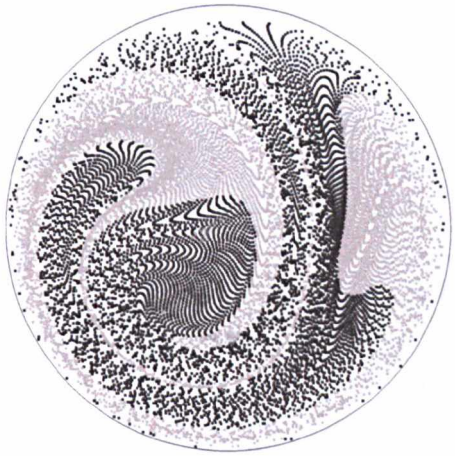


(f) 6 Pitch Lengths

Figure 4.4: Particle trajectory slices, $R_A = 0.35$ and $R_B = 0.3$



(a) 1 Pitch Length



(b) 2 Pitch Lengths



(c) 3 Pitch Lengths



(d) 4 Pitch Lengths

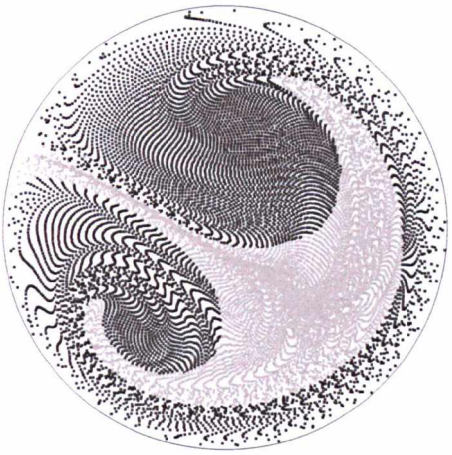


(e) 5 Pitch Lengths

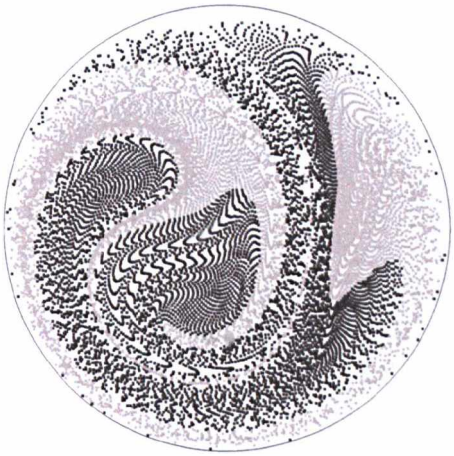


(f) 6 Pitch Lengths

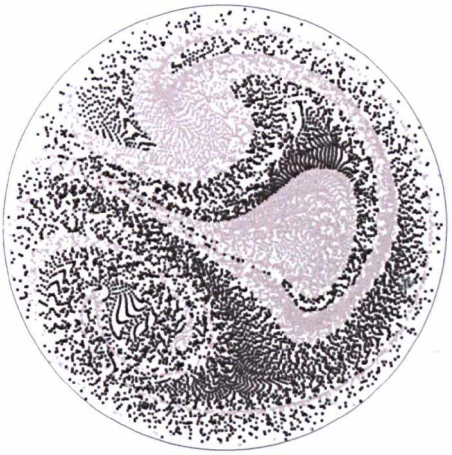
Figure 4.5: Particle trajectory slices, $R_A = 0.4$ and $R_B = 0.2$



(a) 1 Pitch Length



(b) 2 Pitch Lengths



(c) 3 Pitch Lengths



(d) 4 Pitch Lengths

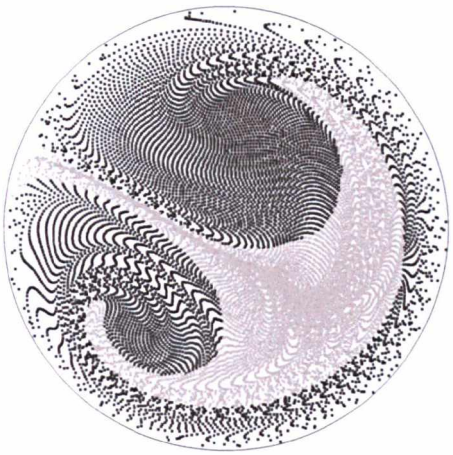


(e) 5 Pitch Lengths



(f) 6 Pitch Lengths

Figure 4.6: Particle trajectory slices, $R_A = 0.5$ and $R_B = 0.2$



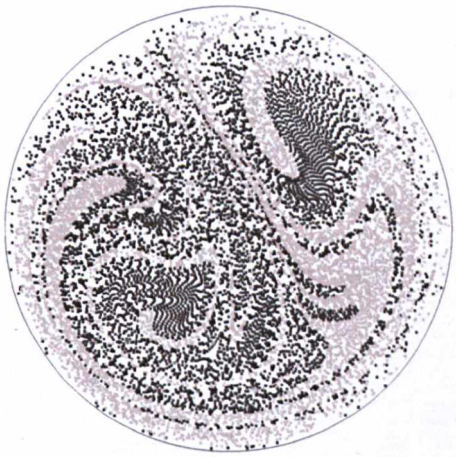
(a) 1 Pitch Length



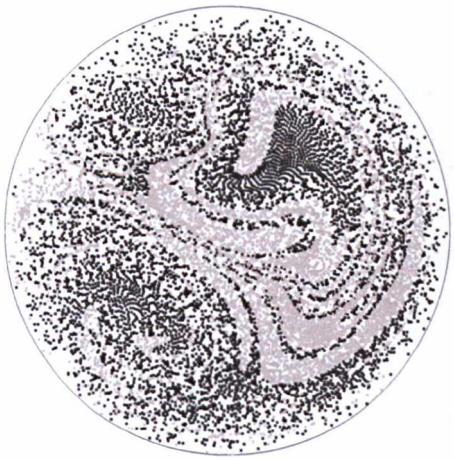
(b) 2 Pitch Lengths



(c) 3 Pitch Lengths



(d) 4 Pitch Lengths



(e) 5 Pitch Lengths

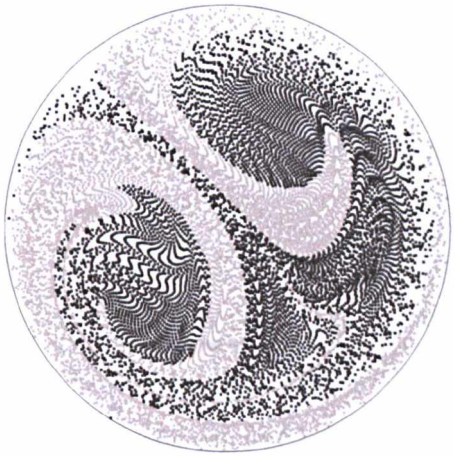


(f) 6 Pitch Lengths

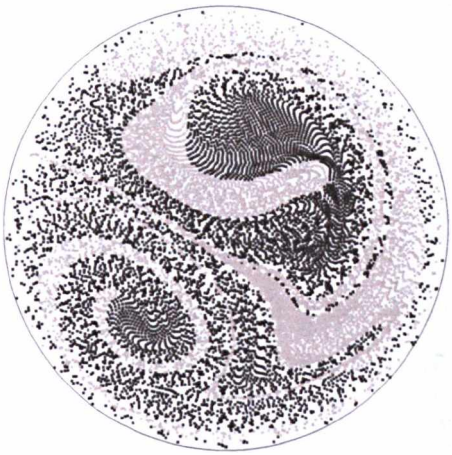
Figure 4.7: Particle trajectory slices, $R_A = 0.5$ and $R_B = 0.25$



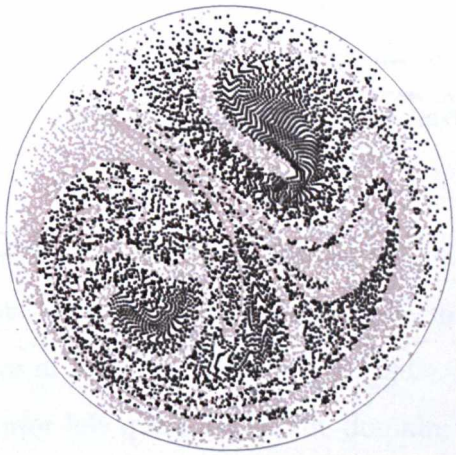
(a) 1 Pitch Length



(b) 2 Pitch Lengths



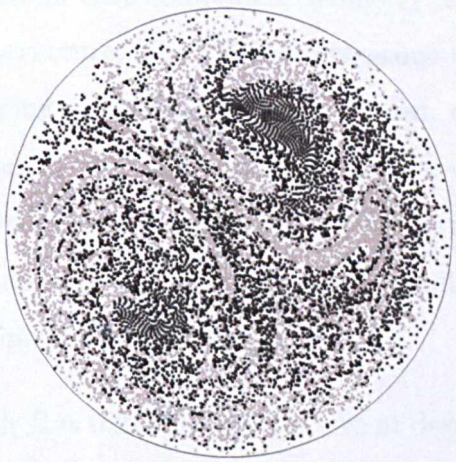
(c) 3 Pitch Lengths



(d) 4 Pitch Lengths



(e) 5 Pitch Lengths



(f) 6 Pitch Lengths

Figure 4.8: Particle trajectory slices, $R_A = 0.5$ and $R_B = 0.3$

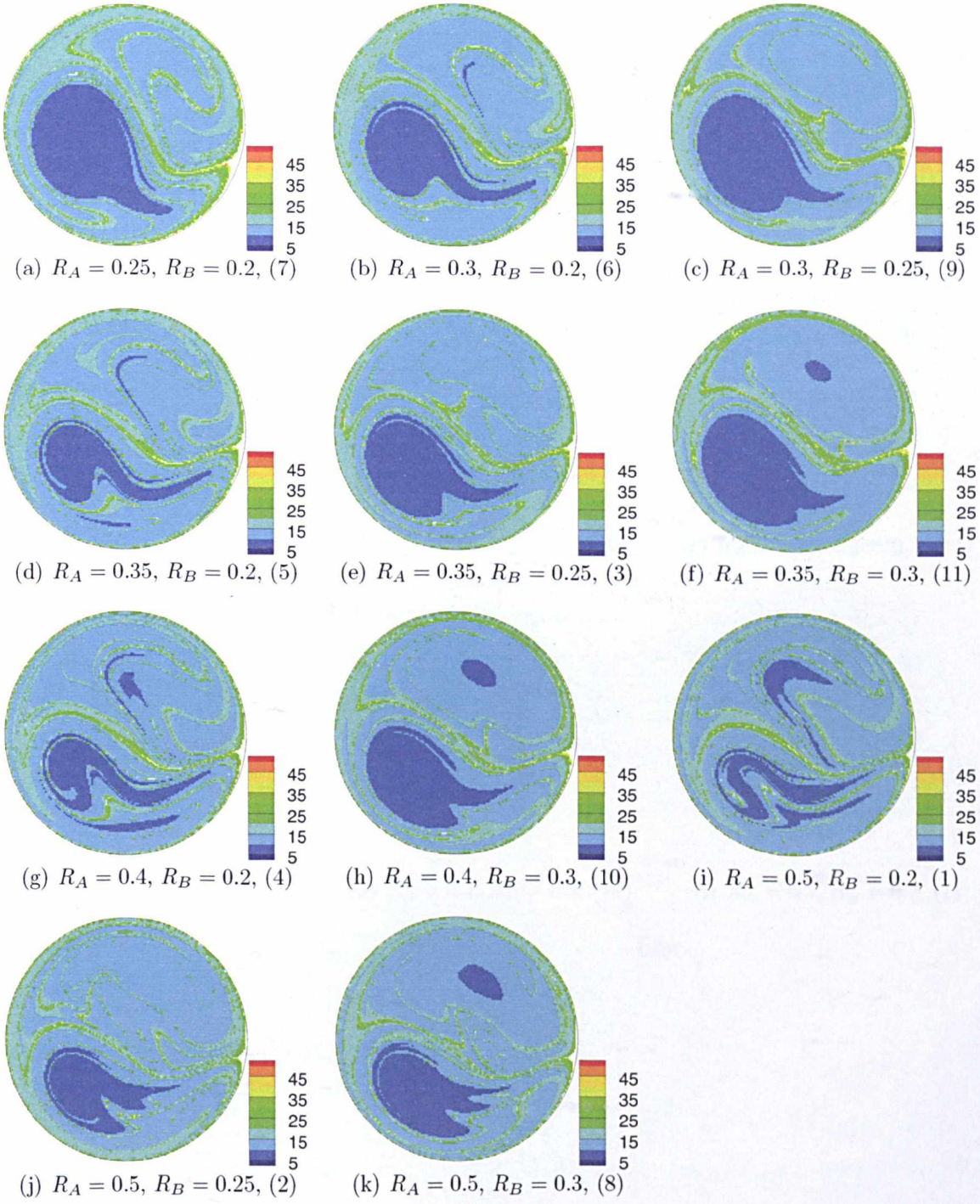
4.3.2 Residence time distributions and Poincaré sections

Residence time distributions, in particular their statistical properties, were used in Chapter 3 as a means of quantifying the mixing in single helical geometries. For more complicated mixing behaviour further insight can be obtained by looking at iso-residence distribution scatter plots. These are shown in Figure 4.9, and are simply the initial grid of particles coloured by their subsequent total residence time over six pitch lengths ($36D$). A correspondence between the structures visible in iso-residence time plots and the Poincaré section was first noted by (Khakhar, Franjione, & Ottino 1987), a correspondence which improves with each successive iteration of the mapping. This relationship was investigated further by (Mezic, Wiggins, & Betz 1999). They explain that a set of particles with the same residence time are actually on an orbit of the Poincaré map. Furthermore, many different orbits may have the same iso-residence time.

This relationship is useful for identifying orbits in the Poincaré map, which correspond to islands of regular flow, and which can ultimately reduce the mixing effectiveness of the device. A common feature in many of the plots in Figure 4.9 is a large island of low residence time in the lower-left quadrant of the domain. The island structure has formed due to the large degree of overlap and similarity between the streamlines in that part of the cross-section for each component geometry, which individually would also have a similar island structure. The low residence time value is due to the largest axial velocities also existing in this region. As expected, when the difference between the in-plane flow is small, the size of this island increases. A similar island also forms in the upper-right quadrant of the cross-section, when any geometry of $R > 0.25D$ is paired with another of $R > 0.25D$, as the similarity between the cross-sectional flows are again similar and overlap well.

These plots show that pairing a geometry with $R = 0.2D$ is very effective at destroying the island in the upper-right quadrant, due to the upper-vortex in the $R = 0.2D$ solution being very different from those for $R > 0.25D$, which creates large angles between the streamlines at each point in this part of the domain. In the lower-left

section of the domain the crossing of streamlines is less severe, although when paired with $R = 0.5D$ the lower island is considerably reduced in size.



(a) $R_A = 0.25$, $R_B = 0.2$, (7) (b) $R_A = 0.3$, $R_B = 0.2$, (6) (c) $R_A = 0.3$, $R_B = 0.25$, (9)

(d) $R_A = 0.35$, $R_B = 0.2$, (5) (e) $R_A = 0.35$, $R_B = 0.25$, (3) (f) $R_A = 0.35$, $R_B = 0.3$, (11)

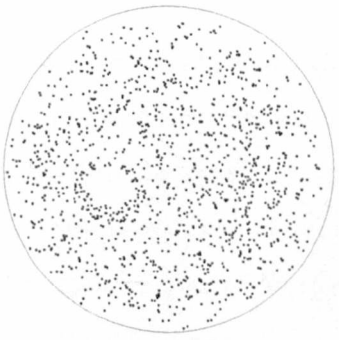
(g) $R_A = 0.4$, $R_B = 0.2$, (4) (h) $R_A = 0.4$, $R_B = 0.3$, (10) (i) $R_A = 0.5$, $R_B = 0.2$, (1)

(j) $R_A = 0.5$, $R_B = 0.25$, (2) (k) $R_A = 0.5$, $R_B = 0.3$, (8)

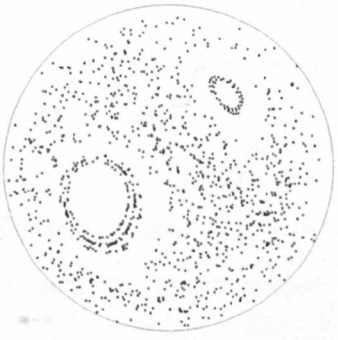
Figure 4.9: Initial particle distribution, coloured by total residence time of the particle over six pitch lengths.



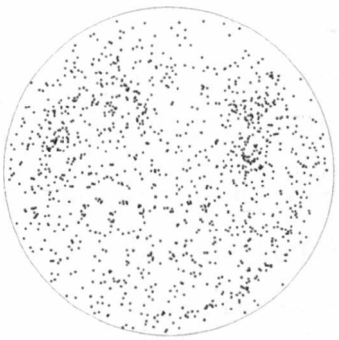
(a) $R_A = 0.25$, $R_B = 0.2$, (7)



(b) $R_A = 0.3$, $R_B = 0.2$, (6)



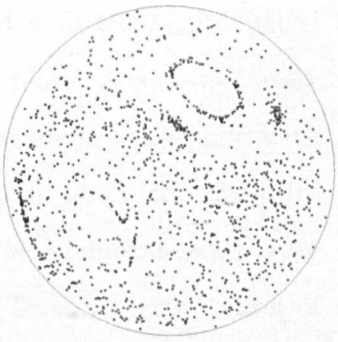
(c) $R_A = 0.3$, $R_B = 0.25$, (9)



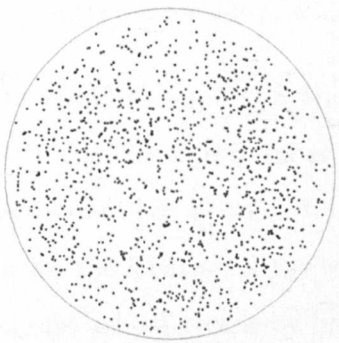
(d) $R_A = 0.35$, $R_B = 0.2$, (5)



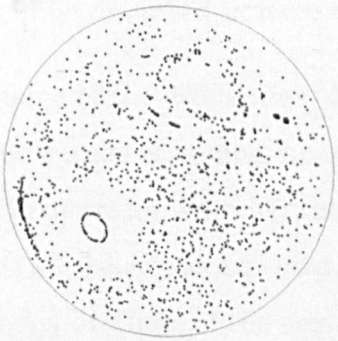
(e) $R_A = 0.35$, $R_B = 0.25$, (3)



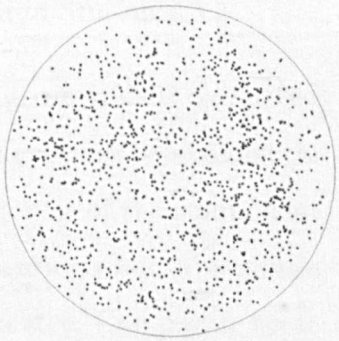
(f) $R_A = 0.35$, $R_B = 0.3$, (11)



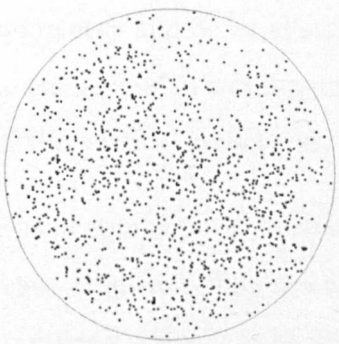
(g) $R_A = 0.4$, $R_B = 0.2$, (4)



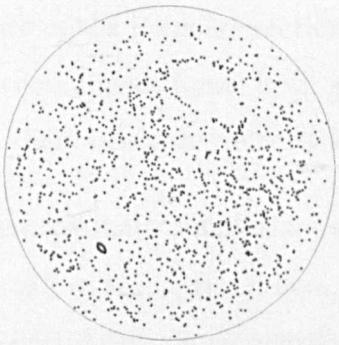
(h) $R_A = 0.4$, $R_B = 0.3$, (10)



(i) $R_A = 0.5$, $R_B = 0.2$, (1)



(j) $R_A = 0.5$, $R_B = 0.25$, (2)



(k) $R_A = 0.5$, $R_B = 0.3$, (8)

Figure 4.10: Poincaré sections generated by 50 iterations of the combined mapping.

An interesting feature on these plots is the notch that is visible on the lower right-hand side of the cross-section. This corresponds to "stuck" particles that have been advected very close to the wall, and hence have very high residence times, so long in fact that they do not travel through the geometry in a reasonable computational time. This notch of missing particles is also visible on the particle trajectory slices, but at the opposite side of the geometry, that is, at the location where the particles separate from the wall.

Figure 4.10 shows the Poincaré sections, with each geometry in the same spatial location, for easy comparison with the residence time scatter plots. It is immediately obvious that the islands structures in the Poincaré section do indeed correspond with iso-contours in the residence time plots. For these particular plots, the Poincaré sections offer a more precise definition of the boundaries of the islands. From Figure 4.10, islands can be detected in seven of the eleven figures. To aid interpretation of the results, the caption for each sub-figure includes the ranking of the geometry by the entropic measure, which will be discussed in more detail in Section 4.3.3.

As would be expected, the ranking of the geometries of the geometries is correlated with the size and number of the islands of mixing, although this will be explored in more detail in Section 4.3.3. Furthermore, knowing the structure of the component flows, the location of the islands are exactly as expected, appearing when streamlines in one helical geometry lie roughly on those of the next geometry. Comparing these results with those presented in (Jones, Thomas, & Aref 1989), there is a lack of symmetry and ordered structure in the Poincaré sections. This is thought to be due to the lack of symmetry in the component flows, both in terms of the area of extent of the vortical structures, and their strength (velocity magnitude).

It is of course possible that there are many more islands that exist for all the geometries. However, they are too small to be captured here, and their detrimental effect to mixing is likely to be small, particularly in comparison with the large islands that exist in some of the Poincaré sections.

4.3.3 Entropic measure

The entropic measure of mixing used in Chapter 3, is again used to quantify the degree of mixing in the combined helical geometries. For quantifying the mixing in the single geometries, the entropic measure provided little extra information, given that residence time statistics showed the same trends, and that a physical understanding of the mixing behaviour was attained. For the more complicated mixing behaviour in the combined geometries, the entropic measure is much more useful, and also allows an easy comparison in mixing quality between these new combined geometries, and the single helices.

Figure 4.11 shows the relative entropy increase, K, evaluated at six pitch lengths ($z = 36D$), plotted against the associated normalised pressure drop. It is assumed that the total pressure drop in the combined geometries is simply the sum of the pressure drop for each component helix. In reality, the transition between the two velocity fields will incur an additional pressure drop, but it is thought that this will not significantly affect the ranking of the geometries. The black lines on the plot represent the trend for the single helical geometries. The number is purely used as a convenient symbol, and does not imply a ranking of the results.

It is immediately clear that all the combined geometries tested, apart from one, achieve better mixing than the single geometries. This geometry is $R_A = 0.35D$ and $R_B = 0.3D$, which Table 4.1 shows as having a 6 degree angle between the in-plane vortices. It does however achieve mixing slightly better than either component geometry. The benefit of the combined helical geometries is most directly observed by comparing the single geometry $R = 0.25D$ (considered to be optimal in Chapter 3), and the combination $R_A = 0.3D$ & $0.2D$. These possess approximately equal pressure losses, however, the combined geometry generates a 60% improvement in K. The reason is clear from the Poincaré section, Figure 4.10(b), which possesses a relatively small island of regular flow, in the lower-left portion of the cross-section, a stark contrast to the two large islands that fill the cross-section for $R = 0.25D$.

The geometries possessing the best overall mixing are $R_A = 0.5D$ & $R_B = 0.2D$, and $R_A = 0.5D$ & $R_B = 0.25D$, having approximately the same value of K. However, the former geometry is more favourable for use as a prosthetic graft, due to its lower total pressure loss.

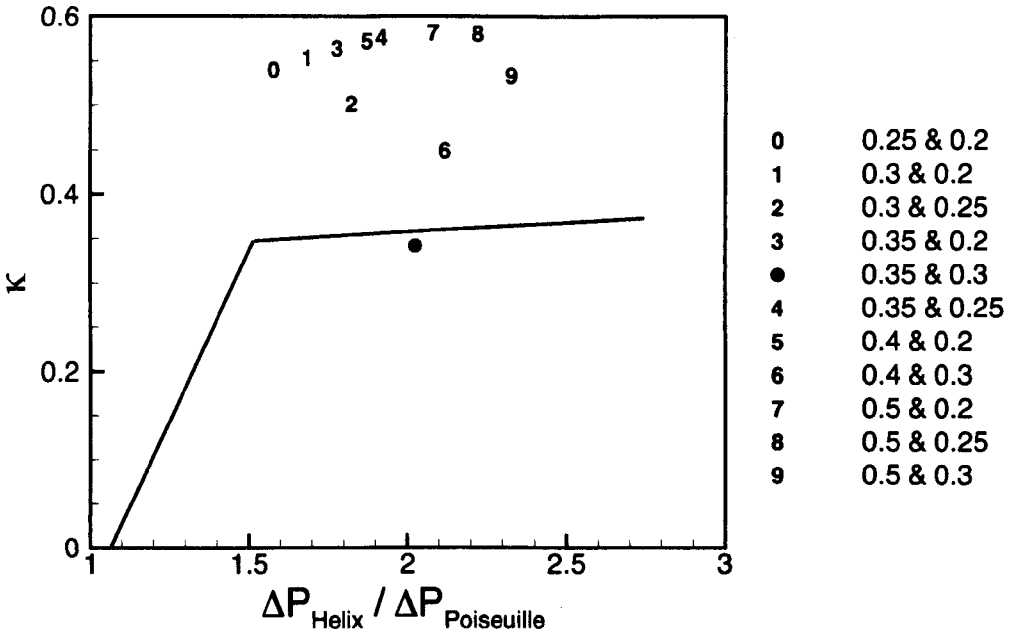


Figure 4.11: Relative entropy increase, K, plotted against normalised pressure drop for one pitch length of the geometry. The black line indicates the trend for the single helical geometries, and the black dot the only combined geometry that does not enhance mixing. All other combined geometries show a substantial increase in K.

The crossing angle of the vortex dividing lines was the key selection criteria for the geometries, and it is expected that increasing this angle, will cause a corresponding increase in mixing. Figure 4.12 shows the relative entropy increase, K, plotted against this angle. In the range 5 to 17 degrees, there is an approximately linear relation between the two quantities. For angles above 17 degrees, there appears to be two separate relationships, which are marked on the plot. This occurs due to the effect of a confounding factor, which is not included in this plot. At an angle of 17 degrees there are two different data points. The lower point corresponds to a geometry $R_A = 0.25D$ & $R_A = 0.2D$, with the upper point corresponding

to $R_A = 0.35D$ & $R_A = 0.25D$. The magnitude of $\mathbf{V}_{in-plane}$ for $R = 0.2D$ is smaller than that for both $R = 0.25D$ and $R = 0.35D$. Therefore, although the overall crossing angle is the same, the particles in the geometry $R_A = 0.35D$ will be advected further in each pitch length of the geometry, causing longer stretching of material lines, and generating better mixing of the initial distribution of particles. This weaker in-plane flow is only overcome when coupled with $R = 0.5D$, which has the strongest in-plane flow of all the geometries, and also generates the largest crossing angle.

The other factor which prevents a straightforward relation between K and crossing angle, is that the crossing angle is a bulk characteristic, that does not account for the change in distribution of vortical structures with R, and therefore, the angle of streamline crossing distributed throughout the cross-section, may be indicative of a greater crossing angle, than that given from the vortex dividing lines. For example, the Poincaré section for $R_A = 0.35D$ & $R_A = 0.25D$ shows a smaller island of regular flow in the lower-left part of the domain, than exists for $R_A = 0.25D$ & $R_A = 0.2D$, which can be attributed to greater local streamline crossing angles.

From the results for K, the geometries $R_A = 0.5D$ & $R_B = 0.2D$, and $R_A = 0.5D$ & $R_B = 0.25D$ generated the most mixing after 6 pitch lengths. However, based on a comparison of the residence time distributions, it is thought that $R_A = 0.5D$ & $R_B = 0.2D$ is the more effective mixing device, as the islands in the residence time distribution are smaller than for $R_B = 0.25D$.

4.3.4 Optimal mixing - finite time vs. infinite time

In his paper on the generation of chaotic advection by blinking vortex systems, Aref showed that as the blinking period T tends to infinity, the mixing is optimised (Aref 1984). For the case of combined helical pipes, this corresponds to two infinitely long sections of each geometry, which is somewhat unhelpful. In a practical mixing system we generally require that the mixing is optimal after a reasonable, finite-

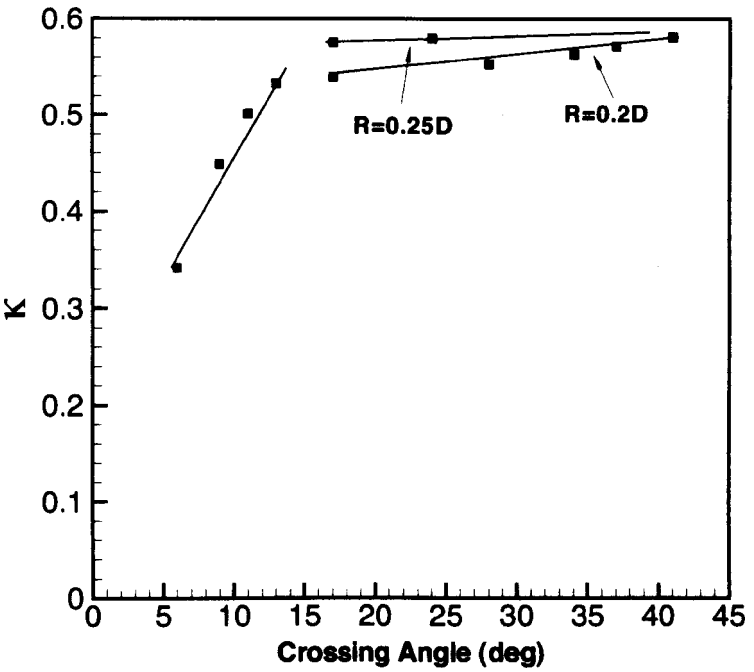


Figure 4.12: Relative entropy increase, K, plotted against angle between the vortical dividing lines of the combined geometries.

time or, equivalently, distance. In terms of analysing the mixing, this means that information entropy, or some other box-counting measure, may be more useful than a Poincaré section, the latter revealing nothing about the rate at which mixing occurs. The following points are intended to provoke discussion on possible future directions.

For the problem of optimising the mixing in a medical device this raises two related questions. Firstly, given a fixed distance how many sections of each geometry should there be? Secondly, should the two geometries have equal distributions of length?

The second question is perhaps more easily dealt with initially, by once again referring to the blinking vortex system. In that system the point vortices have equal strength (circulation) and blinking period. These two parameters are combined into a single non-dimensional parameter. If each vortex had a distinct circulation then the blinking periods of the vortices would be altered such that the relevant non-

dimensional parameter was equal for each vortex. The blinking period, is of course, conceptually the same as the pipe length. However, this is complicated by the presence of two vortices of differing strengths in each geometry, which then overlap with two other vortices. It is possible that an area-weighting approach may guide this optimisation.

With this ratio now set, it is less obvious how the geometries should be distributed. A discussion of possible solutions is only sensible within the context of a specific mixing target. A typical design criteria for an industrial mixer would be to maximise the mixed state of two substances at the end of the mixing device. For the medical application considered here, some limits on the quality of mixing through the device also seem to be necessary. A sensible starting point would be to set an upper bound on residence time, derived from biological data, and enforce conditions on residence time, such that the number of particles above this limit are minimised, with a corresponding upper bound on the standard deviation of the residence time. This means that alternating sections of different geometries, as examined here, may be preferable to having a geometry split into just two different sections (e.g. 3 pitch lengths of one helix, followed by 3 of a different helix), even if this second configuration may possibly exhibit better mixing at the end of the device.

4.4 Conclusions

The results presented in this Chapter provide a proof-of-concept of the combined helical geometry, as a means of achieving enhanced mixing. Significant increases to the relative entropy increase, K, are achieved for almost all of the geometries considered. Poincaré sections and residence time plots show that the large degree of streamline crossing, is very effective at reducing the size of, or destroying, islands of regular flow. It has been found that K correlates well with the crossing angle of the vortical structures, but can be affected by the relative strengths of these structures. The geometries $R_A = 0.5D$ & $R_B = 0.2D$, and $R_A = 0.5D$ & $R_B = 0.25D$ produce

the highest values of K, although the residence time distribution suggests that $R_A = 0.5D$ & $R_B = 0.2D$ is slightly more effective, and given its lower pressure loss, is likely to be the optimal design for use as a prosthetic graft. These two geometries will be examined more closely in Chapter 5 to confirm this result.

Chapter 5

Steady Flow in Multiple Helical Geometries

This Chapter discusses both the velocity field and mixing properties of flow in combined helical pipe geometries, which have periodic boundary conditions in the axial direction. The velocity field is examined in Section 5.2, in particular the persistence of the secondary flow structures, and their deviation from the periodic single geometry solution. The resultant mixing behaviour is examined in Section 5.3, and compared with the idealised predictions made in Chapter 4. Conclusions are presented in Section 5.4, along with recommendations for future designs of prosthetic grafts.

5.1 Introduction

5.1.1 Numerical implementation

As in Chapter 3 the combined helical geometry, shown in Figure 5.1, is defined using the coordinate transformation of the Navier-Stokes equations. However, at the junction between the two different helical geometries, there is a discontinuity

in the curves' gradients (and subsequent derivatives). Although this can be easily implemented within the solver, the discontinuity will be difficult for the Fourier modes to resolve, hindering the exponential convergence of the solution. Physically, such a discontinuity could also provoke undesirable flow separation at the joint, and it is unlikely that any manufactured geometry would contain such a discontinuity, particularly if constructed from ePTFE as commonly used in medical devices.

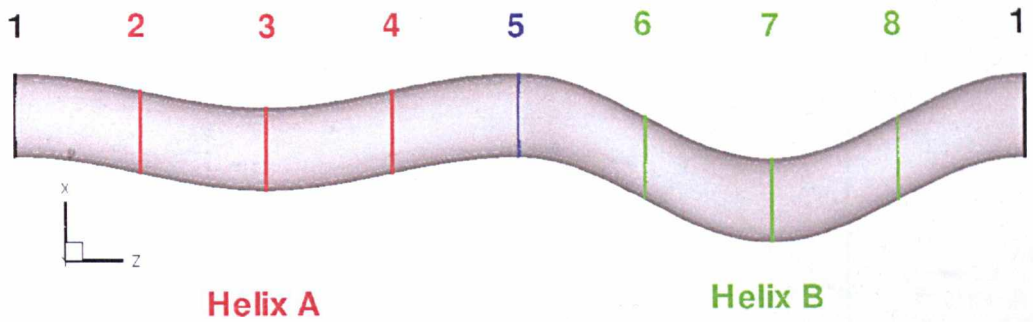


Figure 5.1: Locations of the slices of the velocity field, shown on geometry $R_A = 0.2D$ and $R_B = 0.5D$

To remove this discontinuity a spline is defined to span the transition region between the points $z/c = 7\pi/4$ and $z/c = 9\pi/4$, and pass through the known point at $z/c = 2\pi$. Equation (2.72) shows that the body force terms include derivatives of the mappings ξ_x and ξ_y upto the 3rd order. Therefore we require that at the endpoints of the spline, the 1^{st}, 2^{nd} and 3^{rd} derivatives of the spline match those of the helical functions. This enforces a requirement for a seventh-order spline function. A general spline function is used, which takes as arguments the radii of both geometries, the exact form of which is given in Appendix A. These spline function coordinate mappings are then used in exactly the same way as the helical functions. Figure 5.2 shows the comparison of the spline fits for both the sine and cosine functions, over the entire range for which the functions are valid. It is clear that the cosine functions are approximated very well indeed by the spline, being almost indistinguishable from the helical function, however, there is some discrepancy with the sine functions. The cosine is approximated more accurately

because there is no discontinuity in gradient at $z = 6$, whereas there is for the sine functions. The gradient of the sine spline-fit at $z = 6$ is the mean of the gradients of the component sine functions, and given the constraints on smoothness, causes the undershoot that is clearly visible in Figure 5.2.

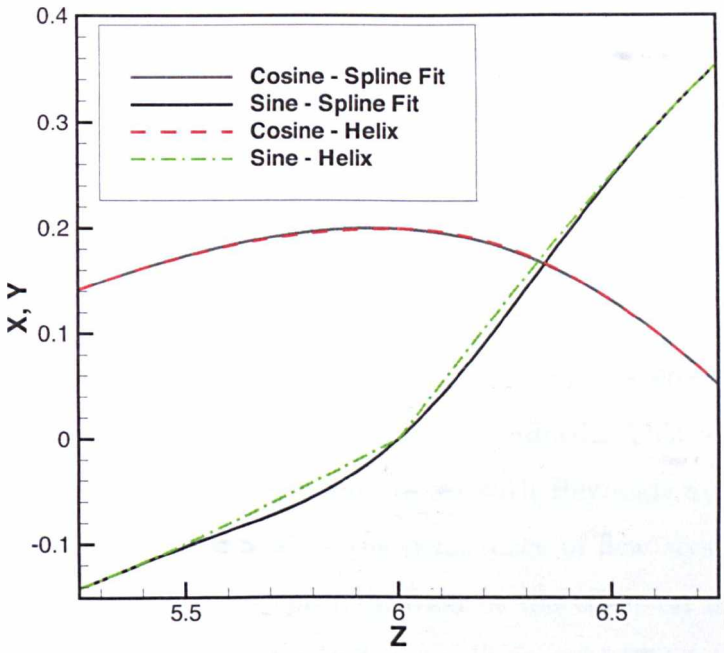


Figure 5.2: Spline fit in the region of the joint, showing that the approximation to the sinusoidal functions is good, yet attaining a smooth transition at the joint

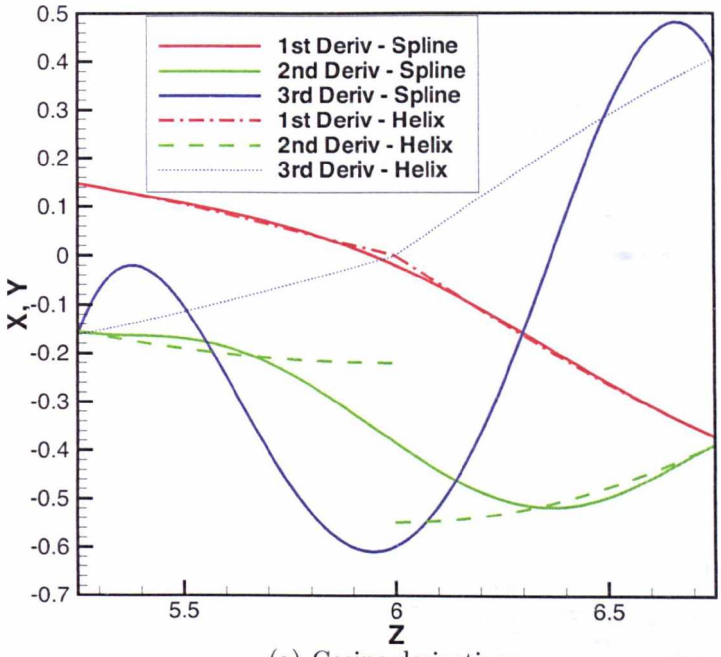
The spline functions clearly match the helical curves very well, however, it is their derivatives that affect the body force term **A**, and therefore it is useful to examine these more closely to ensure that they match the derivatives of the helical functions. Figures 5.3(a) & 5.3(b) show this comparison in the region $z = 5.25D$ to $z = 6.75D$. By far the most important derivative is the first derivative, since this appears in 27 of the 39 total terms in body force term **A**, and often powers of the derivative exist. By contrast, the 2^{nd} derivatives appear in 14 of the 39 terms, and the 3^{rd} derivative in only 2 terms. For both the cosine and sine functions, the 1^{st} derivative is captured very well, and varies smoothly from one geometry to the next, particularly for the

cosine. For the cosine function, the 2^{nd} derivatives are no longer continuous at the junction, therefore causing the same type of transition that exists for the 1^{st} derivative of the sine function. However, for both sine and cosine the magnitudes of the 2^{nd} derivatives match those of the component helices reasonably closely. It is only the 3^{rd} derivatives that vary strongly from those of the helical functions. However, since these terms are relatively unimportant to the body forcing, it is likely that they will not complicate the results. In any case, all of these terms merely reflect the reality of any device that is constructed using this geometric definition.

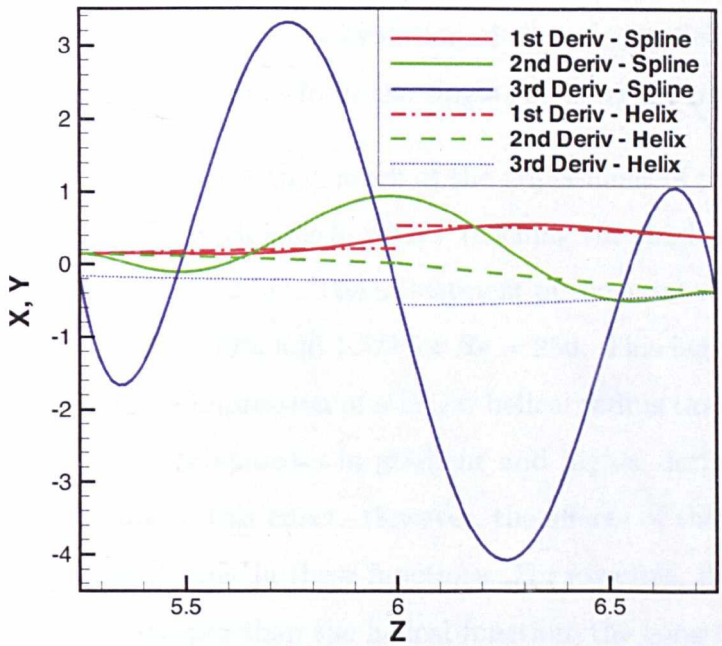
5.2 Velocity field

A Reynolds number of 250 is once again used, in accordance with the work on single helical geometries, but other values are also examined. This is to provide some insight into how the flow re-adjustment varies with Reynolds number, which may be of some benefit for understanding the persistence of flow structures in arteries. Furthermore, it also provides some indication of the effect on mixing in a single helical geometry under a quasi-steady flow condition, which is an approximation to unsteady physiological flow. The pitch is fixed at six pipe diameters ($6D$) for both geometries, again as in the previous computations, which obviously implies that the total length of the geometry is $12D$. The helical radius of the first geometry is again designated R_A, and that of the second, R_B. Results are presented for the case $R_A = 0.2D$ and and $R_B = 0.5D$, for Re of 125 and 250. Slices of the velocity field are taken at intervals of $z/c = \pi/2$, as shown in Figure 5.1.

Figures 5.4, 5.5, 5.7 and 5.8 show the axial velocity and vorticity results for the geometry, $R_A = 0.2$ and $R_B = 0.5$. For comparison purposes, the corresponding axial velocity and vorticity contour plots for the single helix geometries are shown at the top of each figure. For both Reynolds numbers investigated, it is clear that the axial velocity profile throughout helix A is very different to that for $R = 0.2$, and is typical of that in a larger helical radius. In helix B the velocity profile is again



(a) Cosine derivatives



(b) Sine derivatives

Figure 5.3: Comparison of the derivatives of the spline functions and the helical functions in the region of the junction.

different from $R = 0.5$. Examining each slice in sequence shows that Slice 1, (Figs. 5.4(c) & 5.7(c)), which is the outlet of geometry B & the inlet to geometry A, has a velocity profile similar to the single geometry solution, particularly for $Re = 125$. Slices 2-4 (Figs. 5.4(d)-5.4(f) & 5.7(d)-5.7(f)) show that the peak value of the axial velocity moves away from the wall, until slice 5 (Figs. 5.4(g) & 5.7(g)), which is the outlet of geometry A. The velocity profile at this point, whilst somewhat different to that in geometry B, has still not returned to the single pipe profile in Figure 5.7(a). Slices 6-8 (Figs. 5.4(h)-5.4(j) & 5.7(h)-5.7(j)) show the reverse process occurring in helix B, as the flow gradually establishes itself in response to the larger helical radius.

The results presented in Chapter 3 show that the emergence of a second vortex in $\mathbf{V}_{in-plane}$ was directly linked to an increase in the radial offset of peak axial velocity, and increased circulation of the secondary flow, Γ. In order to explain the likely impact on particle mixing, the evolution of these two quantities with axial position is shown in Figures 5.10(a) - 5.11(b). This information also allows more precise statements to be made regarding the evolution of the velocity field. Included in the figures are the appropriate values from the single geometry solutions.

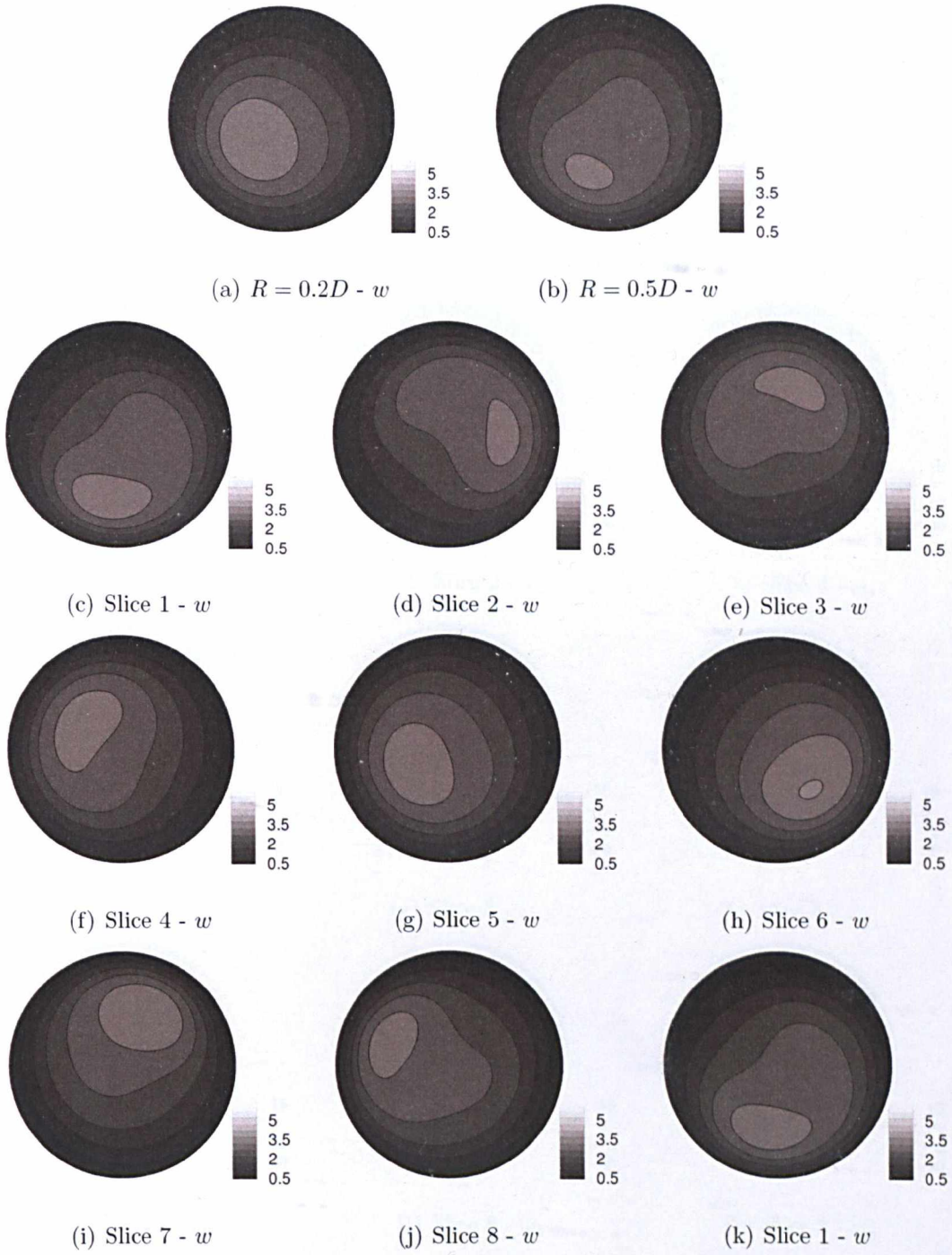
Figures 5.11(a) & 5.11(b) show that much of the adjustment of the vortex strength occurs over a quarter of a pitch length, with Γ reaching the single geometry solution after approximately $1.75D - 2.5D$. The adjustment of the axial velocity lags that of the vortex, by $1D$ for $Re = 125$, and $1.5D$ for $Re = 250$. This lag contributes to the overshoot of Γ, giving the impression of a larger helical radius than is actually used. It is possible that the discrepancies in gradient and higher derivatives of the sine function also contribute to this effect. However, the effects of this are mitigated by the symmetry that must exist in these functions. For example, if part of the spline has a gradient that is steeper than the helical function, the constraint of fitting the end points implies that elsewhere the gradient must be shallower. Therefore, any additional forcing that occurs in one part of the spline, will be offset by weaker forcing elsewhere. Furthermore, this effect only applies to the sine function, since the spline matches the cosine almost perfectly.

Blyth *et al.* (Blyth, Mestel, & Zabielski 2002) suggest that inviscid flow readjustment occurs over a distance of one pipe diameter, but that the presence of core vorticity slows flow development. In the preliminary results of Caro *et al.* (Caro, Cheshire, & Watkins 2005) it is found that helical flow develops from a parabolic inflow condition over approximately two pitch lengths, although they do not provide any detailed quantification of this observation. For the case of a helical pipe, with an inflow condition of a weaker helical flow, it would be expected that the transition distance will lie somewhere between these two limits. Indeed, the transition occurs after a full pitch length of each helix, without quite reaching the solutions found in the single geometry results. However, the trends for Γ at $z = 6$ & 12, suggest that the flow is beginning to asymptote toward the corresponding single geometry solution, and would attain this state in a further three diameters or half a pitch length.

It has been established that the values of radial offset of axial velocity and Γ for the single geometries, in Figures 5.10(b) & 5.11(b), correspond to the particle trajectories and velocity, $\mathbf{V}_{in-plane}$, shown in Figures 5.12(a) & 5.13(b). This means that the second, upper vortex in $\mathbf{V}_{in-plane}$ will never become as small or weak as it would for $R = 0.2D$, but due to the larger offset and larger Γ that are reached, this vortex will become larger and stronger than for $R = 0.5$. Therefore, the idealised prediction of the mixing will not capture this aspect, and neither does it account for the transition between the two velocity fields occurring over the entire geometry, rather than discontinuously. However, the change in $\mathbf{V}_{in-plane}$ with axial position in the combined geometry will still produce an improvement in mixing, compared with using a single helical geometry for the equivalent two pitch lengths.

5.2.1 Pressure loss

Although the combined geometry may provide enhanced mixing, in the context of medical applications, it is desirable that any additional pressure loss is not excessive. Table 5.1 shows the pressure drop that would occur in the component geometries,



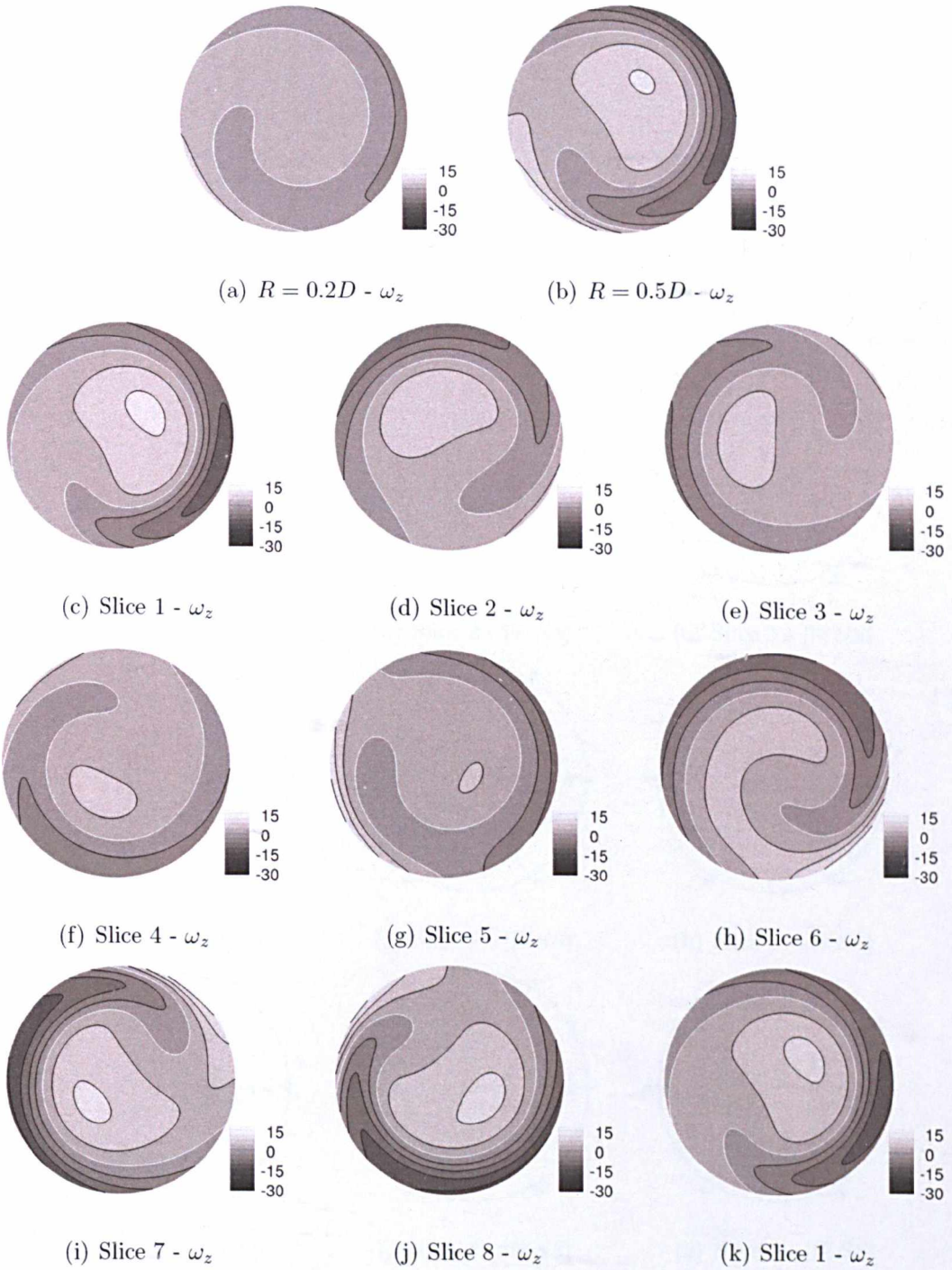
(a) $R = 0.2D$ - w (b) $R = 0.5D$ - w

(c) Slice 1 - w (d) Slice 2 - w (e) Slice 3 - w

(f) Slice 4 - w (g) Slice 5 - w (h) Slice 6 - w

(i) Slice 7 - w (j) Slice 8 - w (k) Slice 1 - w

Figure 5.4: Axial velocity (cm/s) contours for case $R_A = 0.2D$ and $R_B = 0.5D$, $Re = 125$.



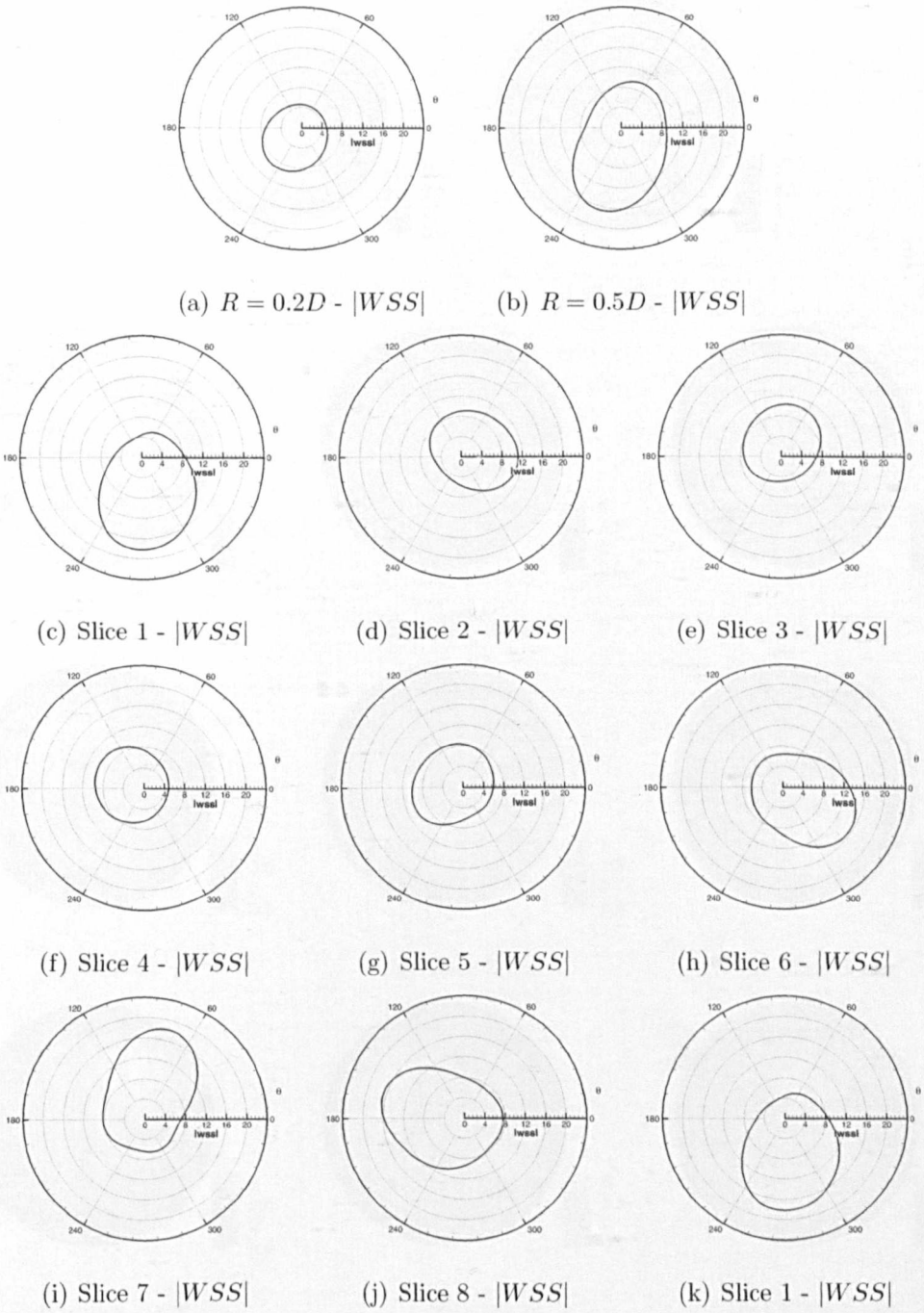
(a) $R = 0.2D$ - ω_z (b) $R = 0.5D$ - ω_z

(c) Slice 1 - ω_z (d) Slice 2 - ω_z (e) Slice 3 - ω_z

(f) Slice 4 - ω_z (g) Slice 5 - ω_z (h) Slice 6 - ω_z

(i) Slice 7 - ω_z (j) Slice 8 - ω_z (k) Slice 1 - ω_z

Figure 5.5: Vorticity (s^{-1}) contours for case $R_A = 0.2D$ and $R_B = 0.5D$, $Re = 125$. The zero vorticity contour line is coloured white to highlight the vortical structure



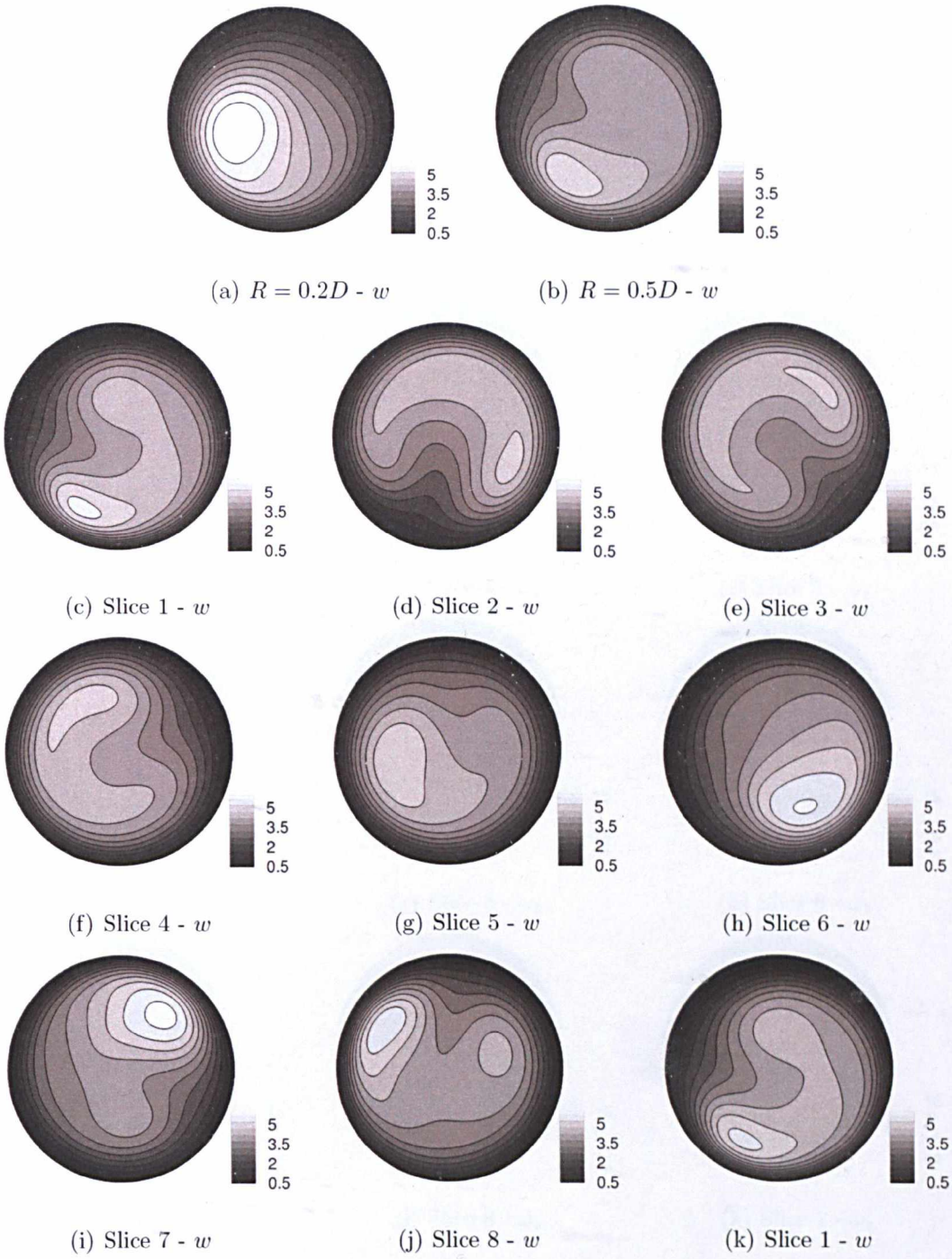
(a) $R = 0.2D$ - $|WSS|$ (b) $R = 0.5D$ - $|WSS|$

(c) Slice 1 - $|WSS|$ (d) Slice 2 - $|WSS|$ (e) Slice 3 - $|WSS|$

(f) Slice 4 - $|WSS|$ (g) Slice 5 - $|WSS|$ (h) Slice 6 - $|WSS|$

(i) Slice 7 - $|WSS|$ (j) Slice 8 - $|WSS|$ (k) Slice 1 - $|WSS|$

Figure 5.6: Wall shear stress (N/cm^2) magnitude for case $R_A = 0.2D$ and $R_B = 0.5D$, $Re = 125$



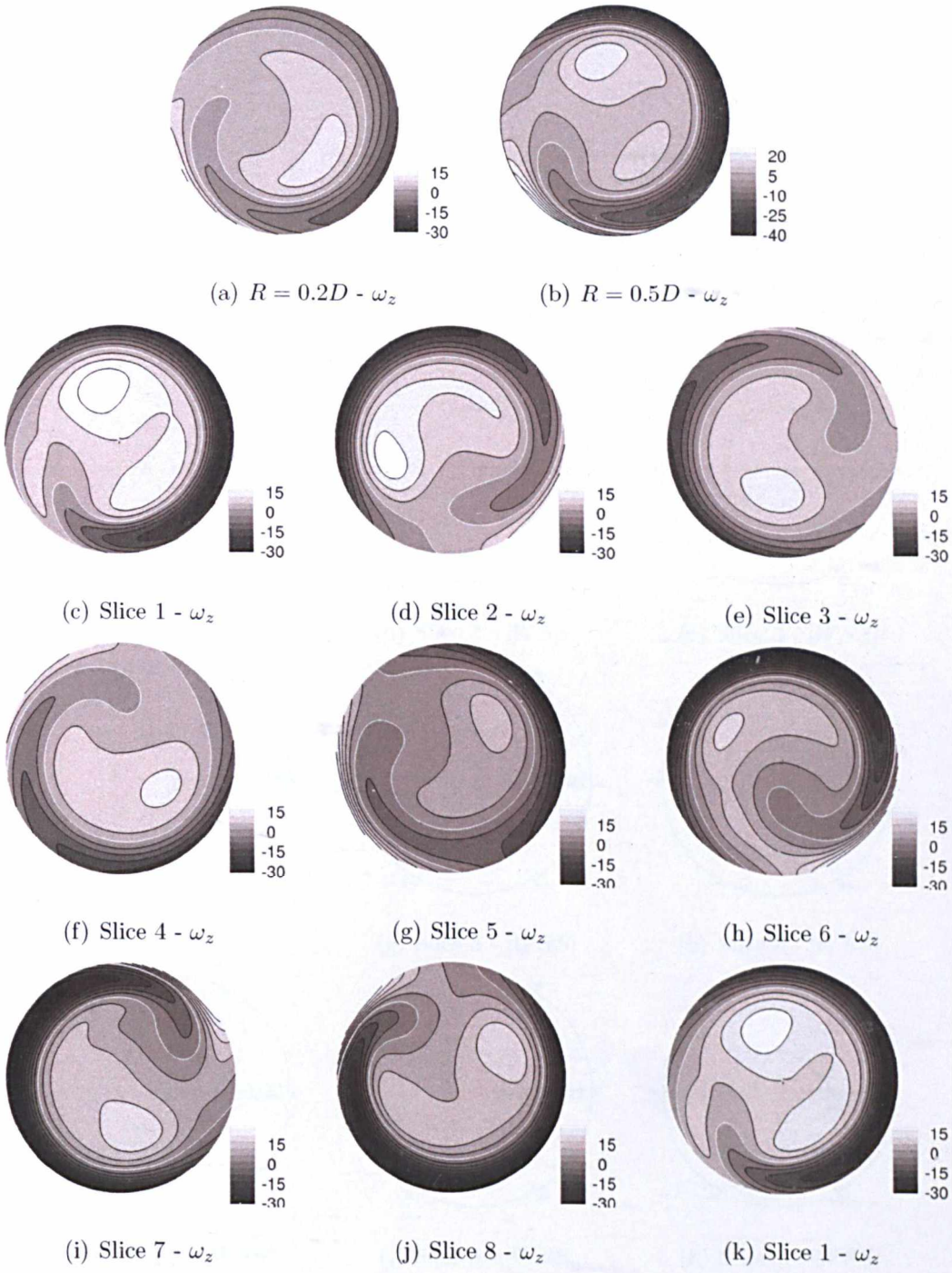
(a) $R = 0.2D$ - w (b) $R = 0.5D$ - w

(c) Slice 1 - w (d) Slice 2 - w (e) Slice 3 - w

(f) Slice 4 - w (g) Slice 5 - w (h) Slice 6 - w

(i) Slice 7 - w (j) Slice 8 - w (k) Slice 1 - w

Figure 5.7: Axial velocity (cm/s) contours for case $R_A = 0.2D$ and $R_B = 0.5D$, $Re = 250$.



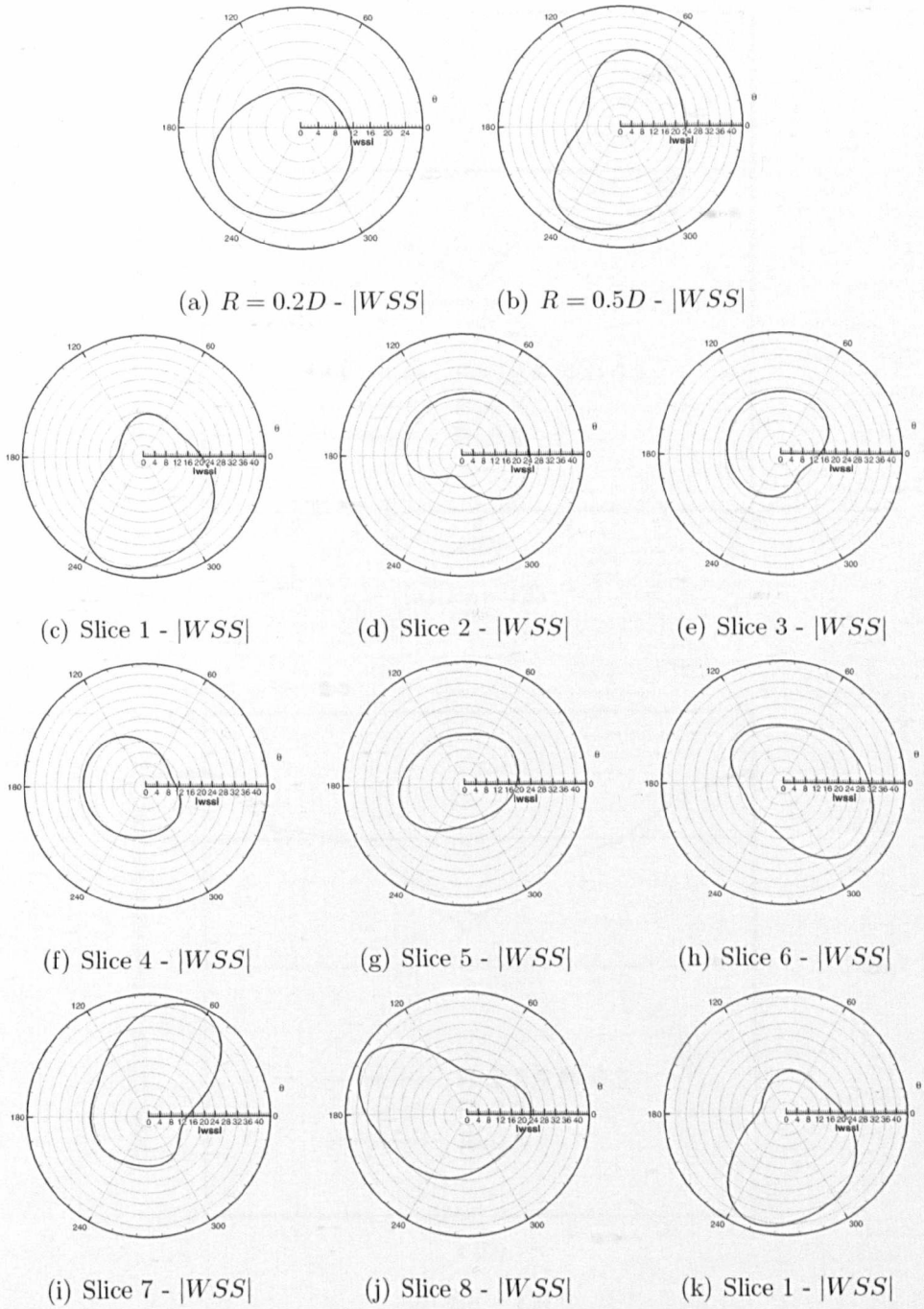
(a) $R = 0.2D$ - ω_z (b) $R = 0.5D$ - ω_z

(c) Slice 1 - ω_z (d) Slice 2 - ω_z (e) Slice 3 - ω_z

(f) Slice 4 - ω_z (g) Slice 5 - ω_z (h) Slice 6 - ω_z

(i) Slice 7 - ω_z (j) Slice 8 - ω_z (k) Slice 1 - ω_z

Figure 5.8: Axial vorticity (s^{-1}) contours for case $R_A = 0.2D$ and $R_B = 0.5D$, $Re = 250$. The zero vorticity contour line is coloured white to highlight the vortical structure



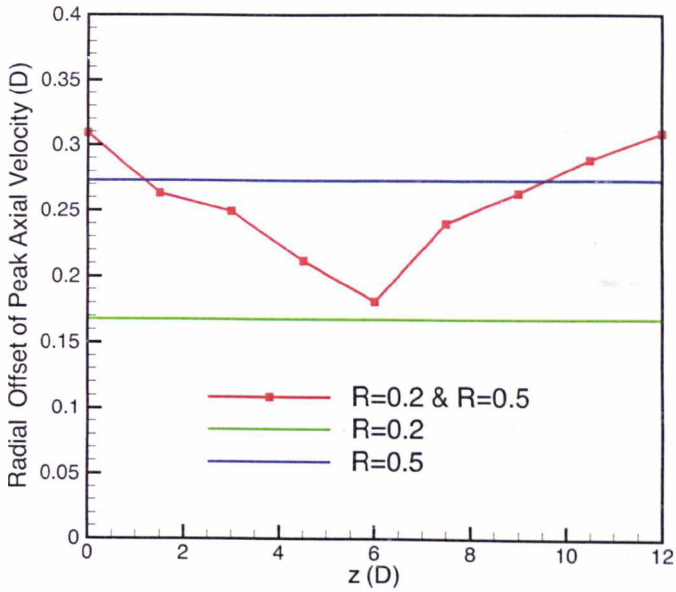
(a) $R = 0.2D$ - $|WSS|$ (b) $R = 0.5D$ - $|WSS|$

(c) Slice 1 - $|WSS|$ (d) Slice 2 - $|WSS|$ (e) Slice 3 - $|WSS|$

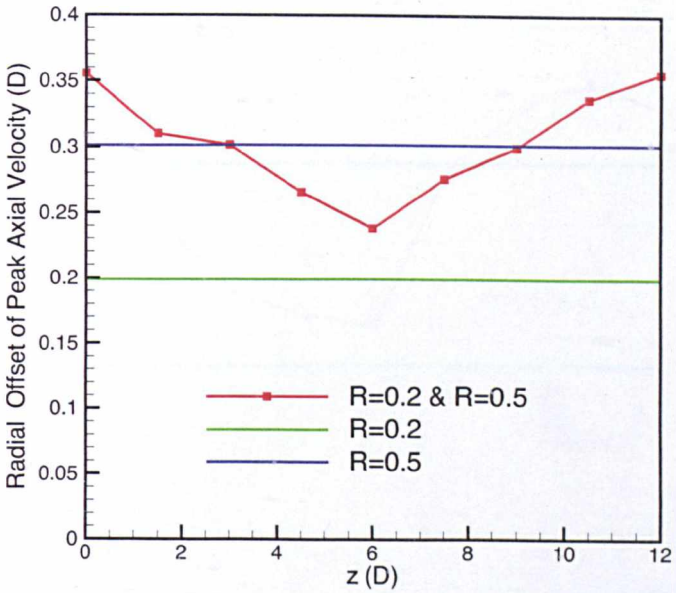
(f) Slice 4 - $|WSS|$ (g) Slice 5 - $|WSS|$ (h) Slice 6 - $|WSS|$

(i) Slice 7 - $|WSS|$ (j) Slice 8 - $|WSS|$ (k) Slice 1 - $|WSS|$

Figure 5.9: Wall shear stress (N/cm^2) magnitude for case $R_A = 0.2D$ and $R_B = 0.5D$, $Re = 250$

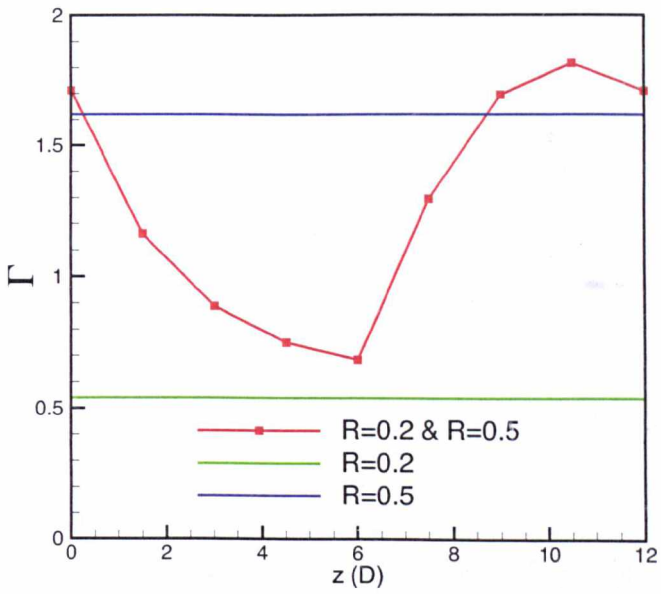


(a) $Re = 125$

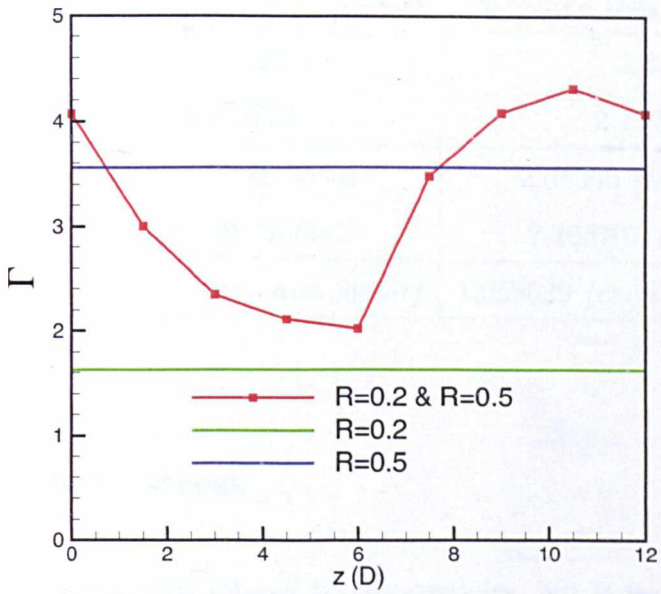


(b) $Re = 250$

Figure 5.10: Radial offset of the peak axial velocity for flow in the combined geometry of $R_A = 0.2D$ and $R_B = 0.5D$, showing the comparison with the respective single geometry results, for $Re = 125$ and $Re = 250$



(a) $Re = 125$



(b) $Re = 250$

Figure 5.11: Circulation (cm^2/s) of dominant vortical structure for flow in the combined geometry of $R_A = 0.2D$ and $R_B = 0.5D$, showing the comparison with the respective single geometry results, for $Re = 125$ and $Re = 250$

and the idealised prediction calculated from the mean of these two values. This can then be compared with the pressure drop that was found from the numerical simulation in the combined geometry. For both Reynolds numbers, the pressure loss increases by approximately 5% from the idealised value. In Chapter 3 the optimal geometry was found to be approximately $R = 0.25D - 0.3D$, which incurred pressure losses of 1.72 and 1.93 respectively. The combined geometry therefore has a $20-30\%$ increase in pressure loss compared with the single geometries with $R = 0.25D - 0.3D$. However, this is a lower pressure loss than the single helical geometries for $R \geq 0.4D$.

Table 5.1: Pressure loss for combined helical geometries, showing the pressure loss for each component geometry, the idealised prediction (simply the mean of the components) and the actual pressure loss incurred. The values of the pressure loss have been normalised by that for Poiseuille flow at the same Reynolds number. The final row shows the correction factor to be applied to the idealised prediction of pressure loss.

R_A	R_B	**Pressure loss - Re = 125**	**Pressure loss - Re = 250**
0.2	-	1.207283	1.44
0.5	-	2.198754	2.72701
0.2	0.5	1.703019 *(idealised)*	2.08355 *(idealised)*
0.2	0.5	1.796559 *(actual)*	2.205707 *(actual)*
0.2	0.5	1.054926 *(correction factor)*	1.058629 *(correction factor)*

5.2.2 Wall shear stress

Wall shear stress is of course related to the vorticity, but it is useful to determine the extent to which the transition between two different helical geometries alters the wall shear stress near the joint. Without the spline-fitted smoothing of the junction, a discontinuity, or at the very least, steep gradients of WSS might exist, which are biologically unfavourable. In common with the other features of the flow, the wall shear stress distributions never reach those from the single geometry solutions.

The notch of minimum wall shear stress appears when there is a significant second vortex in the in-plane velocity field, and the maximum where the peak axial velocity is located. The only deviation from this general trend appears to occur in slices 5 and 6, where the notch is very small. Also, the minima notches are much smaller, and less sharply defined for $Re = 125$, than for $Re = 250$.

5.3 Mixing performance

The data presented in Section 5.2 shows a significant change in the velocity field with axial position, suggesting that the mixing behaviour may similarly vary from the idealised prediction made in Chapter 4. Therefore, to test the quality of those predictions, and help to identify the best performing designs, the actual mixing properties of the two most promising geometries will now be determined. The geometries considered are therefore $R_A = 0.2D$ & $R_B = 0.5D$ and $R_A = 0.25D$ & $R_B = 0.5D$.

5.3.1 Particle trajectories

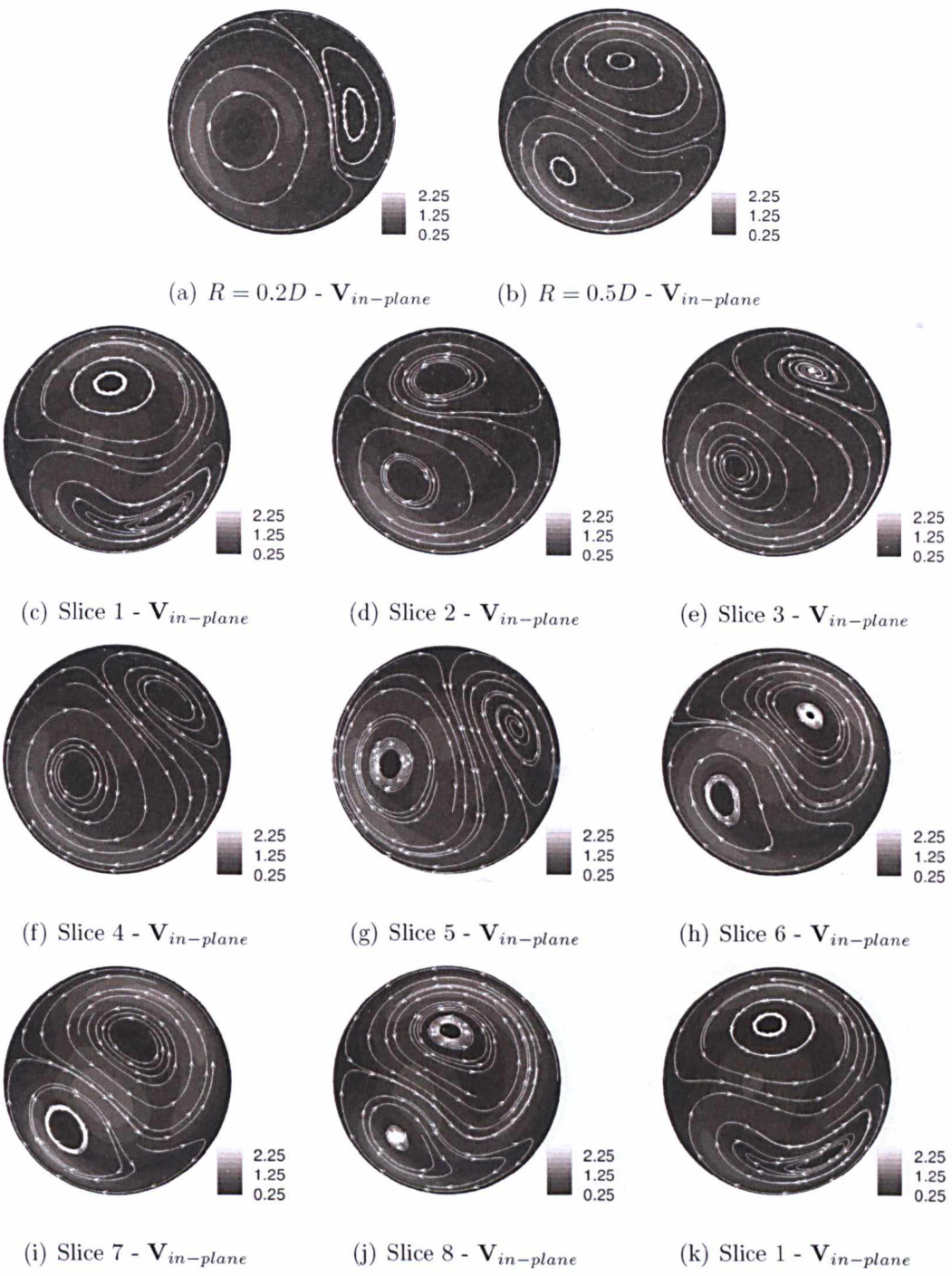
Figures 5.12 & 5.13 show the streamtraces of $\mathbf{V}_{in-plane}$, obtained using the same principles as described in Chapter 3. Due to the co-ordinate transformation involved, the angular rotation at each slice location has been removed, and therefore these plots should be interpreted as though lying within a cylinder. For both geometries, as expected from the velocity field data, $\mathbf{V}_{in-plane}$ found in the single geometries is not observed in the combined geometry. However, there is still a large degree of change in the streamtraces with axial distance, though without the discontinuous change that was assumed in the idealised model of Chapter 4.

The plots of radial offset of axial velocity and Γ help to explain the structure of $\mathbf{V}_{in-plane}$ and show clearly why the single geometry solution is never attained. A crucial difference between $\mathbf{V}_{in-plane}$ in the single and combined geometries, is that

the streamtraces no longer form closed loops that signify two distinct regions of the flow. Instead, a sink and source now exists, with the streamtraces from the source feeding into the sink. This means that the dividing line between the vortices, is no longer a single line, but a region over which the transfer of fluid particles occurs. This is necessary since the relative sizes of the structures vary with axial position, and must allow for the transport of particles from one region to the other.

Figures 5.12 & 5.13 show that $\mathbf{V}_{in-plane}$ is actually very similar for both geometries, over the whole length of the geometry. In particular slices 1, 2, 6, 7 & 8 are very similar both in structure, and velocity magnitude. There is a greater difference evident for slices 3, 4, & 5, with the vortex dividing line closer to the vertical, and the upper-vortex smaller, for the geometry $R_A = 0.2D$ and $R_B = 0.5D$. This is expected from the respective single helical solutions, however, the difference is not as great as for those velocity fields. From the slices of $\mathbf{V}_{in-plane}$ it is expected that the resultant mixing behaviour will be very similar, but with slightly more mixing for $R_A = 0.2D$.

Figure 5.14 shows slices of the particle trajectories in the range $z = 0$ to $z = 12D$, that is, one iteration of the combined geometry $R_A = 0.2D$ and $R_B = 0.5D$. Some comparison can be made between these slices, and the streamtrace slices shown in Figure 5.12, with the general structures obvious. However, since $\mathbf{V}_{in-plane}$ is varying continually throughout the geometry, it is not possible to make the same direct comparison between the streamtraces and particle slices at a given locations, which could be made in Chapter 3 when $\mathbf{V}_{in-plane}$ collapsed onto a plane.



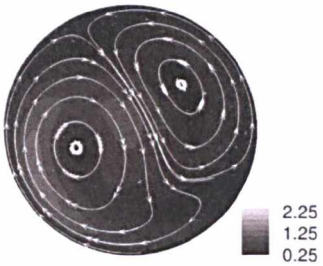
(a) $R = 0.2D$ - $\mathbf{V}_{in-plane}$ (b) $R = 0.5D$ - $\mathbf{V}_{in-plane}$

(c) Slice 1 - $\mathbf{V}_{in-plane}$ (d) Slice 2 - $\mathbf{V}_{in-plane}$ (e) Slice 3 - $\mathbf{V}_{in-plane}$

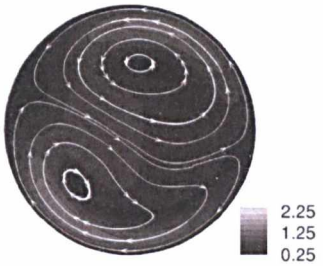
(f) Slice 4 - $\mathbf{V}_{in-plane}$ (g) Slice 5 - $\mathbf{V}_{in-plane}$ (h) Slice 6 - $\mathbf{V}_{in-plane}$

(i) Slice 7 - $\mathbf{V}_{in-plane}$ (j) Slice 8 - $\mathbf{V}_{in-plane}$ (k) Slice 1 - $\mathbf{V}_{in-plane}$

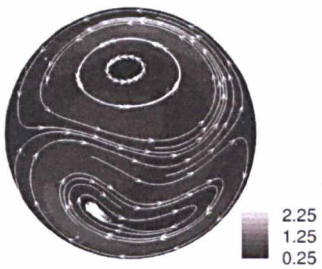
Figure 5.12: Streamtraces of $\mathbf{V}_{in-plane}$ (cm/s) for $R_A = 0.2D$ and $R_B = 0.5D$, $Re = 250$



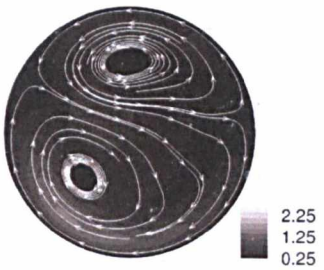
(a) $R = 0.25D$ - $\mathbf{V}_{in-plane}$



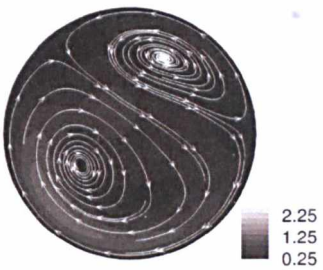
(b) $R = 0.5D$ - $\mathbf{V}_{in-plane}$



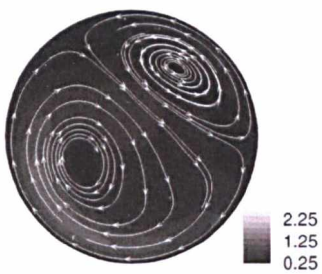
(c) Slice 1 - $\mathbf{V}_{in-plane}$



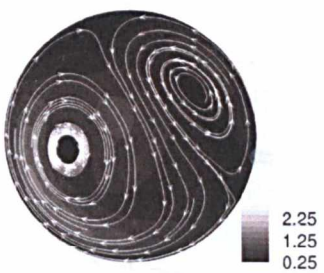
(d) Slice 2 - $\mathbf{V}_{in-plane}$



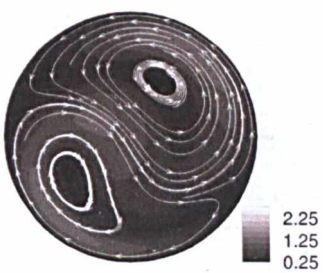
(e) Slice 3 - $\mathbf{V}_{in-plane}$



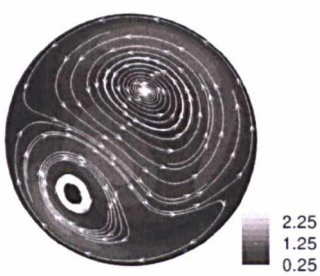
(f) Slice 4 - $\mathbf{V}_{in-plane}$



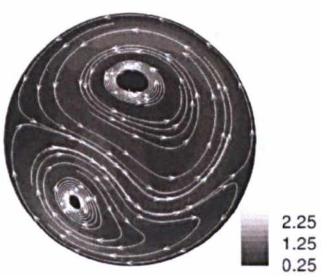
(g) Slice 5 - $\mathbf{V}_{in-plane}$



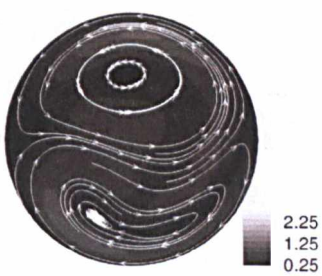
(h) Slice 6 - $\mathbf{V}_{in-plane}$



(i) Slice 7 - $\mathbf{V}_{in-plane}$

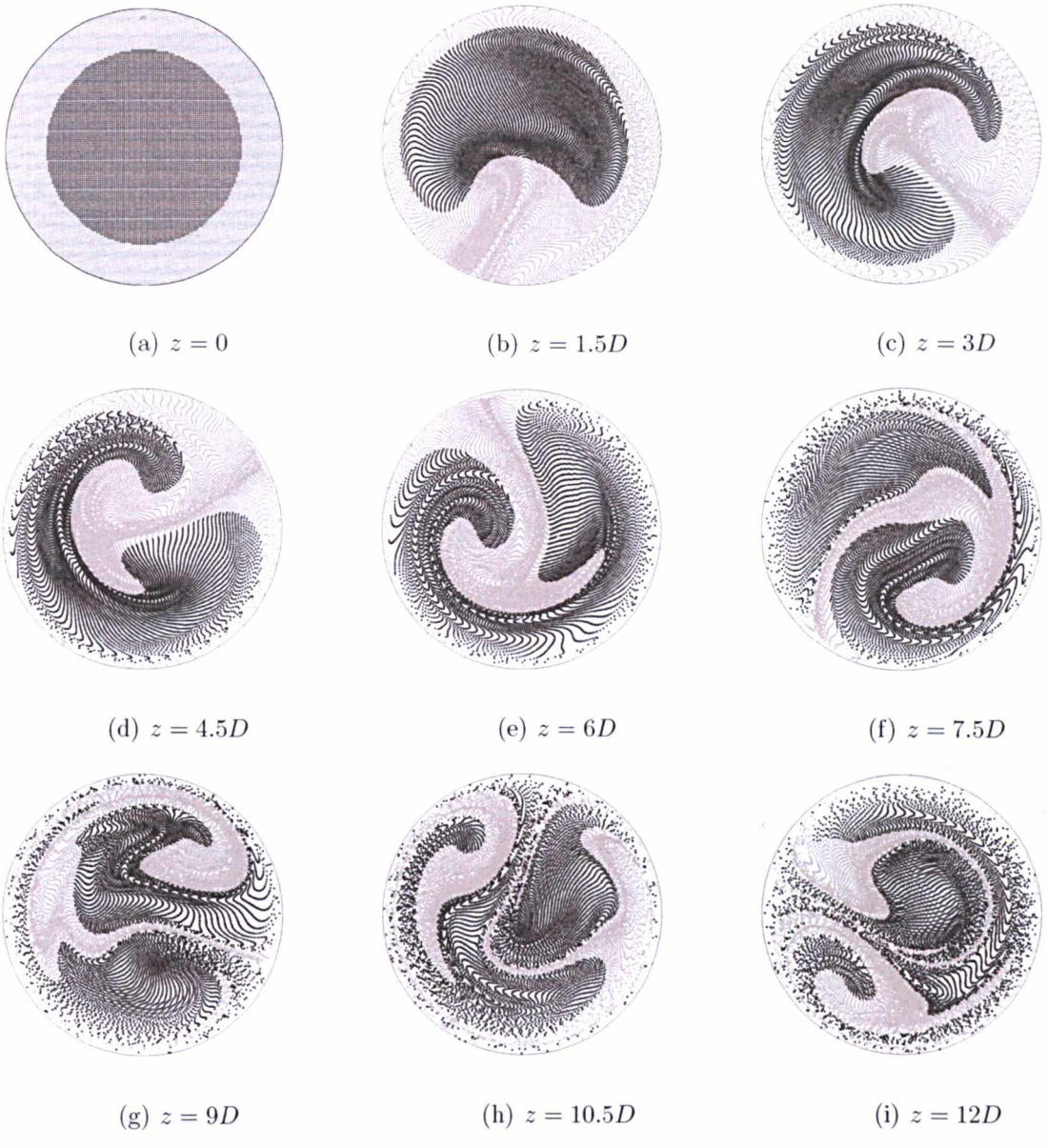


(j) Slice 8 - $\mathbf{V}_{in-plane}$



(k) Slice 1 - $\mathbf{V}_{in-plane}$

Figure 5.13: Streamtraces of $\mathbf{V}_{in-plane}$ (cm/s) for $R_A = 0.25D$ and $R_B = 0.5D$, $Re = 250$

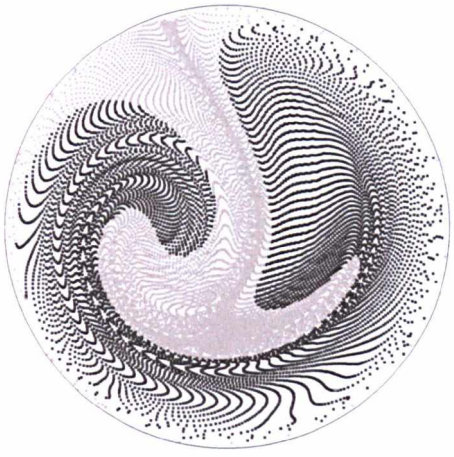


(a) $z = 0$ (b) $z = 1.5D$ (c) $z = 3D$

(d) $z = 4.5D$ (e) $z = 6D$ (f) $z = 7.5D$

(g) $z = 9D$ (h) $z = 10.5D$ (i) $z = 12D$

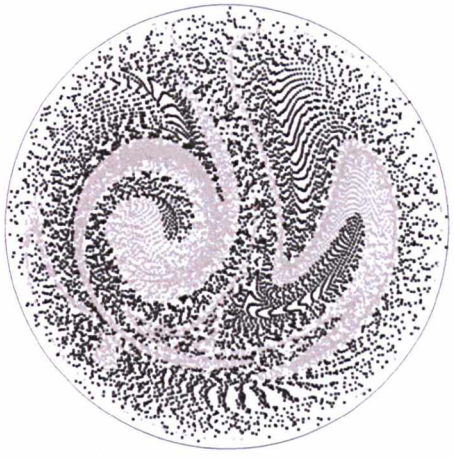
Figure 5.14: Particle trajectory slices, for $R_A = 0.2$ and $R_B = 0.5$ at intervals of $z = 1.5D$



(a) 1 Pitch Length



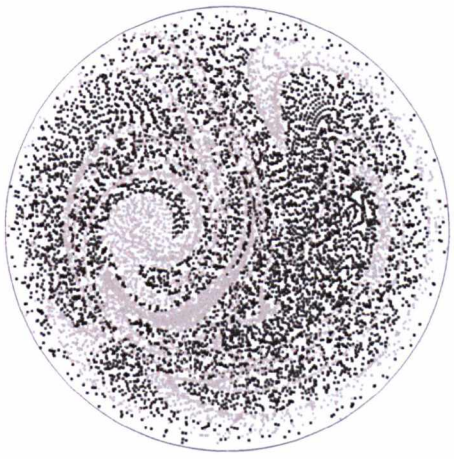
(b) 2 Pitch Lengths



(c) 3 Pitch Lengths



(d) 4 Pitch Lengths

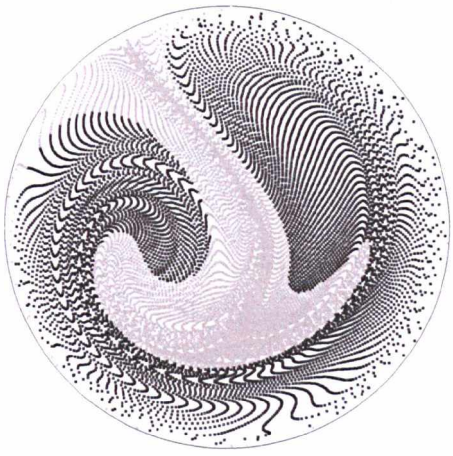


(e) 5 Pitch Lengths



(f) 6 Pitch Lengths

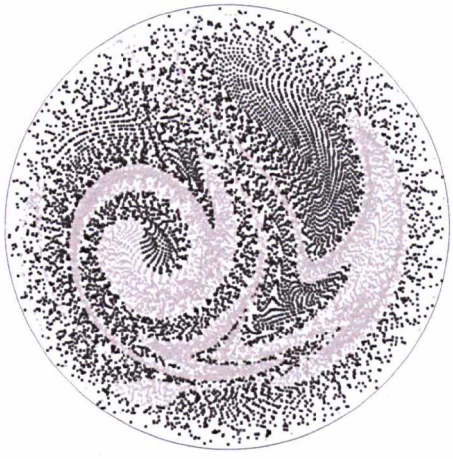
Figure 5.15: Particle trajectory slices, $R_A = 0.2$ and $R_B = 0.5$



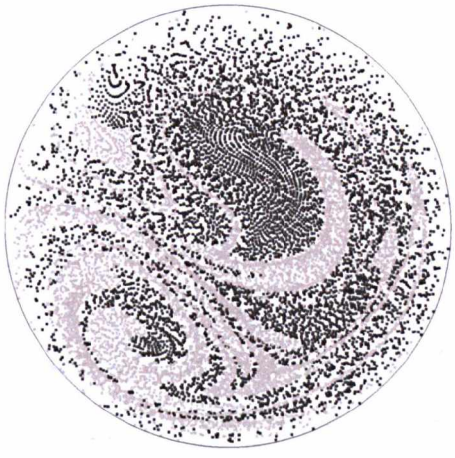
(a) 1 Pitch Length



(b) 2 Pitch Lengths



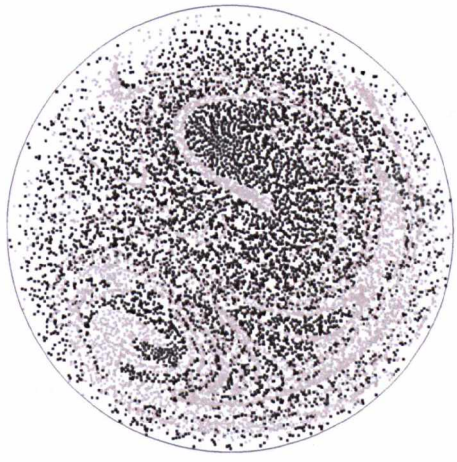
(c) 3 Pitch Lengths



(d) 4 Pitch Lengths



(e) 5 Pitch Lengths



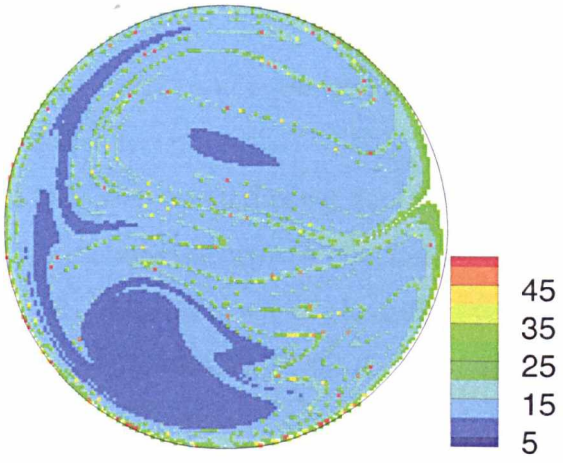
(f) 6 Pitch Lengths

Figure 5.16: Particle trajectory slices, $R_A = 0.25$ and $R_B = 0.5$

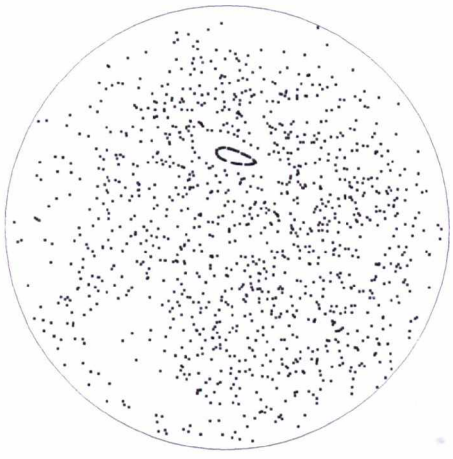
5.3.2 Residence time distribution and Poincaré sections

Figure 5.17 shows the coloured residence time scatter plots, and corresponding Poincaré sections for both geometries. The residence time distributions are very similar, however, the regions of very low residence time are smaller for $R_A = 0.2D$. The key difference is the destruction of the small region of low residence time in the upper half of the domain.

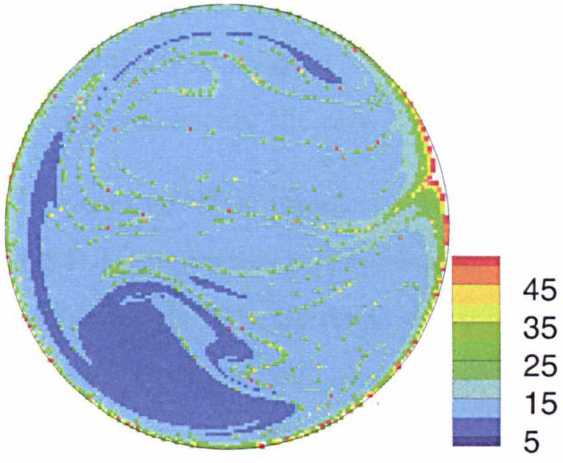
The Poincaré sections confirm these conclusions. For both cases the particle trajectories appear to be chaotic for much of the domain, however, for $R_A = 0.25D$, there is a clear island of no-mixing present, which corresponds to the small region of low residence time. This island does not exist for the same geometry with $R_A = 0.2D$, and this change contributes to the improved mixing of this geometry. This is due to the smaller upper vortex in the flow of $R_A = 0.2D$, visible in slices 3, 4, & 5, creating more streamline crossing behaviour. It is interesting to note that the Poincaré sections shown here have far fewer obvious islands of mixing (and any that do exist are rather small), than those presented for the twisted pipe layout (Jones, Thomas, & Aref 1989). It is thought that is due to the lack of symmetry possessed by the flow, and the continuously varying, rather than discontinuously, in-plane flow.



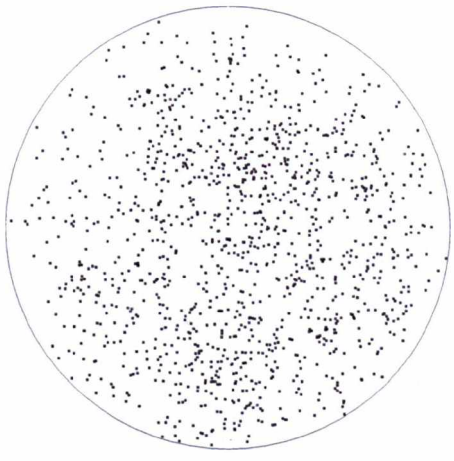
(a) $R_A = 0.25$ & $R = 0.5$



(b) $R_A = 0.25$ & $R = 0.5$



(c) $R_A = 0.2$ & $R = 0.5$



(d) $R_A = 0.2$ & $R = 0.5$

Figure 5.17: Residence time colour scatter plot (left) and Poincaré sections (right).

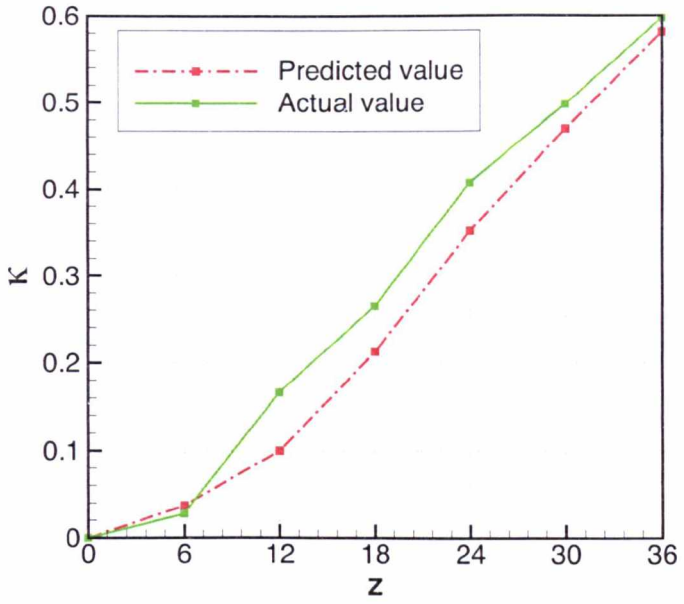
5.3.3 Entropic measure

Figure 5.18 shows the evolution of relative entropy increase, K, with axial distance for both geometries, for both the idealised model presented in Chapter 4 and using the velocity field discussed in this chapter. From the examination of $\mathbf{V}_{in-plane}$ and the particle trajectory slices of Figures 5.16 &5.16 it is expected that the values of K will be similar for both geometries, but slightly larger for $R_A = 0.2D$. Indeed, this is the case, with the presence of the small region of no-mixing, likely accounting

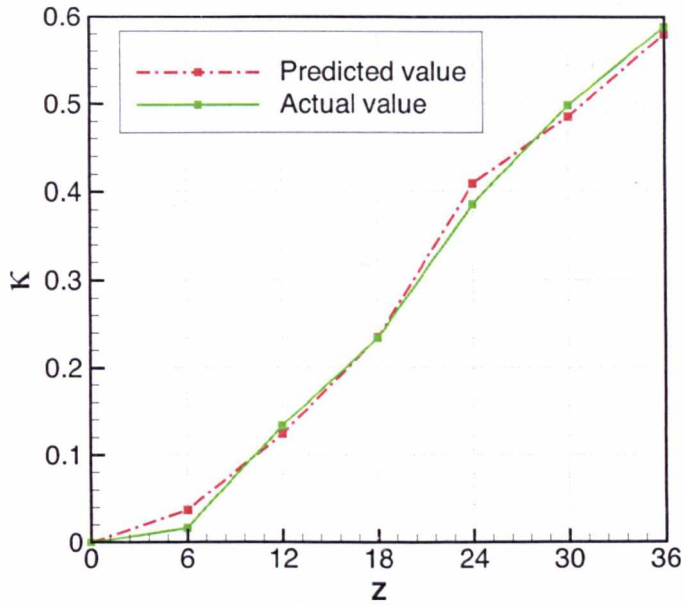
for the smaller value of K for $R_A = 0.25D$.

The predicted and actual values of K are close for both cases, however, the difference is larger for $R_A = 0.2D$. This is because the difference between the velocity fields of the component helical geometries is larger, and therefore the velocity field in the combined geometry deviates more from the idealised prediction, than it does for $R_A = 0.25D$, where the difference is smaller. Indeed, examining $\mathbf{V}_{in-plane}$ for $R_A = 0.25D$ & $R_B = 0.5D$ shows that a good correspondence for the respective single helical velocity fields, and for more of the geometry, than is the case for $R_A = 0.2D$. For both geometries, the slightly larger value of K compared with the predicted value is possibly due to the larger magnitudes of the velocity $\mathbf{V}_{in-plane}$, which will advect the particles a longer distance in each pitch length of the geometry, therefore enhancing the rate of mixing, if not the structure itself.

The closeness of the prediction of K to the actual value, means that the idealised model of Chapter 4 is a useful tool for guiding designs. It is computationally cheaper to solve for the velocity field, and track particles through single helical geometries, than it is the combined geometries. Therefore, a larger portion of the parameter space can be investigated using the idealised model, than would be possible using the methodology presented in this Chapter.



(a) $R_A = 0.2$, $R_B = 0.5$



(b) $R_A = 0.25$, $R_B = 0.5$

Figure 5.18: Relative entropy increase, K, for combined geometries, showing evolution with axial location, and comparing idealised prediction with particle tracking in actual velocity field.

Table 5.2 shows the pressure loss for both of the combined geometries examined, at a Reynolds number of 250. The agreement for all cases is good, with no more than 6% deviation. For the case $R_A = 0.25D$ and $R_B = 0.5D$ the difference is much smaller, less than 2%. This is because this combination has a smaller difference between the component velocity fields. As this difference grows, the additional pressure loss increases.

Table 5.2: Pressure loss, at $Re = 250$, for the two combined helical geometries considered in this Chapter, compared with the idealised prediction from Chapter 4.

$\mathbf{R_A}$	$\mathbf{R_B}$	Δp - predicted	Δp - actual	**Correction factor**
0.2	0.5	2.08355	2.205707	1.058629
0.25	0.5	2.22392	2.263058	1.017599

The velocity fields examined in Section 5.2 clearly show a large degree of variation from the idealised model, with the transition between the two geometries occurring along the full length of the combined geometry. However, the pressure drop appears to be well predicted, and with sufficient accuracy for it to be used as a basis for design decisions, particularly with the knowledge that the bigger the difference between component velocity fields, the larger the error will be, in both the pressure loss and K.

5.4 Conclusions

It is found that the flow adjusts to the change in geometry over the whole length, though the vortical structure adapts to the new geometry more quickly than the axial velocity. Significantly, the velocity fields never quite attain their respective single helix solutions, vindicating the decision to perform these flow calculations. The in-plane velocity field varies correspondingly, and is far from changing discontinuously as in the idealisation.

However, despite this, the results here confirm the prediction made in Chapter 4 that the geometry $R_A = 0.2D$ & $R_B = 0.5D$ produces greatly enhanced mixing, and out of the combinations considered, performs the best. The combination $R_A = 0.25D$ & $R_B = 0.5D$ is almost as effective, but generates a larger pressure loss, and therefore is less attractive for medical applications. Indeed, the pressure loss incurred by both geometries may be too large, and therefore a more appropriate choice of design is $R_A = 0.2D$ & $R_B = 0.35D$, which is predicted to generate enhanced mixing, for a pressure loss only slightly larger than that for $R = 0.25D$ (see Chapter 3). Ultimately, the relative importance of mixing, K and pressure loss in selecting an optimal geometry can only be determined through *in vivo* trials of several different geometries, using the results shown here to guide the selection. Furthermore the results suggest that the idealised model of mixing presented in Chapter 4 is sufficiently accurate for guiding future designs of bypass grafts and A-V shunts that utilise combined helical geometries.

The numerical methodology shown here, and in Chapter 2, can in principle be applied to solve the flow in any spline fitted pipe geometry, where the splines are functions only of z, and periodic boundary conditions apply. For the helical geometry case this could involve looking at different pitch lengths of each helical geometry, or more complicated sequences composed of many different geometries. From the perspective of mixing applications, it is unlikely that the optimal configuration is equal lengths of each geometry, and this is an obvious next step, though the possibilities are limited only by imagination and the computational resources at hand. Furthermore, a fuller investigation of developing helical flow can be made, by using the coordinate transformation formulation to create a geometry consisting of a long straight pipe, joined to several pitch lengths of a helical geometry. If the straight pipe is sufficiently long, then it will be possible to use a periodic boundary condition.

Chapter 6

Conclusions and Further Work

6.1 Summary of key results

The flow in small-amplitude helical pipes has been investigated, using an approximation to the helical pipe geometry, in combination with a coordinate transformation of the Navier-Stokes equations. The resulting equations were solved using a Fourier decomposition in the periodic coordinate direction, and a two-dimensional planar mesh used in the circular cross-section. Helical pipes, for a range of helical radii, were examined for physiologically realistic Reynolds numbers.

For all the geometries examined the velocity field comprised an asymmetric axial velocity profile and a single, dominant vortical structure in the secondary flow, as identified by several metrics. The radial offset of peak axial velocity was strongly linked to the presence, and extent, of a *line-of-sight* region, which exists due to the helical radius being smaller than the pipe diameter. Particle tracking performed in these velocity fields shows a gradual emergence of a double-vortex structure, with increasing helical radius. The apparent discrepancy between the unimodal vortical structure and the bimodal mixing structure, is shown to be resolved using a sequence of translating and rotating reference frame changes or coordinate transformations. The velocity field transporting the particles can be determined explicitly

from the calculated velocity field, and the velocities associated with the reference frame changes, with the relative magnitudes of these different velocities determining the structure of the observed particle trajectories.

It has also been found that the degree of mixing, which is directly related to the emerging double-vortex structure, asymptotes as the helical radius reaches $R = 0.5D$, as shown by considering statistics of the particle residence time distributions and an information entropy measure. In the context of medical applications the optimal trade-off of mixing and pressure loss is found for $R = 0.25D$, assuming a pitch length of $6D$.

In order to overcome the limit on the mixing attainable in single helical pipes, the principle of 'streamline crossing' is harnessed by combining helical geometries of differing helical radius. Using the velocity fields obtained previously, an idealised prediction of the mixing generated by various combinations of helical pipes could be easily made. It is found that for almost all combinations a significant increase in mixing is generated, with only small increases in pressure loss predicted. The most effective geometry, of those investigated, combines the helical radii of $0.2D$ and $0.5D$, producing approximately a 70% increase in the information entropy measure of mixing.

Using the same coordinate transformation of the Navier-Stokes equations, as that applied to single helical geometries, in combination with spline functions, (which remove the discontinuity in gradient at the joint), the true velocity field in combined helical geometries is determined. The idealised prediction of mixing in combined geometries assumed an instantaneous change in velocity field from one geometry to the next. In actuality, the velocity field is continuously changing throughout the whole length of the geometry, and it is thought that an additional $50-100\%$ increase in length would be needed for a steady state to be reached in either component geometry.

Whilst this assumption of instantaneous change was thought to be essential for generating efficient mixing, the idealised prediction of a global mixing metric (infor-

mation entropy) is in very good agreement with the true case, as are the Poincaré sections and residence time distributions. This means that the idealised prediction can be used for guiding future refinements of the combined geometry designs, in a more efficient manner than could be achieved if the full problem had to be solved for each trial geometry.

To conclude, the results in this thesis improve the understanding of the fluid mechanical properties of helical pipe geometries, particularly in explaining the structure of particle trajectories. This enables any future design optimisation of small amplitude helical pipe prostheses, to be better directed, whether the proposed design uses a single geometry configuration, a combination of different geometries or some other variant.

6.2 Further work

The proposed extensions to the work can be broadly categorised in the following way; assessing the behaviour of helical pipe geometries under operating conditions that are more physiologically realistic, further refinements to the concept of multiple helical geometries to optimise the mixing performance, and finally, investigating the implications of vortical structure definitions for arbitrary pipe flows, particularly those representative of flow in arterial geometries.

6.2.1 Physiologically realistic operating conditions

Steady flow has been assumed throughout, with the results being the fully developed, periodic solution. However, is likely, due to the unsteady nature of blood flow, and the relatively short distance over which a helical pipe would be used, that the *in vivo* flow will not attain this solution. Therefore, all of the results presented in this thesis must be viewed with this caveat in mind.

This suggests that the most important extension to this work is to consider the

effect of unsteady flow, on both the velocity field, and the mixing. Assuming a quasi-steady approximation, the results of Chapter 5 give some indication as to the likely qualitative effect. However, to determine the full effect of unsteady flow, the starting point would be to force the flow using a pressure gradient composed of a mean component plus a sinuosoidal component. This can be further refined to incorporate realistic pressure waveforms composed of several harmonics, or to use the numerical data given in McDonald (McDonald 1974), and used by Zabielski & Mestel (Zabielski L. 1998).

If an unsteady boundary condition is applied, the issue of wall compliance then becomes of increased interest. Although the assumption of rigid walls is reasonable, particularly for prosthetic devices, even the addition of a small degree of compliance can affect the secondary flow in a curved pipe. In addition, it is suggested that locations of the vasculature encountering a large phase difference between time-varing wall shear stress and circumferential stress, are susceptible to the initiation of atherosclerosis (Tada & Tarbell 2005). It is proposed that research into the effects of compliance can proceed in two directions. The first is to examine the problem analytically, using perturbation methods and matched asymptotic expansions for the Navier-Stokes equations in a helical coordinate system. The second is to perform a numerical investigation for physiological values of compliance, Reynolds number and pressure waveform.

A further refinement, but likely the least significant, would be to use a non-Newtonian model of blood viscosity, to determine the effect that shear-thinning has on both the velocity field and on the mixing behaviour.

In order to extend the results more fully to the range of Reynolds number appropriate to an A-V shunt application, a stability analysis of the flow in small amplitude helical pipes should be performed. This would reveal the Reynolds number at which transition occurs, and provide insight into the physical mechanisms by which curvature and torsion influence stability of pipe flows. Although an attempt has been made previously (Yamamoto, Yanase, & Jiang 1998), the geometries considered did

not possess a *line-of-sight* region, that is, the helical radius was larger than the pipe diameter, for all cases. It is therefore possible that those results may not readily apply to the small amplitude geometries proposed for use as A-V shunts.

All of the helical geometries and boundary conditions considered in this thesis are idealised, to allow maximum understanding of the fundamental physical principles of helical pipe flow. It is therefore of interest to apply these general insights to *in vivo* graft configurations and flow conditions. This can be accomplished by using magnetic resonance imaging (MRI) or computed-tomography (CT) scans to obtain patient specific geometries of arteries and prosthetic devices. The flow in these realistic geometries can be compared with that in idealised representations of these configurations, again allowing general principles to be discerned.

To test the hypothesis that fluid mixing prevents thrombosis in prosthetic devices, it may also be possible to link the flow simulations to one of the several thrombosis models in the literature, such as those proposed by Fogelson (Fogelson & Guy 2004) or Harrison *et al.* (Harrison, Smith, Bernsdorf, Hose, & Lawford 2007). At this stage, these tend to be computationally expensive, often prohibitively so, for full three-dimensional simulations. However if a simplified model that captures the key features of thrombosis formation can be validated, this may be a realistic proposition in the near future.

6.2.2 Optimisation of multiple helical geometries

In Chapters 4 & 5 the combination of helical geometries was the simplest possible, in that two geometries of differing helical radius, but equal pitch length, were concatenated. Given that the velocity magnitudes of the in-plane field differ between geometries, this is unlikely to be the optimal configuration. To compensate, the lengths of each section can be scaled by the ratio of the in-plane velocity magnitudes, so that each section is stretching the fluid elements by approximately the same amount. That is one possible approach, another is to keep the ratio of lengths

at 1 : 1, but to use a shorter or longer section than the pitch length of the helix. Obviously, both approaches can be used simultaneously, and made general by allowing both the helical radius and pitch length of each geometry to be varied, along with the lengths of each section. The parameter space thus generated is large, and a sensible approach to exploring it would be required. An even more general approach is to compose the geometry entirely of spline functions, and vary the geometry continuously along its length. Optimising this configuration would however, require an approach different to that used in Chapter 4.

It is likely that the optimal configuration of combined helical geometries will be different for the two intended applications. The most significant reason is due to the Reynolds number differing by a factor of approximately 5, which means the secondary flow will vary significantly. This implies that the 'streamline crossing' of a particular configuration will also change. Furthermore, when designing an A-V shunt, an additional requirement or constraint may be the reduction/elimination of transition to turbulence, which may necessitate a trade-off in the mixing that can be generated.

6.2.3 General pipe flows

The results presented in Chapter 3 show that a discrepancy exists between vortical structures and the motion of particles, leading to questions of the appropriate definition of a vortex for pipe flows. Much of the research on idealised modelling of arteries assumes planar curved geometries, which means that the particle transport is trivially related to the secondary flow. Given that arterial geometries are seldom planar, but helical (Zabielski & Mestel 1998), this simple relationship no longer holds. It seems that an *objective* measure such as that proposed by Haller (Haller 2005) may be more appropriate. It is therefore sensible to review current findings on arterial flows, particularly regarding vortical structures, in the light of these preliminary results.

On a final note, helical symmetry is often present in other flows, such as the vortical filaments shed by vortex generators on aircraft wings, and in cytoplasmic nutrient transport (van de Meent, Tuval, & Goldstein 2008). The findings presented here may find further utility in such research.

Bibliography

Allender, S., Peto, V., Scarborough, P., Kaur, A., & Rayner, M. (2008). Coronary Heart Disease Statistics. Technical report, British Heart Foundation.

Aref, H. (1984). Stirring by chaotic advection. *Journal of Fluid Mechanics 143*, 1–21.

Aref, H. & Balachandar, S. (1986). Chaotic advection in a Stokes flow. *Physics of Fluids 29*(11), 3515–3521.

Berger, S. A., Talbot, L., & Yao, L. S. (1983). Flow in Curved Pipes. *Annual Review of Fluid Mechanics 15*, 461–512.

Bludzuweit, C. (1994). Ph. D. thesis, University of Strathclyde, Glasgow.

Blyth, M. G., Mestel, A. J., & Zabielski, L. (2002). Arterial bends: The development and decay of helical flows. *Biorheology 39*, 345–350.

Bryan, A. J. & Angelini, G. D. (1994). The biology of saphenous vein graft occlusion: etiology and strategies for prevention. *Current opinion in cardiology 9*(6).

Butler, J. P. & Tsuda, A. (1997). Effect of convective stretching and folding on aerosol mixing deep in the lung, assessed by approximate entropy. *J Appl Physiol 83*, 800–809.

Camassa, R. & Wiggins, S. (1991). Chaotic advection in a Rayleigh-Bénard flow. *Physical Review A 43*(2), 774–798.

Caro, C. G., Cheshire, N. J., & Watkins, N. (2005). Preliminary comparative study of small amplitude helical and conventional ePTFE arteriovenous shunts in pigs. *Journal of The Royal Society Interface 2*, 261–266.

Caro, C. G., Fitz-Gerald, J. M., & Schroter, R. C. (1971). Atheroma and Arterial Wall Shear Observation, Correlation and Proposal of a Shear Dependent Mass Transfer Mechanism for Atherogenesis. *Proceedings of the Royal Society of London. Series B, Biological Sciences 177*(1046), 109–133.

Caro, C. G., Watkins, N. V., & Sherwin, S. J. (2005, December). Helical Graft. EP1605868.

Caro, C. G., Doorly, D. J., Tarnawski, M., Scott, K. T., Long, Q., & Dumoulin, C. L. (1996). Non-Planar Curvature and Branching of Arteries and Non-Planar-Type Flow. *Proceedings: Mathematical, Physical and Engineering Sciences 452*(1944), 185–197.

Chandran, K. B. (1993, November). Flow Dynamics in the Human Aorta. *Journal of Biomechanical Engineering 115*, 611–616.

Chemineer (2009). www.chemineer.com.

Chen, W. & R., J. (1992). The characteristics of laminar flow in a helical circular pipe. *Journal of Fluid Mechanics 244*, 241–256.

Chong, M. S., Perry, A. E., & Cantwell, B. J. (1990). A general classification of three-dimensional flow fields. *Physics of Fluids A 2*(5), 765–777.

Colombo, A. & Tobis, J. M. (2000). *Techniques in Coronary Artery Stenting*, Chapter 2, pp. 39–70. Number 1853177164. Informa Health Care.

Coppola, G. & Caro, C. (2008a). Arterial geometry, flow pattern, wall shear and mass transport: potential physiological significance. *Journal of The Royal Society Interface*, –.

Coppola, G. & Caro, C. (2008b). Oxygen mass transfer in a model three-dimensional artery. *Journal of The Royal Society Interface 5*(26), 1067–1075.

Coppola, G., Sherwin, S. J., & Peiro, J. (2001). Non-linear particle tracking for high-order elements. *Journal of Computational Physics 172.*

Cucitore, R., Quadrio, M., & Baron, A. (1999). On the effectiveness and limitations of local criteria for the identification of a vortex. *European Journal of Mechanics - B/Fluids 18*(2), 261–282.

Dammers, R., Planken, R. N., Pouls, K. P. M., van Det, R. J., Burger, H., van der Sande, F. M., & Tordoir, J. H. M. (2003). Evaluation of 4-mm to 7-mm versus 6-mm prosthetic brachial-antecubital forearm loop access for hemodialysis: Results of a randomized multicenter clinical trial. *Journal of Vascular Surgery 37*, 143–148.

Daskopoulos, P. & Lenhoff, A. M. (1989). Flow in curved ducts: bifurcation structure for stationary ducts. *Journal of Fluid Mechanics 203*, 125–148.

Dean, W. R. (1928). The streamline motion of fluid in a curved pipe. *Philos. Mag. 30*, 673–93.

Dennis, S. C. R. & Ng, M. (1982). Dual Solutions for Steady Laminar Flow Through a Curved Tube. *Quarterly Journal of Mechanics and Applied Mathematics 35*(3), 305–324.

Doorly, D. J. (1999). Flow Transport In Arteries. In S. G. Sajjadi, G. B. Nash, & M. W. Rampling (Eds.), *Cardiovascular Flow Modelling And Measurement With Application To Clinical Medicine*, pp. 67–81. Oxford University Press.

Doorly, D. J., Sherwin, S. J., Franke, P. T., & Peiro, J. (2002). Vortical flow structure identification and flow transport in arteries. *Computer Methods in Biomechanics and Biomechanical Engineering 5*(3), 261–275.

Eustice, J. (1910, July). Flow of Water in Curved Pipes. *Proceedings of the Royal Society of London. Series A, Containing Papers of a Mathematical and Physical Character 84*(568), 107–118.

Eustice, J. (1911, April). Experiments on Stream-Line Motion in Curved Pipes.

Proceedings of the Royal Society of London. Series A, Containing Papers of a Mathematical and Physical Character 85(576), 119–131.

Fogelson, A. L. & Guy, R. D. (2004). Platelet–wall interactions in continuum models of platelet thrombosis: formulation and numerical solution. *Mathematical Medicine and Biology 21*(4), 293–334.

Franjione, J. G. & Ottino, J. M. (1991, November). Stretching in duct flows. *Physics of Fluids A: Fluid Dynamics 3*(11), 2819–2821.

Franjione, J. G. & Ottino, J. M. (1992, February). Symmetry Concepts for the Geometric Analysis of Mixing Flows. *Philosophical Transactions: Physical Sciences and Engineering 338*(1650), 301–323.

Friedman, M. H. (1993). Arteriosclerosis research using vascular flow models: from 2-D branches to compliant replicas. *Journal of biomechanical engineering 115*(4B), 595–601.

Gammack, D. & Hydon, P. E. (2001). Flow in pipes with non-uniform curvature and torsion. *Journal of Fluid Mechanics 433*, 357–382.

Germano, M. (1981). On the effect of torsion on a helical pipe flow. *Journal of Fluid Mechanics 125*, 1–8.

Germano, M. (1989). The Dean equations extended to a helical pipe flow. *Journal of Fluid Mechanics 203*, 289–305.

Hadi, A. M. A. & Sharma, K. C. (2002). Flow of non-Newtonian fluid in a helical pipe with an elliptical cross-section. *India Journal of Pure and Applied Mathematics 33*(1), 131–145.

Hakaim, A. G. & Oldenburg, W. A. (2001). *Dialysis Access: Current Practice*, Chapter Use of Autogenous Vein or Synthetic Grafts, pp. 181–210. Number 9. Imperial College Press.

Haller, G. (2005). An objective definition of a vortex. *Journal of Fluid Mechanics 525*, 1–26.

Harrison, S. E., Smith, S. M., Bernsdorf, J., Hose, D. R., & Lawford, P. V. (2007). Application and validation of the lattice Boltzmann method for modelling flow-related clotting. *Journal of Biomechanics 40*, 3023–3028.

How, T. V., Fisher, R. K., Brennan, J. A., & Harris, P. L. (2006). Swirling flow pattern in a non-planar model of an interposition vein cuff anastomosis. *Medical Engineering & Physics 28*, 27–35.

Huber, T. S., Carter, J. W., Carter, R. L., & Seeger, J. M. (2003). Patency of autogenous and polytetrafluoroethylene upper extremity arteriovenous hemodialysis accesses: A systematic review. *Journal of Vascular Surgery 38*(5), 1005–1011.

Huijbregts, H. J. T. A. M., Blankestijn, P. J., Caro, C. G., Cheshire, N. J. W., Hoedt, M. T. C., Tutein Nolthenius, R. P., & Moll, F. L. (2007). A Helical PTFE Arteriovenous Access Graft to Swirl Flow Across the Distal Anastomosis: Results of a Preliminary Clinical Study. *European Journal of Vascular and Endovascular Surgery 33*(4), 472–475.

Hunt, J. C. R., Wray, A. A., & Moin, P. (1998). Eddies, stream, and convergence zones in turbulent flows. Technical Report CTR-S88, Center for Turbulence Research.

Hwang, W. R. & Kwon, T. H. (2003, April). Chaotic Volumetric Transports in a Single-Screw Extrusion Process. *Polymer Engineering and Science 43*(4), 783–797.

Ito, H. (1987). Flow in Curved Pipes. *Bulletin of the JSME 30*(262), 543–552.

Jeong, J. & Hussain, F. (1995). On the identification of a vortex. *Journal of Fluid Mechanics 285*, 69–94.

Jones, S. W., Thomas, O. M., & Aref, H. (1989). Chaotic advection by laminar flow in a twisted pipe. *Journal of Fluid Mechanics 209*, 335–357.

Ju, H., Huang, Z., Xu, Y., Duan, B., & Yu, Y. (2001). Hydraulic Performance of Small Bending Radius Helical Coil-Pipe. *Journal of Nuclear Science and Technology 38*.

Kang, T. G. & Kwon, T. H. (2004). Colored particle tracking method for mixing analysis of chaotic micromixers. *Journal of Micromechanics and Microengineering 14*, 891.

Kao, H. C. (1987). Torsion effect on fully developed flow in a helical pipe. *Journal of Fluid Mechanics 184*, 335–356.

Karniadakis, G. E., Israeli, M., & Orszag, S. A. (1991). High-Order Splitting Methods for the Incompressible Navier-Stokes Equations. *Journal of Computational Physics 97*, 414–443.

Khakhar, D. V. (1986). Analysis of chaotic mixing in two model systems. *Journal of fluid mechanics 172.*

Khakhar, D. V., Franjione, J. G., & Ottino, J. M. (1987). A case study chaotic mixing in deterministic flows: the partitioned pipe mixer. *Chemical Engineering Science 42*, 2909–2926.

Kin, E. & Sakajo, T. (2005). Efficient topological chaos embedded in the blinking vortex system. *Chaos 15.*

Koberg, W. H. (2008). *Turbulence control for drag reduction with active wall deformation.* Ph. D. thesis, Imperial College London.

Krasnopolskaya, T. S., Meleshko, V. V., Peters, G. W. M., & Meijer, H. E. H. (1999). Mixing in Stokes flow in an annular wedge cavity. *European journal of mechanics. B, Fluids 18*(5).

Laine-Pearson, F. E. & Hydon, P. E. (2006). Particle transport in a moving corner. *Journal of Fluid Mechanics 559*, 379–390.

Ling, F. H. (1993). The effect of mixing protocol on mixing in discontinuous cavity flows. *Phys. Lett. A 177*, 331–337.

Liu, R. H., Stremler, M. A., Sharp, K. V., Olsen, M. G., Santiago, J. G., Adrian, R. J., Aref, H., & Beebe, D. J. (2000). Passive mixing in a three-dimensional

serpentine microchannel. *Microelectromechanical Systems, Journal of 9*, 190–197. 1057-7157.

Liu, S. M. J. H. (1993). Axially invariant laminar flow in helical pipes with a finite pitch. *Journal of Fluid Mechanics 251*, 315–353.

McDonald, D. A. (1974). *Blood flow in arteries.* The Camelot Press Ltd.

M.D. Finn, S.M. Cox, H. B. (2004). Mixing measures for a two-dimensional chaotic Stokes flow. *Journal of engineering mathematics 48*(129-155).

Metcalfe, G., Bina, C. R., & Ottino, J. M. (1995, April). Kinematic considerations for mantle mixing. *Geophysical Research Letters 22*(7), 743–746.

Mezic, I., Wiggins, S., & Betz, D. (1999). Residence-time distributions for chaotic flows in pipes. *Chaos: An Interdisciplinary Journal of Nonlinear Science 9*(1), 173–182.

Moore, J. A., Steinman, D. A., Prakash, S., Johnston, K. W., & Ethier, C. R. (1999, June). A Numerical Study of Blood Flow Patterns in Anatomically Realistic and Simplified End-to-Side Anastomoses. *Journal of Biomechanical Engineering 121*, 265–272.

Murata, S., Miyake, Y., Inaba, T., & Ogawa, H. (1981, February). Laminar Flow in a Helically Coiled Pipe. *Bulletin of the JSME 24*(188), 355–362.

Newman, D. (1996). *A computational study of fluid/structure interactions: flow-induced vibrations of a flexible cable.* Ph. D. thesis, Princeton University.

Nielsen, L. B. (1996). Transfer of low density lipoprotein into the arterial wall and risk of atherosclerosis;. *Atherosclerosis 123*(1-2), 1–15.

Ottino, J. M. (1989). *The kinematics of mixing: stretching, chaos, and transport.* Cambridge University Press. 0-521-36878-2.

Papaharilaou, Y., Doorly, D. J., & Sherwin, S. J. (2002). The influence of out-of-plane geometry on pulsatile flow within a distal end-to-side anastomosis. *Journal of Biomechanics 35*, 1225–1239.

Pitt, R. (2005). *Numerical Simulation of Fluid Mechanical Phenomena in Idealised Physiological Geometries: Stenosis and Double Bend.* Ph. D. thesis, University of London.

R. Haimes, M. G. (1991). VISUAL3: Interactive unsteady 3D visualization. *AIAA.*

Ramstack, J. M., Zuckerman, L., & Mockros, L. F. (1979). Shear-induced activation of platelets. *Journal of Biomechanics 12*(2), 113–125.

Rennie, T. J. & Raghavan, V. G. S. (2006). Numerical studies of a double-pipe helical heat exchanger. *Applied Thermal Engineering 26*, 1266–1273.

Scofield, P. D. (1995). Curves of Constant Precession. *The American Mathematical Monthly 102*(6), 531–537.

Shannon, C. E. (1948). A Mathematical Theory of Communication. *Bell System Technical Journal 27*, 379–423.

Sherwin, S. J., Doorly, D. J., Franke, P., & Peiro, J. (2002). Unsteady Near Wall Residence Times and Shear Exposure in Model Distal Arterial Bypass Grafts. *Biorheology 39*, 365–71.

Sherwin, S. J. & Karniadakis, G. E. (2005). *Spectral/hp Element Methods for Computational Fluid Dynamics.* Oxford Science Publications.

Sherwin, S. J., Shah, O., Doorly, D. J., Peiro, J., Papaharilaou, Y., Watkins, N., Caro, C. G., & Dumoulin, C. L. (2000). The Influence of Out-of-Plane Geometry on the Flow Within a Distal End-to-Side Anastomsis. *ASME J. Biomech 122*, 86–95.

Siggers, J. H. & Waters, S. L. (2008). Unsteady flows in pipes with finite curvature. *Journal of Fluid Mechanics 600*, 133–165.

Stroock, A. D., Dertinger, S. K. W., Ajdari, A., Mezic, I., Stone, H. A., & Whitesides, G. M. (2002). Chaotic Mixer for Microchannels. *Science 295*, 647–651.

Sturman, R., Ottino, J. M., & Wiggins, S. (2006). *The Mathematical Foundations of Mixing: The Linked Twist Map as a Paradigm in Applications: Micro to Macro, Fluids to Solids.* Cambridge University Press.

Tada, S. & Tarbell, J. M. (2005, September). A Computational Study of Flow in a Compliant Carotid Bifurcation - Stress Phase Angle Correlation with Shear Stress. *Annals of Biomedical Engineering 33*(9), 1202–1212.

Taylor, G. I. (1929). The Criterion for Turbulence in Curved Pipes. *Proceedings of the Royal Society of London. Series A, Containing Papers of a Mathematical and Physical Character 124*, 243–49.

Tricht, I. V., Wachter, D. D., Tordoir, J., & Verdonck, P. (2006). Comparison of the hemodynamics in 6mm and 4-7mm hemodialysis grafts by means of CFD. *Journal of Biomechanics 39*, 226–236.

Tuttle, E. R. (1990). Laminar flow in twisted pipes. *Journal of Fluid Mechanics 219*, 545–570.

van de Meent, J.-W., Tuval, I., & Goldstein, R. E. (2008). Nature's Microfluidic Transporter: Rotational Cytoplasmic Streaming at High Peclet Numbers. *Physical Review Letters 101.*

Vassilicos, J. C. (2002). Mixing In Vortical, Chaotic and Turbulent Flows. *Phil. Trans. R. Soc. Lond. A 360*, 2819–2837.

Walatka, P. P., Buning, P., Pierce, L., & Elson, P. A. (1990). *PLOT3D User's Manual.* NASA.

Wang, C. Y. (1981). On the low-Reynolds-number flow in a helical pipe. *Journal of Fluid Mechanics 108*, 185–194.

Wang, W., Manas-Zloczower, I., & Kaufman, M. (2003). Entropic characterization of distributive mixing in polymer processing equipment. *AIChE Journal 49*, 1637–1644.

Wang, W., Manas-Zloczower, I., & Kaufman, M. (2005a). Entropy time evolution in a twin-flight single-screw extruder and its relationship to chaos. *Chemical Engineering Communications 192*, 405–423.

Wang, W., Manas-Zloczower, I., & Kaufman, M. (2005b). Influence of initial conditions on distributive mixing in a twin-flight single-screw extruder. *Chemical Engineering Communications 192*, 749–757.

White, C. M. (1929). Streamline Flow through Curved Pipes. *Proceedings of the Royal Society of London. Series A, Containing Papers of a Mathematical and Physical Character 123*(792), 645–663.

Wiggins, S. (2005). The Dynamical Systems Approach To Lagrangian Transport In Oceanic Flows. *Annual Review of Fluid Mechanics 37*, 295–328.

Wiggins, S. & Ottino, J. M. (2004). Foundations of Chaotic Mixing. *Phil. Trans. R. Soc. Lond. A 362*, 937–970.

Yamamoto, K., Akita, T., Ikeuchi, H., & Kita, Y. (1995). Experimental study of the flow in a helical circular tube. *Fluid Dynamics Research 16*, 237–249.

Yamamoto, K., Alam, M. M., Yasuhara, J., & Aribowo, A. (2000). Flow through a rotating helical pipe with circular cross-section. *International Journal of Heat and Fluid Flow 21*, 213–220.

Yamamoto, K., Aribowo, A., Hayamizu, Y., Hirose, T., & Kawahara, K. (2002). Visualization of the flow in a helical pipe. *Fluid Dynamics Research 30*, 251–267.

Yamamoto, K., Yanase, S., & Jiang, R. (1998). Stability of the flow in a helical tube. *Fluid Dynamics Research 22*, 153–170.

Zabielski, L. & Mestel, A. J. (1998). Steady flow in a helically symmetric pipe. *Journal of Fluid Mechanics 370*, 297–320.

Zabielski L., M. A. J. (1998). Unsteady blood flow in a helically symmetric pipe. *Journal of Fluid Mechanics 370*, 321–345.

Zhang, B., Ma, Z., Su, X., & Zhang, J. (2003, May). A Study on the Unsteady Flow in a Helical Pipe. *Applied Mathematics and Mechanics 24*(5), 585–595.

Appendix A

Properties of Space Curves

This Appendix outlines the definitions of curvature and torsion for three-dimensional space curves, and applies them to a helix and the spline functions used in Chapter 5. Consider curves parametrised in the form:

$$r(t) = (x(t), y(t), z(t)) \tag{A.1}$$

Curvature measures a curve's deviation from a straight line and is defined as:

$$\kappa = \frac{[(y''z')^2 + (x''z')^2 + (y''x' - x''y')^2]^{1/2}}{(x'^2 + y'^2 + z'^2)^{3/2}} \tag{A.2}$$

where the prime notation represents a derivative. The torsion, which indicates the rate at which the curve deviates from the plane, is defined as:

$$\tau = \frac{z'''(x'y'' - y'x'') + z''(x'''y' - x'y''') + z'(x''y''' - x'''y'')}{(x'^2 + y'^2 + z'^2)(x''^2 + y''^2 + z''^2)} \tag{A.3}$$

For a helix parametrised in t, the derivatives are as follows:

$$x' = -R\sin t \quad y' = R\cos t \quad z' = c \tag{A.4}$$

$$x'' = -R\cos t \quad y'' = -R\sin t \quad z'' = 0 \tag{A.5}$$

$$x''' = R\sin t \quad y''' = -R\cos t \quad z''' = 0 \tag{A.6}$$

For a helix the curvature is therefore:

$$\kappa = \frac{\left[R^2 \sin^2 t.c^2 + R^2 \cos^2 t.c^2 + ((-R\sin t).(-R\sin t) - (-R\cos t.R\cos t))^2\right]^{1/2}}{(R^2 \sin^2 t + R^2 \cos^2 t + c^2)^{3/2}} \tag{A.7}$$

$$\kappa = \frac{(R^4 + R^2c^2)^{1/2}}{(R^2 + c^2)(R^2 + c^2)^{1/2}} = \frac{R}{R^2 + c^2} \tag{A.8}$$

The torsion, τ, is:

$$\tau = \frac{(((-R\cos t).(-R\cos t)) - (R\sin t.(-R\sin t)))c}{(R^2 \sin^2 t + R^2 \cos^2 t + c^2)(R^2 \cos^2 t + R^2 \sin^2 t)} \tag{A.9}$$

$$\tau = \frac{R^2 c}{(R^2 + c^2)R^2} = \frac{c}{R^2 + c^2} \tag{A.10}$$

Note that curvature only includes terms upto second order, however torsion also involves third order derivatives. This implies that the third order derivatives in the body force terms **A** derived in Chapter 2, can be attributed solely to effects of torsion.

These formulae are similarly applied to the spline equations used in Chapter 5 which are of the form:

$$x(t) = a_7 t^7 + a_6 t^6 + a_5 t^5 + a_4 t^4 + a_3 t^3 + a_2 t^2 + a_1 t + a_0 \tag{A.11}$$

However in that formulation, the parameterisation is such that $z = t$, and thus $z' = 1$. The spline was implemented computationally by defining it as a function of R_A, R_B and z. This eliminated the need for recoding the function for each geometry. In all, there are four functions that define the geometry. For the general spline equation (A.11) the functions have the following coefficients.

Cosine - $5.25 < z < 6$

$$
\begin{aligned}
a_7 &= (0.076228172730790554707 * R_A) + (-0.076311923539339359980 * R_B) \\
a_6 &= (-3.2025281079870953740 * R_A) + (3.2041559353583610429 * R_B) \\
a_5 &= (57.441304569237002621 * R_A) + (-57.436590743339669915 * R_B) \\
a_4 &= (-570.13388546247788873 * R_A) + (569.79671831045797727 * R_B) \\
a_3 &= (3381.8871165635101312 * R_A) + (-3378.7253598061659128 * R_B) \\
a_2 &= (-11989.150139055338014 * R_A) + (11976.367653701758204 * R_B) \\
a_1 &= (23523.721458612015963 * R_A) + (-23499.630106399945904 * R_B) \\
a_0 &= (-19711.468049734367156 * R_A) + (19692.960820952762213 * R_B) \quad \text{(A.12)}
\end{aligned}
$$

Sine - $5.25 < z < 6$

$$
\begin{aligned}
a_7 &= (-3.0045390642772030464 * R_A) + (3.0042743117852417453 * R_B) \\
a_6 &= (121.10748859491345183 * R_A) + (-121.09636899025107718 * R_B) \\
a_5 &= (-2088.4328134603235847 * R_A) + (2088.2431473023911971 * R_B) \\
a_4 &= (19972.484324486526127 * R_A) + (-19970.797397427009372 * R_B) \\
a_3 &= (-1.1440236541330251266e+5 * R_A) + (1.1439394006776328742e+5 * R_B) \\
a_2 &= (3.9249892402644466306e+5 * R_A) + (-3.9247489724216952132e+5 * R_B) \\
a_1 &= (-7.4684549101941671535e+5 * R_A) + (7.4680735561820026928e+5 * R_B) \\
a_0 &= (6.0802414298399459e+5 * R_A) + (-6.0799651612071791e+5 * R_B) \quad \text{(A.13)}
\end{aligned}
$$

Cosine - $6 < z < 6.75$

$$
\begin{aligned}
a_7 &= (0.076311923539339359980 * R_A) + (-0.076228172730790554707 * R_B) \\
a_6 &= (-3.2060456419461451954 * R_A) + (3.2006384013993112214 * R_B) \\
a_5 &= (57.504620180499899407 * R_A) + (-57.373275132076773129 * R_B) \\
a_4 &= (-570.76704157510685660 * R_A) + (569.16356219782900941 * R_B) \\
a_3 &= (3385.6860532392839384 * R_A) + (-3374.9264231302921057 * R_B) \\
a_2 &= (-12002.826311088123720 * R_A) + (11962.691481668972498 * R_B) \\
a_1 &= (23551.073802677587375 * R_A) + (-23472.277762334374492 * R_B) \\
a_0 &= (-19734.912916076285509 * R_A) + (19669.515954610843860 * R_B) \quad \text{(A.14)}
\end{aligned}
$$

Sine - $6 < z < 6.75$

$$
\begin{aligned}
a_7 &= (3.0042743117852417453 * R_A) + (-3.0045390642772030464 * R_B) \\
a_6 &= (-131.26267319970922942 * R_A) + (131.27379280437160407 * R_B) \\
a_5 &= (2454.2300988428846778 * R_A) + (-2454.4197650008170654 * R_B) \\
a_4 &= (-25454.144798545556498 * R_A) + (25455.831725605073254 * R_B \\
a_3 &= (1.5815740932488998310e+5 * R_A) + (-1.5816583467042920833e+5 * R_B) \\
a_2 &= (-5.8871626503104832165e+5 * R_A) + (5.8874029181532346339e+5 * R_B) \\
a_1 &= (1.2155848870955692541e+6 * R_A) + (-1.2156230224967857001e+6 * R_B) \\
a_0 &= (-1.0740590382574219e+6 * R_A) + (1.0740866651206986e+6 * R_B) \quad \text{(A.15)}
\end{aligned}
$$

Publications

The work presented in this thesis has been published in the form of journal articles, oral presentations and posters.

Journal Publications

The majority of the results presented in Chapter 3 have been published in *Annals of Biomedical Engineering*, particularly focusing on the mixing data. The velocity field results of Chapter 5, along with the coordinate transformation methodology of Chapters 2 & 5, has been published in the *Journal of Computational and Applied Mathematics*. It is intended that a further paper will be published, containing the mixing results of Chapters 4 & 5. The full details of the publications follow.

- Mixing Through Stirring of Steady Flow in Small Amplitude Helical Tubes, A. N. Cookson, D. J. Doorly, S. J. Sherwin. *Annals of Biomedical Engineering*, Vol. 37, No. 4, April 2009, pp. 710-721.
- Using Coordinate Transformation of Navier-Stokes Equations to Solve Flow in Multiple Helical Geometries, A. N. Cookson, D. J. Doorly, S. J. Sherwin. *Journal of Computational and Applied Mathematics*, 2009, doi:10.1016/j.cam.2009.08.065.

Oral Presentations

- Combining Differing Small Amplitude Helical Pipes to Generate Efficient Mixing for Medical Applications, A. N. Cookson, D. J. Doorly, S. J. Sherwin. *Bioengineering '09*, September 2009. Oxford, UK.

- Mixing in Steady flow in Small Amplitude Helical Pipes, A. N. Cookson, D. J. Doorly, S. J. Sherwin. *EFMC7*, September 2008. Manchester, UK.

- Mixing Behaviour of Steady flow in Helical Pipes for Medical Applications A. N. Cookson, D. J. Doorly, S. J. Sherwin. *16th Congress of the European Society of Biomechanics*, 6 - 9th July 2008. Lucerne, Switzerland.

- Investigation of the Fluid Dynamical Properties of Helical Pipes from a Mixing Perspective A. N. Cookson, S. J. Sherwin, D. J. Doorly. *3rd International Symposium on Modelling of Physiological Flows*, 25 - 27th September 2006. Bergamo, Italy.

Poster Presentations

- Mixing Through Stirring of Steady Flow In Small Amplitude Helical Pipes, A. N. Cookson, D. J. Doorly, S. J. Sherwin. *Newton Institute Programme: The Cardiac Physiome Project*, July 2009, Newton Institute, Cambridge, UK.

- Mixing Through Stirring of Steady Flow In Small Amplitude Helical Pipes, A. N. Cookson, D. J. Doorly, S. J. Sherwin. *Aeronautics Research Colloquium 2008*, November 2008, Imperial College London, UK.

- Quantifying Mixing in Helical Pipe Flows, A. N. Cookson, S. J. Sherwin, D. J. Doorly. *Fifth Physiological Flow Meeting: Size, Sex and Sight*, 3-4 September 2007. Imperial College London, UK.

- Quantifying Mixing in Helical Pipe Flows, A. N. Cookson, S. J. Sherwin, D. J. Doorly. *Fourth Physiological Flow Meeting: Respiratory Biomechanics and Physiological Fluid-Structure Interactions Problems*, 2-3 April 2007. Manchester University, UK.

- Fluid Dynamical Properties of Helical Pipes, A. N. Cookson, S. J. Sherwin, D. J. Doorly. *2nd Symposium of the Cardiovascular Technology Network*, 27 February 2007. Imperial College London, UK.

- Investigation of the Fluid Dynamical Properties of Helical Pipes from a Mixing Persepective, A. N. Cookson, S. J. Sherwin, D. J. Doorly. *5th World Congress of Biomechanics*, 29 July - 4 August 2006. Munich, Germany.

- Investigation of the Fluid Dynamical Properties of Helical Pipes from a Mixing Perspective, A. N. Cookson, S. J. Sherwin, D. J. Doorly. *Third Physiological Flow Meeting: Imaging and Modelling for Interventional Planning*, 18-19 April 2006. Oxford UK.